Novel Developments and Applications of Dosimetry in Radiation Therapy Treatment

by

Noora H. Ba Sunbul

A dissertation submitted in partial fulfillment
of the requirements for the degree of
Doctor of Philosophy
(Nuclear Engineering and Radiological Sciences)
in the University of Michigan
2022

Doctoral Committee:

Dr. Martha M. Matuszak, Co-Chair
Professor Sara A. Pozzi, Co-Chair
Professor Emeritus Paul Carson
Dr. Shaun D. Clark
Professor Issam El-Naqa

Noora H. Ba Sunbul

nooraba@umich.edu

ORCID iD: 0000-0001-8321-5995

DEDICATION

“Praise be to God, who guided us to this: had God not guided us, we would never have found the way “(The Qur'an,8:43)

This dissertation was conducted with the hopes to improve the radiation therapy treatment process to help cancer patients undergoing radiation therapy fight cancer.

ACKNOWLEDGEMENTS

First of all, I would like to thank God “Allah” for guiding me throughout this journey extending grace and mercy, and being behind all the main reasons for accomplishing this work. I am so grateful for all the incredible individuals God has placed in my path to support me and have made me the person I am and gotten me to this point in my life.

Mom, Dad, my lovely sisters and brother, my family, and Dr. Al Haiqi’s family, you mean the world to me. I am so blessed to have you in my life, you have always been the stars that shine in my life. I am so grateful for your overwhelming love and support; I couldn’t have made it without your prayers and your patience in listening to my research ideas and complaints. From day one, my dad, Hussein, and my mom, Shafiqa, through their appreciation for education and hard work have influenced my ambition driving me to pursue and complete a doctorate degree. Special thanks to my dad who has shared the first years of my undergrad with me and taught me to be a self-motivated and independent woman abroad in a foreign country. He followed my dream with me just to be the person I am today.

Special thanks to all my friends I am lucky to have throughout my life; back home, during my undergrad, and graduate school who have always been my second family providing me with love and support even though we aren’t always together.

I am so grateful to my spiritual father, Eng. Abdullah Bugshan, who has supported me throughout my graduate studies. He has introduced me to the Hadramout Foundation which has opened the door to supporting me with a full scholarship to pursue my Masters’s degree in the field of my interest. Without their support throughout my graduate studies, I couldn't have started this journey and made my dream come true. Thank you for supporting this work before it has even been started.

Academically, I would first like to express my sincerest gratitude to my first academic and research advisor, Dr. Martha Matuszak, who has introduced me to the field of medical physics and to my other co-advisors; Prof. Sara Pozzi and Prof. Issam El Naqa. I am blessed to have a group of wonderful advisors who have different research backgrounds and expertise. They have continually provided me with mentorship, funding, and opportunities. Their valuable comments, suggestions, and revisions of my research are the fuel to succeed with this dissertation. I am grateful for my other two committee members, Dr. Shaun Clarke and Pro. Paul Carson for their hard work and their support to mentor me and share their experiences and feedback.

I am extremely grateful for the different research groups that I have been part of; the Detection of Nuclear Non-proliferation Group (DNNG) at the Nuclear Engineering department led by Prof. S. Pozzi, Radiation Acoustic Group led by Prof. Issam El Naqa and Prof. Xueding Wang, and Advanced Treatment Planning Research Group led by Dr. Martha Matuszak. Within these groups, I got the chance to meet research scientists, physicists, and young students and got access to many lab spaces and equipment. I am so blessed and honored to have worked with such an incredible group of researchers and young investigators without whom this dissertation would not have been possible.

Special thanks and great appreciation to the University of Michigan Department of Radiation Oncology for providing the support I need to facilitate my research and for giving me access to the clinical resources that supported my work. In addition to the University of Michigan Department of Nuclear Engineering for providing me with comprehensive education and research opportunities. Too many mentors from the radiation oncology and NERS departments and many DNNG students, past, and present. Special thanks to Prof. Jean Moran, Dr. Benjamin Rosen, Dr. Ibrahim Oraiqat, Dr. Wei Zhang, Dr. Dale Litzenberg, Dr. Kwok Lam, Dr. Kyle Cuneo, Prof. Xueding Wang, Dr. Cameron Miller, and Chris Meert for their contributions to this dissertation. I would like to thank Chris Meert, Stefano Marin, and Abbas Jinia for reviewing the dissertation.

Finally, I would like to thank the funding sources that have supported me financially during my study and enable me to conduct the research work of this dissertation. This dissertation work was funded in part by the National Institutes of Health (Grant R37CA222215), US Department of Homeland Security, Countering Weapons of Mass Destruction Office, Academic Research Initiative (Grant No. 2016-DN-077-ARI106), University of Michigan MCubed research funding, Consortium for Monitoring, Technology, and Verification (MTV), and Hadramout Foundation. Special thanks to Modus Medical London, Ontario for providing Clearview gels. I would also like to thank Cliff Hammer from the University of Wisconsin Medical Radiation Research Center for providing independent absolute TLD dose verification for linac commissioning.

TABLE OF CONTENTS

Chapter 3 Application of Radiochromic Gel Dosimetry to Commissioning of a Megavoltage Research Linear Accelerator for Small-Field Animal Irradiation Studies 32

Chapter 4 Monte Carlo Simulations for Commissioning of a Megavoltage Research Linear Accelerator 66

LIST OF TABLES

LIST OF FIGURES

LIST OF ABBREVIATIONS

AAPM	American Association of Physicists in Medicine
CT	Computed Tomography
DICOM	digital imaging and communications in medicine
EBRT	External Beam Radiation Therapy
EPID	Electronic Portal Imaging Device
FFF	Flattening Filter Free
Gy	Gray
HVL	Half-Value Layer
IRAI	Ionizing Radiation Acoustic Imaging
IMRT	Intensity Modulated Radiation Therapy
ICRP	International Commission on Radiological Protection
keV	kiloelectron volt
LET	Linear Energy Transfer
Linac	Linear Accelerator
FWHM	Full Width at Half Maximum
MeV	Mega Electron Volt
MOSFET	Metal oxide semiconductor field-effect transistors
MRI	Magnetic Resonance Imaging

MU	Monitor Unit
MC	Monte Carlo
OAR	Organ At Risk
OSLD	Optically Stimulated Luminescence Dosimeter
OS	Organic Scintillators
OGS	Organic Glass Scintillator
PDD	Percent Depth Dose
PSD	Pulse Shape Discrimination
QA	Quality Assurance
RT	Radiation Therapy
ROF	Relative Output Factor
SSD	Source to Surface Distance
SRS	Stereotactic Radiosurgery
TG	Task Group
TLD	Thermo Luminescent Dosimeter
TPS	Treatment Planning System
TR	Time Reversal
US	Ultrasound
UHDR	Ultra-High Dose Rate
VMAT	Volumetric Modulated Arc Therapy

XACT	XACT X-ray Acoustic Computed Tomography

LIST OF APPENDICES

ABSTRACT

Advanced treatment planning and treatment delivery techniques in radiation therapy have increased the need for comprehensive machine commissioning, quality assurance (QA), and patient-specific QA to ensure that treatments are delivered with precision and accuracy. *In vivo* dosimetry has an important role in verifying the treatment delivery and it is recommended for high dose irradiations, special procedures, and when implementing new treatment techniques. Most of the currently available *in vivo* radiation dosimeters can only provide point measurements or 2D superficial dose measurements, which are not accurate surrogates for the full 3D dose distribution. Ionizing radiation acoustic imaging (iRAI) is a novel 3D dosimetry tool, that has the potential for fast, non-invasive, per pulse dose measurement capability. This research focuses on detailed 3D dosimetry studies testing the feasibility of iRAI in ultra-high dose rate (FLASH) and conventional radiation therapy. A full simulation study was developed to test the potential of iRAI in FLASH-RT for the first time. This study demonstrated the feasibility of iRAI in beam characterization and localization and studied the effect of the linear accelerator (linac) operational parameters and their effect on iRAI imaging.

As part of this work, a customized 2D array transducer was used to study the implementation of iRAI in conventional radiation therapy. Different treatment plan dose distributions were measured and verified with 3D gel dosimetry measurements. IRAI was capable of measuring shifts in the radiation fields within 0.3cm relative to gel results. Additionally, iRAI efficiently detected the radiation field sizes within 0.35cm. The repeatability and dosimetric evaluation of the acquired iRAI dose-related images were promising for relative 3D plan verification and monitoring.

This dissertation also describes the full commissioning of a megavoltage research linac for small-field animal irradiation studies. An efficient and accurate full commissioning procedure has been developed and implemented using 1D, 2D, and 3D gel dosimeters. The characterized 3D gel dosimeters provide a full representation of 3D dose, and dosimeter misalignment corrections, and demonstrated high reproducibility with low interdosimeter variability. Gels have resulted in fast, full relative dosimetry commissioning and beam characterization for non-standard small radiation fields. Dosimetric characteristics have been measured with gels including, the linatron calibration factor, variability with time, beam divergence, dose profiles, percent depth dose curves, and relative output factors. Monte Carlo-based optimization and validation with the experimentally acquired beam characterization results have been implemented. The simulation of the linatron components and the optimization of its initial source has provided a full representation of the dose. The initial linac source parameters were investigated to be 9.8±0.2 MeV beam energy, with a 0.5°±0.1° angular distribution and 0.15±0.025 cm, 0.075±0.025 cm horizontal and vertical radial intensities respectively. The full phase-space files of the linatron static field and the different collimated small beam sizes have been scored. The phase-space files can be used as the source files for MC-based dosimetric pre-treatment validations, simulating the experimental setup, and work as a dosimetric planning and evaluation system for future small field animal-based treatments.

The results of this research will enable and enhance the implementation of dosimetry tools throughout the radiation therapy treatment process. IRAI can be implemented for deep-tissue *in vivo* dosimetry to enhance treatment monitoring and verification. Additionally, the 3D dosimetric capability of gel dosimetry has demonstrated a valuable role in improving the beam characterization and commissioning of non-standard radiation fields.

Chapter 1

Introduction

1.1 Motivation and Significance of Work

1.1.1. Motivation

Radiation therapy generally aims to deliver a radiation dose to the tumor to kill cancerous cells while preventing and minimizing the toxic effect on the surrounding normal tissues. To meet this goal, the treatment planning and delivery techniques of radiotherapy have been steadily becoming more advanced and complex as summarized in Figure 1.1. The advanced treatment delivery techniques have increased the need for comprehensive machine commissioning and quality assurance (QA) in addition to patient-specific QA which are key components for accurate radiation therapy treatment.

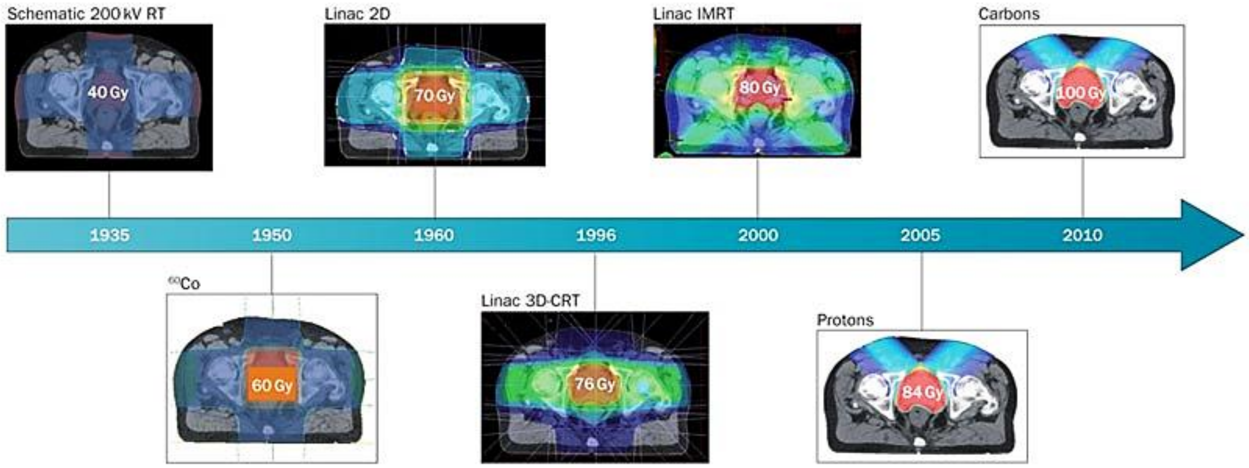

Figure 1.1: The advancement in the treatment planning and plan complexity for prostate cancer 1935–2010 [1]. Figure used with permission.

The currently available dosimeters for real-time radiation dose measurements are either 1D or 2D superficial dosimeters, which have limited applicability in some advanced applications. With the increased complexity of radiotherapy treatment plans and delivery techniques, there is a growing demand for more precise treatment planning and verification dosimetry tools that are capable of sampling 3D volumes.

Commonly used treatment delivery techniques include Intensity Modulated (IMRT), Stereotactic Radiosurgery (SRS), and Volumetric Arc Radiation Therapy (VMAT). 3D gel dosimetry is a promising dosimetry tool that has been investigated and has gained recent growing interest in research. The main advantage of 3D gel dosimetry over many conventional dosimeters is their ability to precisely measure dose distributions in a three-dimensional volume with relatively high resolution (sub-mm spatial resolution).

One of the main applications of gel dosimeters is in basic dosimetry measurements for electron and photon dosimetry and characterization measurements such as beam profiles and percent depth doses. Another common application of gel dosimeters is in patient-specific QA and to verify advanced treatment plans before delivery such as in SRS, IMRT, and VMAT [2]–[8].

The goal of *in vivo* dosimetry is for quality assurance of the radiation therapy delivery through real-time measurements of the dose delivered to ensure that radiation treatment is delivered as planned. *In vivo* dosimetry has an essential role and has increasing applicability throughout the treatment delivery process for patient dose measurement and verification. The advancement and complexity of the treatment planning and delivery techniques have expanded the role of *in vivo* dosimetry to assess and quantify the accuracy and precision of dose planning, delivery, machine-specific uncertainties, and systematic error detection. The feedback of the measured *in vivo* dosimetry plays an essential part in measuring over and under-exposure to dose during the treatment session, hence allowing for adjustments and re-evaluation of the dose delivery throughout the course of treatment.

Most commonly used *in* vivo dosimeters are either used for entrance, skin, or exit dose measurements, hence they are single point (1D) dosimeters. Entrance dose measurements allow for error detection in patient set-up (SSD, SAD errors), beam calibration, and machine output stability. Exit dose measurements provide additional patient-specific radiological thickness and heterogeneity information.

Despite their important role, clinically used *in vivo* dosimeters are limited to superficial 1D measurements. Given the growing interest in *in vivo* dosimetry in radiation therapy, advanced 3D dosimeters that can measure deep in tissue doses are crucial and essential for complex treatment plan verification and dose monitoring throughout the treatment course [9]–[11].

One of the main advancements in the radiation therapy field is Ultra-high dose rate irradiation UHDR-RT, also known as FLASH. UHDR-RT involves high treatment dose rates on the order that is higher than 40 Gy/s. Such dose rates are a few hundred orders larger than those delivered in conventional radiation therapy [12]. As concluded in some preclinical studies, UHDR-RT has shown potential in increasing the therapeutic index. The improvement in the UHDR-RT therapeutic index is achieved by increasing the normal tissue sparing effect (decreasing the normal tissue toxicity) while maintaining the same dose per pulse tumor-killing effectiveness [13]–[18]. This preclinically proven advantage of UHDR-RT has increased the potential for its applicability in radiation therapy.

Since in UHDR-RT higher dose is delivered during each pulse of radiation, more efficient and accurate dosimetry tools are essential to support instant per pulse basis measurements compared to conventional RT. The currently available online dosimeters, such as ionization chambers and semiconductors, have sensitive dose rate threshold limitations. The high dose per pulse rates of UHDR-RT have resulted in dose saturation problems in those commonly used dosimeters. Hence, limiting their applicability on dose per pulse basis measurements in UHDR-RT. Ionization chambers have shown ion recombination problems at higher dose per pulse values. While semiconductors show uncorrectable saturation for UHDR dose rates [19].

Active research work is still currently ongoing to identify and test suitable online dosimeters for UHDR dosimetry. For a dosimeter to be clinically implemented in UHDR-RT for in-depth (deep) treatment delivery monitoring, advanced dosimetry techniques are desirable to provide in-depth dose measurement in real-time (*in vivo*) per linac pulse. The areas of implementation for dosimeters in UHDR-RT are real-time internal dose measurements beyond superficial depths for dose monitoring and beam localization.

1.1.2. Dissertation Contribution and Objectives

The purpose of this research is to investigate novel developments and applications of dosimetry throughout the radiation therapy treatment process: (1) testing the feasibility of Clearview 3D gel dosimeters in radiation therapy and to broaden their applications, especially in characterizing and commissioning small radiation fields (2) optimizing and investigating the initial source of a research linac using MC simulation for dosimetry verification and quality assurance (3) validate the feasibility of iRAI technique in in vivo 3D dosimetry and beam localization during Ultra-High dose-rate radiation therapy (UHDRT) and in conventional radiation therapy (4) investigate the applicability of organic scintillators in dual dosimetry measurements for adiation protection and safety. The main objectives and the contribution of this work are summarized as follows:

Comprehensively develop a commissioning procedure to fully characterize the beam of an MV research accelerator. The procedure was accomplished by conducting a detailed dosimetric evaluation for implementation in non-standard megavoltage small animal irradiation studies. Additionally, testing, against traditional film dosimetry, the effectiveness and applicability of Clearview gels for 3D dosimetry and characterization of small radiation fields.

Comprehensively, through MC simulations, investigate the initial linatron source characteristics. Studying their effect on the measured linac beam characteristics. Implementing the simulated MC results to develop an MC-based Linatron specific dose delivery verification system to ensure accurate dose delivery as it is implemented for pre-clinical animal studies.

Investigate, through simulations, the applicability of iRAI in UHDR-RT as a 3D relative in vivo dosimetry tool. In addition to exploring the effect of the different transducer distribution on the reconstructed image quality and the extracted radiation beam characteristics. Moreover, investigating the effect of the different linac operating parameters on the final reconstructed dose-related (acoustic) images.

Experimentally evaluate the feasibility of iRAI in acquiring the 3D relative dose distributions using a customized 2D array transducer. The quantitative dose capability of iRAI was validated with Clearview gels in conventional radiation therapy. Demonstrating and verifying the applicability of iRAI in clinical setups for relative dosimetry and beam localization in conventional RT. Hence, comprehensively discussing the feasibility and the limitations of phantom-based (commercial gel dosimeter) iRAI in a clinical setting for in vivo dosimetry.

Testing the applicability of organic scintillator in mixed radiation (neutrons and photons) environments for radiation protection and safety. The efficiency of the organic scintillators are compared to the conventional dosimeters for personal protection and dose monitoring.

1.2 Dissertation Outline

This dissertation work serves as a detailed implementation of two novel 3D dosimetry tools in the different stages of the radiation therapy treatment process: Clearview radiochromic gel dosimeters and Ionizing Radiation Acoustic Imaging (iRAI). The schematic representation of the main dissertation-covered topics and studies is plotted in Figure 1.2. The implementation of radiochromic gel dosimeters as a tool for commissioning non-standard small fields of research accelerators has been investigated in this dissertation. These investigations have resulted in widening the applicability of the 3D dosimeters in commissioning small fields. Given the 3D advantages of gel dosimeters which allows for full representation of dose and beam characteristics allowing for dosimeter misalignment corrections and high reproducibility with low inter-dosimeter variability. In addition, iRAI implementation as a dosimetric tool in UHDRT (FLASH-RT) given their ability to measure the instantaneous 3D dose distributions on a per pulse basis has been investigated. Moreover, the applicability of organic glass scintillators has been investigated as a dual dosimeter for mixed radiation environments. The dissertation chapters were organized based on the major aims of this dissertation. Chapter 2 provides background and relevant information on the topics that provide a framework for this dissertation. Discussing the different types of dosimeters used clinically throughout the radiation therapy treatment process; emphasizing the clinically used dosimeters and looking at their differences in dose calculations and their corresponding applications based on their advantages and disadvantages. This chapter also describes in detail the two major 3D dosimetry tools studied in this dissertation: radiochromic gel dosimeter (Clearview) and Ionizing Radiation Acoustic Imaging (iRAI). The detailed implementation of Clearview gels for commissioning non-standard small fields is fully described in Chapter 3. This chapter covers the full characterization of the research accelerator Linatron M9 using absolute 1D, and relative 2D in addition to the 3D gel dosimetry. Chapter 4, covers the characterization of the research accelerator as an animal irradiator for preclinical studies. This chapter describes the optimization and the investigation of the initial electron source of the Linatron to develop a full Monte-Carlo (MC) based model of the Linatron. The experimental commissioning results of Chapter 3 were used to validate the simulation study and develop a full model of the accelerator. The MC-based modeling has resulted in acquiring full phase-space files of the beam, which were then used as the source to develop pre-treatment dosimetry verification for any future animal irradiation applications. The other part of the dissertation focuses on implementing iRAI imaging in *in vivo* dosimetry. Chapter 5 is a simulation-based study testing the implementation of iRAI as an *in vivo* relative dosimetry tool in Ultra-High Dose Rate radiation therapy (UHDR-RT). This chapter tests the effect of the different transducer configurations on the acquired reconstructed acoustic images in addition to the effect of the different linac parameters on the acoustic signal amplitude and the fidelity of acquiring the radiation beam characteristics. Chapter 6 is an experimental-based study of the applicability of iRAI as a 3D dosimetry tool in conventional radiation therapy. The iRAI images acquired with a customized array transducer were validated against 3D dose distributions acquired with the Clearview radiochromic gels. Chapter 7 is an experimental-based application of an organic scintillator as a dual particle dosimeter. The dosimeter depends on the pulse shape discrimination (PSD) capability of such detector to be used in mixed source environments for dual particle (neutrons and photons) dosimetry. The calculated dose measured with the organic scintillator was then compared with some conventional dosimeters measured results. Chapter 8 summarizes the major findings of the different chapters of this dissertation and summarizes its conclusions, limitations, and future directions.

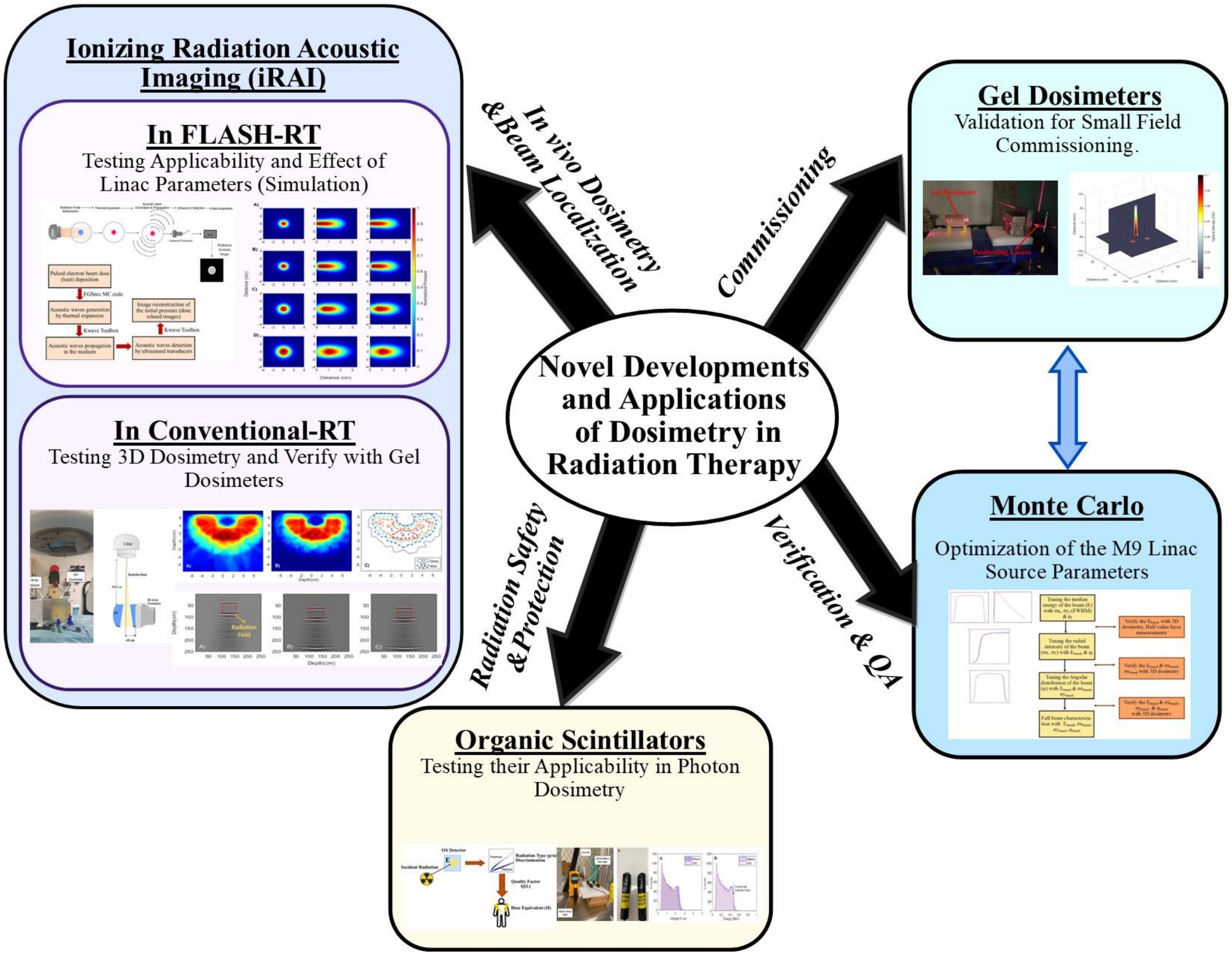

Figure 1.2: Schematic representation of the main covered dissertation topics and studies at the different stages of the radiation therapy treatment process including; using 3D gels and MC simulations for commissioning and characterizing nonstandard small fields, using iRAI for 3D *in vivo* dosimetry in FLASH-RT and conventional RT and beam localization, and using small organic scintillators for photon dose equivalent measurement for radiation protection and safety.

Chapter 2

Background and Historical Context

2.1. Dosimetry in Radiation Therapy

A variety of dosimeters are used throughout the various stages of the radiation therapy treatment process to ensure its accuracy. Radiation dosimetry is crucial for QA, treatment plan verification, plan evaluation and assessment, treatment monitoring, and even personnel protection and safety. The ability of the dosimeter to accurately and efficiently measure the dose deposited in its effective volume is the main factor that determines its applicability in dosimetry. Thus, each dosimeter has its advantages and limitations that govern its application clinically. An ideal dosimeter has a linear signal response to measured dose, is reproducible, has an accurate response, good spatial resolution, and no response dependency on dose rate, beam energy, and angular orientation of the dosimeter.

Practically, no dosimeter has all the above-mentioned characteristics for all the different dosimetry applications. As per the needed application, there are a variety of dosimeters that can be used clinically. Given that correction factors are implemented to correct for any dosimeter response dependencies the dose can be measured within certain measurement uncertainty that can be quantified. The theory and the different applications of some of the clinically used dosimeters are briefly discussed in this section.

Ionization Chambers (IC):

Ionization chambers, IC, are the most commonly used dosimeters in linac beam dosimetry and are available in different sizes and geometries depending on their application. ICs are gas-filled detectors that are mainly consisting of the chamber wall and a central charge collecting Electrode. The generated charge due to radiation interaction in the IC cavity is collected through applying a polarizing voltage and the response (collected charge) is read out by the electrometer and related to the radiation dose.

ICs are direct reading dosimeters and can measure in both integral and differential modes which makes their implementation more convenient clinically. Additionally, they are reusable with a stable sensitivity throughout their lifespan and they have high reproducibility, hence they are used for reference dosimetry protocols and linac commissioning and calibration [20].

The size of the ionization chamber should be large enough to provide the required dose sensitivity yet smaller enough to minimize the volume averaging effect specifically for small field dosimetry applications. Pinpoint microchambers has the advantage of partially overcoming this problem [21]. The commonly used type of ICs is the Farmer chamber, and it is also known as the thimble IC as its sensitive volume resembles a thimble as shown in Figure 2.1. The wall of IC is usually made of a low atomic number (Z) material such as aluminum, so it is tissue or air equivalent for dosimetry [22].

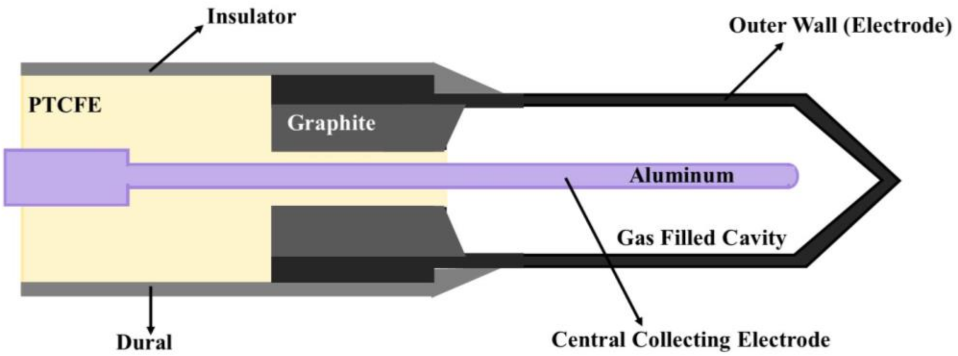

Figure 2.1: Basic design of the cylindrical Farmer ionization chamber. Figure reproduced with permission from IAEA [22].

Films:

The most used films clinically are radiochromic films that are made of nearly tissue equivalent material with a marker dye. Films experience changes in their optical density once exposed to radiation and that change can be read out with an optical densitometer and film scanners and used to determine the measured dose. Film data are acquired using the red, green, and blue color channels of the scanner, and some studies use the red color response only. The color channel readings (pixel values) are calibrated to dose [23].

The main advantage of films is their excellent 2-D spatial resolution (submillimeter), so they are suitable for high gradient dose regions [23]. Thus, the spatial accuracy of point dose measurements is limited by the resolution of the readout system. Films are passive dosimeters that require post-exposure processing and can measure in the integrated mode only, so they are not suitable for real-time dose rate measurements. Films are single exposure dosimeters and are not reusable [21].

Careful handling and accurate calibration and read-out of films are crucial for the accuracy of measured dose. Following the recommended film measurement protocols and procedures helps in measuring a dose within a 2% precision [23]. Hence, widening their applicability in linac quality control and treatment plan verifications.

Luminescent dosimeters:

Thermoluminescent dosimeters (TLDs) and optically stimulated luminescence dosimeters (OSLDs) are dosimeters that rely on the luminescence phenomenon to measure the dose delivered by an ionizing radiation beam. The luminescence phenomenon is the subsequent release of part of the absorbed energy of radiation in the form of ultraviolet, visible, or infrared light. Heat or light are used to accelerate the luminescence emission serving as excitation agents.

TLDs used in radiotherapy are tissue equivalent dosimeters made of doped lithium fluoride or lithium borate crystals. OSLD are typically carbon-doped aluminum oxide crystals. TLDs and OSLDs are passive dosimeters that require dedicated read-out equipment and there is a delay between the measurement and the signal read-out. A basic TLD, OSLD read-out system consists of a heating planchet or laser to excite the TLD and the OSLD respectively and a photomultiplier tube (PMT) to detect the induced thermoluminescence light emission and convert it into an electrical signal that is recorded by an electrometer.

TLDs and OSLDs have the advantage of the availability of very small dimensions which make them to a great extent suitable for point dose measurement. TLDs are mostly used for *in vivo* dosimetry on patients for QA and dose monitoring, treatment plan verification, and dosimetry audits and personal protection. One of the main disadvantages of TLDs and OSLDs is that they can measure in the integrated mode only and need a dedicated readout system which makes them not suitable for real-time or dose rate measurements and they are typically limited to surface measurements *in vivo*. Additionally, TLDs are not rugged and therefor sensitive to handling [21]. Recently, OSLDs made of potassium bromide doped with europium have shown to have a short trap emptying time (~25 ms) and short luminescence lifetime (1.1 μs) that enable them to be considered as real-time dosimeters, as the OSLD probe can be read out repeatedly during continuous exposure [24].

Diodes:

Silicon diode semiconductor dosimeters create electron-hole pairs once irradiated and generate an electrical current across their p-n junction operating at the short circuit mode. The measured charge is linearly related to the dose. Diodes can operate without an external bias voltage to decrease the leakage current; thus, they are mainly used for applications that involve *in vivo* dosimetry. Diodes are available in small sizes, so they are useful for phantom measurements of small fields. Diodes are used in stereotactic radiosurgery or high dose gradients; penumbra region, in addition to electron depth dose measurements. Diodes are common detectors used for array dosimetry and are used for treatment planning QA with a dose uncertainty of 3% [10].

Diodes need periodic calibrations to compensate for their sensitivity changes with irradiations for implementation as an *in vivo* dosimeter. Diodes are relative dosimeters and can not be used for beam calibration as they experience sensitivity changes due to radiation damage. Additionally, they have directional dependence based on the angle of incidence of the radiation beam. To correct for the angular dependence, the dosimeter should be used at the same geometry as that in which they are calibrated. One of the main disadvantages of diodes is the temperature and dose rate dependency of their dose-response [17].

Metal oxide semiconductor field-effect transistors (MOSFETs):

A metal-oxide-semiconductor field-effect transistor (MOSFET) are dosimeters that experience a change in the threshold voltage caused by the generated charge that is permanently trapped once irradiated. The threshold voltage change is a linear function of the absorbed dose, and the integrated dose can be measured during real-time dose measurement, or after irradiation.

MOSFET has a thin dosimetric volume, which enables them to be efficient for surface dose measurements in the case of appropriate packaging [25]. The smaller effective volume of MOSFETs is particularly useful to provide good spatial resolution measurements for implementation in high-dose gradients radiation fields such as IMRT, radiosurgery, and brachytherapy. Other clinically relevant advantages of MOSFETs are the possibility of real-time readout, simple instrumentation, and robustness. Thus, MOSFETs are used for in vivo dosimetry for various radiation therapy techniques such as IMRT and total body irradiation (TBI). However, MOSFETs have a limited lifetime and have shown some angular and temperature dependencies additionally they are sensitive to perturbations in the bias voltage during irradiation [9], [22].

Electronic portal imaging devices (EPIDs):

EPIDs use amorphous silicon photodiode technology to detect the megavoltage linac beam and are made of phosphor scintillator, usually gadolinium oxysulphide. Currently, all linear accelerators are equipped with EPIDs. This enhances their implementation for dosimetry since they are widely available with a defined and fixed position in the linac making the setup to be quick and establishing a connection between phantom and patient dosimetry in vivo. EPIDs also have a high spatial detector resolution (<< 1 mm) with a relatively fast readout reading any gantry angular incident. Although the primary application of EPID was inpatient setup and target and organ motion assessment, they have currently expanded their applicability for treatment machine QA and patient dosimetry. EPIDs can also provide an estimate of 3D dosimetry by combining the 2D images with either a back-projection or dose calculation methods to acquire the full 3D dose distributions [11], [26]–[28].

The main challenges with EPIDs are the low contrast and their highly energy-dependent response which causes ghosting artifacts and introduces some challenges for their *in vivo* transit dosimetry implementation. Several correction factors are required to compensate for the energy dependency and to use EPID images for dose measurements. Alternatively, the energy dependency can be corrected through the forward modeling of the EPID image and comparing it to the EPID measurement [28].

Gel dosimeters:

Gels share most of the features of films except they are 3D dosimeters. They have an excellent 3-D spatial resolution (~ 1 mm) that is limited by the resolution of the readout system [2]. Like films, gels are passive dosimeters and require post-exposure processing, can measure in the integrated mode, and are not reusable, so they are not suitable for real-time measurements [21]. Gels have a considerably time-consuming and difficult preparation process A detailed review of the types of the gels and their applications are discussed in the following section 2.2.

2.2. Review of Gel Dosimetry

Gel dosimeters are chemical systems that rely on the induced chemical/optical changes of the dosimeter as it interacts with radiation to quantify the deposited dose. Readout systems are used to image and quantify the radiation response of gels. Gel dosimeters serve as both the phantom and dosimeter which is advantageous for dosimetry applications. Different materials are used for gel dosimetry such as normoxic polymer gels, radiochromic plastics, i.e., PRESAGE and radiochromic gel dosimeters. The first used gel dosimeters were Fricke solution infused gels and currently, there are a variety of gel formulations used for dosimetry and most of them are polymer-based gels [29]. The resolution of the gel dosimetry is mainly dependent on the resolution of the imaging modality used for readout. The most commonly used imaging modalities for 3D dose readout are magnetic resonance imaging (MRI), optical CT (optCT) and X-ray computed tomography (CT) [2], [30], [31][32][33]. The first readout system used with Fricke gels was MRI [34]. Optical readout using optCT was proposed for polymer gels[35] and modified Fricke Xylenol dosimeters [36]. MRI-based dose quantification for gel dosimeters is based on the nuclear magnetic relaxation (NMR) dependence between the dose and the dosimeter properties [2], [3], [30]. Although MRI in principle is an ideal readout technique that has no phantom shape and size limitations, not all clinical MRI systems could be accessible to provide the quantitative relaxation maps needed for gel dosimetry. Thus, the main motivation for developing the X-ray CT and optCT gel readout systems is to make 3D imaging readout more readily available and easily accessible, which has relatively expanded the clinical applicability of gel dosimetry. The initiation of the XCT readout has started implementation with polymer gels [37], [38]. XCT-based dose quantification relies on the radiation-induced changes in the CT number of the irradiated polymer gel. CT number changes are directly related to density changes as XCT quantifies and maps the linear attenuation coefficients [1][36], [37]. The first proposed and implemented XCT readout system in gel dosimetry was for polymer gels [35]. However, it has been the common reading technique for radiochromic gel dosimeters such as Fricke xylenol and various leucodye systems. Both OptCTs and XCTs share the same scanning principle except that OptCTs, as their name indicates, use a visible light source while XCT uses a radiation source. The dose for OptCT-based gels is quantified based on the optical changes in the gels in response to radiation. The induced changes in the transparency of the dosimeter material enable optic imaging, hence dose quantification. In radiochromic dosimeters, the optical response is absorption-based light attenuation. In contrast, polymer gel attenuation changes are light scattering-based optical changes[7]. The absorption-based light response has the advantage of minimizing the scattered light perturbation. The source and detector in OptCT readout systems are stationary, while the dosimeter rotates due to its relatively small size [2][39].

The implementation of 3D dosimetry tools in radiation therapy has gained more interest over the years . However, for efficient clinical implementation of 3D dosimetry tools, the Resolution-Time-Accuracy-Precision (RTAP) performance criteria proposed by Mark Oldham *et al* must be fulfilled. An ideal true 3D dosimetry system, including the dosimeter and associated readout, defined under RTAP is the one capable of delivering 3D dose measurements with 1 mm isotropic spatial resolution in less than one hour with an accuracy of 3% and a precision of 1% [40].

The increased complexity in treatment planning and dose delivery techniques has increased the need for machine quality assurance, patient-specific QA and dose delivery validation. Gels 3D dosimeters have shown an important role in benchmarking the performance of new treatment techniques with promising applicability in complex and advanced treatment delivery QA such as Intensity Modulated (IMRT), and Volumetric Arc Radiation Therapy (VMAT) [4], [6], [33], [41]. Taking the advantage of the 3D dose measurement as gels can provide the integrated dose distributions in 3D with a good resolution based on the used readout system. The motivation behind using gels in QA is to measure the scattering contributions to the dose that may not be accounted for in the computation algorithm, which causes some discrepancies between the planned and the delivered dose specifically for small fields. Additionally, the gel-measured 3D dose distribution will provide full dosimetric info to correct for machine failures and setup errors that could be difficult to acquire with 1D and 2D dosimeters. Gels compare favorably with other common detectors in the main characteristics, including their relative accuracy, volumetric nature, inherent three-dimensionality, high resolution, and lack of energy dependence over much of the important energy range. Hence, they are applicable in basic dosimetry measurements to acquire dosimetry parameters such as beam profiles and percent depth dose in photon and electron beams [4], [5], [42], [43].

One of the main causes of the considerably limited implementation of gel dosimetry clinically is the relatively time-consuming preparation as it requires several actions. Additionally, an optimum 3D dosimetry protocol implementation is essential to ensure suitable handling pre-irradiation, during measurement, readout, and post-irradiation for accurate results.

Some previous studies have reported dose rate dependency for certain polymer gel dosimeters possibly resulting from competing for radiation-induced chemical reactions. This effect has been more pronounced in normoxic THP-based methacrylic acid (MAc) gel dosimeters than in poly-acrylamide-gel (PAG) dosimeters [29], [44]–[46]. PRESAGE™ gels which is one of the commonly used radiochromic polymer gels have a little dependency on dose rate (~2%) [4], [47].

On the other hand, current radiochromic gels, i.e., Clearview gels have been shown to have a linear dose-response up to 80 Gy as shown in Figure 2.2, and to be independent of photon beam energy (4–18 MV) and dose rate (up to 9.9 Gy/min) [48].

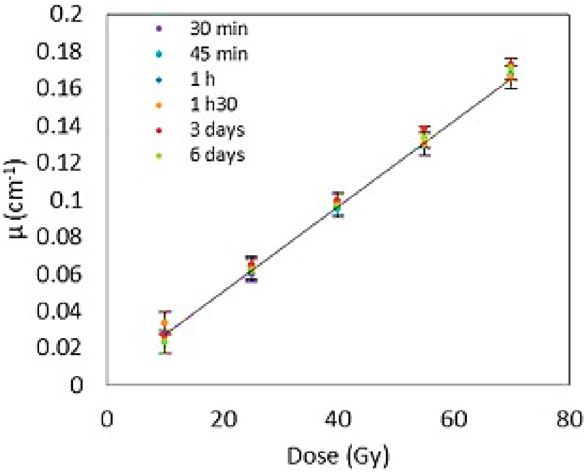

Figure 2.2: The linear response of the Clearview gels for 10–70 Gy dose range at different times after gel irradiation Copywrites request submitted pending the final permission [49].

2.3. Review of IRAI Imaging Technique

2.3.1 Theory of IRAI (Thermoacoustic Effect):

The theory behind the iRAI imaging is based on the thermoacoustic effect. The thermoacoustic effect is generally described by four steps; a pulsed beam of energy interacts with the target medium. Part of the energy is deposited in the medium in the form of heat, and this causes a local increased temperature gradient. Temperature gradients lead to the generation of the acoustic wave through the thermoacoustic effect. The induced acoustic signals are then detected by an ultrasonic transducer and signals are processed to produce acoustic images. In the case of iRAI, the source of energy deposition is a pulsed beam of radiation. The mechanism of iRAI is explained in detail in this section:

Dose deposition and temperature increase

An incident pulsed beam of ionizing radiation hits the target medium, which causes the deposition of energy, radiation dose, in the medium, and part of this energy is converted into heat energy. The pulsed radiation beam could be an electron beam, photon beam, or proton beam. The incident radiation beam interacts with the target medium through different types of interactions depending on the type of radiation and the medium. As an illustration, an electron beam can interact either with the orbital electrons of the exposed medium or with the nuclei of the medium. Those interactions result in atom ionization and/or excitation together with electron scattering or the generation of X-ray photons (bremsstrahlung) because of electron deceleration and the continuous energy loss of its energy. The deposited dose $D_r(r,t)$ is then quantified by the total energy deposited per unit mass in the medium measured in Gy (1Gy=J/kg). While most of the deposited dose is converted into heat, some energy losses could contribute and participate in chemical reactions [50] or other optical emissions[51]. The local heat deposited due to the radiation dose is then given by [52], [53]:

$$\mathrm{H(r,t)} = \eta_{th} \rho \mathrm{D}_r \mathrm{(r,t)}\,, \tag{2-1}$$

where H($\boldsymbol{r}$,t), $\mathrm{D_r}$(r,t) are the heat absorption rate and absorbed dose at position $\boldsymbol{r} \in \boldsymbol{R}^3$ and time t respectively, ρ is the density of the medium, and η_{th} refers to the thermal heat efficiency. Thermal heat efficiency refers to the amount of energy deposited as heat energy, and it depends on both the type of ionizing radiation and irradiated medium. The losses due to the chemical reactions, and radiation-induced acoustic and optical emissions all contribute to the reduction in heat efficiency [50], [51], [54]. The heat absorption rate, H($\boldsymbol{r}$,t), resulted in temperature gradients in the medium $T(\boldsymbol{r},t)$ that has spatial and temporal distribution following the heat transfer equation:

$$\rho \mathrm{C}_v \frac{\partial T\mathrm{(r,t)}}{\partial t} = \lambda \nabla^2 T\mathrm{(r,t)} + H\mathrm{(r,t)}\,, \tag{2-2}$$

where $\mathrm{C_v}$ is the constant volume-specific heat capacity and λ is the thermal conductivity. This equation can be solved with Green’s function approach, with the thermal diffusion distances being much smaller than the scale of spatial resolution and unit volume (the relatively large linac pulse duration of 3-6 µs [21]). Using the same approach published by Lei et al [53], the resulted temperature rise can be rewritten based on the temporal dose rate by omitting the first term on the right-hand side of the equation (2-2) so it is simplified to

$$\frac{\partial T(r,t)}{\partial t} = \frac{\eta_{th} D_r(\mathrm{r,t})}{\mathrm{C}_v}, \tag{2-3}$$

Initial pressure generation and propagation:

The wave equation governs the generation of the radiation-induced acoustic pressure and its corresponding propagation in the medium, and is given by [52], [53]:

$$(\nabla^2 - \frac{1}{v_s^2}\frac{\partial^2}{\partial t^2})\, p(\mathrm{r,t}) = -\frac{\beta K_T \eta_{th}}{v_s^2 \mathrm{C}_v}\frac{\partial D_r(\mathrm{r,t})}{\partial t}, \tag{2-4}$$

where β is the volumetric thermal expansion coefficient, K_T is the isothermal bulk modulus, and $v_s = \sqrt{K_T / \rho}$ is the speed of sound in the medium. The dose rate of a single clinically used radiation pulse can be treated as a Dirac delta function. This approach is selected to satisfy the stress confinement condition ($\tau \cdot vs \ll$ spatial resolution) by selecting a low-frequency acoustic detection range, that leads to lower spatial resolution where τ is the linac pulse duration. The relatively long pulse duration of 3–6 µs of clinical linac has resulted in a considerably low spatial resolution in the range of a few millimeters. The instantaneous spatial iRAI pressure can then be detected at position r and time t through solving the wave propagation equation:

$$p(\mathrm{r,t}) = \frac{1}{4\pi v_s^2}\frac{\partial}{\partial t}\int dr' \frac{1}{|r-r'|}\frac{\Gamma \eta_{th}\rho}{\tau_e} D_p(r')\delta(t-\frac{|r-r'|}{v_s}), \qquad (2\text{-}5)$$

where $D_p(r')$ is the dose deposited during a single linac beam pulse duration (τ). Meanwhile, the initial radiation-induced acoustic pressure $p(r,0) = p_0(r)$ can be calculated by:

$$p_0(\mathrm{r}) = \Gamma \eta_{th}\rho D_p(r), \qquad (2\text{-}6)$$

where Γ is the material-specific Grüneisen coefficient defined as:

$$\Gamma = \frac{\beta K_T}{C_v \rho}, \qquad (2\text{-}7)$$

Γ is a dimensionless material-specific constant that relates the pressure increase linearly to the deposited heat energy and governs the pressure-dose linear proportional relation. The detected instantaneous pressure signals show the temporal pressure changes and generate information regarding the initial spatial pressure distribution induced following a pulse of radiation. The induced acoustic signals are then acquired at multiple projections (angles) surrounding the irradiated region to form acoustic images of the initial pressure distribution, which are linearly related to the deposited dose. The theory of iRAI and the thermoacoustic effect is summarized in Figure 2.3.

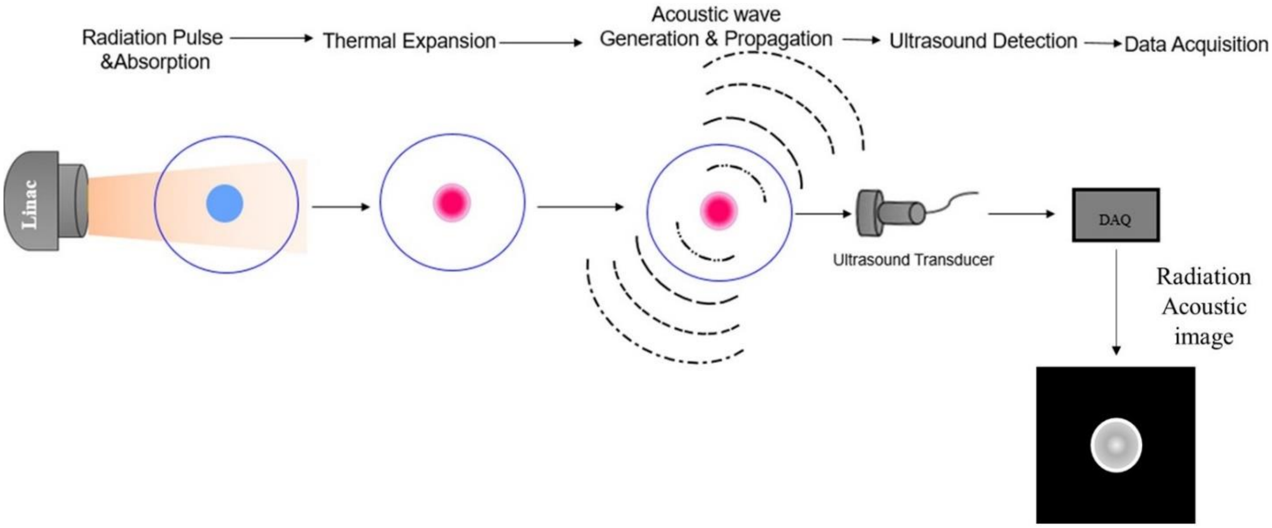

Figure 2.3: A diagram describing the thermoacoustic effect and the theory of iRAI imaging.

2.3.2 History of IRAI and Previous Studies:

The generation of the acoustic signal induced by x-rays from a synchrotronic source was first demonstrated in 1983 [55]. In 1991, the generation and detection of acoustical waves were achieved using a therapeutic x-ray source [56]. It was not until 2013 that X-ray-induced acoustic waves were used for tomographic imaging. A 2D acoustic image was generated using a 500 kHz central frequency transducer [57], [58]. Those studies showed that X-ray-induced ultrasound waves propagating in 3D can be imaged and provide information about deeper structures and properties in the medium. The linear proportionality of the generated acoustic signal to the deposited dose has demonstrated the potential for its implementation in dosimetric and low dose imaging and monitoring applications in radiation therapy.

Since then, the feasibility of using ionizing radiation-induced acoustic imaging has been continued to explore different applications in non-destructive testing and different biomedical applications in radiation therapy and imaging. One of the main areas of applicability of iRAI in medicine that has been investigated in the literature is radiation dosimetry and radiation therapy beam monitoring [53], [59]–[63]. The main characteristic of iRAI that has proven its feasibility for dosimetry is the dose and induced pressure, acoustic signal, and linearity in addition to energy and dose rate independence. IRAI is independent of the average operational dose rate of the linac measured in Gy/min or Gy/s; however, the radiation-induced acoustic signal is dependent on the instantaneous dose rate during the linac pulse measured in Gy/pulse/s. Additionally, the iRAI transducer is placed outside of the radiation beam field, which eliminates the perturbation effect in measurements and the need for corresponding correction factors. Simulation studies were also performed developing a full simulation analysis to model the generation and propagation of acoustical signals. Simulations were performed for validating the experimental results and as a preliminary step to optimize the experimental setups and test the feasibility of future applications [64]–[68].

The progress in the field started with experimental studies in metals and high acoustical signal samples then progressed to a more representative medium; water tank-based work, phantoms, and tissue samples [69], [70]. The most recent experimental feasibility of iRAI as an *in vivo* dosimeter during conventional external beam radiation therapy was an animal-based study using a single element transducer. A dual ultrasound-based image-guided radiotherapy system holds great potential for personalized cancer treatment and better outcomes [63].

Most experimental studies were implemented using single element transducers, which limited the extracted dosimetric information and resulted in a long imaging time. Transducers need to be rotated to acquire sufficient angular projection data to construct 2D images. However, transducers arrays can construct 3D images taking advantage of the nature of the spherical nature of the induced acoustic signals to propagate in the medium in 3D. 2D array detection systems will have better implementation for 3D *in vivo* dosimetry.

Another area of implementation of iRAI is in low dose imaging since iRAI can measure the dose per pulse resolution. 2D images with acceptable SNR were reconstructed using dose levels as low as 11.6 mGy [62]. The spherical nature of 3D signals is the key feature that enables iRAI to generate 3D images through only a single projection. This decreases the total dose exposure to the patient and makes it a promising low dose modality. The main limitation of iRAI-based imaging is the relatively long pulse duration of the linac, which causes the generation of acoustical signals with a low-frequency component that negatively affects the resolution of the reconstructed images. To overcome this, low-frequency transducers may be used for imaging or shorter linac pulses that are associated with induced signals at higher ultrasound frequencies to construct high-resolution iRAI images are desired. Moreover, the imaging transducer should have a wider bandwidth to detect generated signals. The limited bandwidth of the transducer prevents the detection of signals with high-frequency components. Simulation-based studies showed the potential implementation of iRAI in detecting breast lesions at early stages and for bone density imaging [67], [68]. The sensitivity, bandwidth, number of detection elements, sampling rate, and directionality are key features to allow the 2D arrays to be implemented for iRAI imaging.

The other area of iRAI applicability is for Bragg peak localization in proton therapy. The Bragg peak determines the maximum energy deposition in proton therapy. It is essential to determine where the beam stops and to account for the different uncertainties in the proton therapy range. The proton-induced acoustic signal; a.k.a. protoacoustic or ionacoustic, following irradiations is one of the methods that shows potential to locate the Bragg peak position in real-time. Proton Gaussian pulses in the range of 3 μs FWHM and 1 kHz pulse repetition rate are ideal for acoustic wave generation and ionacoustic range verification. The distance between the detection system (transducer) and the Bragg peak is determined by multiplying the time arrival of the acoustic signal with the speed of sound of the medium. It is essential that the time arrival of the signal and the speed of sound of the medium are well known for accurate determination of the Bragg peak position. With the presence of tissue heterogeneities, it becomes more challenging to determine the speed of sound on which the time of flight and range determination will highly rely. One possible way to overcome this challenge is to determine the speed of sound through CT-based Kwave simulations so that the speed of sound and Grüneisen coefficient of each voxel of tissue can be determined based on the Hounsfield Unit value. As with the other applications of iRAI, it is essential to have a reliable transducer system to allow for accurate detection of the low frequency generated acoustic signal in real-time and verify the beam range and possibly provide dose distribution imaging [70].

2.4. Conclusions:

Different dosimeters are commonly used in the radiation therapy treatment process including ionization chambers, films, TLD, OSLD, MOSEFT, and EPIDs. However, each dosimeter has its limitations and features that govern its applicability in radiation therapy dosimetry whether it is a point dosimeter, has dose rate and energy-dependent behavior, needs post-processing (not real-time), or displays response drift with time. The increased complexity and advancement in treatment planning and delivery techniques; IMRT, VMAT, and *in vivo*, has expanded the role of dosimetry to assess the dose delivery during the radiation therapy procedure. The role of *in vivo* dosimetry is for target dose verification, organs at risk (OAR) dose verification, out-of-field dose measurements, and treatment dose verifications during IMRT and VMAT. Moreover, the International Atomic Energy Agency (IAEA) recommends wide spreading the role of in vivo dosimetry to include verification of treatment delivery that involves high doses, new treatment techniques, special treatment procedures such as total body irradiation (TBI), and total skin electron irradiation (TSEI), after software/equipment changes, and single fraction treatments, and in more advanced treatment delivery techniques, such as intensity-modulated RT (IMRT) and volumetric arc therapy (VMAT).

Commonly used *in vivo* dosimetry systems are TLDs, MOSFET, OSLDs, and recently EPIDs. These dosimeters are either point detectors or 2D dosimeters (EPID), which limits their applicability to single skin dose measurements. IRAI has shown many advantages which makes it a promising *in vivo* dosimeter; they measure dose in-depth in 3D, has linear proportionality to dose, and can measure on a dose per pulse basis.

Chapter 3

Application of Radiochromic Gel Dosimetry to Commissioning of a Megavoltage Research Linear Accelerator for Small-Field Animal Irradiation Studies

This chapter describes the full procedure developed and followed to commission a research linear accelerator (linac) for its implementation in small-field animal irradiation studies. The aim of this work is to develop a reliable procedure to commission non-standard small fields that have geometrical constraints preventing them to meet the reference standard clinical conditions used in Task Group (TG) commissioning procedures defined by the American Association of Physicists in Medicine (AAPM). The applicability of 3D radiochromic Clearview gel dosimeters in relative dosimetry commissioning of small radiation fields was tested as some of the commonly used dosimeters are considered large concerning the size of the characterized small fields. The main findings of this chapter were published in the peer-reviewed article “Application of radiochromic gel dosimetry to commissioning of a megavoltage research linear accelerator for small-field animal irradiation studies”, Medical Physics Journal, 2021 [71].

3.1. Introduction

The small animal irradiators are accelerators that use ionizing radiation for preclinical and radiobiological research [72] and commonly operate in the kilovoltage and orthovoltage beam energy range of 10-120 kV and 130-320 kV respectively. The kilovoltage animal irradiators, given the advancement in the treatment planning and delivery techniques, are incompatible with modern clinical linear accelerators. The limited energy range of those accelerators has limited their applicability to only partial body or organ-specific irradiations with a limited penetration depth from 0-2 cm [73]. High-energy electron and photon irradiations for preclinical animal studies are mostly achieved by adapting existing commercial modalities to produce three different modes including kV and MV photon modes, and MeV electron mode [74]. Hence, the research Linatron-M9 accelerator with its MV photon energy capabilities is considerably more applicable for dosimetric and radiobiological studies. The higher beam energy (in the MV range) is mimicking the clinical expected dose responses, especially for deep dose and biological measurements.

Full machine commissioning and beam characterization of the Linatron is an important step for its implementation in preclinical dosimetric animal studies. Moreover, several recommendations and guidelines were published to provide comprehensive quality assurance and commissioning procedures to verify the dose delivery of the clinical linear accelerators [20], [75], [76]. Hence, it is strongly recommended to mimic those protocols and guidelines and implement them for commissioning animal irradiators and preclinical radiation research platforms. The aim of the comprehensive commissioning process of the small animal irradiator is to fully characterize its dosimetric characteristics within a level of accuracy that matches the limits (within 5%-point dose errors) employed for clinical radiation therapy treatments [77]. The commissioning procedures are crucial to maximize the impact of the research platforms, hence, translating their radiation therapy-related research findings into the clinic [30], [78].

3.2. The Research Small Field Linear Accelerator

The research linear accelerator (Linatron-M9) is a fixed endpoint photon energy mode 9 MV flattening-filter-free accelerator. The accelerator has a fixed tungsten target and a single electron energy mode (9 MeV), which produces a “9 MV” bremsstrahlung photon beam [79]. Primary collimators were lead collimators of a 5.08 cm in diameter opening used to shape the Linatron beam into a static circular beam. The Linatron exit opening; the primary collimator opening, is at a 161 cm source to surface distance (SSD). The linac has an operating current between 10 and 100 μA, which corresponds to pulse repetition rates (Linac frequency) of 25-250 Hz. The electron pulse width is approximately 4μs. A shielding enclosure was added to the accelerator to limit the extraneous dose to operators and maintain the standard safety dose limits (Figure 3.1A).

The Linatron was installed for active interrogation research and this work aims to widen its applicability and repurpose it as a small animal irradiator. The static linac field was further shaped to smaller fields of 2x2cm^2, 1x1 cm^{2,} and 0.5x0.5 cm^2 for preclinical dosimetric studies using secondary lead collimation bricks that were manually placed at the exit of the Linac beam (Figure 3.1B). The positioning reproducibility of the secondary lead collimators was performed and maintained with the guidance of a set of positioning lasers that were manually integrated into the Linatron to reduce collimator and phantom alignment errors (Figure 3.1C).

Due to the geometrical constraints of the Linac and to achieve high dose rates (machine output) while allowing adequate spatial space for measurement setup, the experimental measurements, and the reference commissioning conditions were set to 220 cm SSD and 2 cm depth in a solid water phantom. The resulting linac field size at the calibration point, measured as FWHM, is 7.5 cm in diameter.

The Linatron output is controlled by a built-in ionization chamber monitor placed at 100 cm from the Linac source either in the unit of the total irradiation time (in seconds) or as the total dose (in Gy).

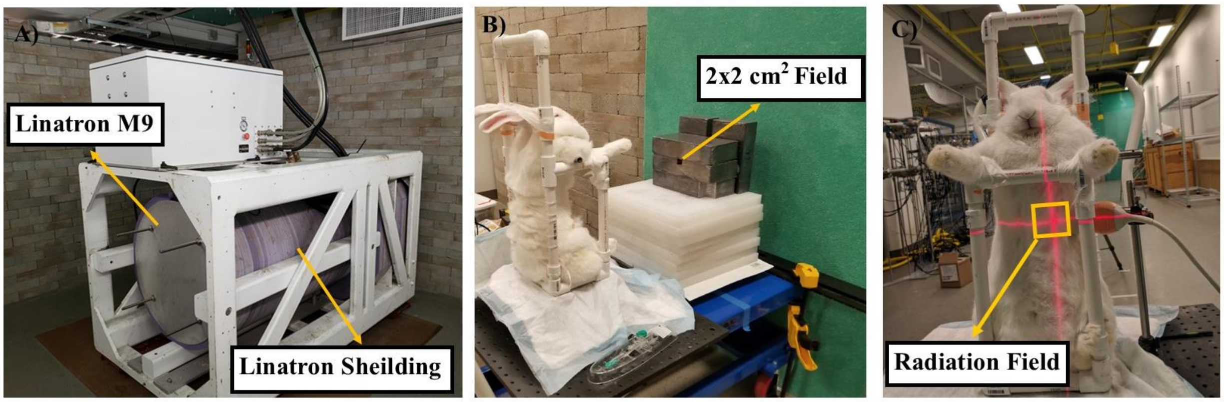

Figure 3.1: The Linatron M9 accelerator and the measurement setup position A) shows the Linatron room and the Linatron encloser shielding, B) shows the 2x2 cm^2 secondary lead collimators in rabbit irradiation at 220 cm SSD C) shows the positioning lasers during the utilization of commissioned Linatron in small animal irradiation studies [71].

3.3. Absolute Dosimetry Measurements

The Linatron output is controlled either per time unit or as total dose (cGy). The absolute dose measurements are point-dose measurements performed to monitor the Linatron output, and its linearity with time in addition to determining the Linac calibration coefficient at the reference conditions using a 15 mm^3 effective volume thimble ionization chamber (A-14) [80]. The Linatron output measurements were performed at the calibration point. The Linatron output is the measured dose rate for the machine-specific static collimated field of the Linatron, 7.5 cm in diameter beam size at the calibration point. The calibration hence the dose was calculated following the AAPM TG-51calibration protocol and the following formula [20],

$$D_w^Q = M N_{D,w}^Q \, , \tag{3-1}$$

where D_w^Q is the absorbed dose to water measured in Gy with the ionization chamber. $N_{D,w}^Q$ is the calibration factor of the Ionization chamber in Gy/C corrected for the beam quality Q. M is the electrometer reading in coulomb (C) corrected for the ion recombination effect, electrometer calibration, polarity effect, pressure, and temperature effect following AAPM TG-51 [20].

The ionization chamber was cross-calibrated using a clinical Varian TrueBeam linac (Varian Medical Systems, Palo Alto, Ca) to ensure higher accuracy of our dose calibration method. The beam quality of the Linatron was calculated using the tissue phantom ratio (TPR) for doses at depths of 20 and 10 cm (TPR20/10) for a field of 11.28 cm diameter (10 cm x 10 cm square equivalent field) [76]. The measured results were compared with the simulated results using EGSnrc (BEAMnrc/DOSXYZnrc) Monte Carlo codes in a water phantom [81], [82]. The relative percentage error between the two methods was ~0.16%.

Some modifications had been made to the AAPM TG51 protocol including the position of the calibration point and the reference field due to the geometrical differences in dimensions and accessibility of the Linatron machine compared to a clinical machine.

3.3.1. Linac Output Stability Measurement

The absolute Linatron output stability was measured with the A-14 IC during its daily operations (at different operation hours) for two different weeks within a month-long period. The variation of the daily first Linatron operation output was measured for each weekly experimental operation of the Linatron during that measurement month.

The Linatron output variability with time after the first irradiation was measured with daily absolute dose readings variability of 0.61% and 0.48% for the first and second day respectively. The Linatron output increases with time after its first operation. The variability of the Linatron output at its first operation was 0.51% corresponding to a weekly absolute dose variability measured with A-14 IC of 0.55% on four different days over nearly a month. Overall, as per the measured absolute dose readings using A-14 IC, the reported variability of the Linatron output during its expected operational hours is always <1%. This measured 1% output variability is comparable to the reported clinical accelerator output variability (Table 3.1and Table 3.2).

Table 3.1: Daily Linatron output variability with time (intra-day variability) for 3 minutes of irradiation

Irradiation Time (Hours)	**5/3/2019**		**5/4/2019**	
	Absolute Dose (cGy/min)	**Linatron Output Reading (cGy/min)**	**Absolute Dose (cGy/min)**	**Linatron Output Reading (cGy/min)**
0.00	146.41±0.49	601.23±0.81	146.64±0.85	603.5±0.95
2.50	147.97±0.28	600.67±1.28	148.05±0.38	601.47±0.36
3.50	148.52±0.47	601.40±0.69	--	--

Table 3.2: First operation Linatron output variability with the date of exposure (inter-day variability)

Date of irradiation	**Absolute Dose (cGy/min)**	**Linatron Output Reading (cGy/min)**
5/3/2019	146.41±0.49	601.22±0.81
21/3/2019	144.58±0.32	595.42±0.86
5/4/2019	146.64±0.85	603.5±0.95
11/4/2019	145.57±0.11	597.76±11.84

3.3.2. Linatron Output Time Linearity

The time linearity of the Linatron output (in minutes) was measured and verified with the A-14 ionization chamber absolute dose readings in Gy. The total dose was measured at variable irradiation times in minutes as the average of three different trials and the error is the standard deviation between the different trials. The total dose was found to be linearly proportional to the irradiation time as theoretically expected. The standard deviation in the total dose readings for both the Linatron output and the IC is always within 0.1 %. Both the A-14 IC dose readings reported in cGy and the Linatron output readings have linear relations with the irradiation time as shown in Figure 3.2. The reported R^2 value for both curves is nearly unity. As verified with measurements, the Linatron output rate (cGy/min) remained constant despite the total irradiation (beam-on) time duration. The average Linatron output value is 600.44± 0.76 cGy/min as controlled by the built-in monitoring chamber at 1m away from the linac target. However, the measured linac output at the reference calibration point corresponds to 145.60±0.29 cGy/min based on the A-14 IC absolute dose measurements.

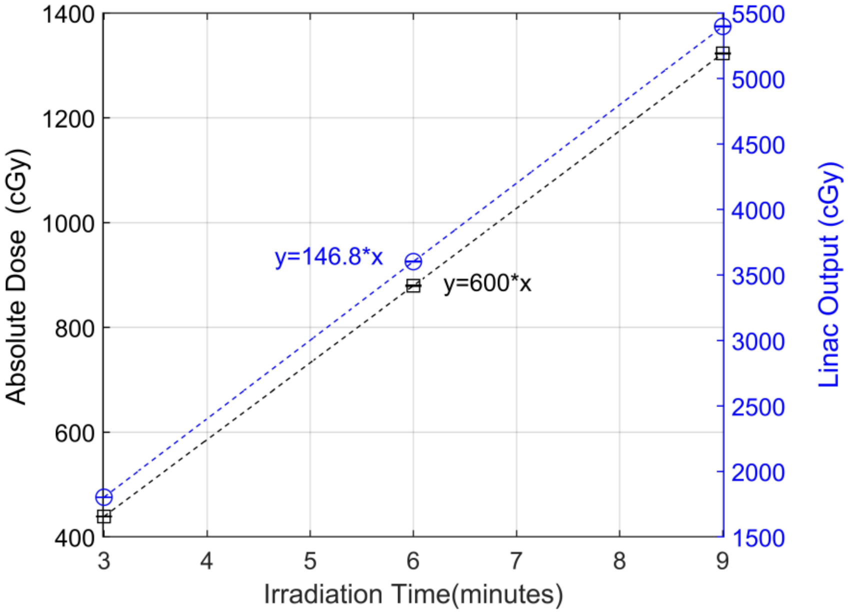

Figure 3.2: Linatron output-timer linearity for absolute measurement verification with A-14 IC. The smaller error bars (much smaller than the marker sizes) represent the reported low uncertainty in the measurements.

3.3.3. Linatron Calibration and Absolute Dose Verification

The Linatron calibration factor was measured to be 600.93 ±1.12 cGy/min. The verification of the Linatron calibration and the absolute dosimetry accuracy was performed by exposing two separate dosimeters (A-14 IC and TLD) to a total dose of 100 cGy. The resulting average readings of the two dosimeters were 101.37±0.52 and 101.09±0.57 cGy. The readings of each dosimeter were compared with the total dose of 100 cGy delivered based on the determined Linatron calibration factor. The uncertainty of Linatron output and calibration was hence verified to be within 1.4% error.

3.4. Relative Dosimetry Measurements

The relative dosimetry measurements are crucial for characterizing the radiation beam including Percent Depth Dose curves (PDD), Relative Output Factors (ROF), beam profiles, and beam divergence measurements. In this work, the applicability of new radiochromic gels as a potential tool for relative dosimetry and hence commissioning small radiation fields was tested and verified. The measured gel results were compared with the film measured results. Similar to the absolute dose measurements, the relative dosimetry measurements were performed at the reference point of 220 cm SSD and 2 cm depth in a solid water phantom for all the three fields of interest in this study; 2x2 cm^2, 1x1 cm^2, and 0.5x0.5 cm^2 (Figure 3.3). SSD and depth of measurements were selected because the reference conditions specified in the standard dosimetry protocols [20] for beam calibrations cannot be met for this research accelerator. A set of positioning lasers were integrated at the beam exit and used to increase collimator and phantom positioning reproducibility and reduce errors (Figure 3.3 B).

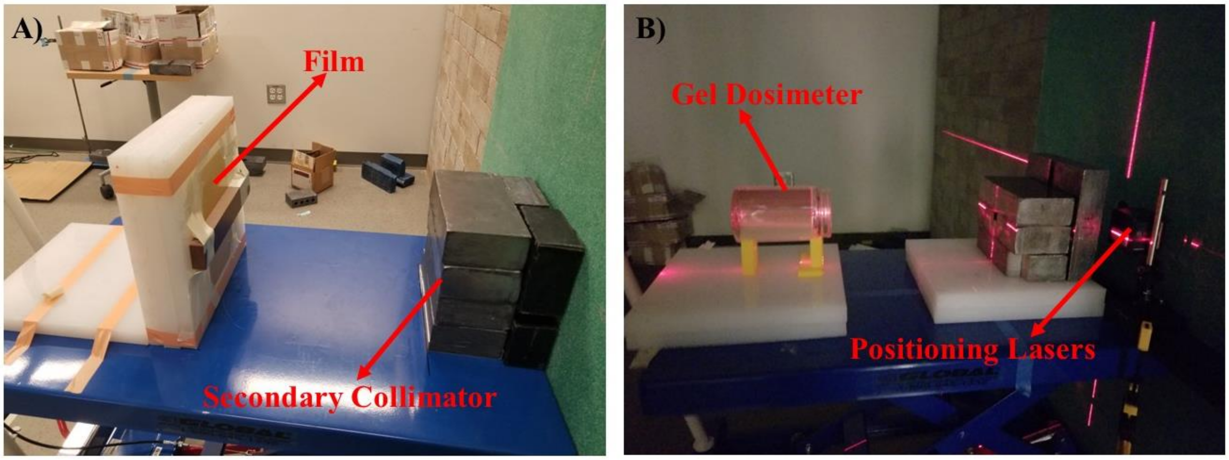

Figure 3.3: Relative dosimetry measurement setup at the reference position at 220 cm SSD and effective measurement depth of 2 cm in phantom (2 cm buildup thickness of solid water (A) or gel phantom (B)) (A) measurements setup using Gafchromic films (B) radiochromic gel jar. (B) shows the integrated positioning lasers [71].

3.4.1. Clearview Gel Measurement

3.4.1.1. Gel Measurement

Various Clearview gel dosimeter jars (Modus Medical Devices Inc.) were used for 3D dosimetry measurements including PDD curves, beam profiles, and output factors of the small fields [83]. All experiments were acquired at the same SSD, 220 cm from the Linatron target, at a relative inter-gel depth of 2 cm (Figure 3.3 B). The measured gel data was compared with films including dosimetry point measurements (ROF), 1D measurement (Profiles, PDD), and 2D dosimetry measurements (Profiles, PDD). Each small field was measured three times using the same gel jar while allowing enough separation between the acquired three fields to ensure that the measured dose distributions are not perturbated (Figure 3.4) [84], [85]. The results of the gel measurement were compared to films and discussed in detail in Gel and Film Results Comparisons section 3.4.3.

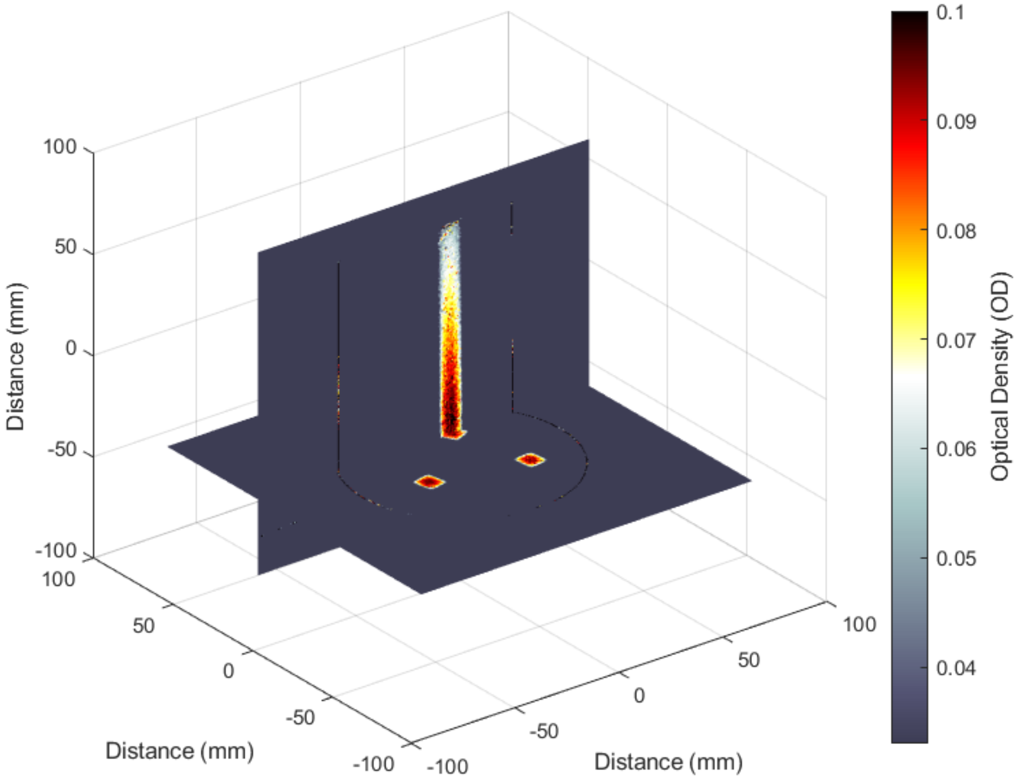

Figure 3.4: 3D view of gel dose measurements (in optical density OD) per pixel position for the 1x1 cm^2 field showing the transverse and sagittal views of dose distributions and the separation between the different trials measured at the same gel jar.

3.4.1.2. Gel processing and calibration

The Clearview gels throughout the measurements were handled following the adopted common procedure for better dose measurement accuracy [49]. The gels were stored in the refrigerator at

~4 °C temperature and were removed from the refrigerator approximately 8 hours before irradiation so that they return to room temperature before irradiation and the readout. Throughout the whole gel handling process, during transport, setup, and handling, gels were sheltered from light as much as possible using light-tight opaque bags.

Gel dosimeters were scanned using a Vista optical CT scanner Model: 16 (Modus Medical, London, Ontario). The scanner resolution was set to 0.5 mm for all scanned gels. For better scanning and image resolution, the iterative back-projection image reconstruction technique was used instead of the simple back-projection reconstruction technique [86]. Each jar was marked for accurate repositioning of the dosimeter relative to the reference background correction scan. The background reference scan of the gels is essential and follows manufacturer recommendations before the gel irradiation exposure to compensate and correct for the gel reading. All irradiated gel jars including the calibration and measurements were all scanned within 24 hours post-exposure to ensure adequate signal stability.

The calibration of the two batches was performed using a clinical Varian TrueBeam linac (Varian Medical Systems, Palo Alto, Ca) to ensure higher accuracy of the dose calibration. The calibration was performed using a 9 MeV electron beam using the standard 10 cm x 10 cm cutout, with SSD=100 cm, and a 30 Gy dose delivered to a d_{max} of 2.0 cm. The 9 MeV electron beam calibration is recommended by the gel manufacturer since it represents a full depth dose curve (100% to <5% dose vales) that can be measured using only a single gel phantom. The electron beam provides a simple way of compressing a wide dynamic dose range into the space of a single gel jar [87]. The Vista Optical-CT scanner was used to measure the central-axis optical density change which represents the attenuation coefficient change of the gel. The attenuation coefficient was then fitted linearly with the corresponding central-axis depth dose. The calibration curve is a linear curve relating the optical density to dose in Gy as shown in Figure 3.5. The calibration procedure followed in this work is considered sufficient since the gels are used only for relative dose measurements. Absolute dosimetry gel measurements will require sufficient additional calibration due to potential energy dependence concerns. The analysis of the gel was performed using in-house developed MATLAB codes that have been validated using spot checks and redundancy algorithms.

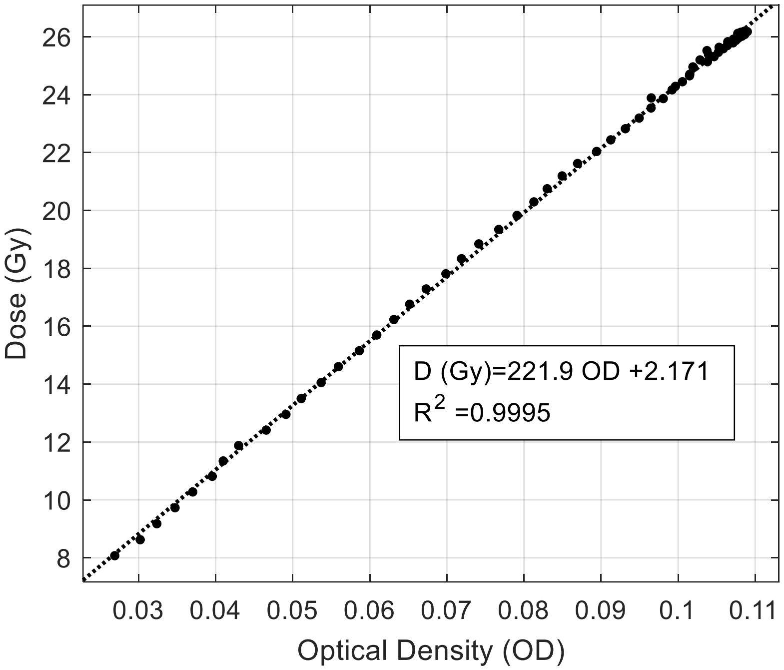

Figure 3.5: Clearview gel calibration curve relating optical density to dose in Gy.

3.4.2. Film Measurement

EBT3 Gafchromic films (Ashland, Bridgewater, NJ) were used in this work to compare to the gel results. The measurement setup was used to obtain detailed 2D relative dosimetry measurements of PDDs, ROFs, beam profiles, and beam divergence. A 2-cm thick slab of solid water (Gammex solid water) was used for dose buildup and to reach the same reference conditions used in gel measurements (Figure 3.3 A).

3.4.2.1 Film Processing Calibration

Films were scanned using EPSON scanner Model: EU-88 set to the professional mode with a 150-dpi resolution for all scanned films. To ensure adequate post-irradiation film saturation, all calibration and measurement films were scanned at least 24 hours after film exposure [88]. The analysis of the film measurement was performed using FilmQA Pro (Ashland Scientific software [89]) and MATLAB codes following the AAPM (TG-47) specifications [90]. The film exposure time was set to be at least 2 minutes to ensure higher optical density values and decrease the effect of noise and the associated errors expected at small optical densities [88]

The film calibration curve was established for the expected range of doses in this work ranging from 0 to 8 Gy as shown in Figure 3.6. The 0 Gy represents the un-irradiated film used to determine the necessary background reading correction. The radiochromic film calibration was performed depending on all the three-color components: red, green, and blue. On the other hand, the dose measurement analysis was performed using the higher sensitivity color component (red color component) [91].

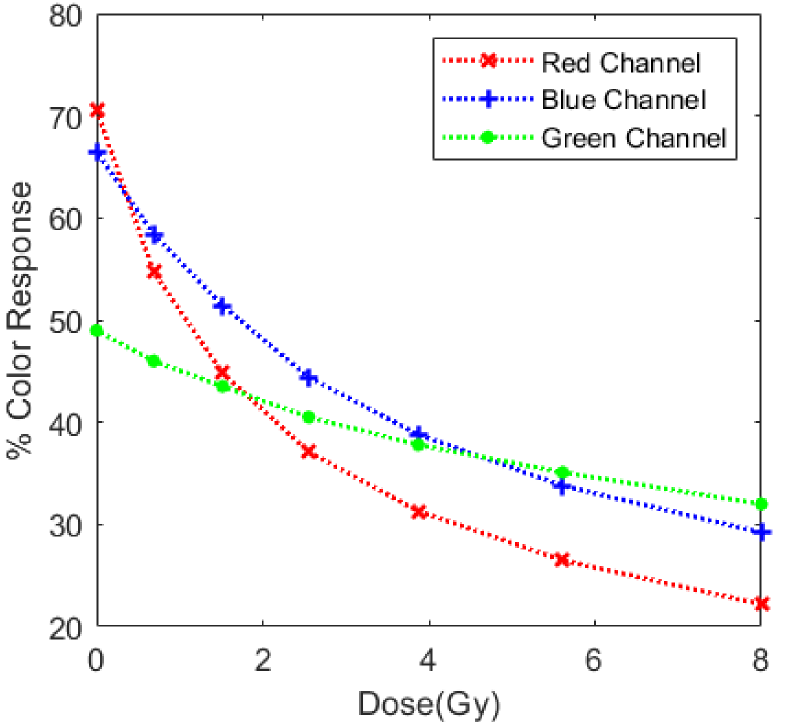

Figure 3.6: Film Calibration curve showing the three-color (red, blue, green) components curves relating the percent color response of the film to dose in Gy.

3.4.2.2 Film measurement

Film measurements were reported as the average of three different trials to inherently assess the overall reproducibility of the measurement and mimic the same gel measurement procedure. The first set of film measurements was used for the full-beam characterization of the three fields

(0.5x0.5 cm^2, 1x1 cm^{2,} and 2x2 cm^2) and compared with the gel results. All experiments were acquired at the same SSD, 220 cm from the Linatron target, and at the reference depth of 2 cm in solid water (Figure 3.3 A). The measured results were compared with gels for dosimetry point measurement (ROF), 1D measurement (Profiles, PDD), and 2D dosimetry measurements for (Profiles, PDD). Those results were fully discussed in the Gel and Film Results Comparisons section.

The other part of film measurement includes the beam divergence, absolute dose measurement for inverse square law and the collimation positioning accuracy measurements were discussed in this section:

A. Beam divergence and inverse square law

The beam divergence measurements were performed for the open bare field of the linac of 5.08 cm diameter field size using EBT3 Gafchromic films at different SSDs to measure the divergence of the beam size with distance. All the measurements were performed at the same depth in solid water of 2 cm. The average film field size was measured as the average of three separate trials at each SSD. Figure 3.7 shows the beam profiles (horizontal and vertical) and the corresponding beam field size; FWHM, that diverges (widens) linearly with the increased SSD. The film measured beam size (FWHM) values agree with the mathematically expected calculated beam divergence values within an approximate 1.8% difference. However, the beam exit point has a higher error of 4.5 % due to the collimation positioning uncertainty incorporated at the beam exit collimation (Table 3.3). Figure 3.7 also shows the effect of the variations in solid water positioning used for 2 cm buildup which has led to some profile asymmetry. As the solid water affected the resulted in-scatter to the films and hence measured film beam profiles symmetry.

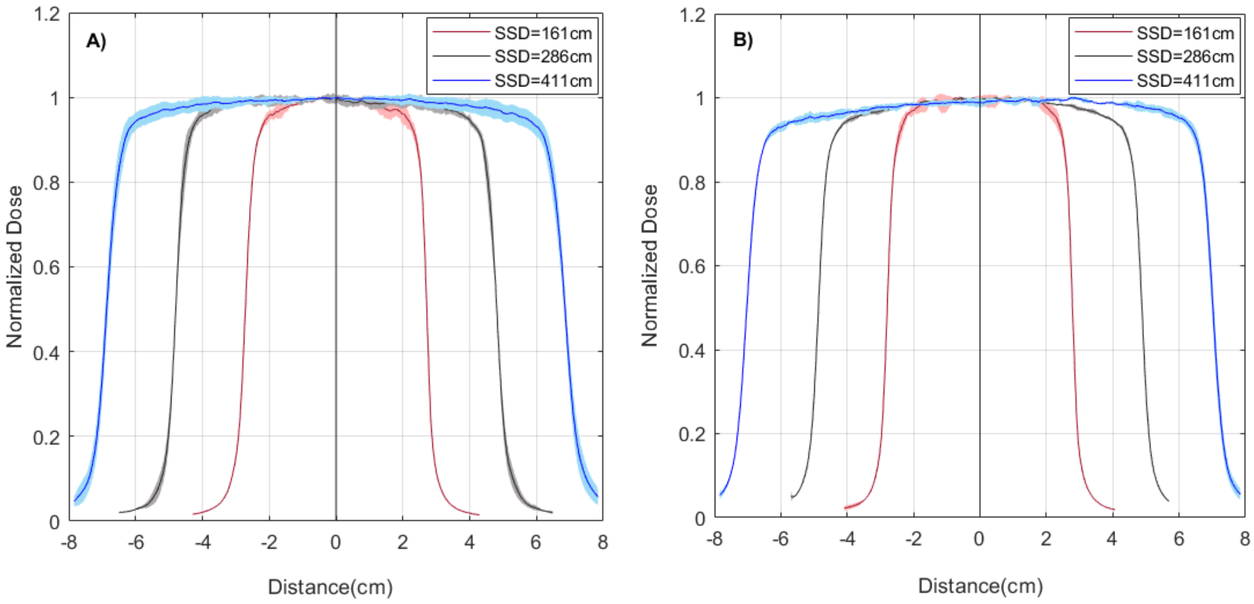

Figure 3.7: Beam profiles of primary collimated Linatron beam divergence (5.08 cm diameter) with distance from the beam exit measured with films at beam exit (161 cm SSD), 1.25 m (286 cm SSD), and at 2.5 m (411 cm SSD) from beam exit. A) horizontal profiles, B) vertical profiles.

Table 3.3: The field size divergence data with distance from the target source

SSD (cm)	Measured Field (cm)	Calculated Field(cm)	Relative % Error
161	5.75	5.49	4.53
286	9.81	9.63	1.83
411	14.00	13.84	1.14

Films were used to measure the absolute dose values at different SSD distances to quantify the reduction of the absolute measured dose with distance and hence quantify the inverse square law relation. The fitting of the absolute dose resulted in an inverse square fitting with an R^2 near unity (0.999), as expected theoretically due to the inverse-square law (Figure 3.8). The higher R^2 value of the fitting indicated a good estimation of the absolute dose value within that SSD measurement range of 161 cm (Linac exit) to 411 cm, where most of the dosimetry experiments are expected to be held.

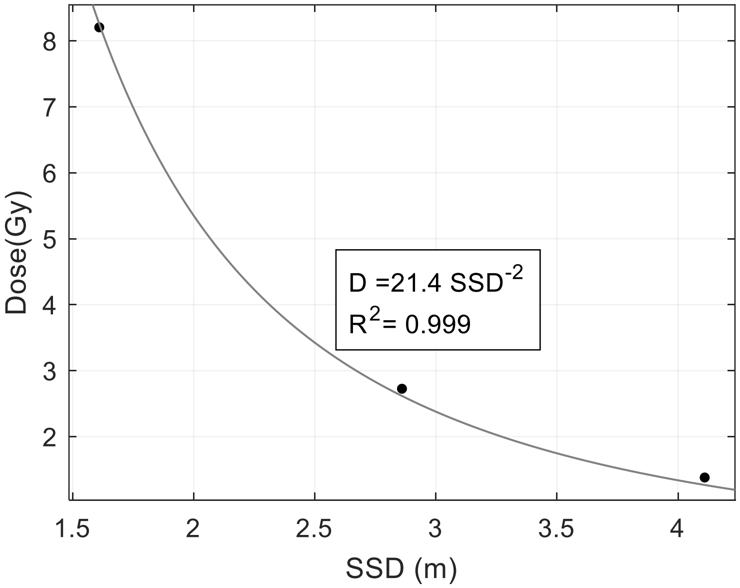

Figure 3.8: Inverse-square law fitting verification of dose (in Gy) measured with films as a function of distance from linac source SSD (in meters).

B. Collimation positioning accuracy measurement

Secondary collimators were manually positioned for shaping the static linac field of 5.08 cm diameter into the smaller fields of 0.5x0.5 cm^2, 1x1 cm^{2,} and 2x2 cm^2. Thus, it is essential to measure and quantify the accuracy of the secondary collimator setup (i.e., the manual collimator positioning misalignment). The collimator positioning uncertainty is measured by evaluating the variability among six different trials (3 different setups per person) and each was performed with a separate positioning of the collimator. The collimator positioning uncertainty is then estimated as the standard deviation of the measured output (D_{max}) of the field. D_{max} refers to the maximum dose at the central 2x2 mm^2 ROI measured for both teste fields of 0.5x0.5 cm^2 and the 2x2 cm^2. The 0.5x0.5 cm^2 is expected to have the highest positioning error and alignment difficulty due to its smaller size, while the 2x2 cm^2 field has the easiest collimator alignment among the three fields of this study. Hence, this analysis aims to quantify the expected range of positioning uncertainty. The overall measured average collimation positioning uncertainty was 1.93% and 4.18% for the tested 2x2 cm^2 and the 0.5x0.5 cm^2 field, respectively. Hence, the maximum expected to affect any mispositioning uncertainty of the collimator is expected to be within 4% of the maximum measured field output. The collimation positioning uncertainty was calculated ignoring the other relevant uncertainties such as film-related uncertainties and the Linatron output variability as each is considered and expected to be less than 1%.

Additionally, the effect of the expected collimation displacement error on the measured D_{max} of the 0.5x0.5 cm^2 field and 1x1 cm^2 field was simulated using the EGSnrc MC code. A 1-mm shift in the secondary lead collimator position horizontally has resulted in as high as 22.1% and 2.8 % reduction in the output of the 0.5x0.5 cm^2 and 1x1 cm^2 fields respectively. An angled 1mm misalignment of the collimator resulted in as high as 21%, and 6.8% reduction in the output of the 0.5x0.5 cm^2 and 1x1 cm^2 fields respectively. The smaller field of 0.5x0.5 cm^2 is highly affected by any collimation misalignment. However, with the aid of the integrated positioning laser system, this effect was reduced, and this reduction was reflected in the considerably lower measured collimation positioning uncertainty of 4.12% compared to the simulated expected 22.1%.

To increase the reproducibility of the lead brick positioning, it is recommended for future measurements to measure the output of the field post collimation positioning before any experiments. This will work as a monitoring technique to maintain and ensure higher accuracy of the dose delivery specifically for the commonly used field for animal irradiation experiments of 2x2 cm^2.

3.4.3. Gel and Film Results Comparisons

The full 3D dose distributions of the three fields of study (0.5x0.5 cm^2, 1x1 $cm^{2,}$ and 2x2 cm^2) were measured with gels and reported as the average of all three trials captured in the same gel jar to decrease the inter-gel variability (Figure 3.9). The beam characteristics and relative dosimetry were extracted at the corresponding orientation (slices of interest) to compare with the measured film results acquired at the same reference conditions including beam profiles, PDDs, and ROFs.

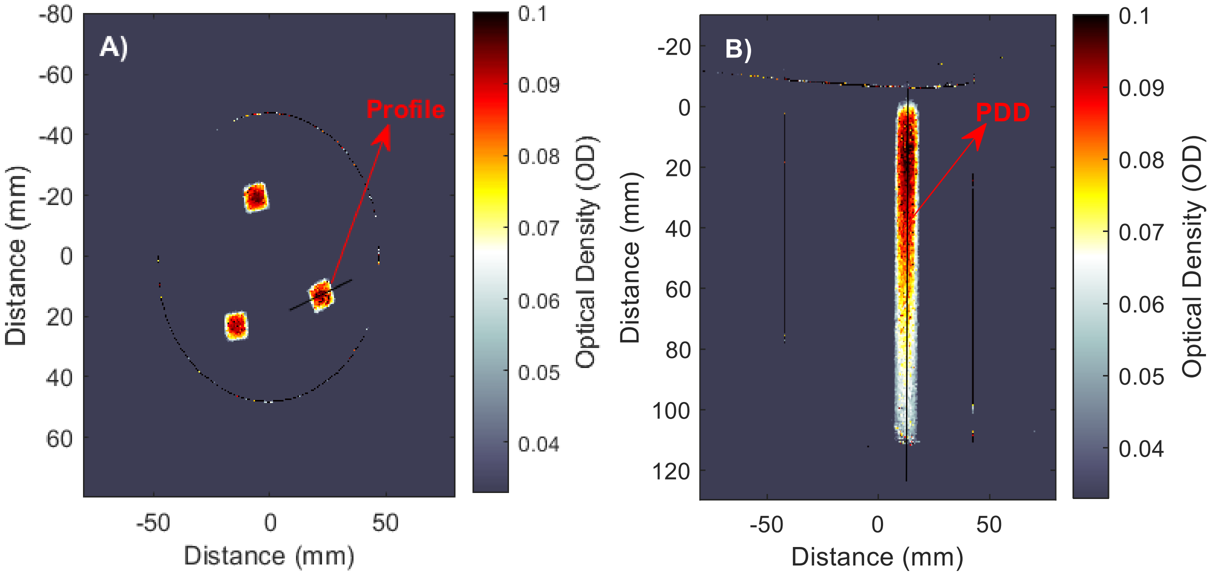

Figure 3.9: Gel extracted dose distributions showing the transverse and sagittal views of dose distributions in A and B for extracting beam profiles at 2 cm depth, and PDD curves at the beam center respectively.

3.4.3.1. Relative Output Factors (Point dose comparisons)

The output factors for the three small fields were measured relative to the 2x2 cm^2 collimated field. The relative output factor of this field was measured previously relative to the static open field of the linac using the A-14 IC. It is expected that the effect of the volume-averaging at this field size will be minimal. The smaller fields have a much smaller size than the average volume of the chamber, hence films and gels are used for those fields relative to the 2x2 cm^2 reference field in this work. The output factor of the 2x2 cm^2 relative to the 5.08 cm diameter reference circular field was measured with the A-14 IC and verified with films to be equal to 0.94±0.002 and 0.94±0.02, respectively. Film and gel output factor measurements were calculated at the reference depth of 2 cm in a region of interest of 2x2 mm^2 for the three field sizes measured. The reference depth throughout the study was selected to be 2 cm to simplify the Linatron output dose calculations for animal irradiations given that the estimated skin to liver depth for rabbit measurement applications is 2 cm. The reported output factor for the fields is the average of at least three different trials and the error is the deviation between these trials.

The relative maximum relative percent difference between gel and film measurements was 4.3 % for the smallest field of 0.5x0.5 cm^2. While the ROF relative error for the 1x1 cm^2 field was within 1.1 % (Table 3.4). The major contribution to those ROF differences between the two methods was the uncertainties in the manual positioning of the collimator. Because both measurements were performed on different days, each measurement has its own independent manual collimation positioning setup.

The output factor for the 2x2 cm^2 field and the 0.5x0.5 cm^2 using films were reported as three different trials per person to decrease the effect of the collimation positioning uncertainty in the overall measurement. This approach was also used to ensure compatibility with the gel results, which were performed at a different collimation setting. Hence the error in the film ROF of those two fields is a combination of trial uncertainty and collimation positioning uncertainty.

The major expected source of measurement variability is the positioning uncertainty of the secondary collimators. Since the smaller collimated field (0.5x0.5 cm^2) exhibits higher uncertainty in the collimation placement, it has a higher relative error in the ROF. On the other hand, the per-field output variability could be 1.1%, as in the case of the 1x1 cm^2 field when the collimation was kept in position.

The positioning lasers help in decreasing the collimation positioning associated uncertainties. It has been noticed that with the repetition of the measurements, the overall collimation positioning becomes more reproducible. This improvement in the reproducibility with time is reflected by the relatively smaller relative percent difference between the gel and film measurements of the ROF that were performed on different days and with independent manual collimation positioning setups.

Table 3.4: ROFs of the Linatron small field sizes measured relative to the reference field of 2x2 cm^2 field

Field Size (cm^2)	**Film ROF**	**Gel ROF**	**Relative % Difference**
0.5x0.5	0.70±0.03	0.67±0.01	4.3 %
1x1	0.89±0.03	0.88±0.02	1.1 %
2x2	1.00±0.05	1.00±0.01	0.00%

The measured ROFs for the 1x1 cm^2 and 0.5x0.5 cm^2 are within a maximum relative error of 0.8% and12.6% from the MC-simulated results respectively. The higher relative error for the smaller field was mainly caused by the collimation positioning error, which was measured to be 4.18% in this study. A 1 mm spatial displacement of the collimation position of the 0.5x0.5 field was simulated to affect the ROF by as high as 21%. Thus, the measured ROF is lower than the simulated value. Another contribution of the simulated and measured ROF differences is that the Monte Carlo methods for very small fields are considerably difficult due to a range of factors; mainly the approximation of a point source that is unable to properly replicate potential source occlusion in dose measurements. Since the two measurement methods (gels and films) congruently indicated lower output factors compared to simulation, it is possible that the source occlusion could be an additional source of uncertainty in MC results.

3.4.3.2. Profiles and PDD (1D dose comparisons)

The 1D beam characteristics, including beam profiles and PDD curves, were measured at the reference conditions and compared for gels and film at the same setup conditions.

A. Beam profiles

The average beam profiles, horizontal and vertical profiles, were measured with gels and films (Figure 3.10) at the reference depth of 2 cm in the phantom. The profile curve is the average of three trials and the error bars for each measurement method (gel, film) represent the deviation between those trials. Since the gels have limited sensitivity for low doses, the gel profiles could not capture the full penumbra region of the fields as shown in Figure 3.10. The absolute dose sensitivity of the gels is limited to doses above 8 Gy. The effect of background-measured OD differences and stray light noise were excluded from the measurement. The penumbra region that represents the profile edges measured with gels has higher error bars between the measurement trials (Figure 3.10), due to the coarser resolution of the gels (0.5 mm) in comparison to the finer film resolution of ~ 0.02 mm.

The main characteristics of each small field, such as beam size measured in FWHM and (20 – 80%) penumbras, were listed in Table 3.5. The maximum spatial differences in the measured beam sizes by gels to the film measured FWHM were within approximately 0.8 mm. The main contribution to those spatial differences is the spatial resolution differences between the two methods.

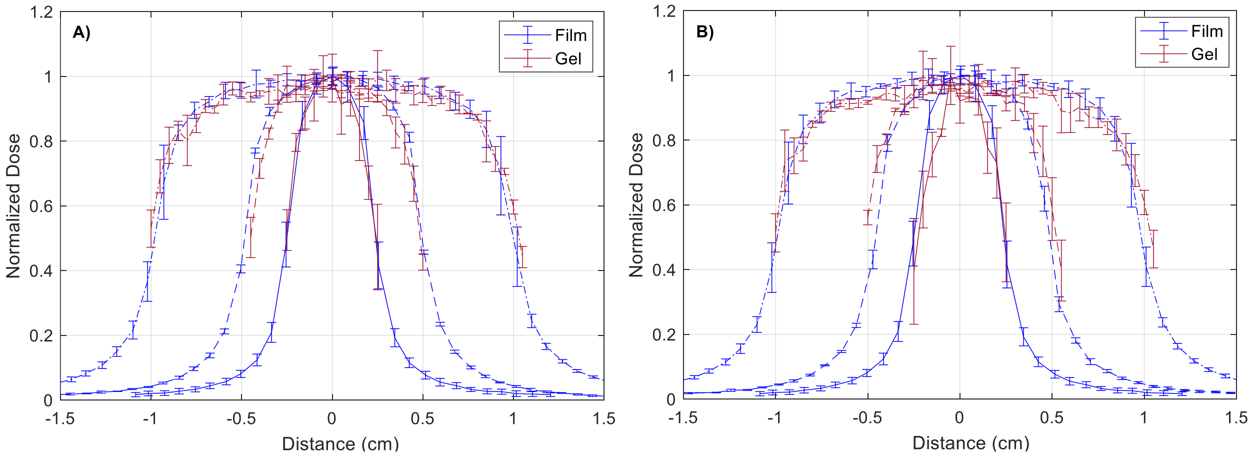

Figure 3.10: 1D beam profiles measured with gel dosimeter and EBT3 films for the three fields (0.5x0.5 cm^2, 1x1cm^2, and 2x2 cm^2) at 2 cm reference depth in phantom; (A) the horizontal (in-plane) beam profiles, (B) the vertical (cross-plane) beam profiles.

Table 3.5: Beam profile characteristics for the different fields measured at 2 cm depth using films and gels

	Field Width (cm)		**Left Penumbra (cm)**		**Right Penumbra (cm)**	
	Film	**Gel**	**Film**	**Gel**	**Film**	**Gel**
0.5x0.5 cm^2	0.48±0.04	0.50±0.01	0.15±0.02	0.19±0.11	0.15±0.01	0.20±0.09
1x1 cm^2	0.96±0.03	0.99±0.05	0.20±0.02	0.23±0.07	0.20±0.07	0.22±0. 01[a]
2x2 cm^2	1.98±0.01[a]	2.06±0.01[a]	0.26±0.01	0.35±0.02	0.34±0.01[a]	0.24±0.01

[A] minimum error value in measurement of 0.01 cm is reported here for the beam profiles extracted from the film. Similarly, the error value in the right penumbra was measured with both gel and films.

B. Percent depth dose curves (PDD)

The percent depth dose (PDD) curves for the three small fields were measured and reported as the average of three trials (Figure 3.11). Data were measured with both EBT3 Gafchromic films and gel dosimeters. The error bars are reported as the standard deviation between the different readings. PDD curves were normalized to the average maximum measured dose using films and gels. Gel-based PDD curves are measured as the average dose readings were acquired along with the central ROI of 2x2 mm^2 on each gel slice centered in the dose center of the field. This approach was performed to correct for any angular misalignments of gel relative to the radiation beam central axis with depth. As a result, the error between the three different trials measured with gels is lower than the film-measured error specifically for the smaller field of 0.5x0.5 cm^2. The higher film error for the smaller field sizes is mainly due to the alignment difficulty of films in the central region of the smaller fields. Films are difficult to place parallel to the beam direction due to the increased possibility of angular misalignment with depth. Hence, Gel dosimetry was expected to be more robust and efficient in capturing the 3D dose distributions and hence the PDD curves at deeper depths (>3 cm) with higher accuracy compared to films.

Although gels can correct for angular misalignment, gel-measured PDDs show higher uncertainty in the buildup region up to 0.5 cm. The effect of image reconstruction artifacts from stray light and light refraction at the surface of the gel is the main source of those dose uncertainties in the buildup region. Hence gels can’t be used for surface dose measurements [49], [85].

The maximum point disagreement in the buildup region, starting from 0.5 cm depth, between the film and gel measurements is within 11%. While the maximum point disagreement at the tail region for depths up to 5 cm is within 2.6 %. For the larger field of 2x2 cm^2, the main field of interest for small animal irradiations, the percent difference error between film and gel acquired PDDs was < 2% for depths from 0.5 cm to 8 cm within which most effective accurate dosimetry measurements were expected to be held.

The depth of the maximum dose, as well as the surface dose (as measured with films in Figure 3.11A), increases with the field size due to the scattering within the phantom.

The gel measured depth of maximum dose was in good agreement with the film results with a maximum spatial difference of 1 mm. This spatial difference is due to differences in the spatial resolution of both methods and mainly due to gel surface artifacts. The uncertainty associated with the gel surface artifacts affected the accuracy of the determination of the startup slice of the gel measured dose. This uncertainty was corrected through maximum dose alignment for the PDDs to well predict the surface slice of the Clearview gel. To eliminate the effect of this uncertainty, it is recommended to mark the relative position of the reference depth of interest at the edge of the gel dosimeter in future measurements.

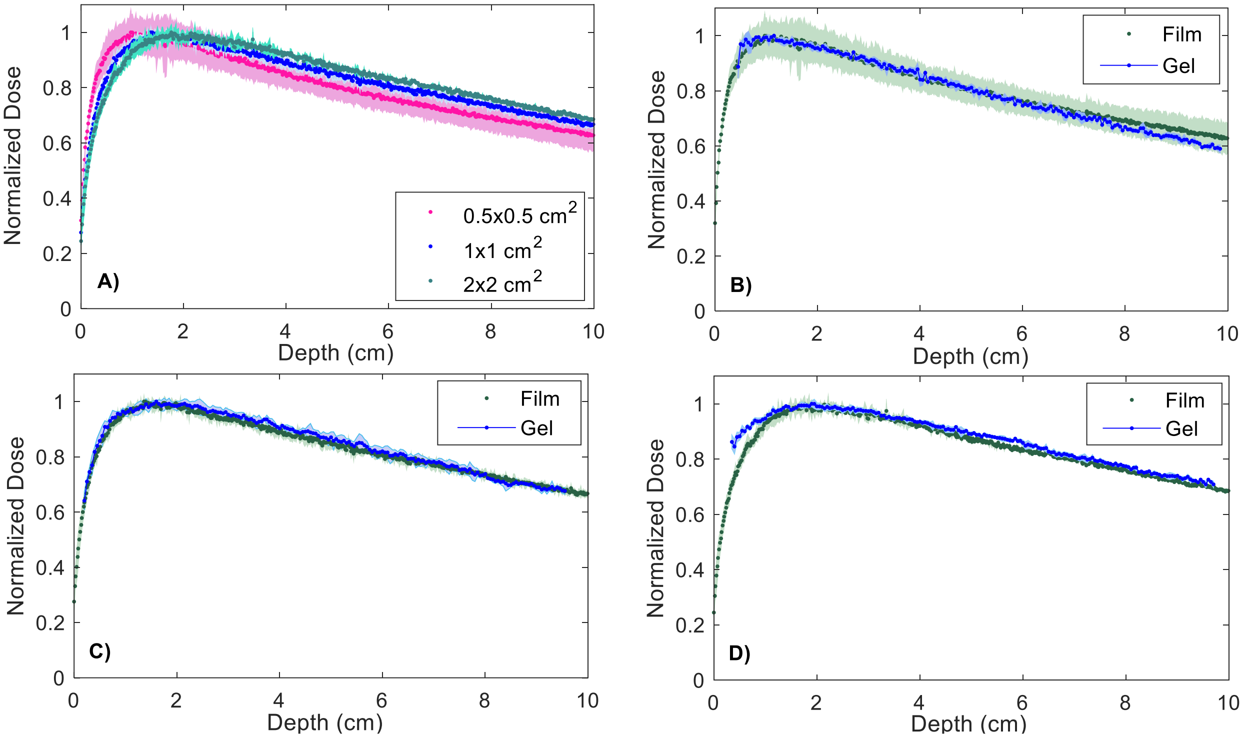

Figure 3.11: PDD curves for each of the small radiation fields (A) Film-based PDDs for all the different fields (B) 0.5x0.5 cm^2, (C) 1x1 cm^2, (D) 2x2 cm^2 measured with gels and films.

3.4.3.3. Profiles and PDD (2D dose comparisons)

The 2D beam characteristics, including beam profiles and PDD curves, were measured at the reference conditions and compared for gels and film at the same setup conditions. The 2D dose distributions were extracted at the slices of interest from the 3D acquired gel dose distributions (Figure 3.9) to meet the film measured dose distributions at the same setup.

A. Beam profiles:

The profile contour plots were extracted at a depth of 2 cm for all field sizes using both the EBT3 and Clearview gels, as shown in Figure 3.12. The isodose lines were reported as the average of three different trials for each measurement method. The isodose contour lines agree within 0.5 mm for the two smaller fields 0.5 x 0.5 cm^2 and 1 x 1 cm^2 and within 1 mm for the 2x2 cm^2 field. The small dimensions of the measured fields and the differences in the spatial resolution of the imaging modalities used in the gel and film measurement were the main sources of the reported differences between the profile dose contours in this study. Overall, these measured isodose lines show excellent agreement between films and gels for the three fields of interest. The reported spatial differences between the film and gel measured results were comparable to the reported values in the literature comparing films to PRESAGE gel [85].

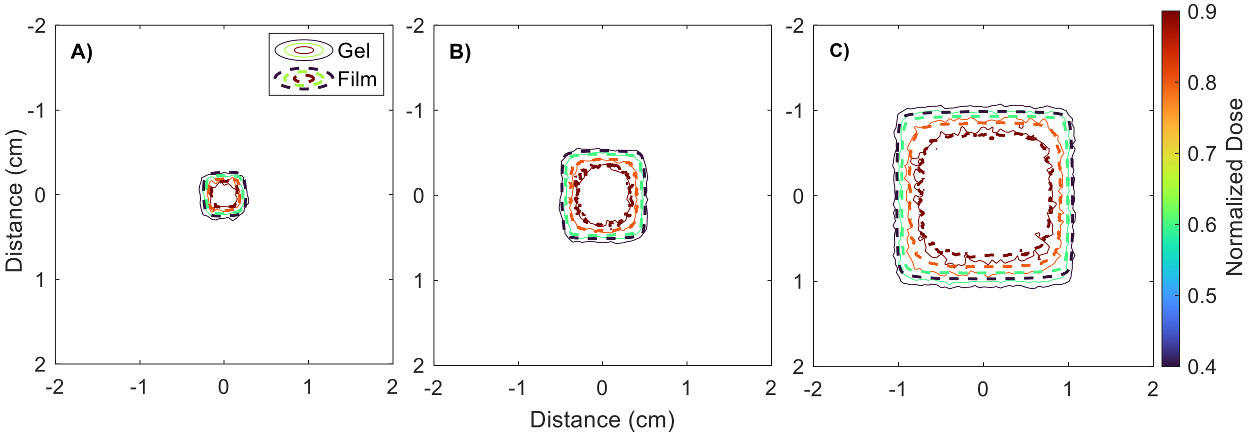

Figure 3.12: Isodose contour plots measured with gels and films of the different small field profiles at the reference 2 cm depth. The plotted isodose lines are 90, 80, 60, and 40%. A) 0.5x0.5 cm^2 field, B) 1x1 cm^2 field and C) 2x2 cm^2 field.

B. Percent depth dose curves (PDD)

The 2D PDD curves were acquired using film and the Clearview gels at the central beam region along the beam direction as the average of three different trials as shown in Figure 3.13. Within the typical therapy region of small animals (1–4 cm), all PDD curves agree within approximately 2% of the maximum dose. EBT3 film measured curves were slightly steeper (~ 12% at 2.5-4 cm) specifically for the smaller field of 0.5x0.5 cm^2. Film misalignment, which causes the curve to fall off more steeply for films in comparison to gel is the main cause of this steep behavior of the film measured PDD and hence the resulting disagreement between the two methods. As reported previously, the inherent collimation placement error is as high as 4.18% for the 0.5x0.5 cm^2 field. This collimation misalignment error also contributes to the measured discrepancy since both measurements (film and gel) were performed at different collimation setups.

To correct for the film positioning relative to the beam center, a correction factor relating the PDD measurement along the beam direction at 2 cm to the output dose measured across the beam direction at 2 cm depth was implemented. This approach was implemented to correct the film misalignment uncertainties. As expected, the implemented correction factor improved the agreement between the film and gel measured PDD curves to be within approximately 5% in the typical therapy region (1–4 cm) for the 0.5x0.5 cm^2 field as shown in Figure 3.13 A.

Even with implementing the correction factor, film-measured PDDs are steeper than those of the gel for all the fields. This effect was also reported in the literature and the main cause of this effect is not clearly known. As reported and concluded in the literature, the main causes of the steeper film measured PDDs are the expected reduction in the accuracy of film data at depths deeper than 2 cm. In addition, the film misalignment is expected to cause the PDD curves to decrease more steeply. The relative differences in electron density of the EBT3 film and gels could contribute to this measured effect as well.

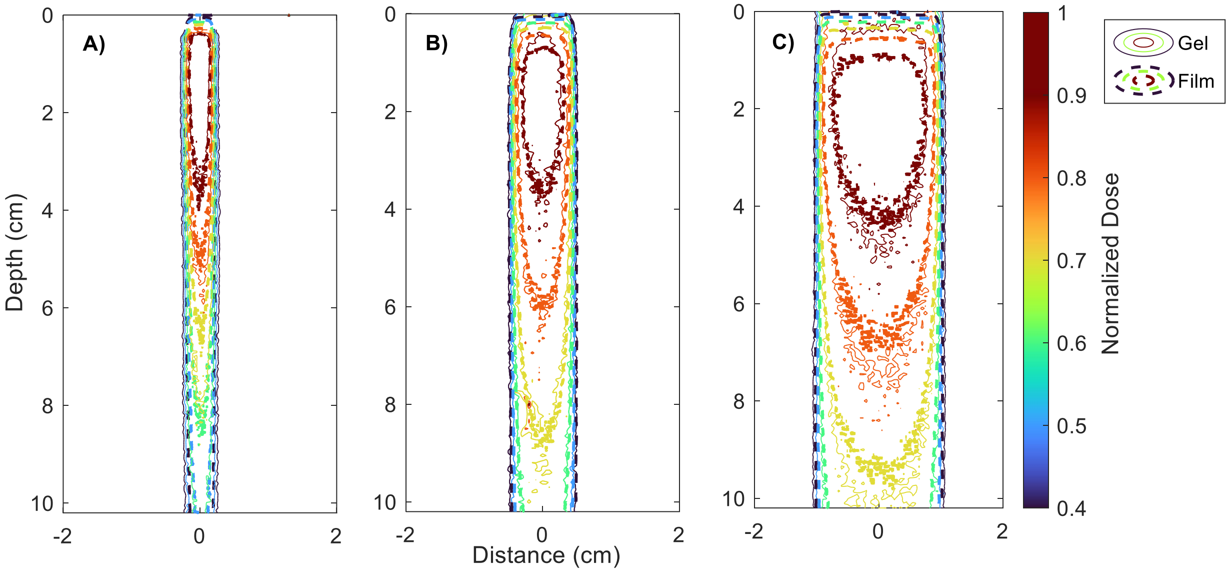

Figure 3.13: Isodose contour plots measured with gels and films for the different small fields. PDDs are normalized to the maximum dose and the plotted isodose lines are (90, 80, 70, 60,50 and 40%. A) 0.5x0.5 cm^2 field, B) 1x1 cm^2 field and C) 2x2 cm^2 field.

3.5. Conclusions

The work in this chapter was performed to provide a simple yet accurate commissioning process to measure the beam characteristics of an MV research accelerator. Hence, this procedure can be followed to fully characterize and commission non-standard radiation fields. The detailed 3D, 2D, and 1D dosimetric evaluation was the primary initial step towards the implementation of the Linatron as a megavoltage small animals irradiator for radiobiological and dosimetric preclinical studies.

The work also demonstrated the effectiveness of the ClearView radiochromic gel dosimetry, given their dose-rate and energy independent response, as a robust and efficient 3D dosimetry tool for small field studies through the relatively acceptable agreement with film measurements.

Although Clearview gels have a limited dose-response measurement in the buildup region due to artifacts near the phantom surface, they provided the full 3D dose measurement allowing for full representation of the dose. In addition, these full dose distribution measurements showed the advantage of minimizing the dosimeter misalignment uncertainties, which is the main challenge in small field measurements. Clearview Gels showed high agreement and less standard deviation between the different gel trials measured using the same gel jar within 4% or less for PDD measurements. That reflects the higher intra-stability of the gel jars. The advantage of measuring multiple small fields and field parameters using the same single dosimeter of Clearview Gels allowed for higher measurement accuracy and reproducibility.

Chapter 4

Monte Carlo Simulations for Commissioning of a Megavoltage Research Linear Accelerator

This chapter describes the full procedure followed to investigate the initial electron source parameters to define the linatron source using MC simulation-based approach. In addition, this investigation aims to fully acquire the phase-space files describing the linac spectrum and investigate both the mean electron energy of the linac and the beam quality. Simulation results were compared and tuned with the dosimetric measured data. Measured data were acquired through implementing a full commissioning procedure for the Linac open static field of 5.08 cm in diameter. The experimental part of this work was discussed in the previous chapter and was published in the article "Application of radiochromic gel dosimetry to commissioning of a megavoltage research linear accelerator for small-field animal irradiation studies", Medical Physics Journal, 2021 [71]. The simulation part of the work will be published in a separate journal article.

4.1. Introduction

Monte Carlo (MC) method is a powerful tool used for dosimetric calculations in radiation therapy, specifically when other simple methods fail to provide accurate dose calculations. Accurate implementation of MC methods in dosimetric calculations depends on the accurate full characterization of the initial radiation source. Hence, initial linac source optimization is an essential primary step for beam characterization and dose calculations.

The initial electron source of the linac interacts with the source target and converter to produce a bremsstrahlung photon source. The initial characteristics and source parameters of the incident electron source are highly affecting the characteristics of the induced photon source, thus the radiation beam characteristics. The initial electron source parameters tuning method is the commonly used technique in literature [92]–[102]. This technique is MC-based such that the full characterizing of the primary electron source is performed through tuning the electron beam intensity, mean energy, and angular distribution. Previous studies concluded that the depth dose curves in water are sensitive to the mean energy of the primary electron source such that the central axis deposited dose increases as the mean energy of the beam increase [94], [98]–[100], [102]–[104]. As a result, the MC-simulated and measured percent depth dose (PDD) curves have been used in some studies for tuning the mean energy of the electron beam [98], [105], [106]. Other studies have recommended using in-air off-axis factors [101]or the beam profiles in addition to the PDD curves for optimal and more accurate electron beam mean energy (endpoint) tuning [94], [98]–[100], [102]–[104]. Previous studies concluded that the PDDs curves are insensitive to the variation in the primary electron beam width (radial beam intensity) for the reference field sizes of 10x10 cm^2 [99], [101], [107]. In contrast, some studies have concluded that the beamwidth of the initial electron source has influenced the rising edge of the depth dose distributions for the radiation field of 10 ×10 cm^2 [99], [108]. The beam profiles, horizontal and vertical, of the dose distributions of large field sizes, are highly sensitive to the primary electron beam width. It has been recommended to use larger field profiles (≥ 10x10 cm^2) and shallower in-phantom depths for tuning the electron beam width [105], [109]. In contrast, other studies have recommended using deeper in-phantom depths of approximately 20 cm for more accurate primary electron beam width optimization[99].

One proposed challenge in implementing this technique is computational expense, and it is also affected by inherent experimental and simulation errors. Since the M9 Linatron is a research accelerator, it has a built-in customized shielding to reduce the expected dose to the personnel and the ambient dose in the lab. The added shielding could have affected the resulting beam characteristics due to its interaction with the secondary scattering radiation component of the radiation beam.

In this work, the tuning-based initial source optimization method was implemented as the first step to developing an efficient and accurate MC-based dosimetric tool to validate the implemented linac commissioning procedure. Additionally, the full phase-space files of the different radiation beams of the linac were used to develop a pre-irradiation simulation-based tool for small field static beam animal irradiation studies.

The full model of the linatron components was developed using the MC code EGSnrc/BEAMnrc, including the source, collimators, IC, shielding, and the secondary collimators as shown in Figure 4.1. The main steps of the implemented parameter tunning approach are shown in Figure 4.2 and include the different parts of the produced photon beam regions that are affected by the tuned electron parameter as proposed in previous studies.

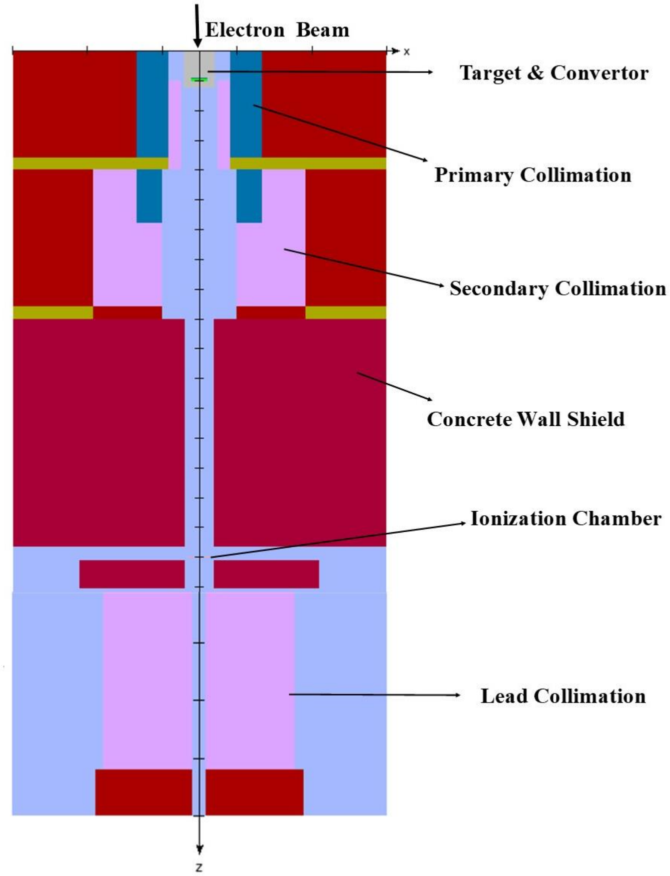

Figure 4.1: The linatron model simulated and plotted in BEAMnrc/EGSnrc MC code [82] showing the XY plane of the model.

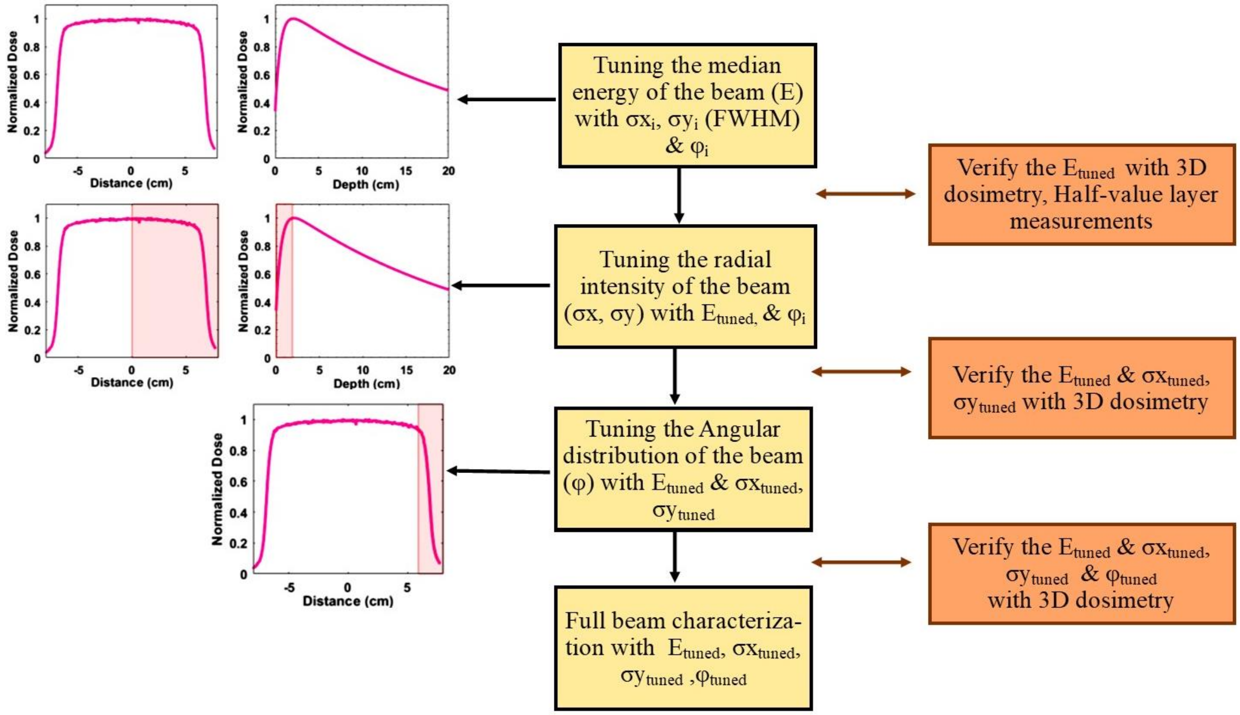

Figure 4.2: The schematic plot illustrating the process of initial electron beam characterization steps and the associated regions of the measured beam data that are affected by each tuned parameter step. Verification steps were introduced after each tuning step to verify the resulting source parameter.

The research Linatron 9MV was fully simulated using EGSnrc based Monte Carlo codes; BEAMnrc and DOSXYZnrc [81], [82]. The Linac head geometry which includes the target, primary collimator, and shielding parts was modeled using BEAMnrc based on the geometries and the material data provided by the vendor. The custom-designed shielding parts were also considered and added to the model to accurately acquire the source phase-space file. Dose distributions were calculated in a 30x30x30 cm^3 water tank phantom placed at 220 cm SSD using DOSXYZnrc user code. Due to the geometrical constraints associated with the linac geometry and to achieve an excellent statistical uncertainty $2x10^8$ histories were simulated. Photon and electron cut-off energies were set to AP=PCUT=0.01 MeV and AE=ECUT=0.521 MeV, respectively. The initial electron source was modeled using forward-directed circular Gaussian spatial distribution monoenergetic electrons (ISOURC=19). Optimization was performed at the reference calibration point at 220 cm SSD. The reference field is 7.5 cm diameter, FWHM, measured at the calibration point at 2 cm relative depth, to achieve a compatible setting corresponding to the linac commissioning reference conditions.

For small field dosimetry commissioning, to improve the computational time, the phase-space file acquired for the open field of the linac (5.08 cm, at the aperture exit) was used as the initial source file to get the final small secondary collimated fields. The resulting collimated phase-space files of each field were then used to characterize the fields, measuring the PDD curves, the beam profiles, and the ROFs for different collimator settings at the point of treatment. 10^9 primary particles were used for the dosimetry simulations and the phase-space simulations. PDD curves were obtained over the central $0.3x0.3\ cm^2$ voxel region with a slice thickness of 0.5 cm to capture the buildup region with acceptable accuracy. The small field simulations were performed using $0.1x0.1x0.5\ cm^3$ voxel size to capture the beam profiles and penumbra with adequate statistics.

4.2. Initial Beam Energy Tuning

As concluded in previous studies, PDD curves are sensitive to the mean energy of the initial electron field and the beam profiles. The initial electron beam energies simulated are 8.4 MeV–

10.6 MeV with 0.2 MeV energy increments for the reference irradiation field of 5.08 cm diameter. In the first step of optimization, the radial intensity and deviation angle of the initial electron beam were set to 0.1 cm and 0.0° respectively. For comparison between calculation and measurements, the dose normalization was performed relative to the value of the dose at a reference depth of 2 cm in the central axis of the beam. Beam profiles were normalized to the central axis-dose readings. Different beam profiles acquired at different SSD distances were used to cover different field sizes. The main field sizes used in the study are the 5.8 cm diameter field measured at 2 cm depth and the other field size of 7.5 cm field measured at 2 cm depth. Larger field sizes were extracted at further distances from the linac exit, which has resulted in higher SSD distances.

The sensitivity of the depth dose curves to initial electron mean energy variation was verified as shown in Figure 4.3. A scaling factor was applied to capture the dose readings in Gy/min based on the average operational current (1.248×10^{14} e/s) and the linac frequency of 45-50 Hz. The Gamma index values (3% /3 mm criteria) quantitative results comparing the measured and simulated data are summarized in Table 4.1 [110]. The optimal mean energy was determined based on gamma test comparisons between the MC simulations and the measured results. The inherent errors in simulations are expected to affect the accuracy of the comparisons. Hence, the resulting optimized energy relied mostly on the PDD comparison, and profiles at the closer SSD to eliminate the effect of simulation error. Simulation inherent uncertainties increase with depth due to the reduction of the NPS that can reach the detector at further distances from the linac exit (SSD).

Films are challenging for dose measurements parallel to the beam direction because of the effect of placement uncertainty[23], [85], [111]. In contrast, a 3D gel dosimeter can acquire the full 3D dose distribution of the beam which allows to correct any misplacement of the phantom relative to the central axis of the radiation field. Hence, gel data was expected to be more accurate than films due to the inherent placement errors that can highly affect the measured PDD with films. To ensure better estimation of the endpoint energy of the beam for the linac, 1D, 2D, and 3D comparisons were performed to get more accurate results as the beam energy highly affects the dose and the main characteristics of the radiation beam. There is no optimized endpoint energy trend for all the different beam characteristics however, on average, the 9.8 MeV beam energy shows the best match for the different beam characteristics including the PDD and the profiles.

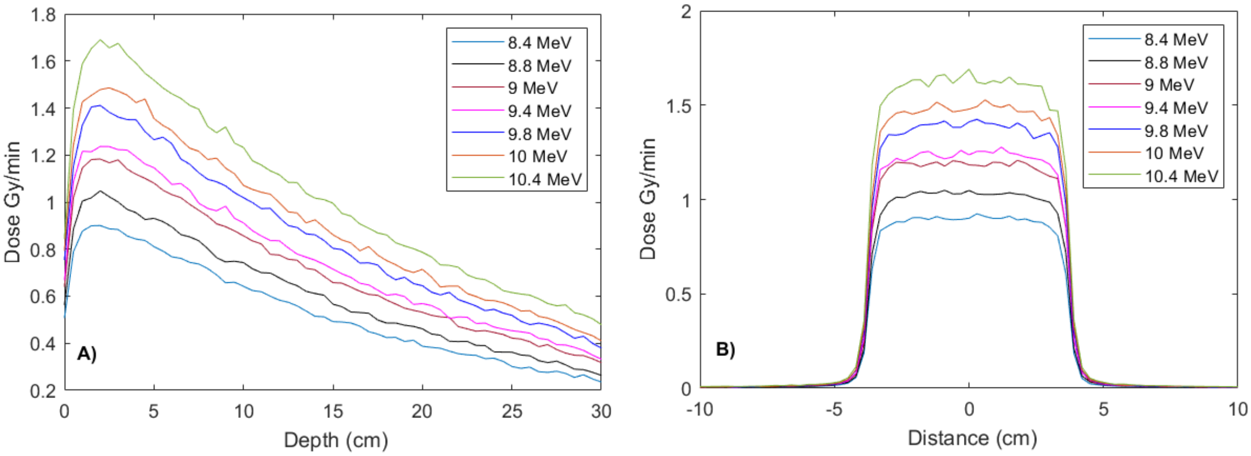

Figure 4.3: The effect of the initial electron beam energy on the simulated absolute dose based on the 45 Hz pulse repetition rate of the linac for photon beam characteristics; A) PDD, B) Horizontal profiles acquired at 2 cm depth of the open linac field measured at the calibration point.

Table 4.1: The resulting passing rates of the 3%/3mm gamma test for endpoint energy optimization

Endpoint E (MeV)	**PDD 3%/3mm**	**5.8 cm Field 3%/3mm**		**7.5 cm Field 3%/3mm**		**2D XZ 3%/3mm**	**2D YZ 3%/3mm**
		Relative	**Absolute**	**Relative**	**Absolute**		
8.4	49.0	100.0	37.8	97.3	44.8	96.9	96.9
8.6	46.9	100.0	37.8	94.6	44.8	96.2	96.9
8.8	26.5	96.6	37.8	86.5	44.8	90.0	91.2
9.0	75.5	96.6	43.2	94.6	48.3	97.4	95.0
9.2	69.4	100.0	40.5	86.5	48.3	96.7	97.6
9.4	93.9	96.6	43.2	94.6	48.3	96.4	98.1
9.6	85.7	100.0	45.9	94.6	48.3	98.3	98.6
9.8	91.8	96.6	91.9	91.9	89.7	97.6	98.8
10.0	100.0	100.0	48.6	94.6	55.2	96.4	98.8
10.2	98.0	96.6	37.8	81.1	41.4	97.6	98.3
10.4	100.0	100.0	37.8	62.2	41.4	92.1	96.2
10.6	100.0	93.1	37.8	100.0	41.4	90.5	88.8

The 2D relative dose results of the 9.8 MeV optimized endpoint energy simulation were compared to the measured gel results as shown in Figure 4.4 for the XZ and the YZ planes of the reference open field of the linac at the reference calibration point. The dose values are normalized to the reference depth of 2 cm in the phantom. There are some reconstruction artifacts at the edges of the XZ plane measured gel data as shown in Figure 4.4. The gels have limited ability to detect the buildup region of the dose, thus doses are reported for depths > 1 cm up to 9 cm, due to the limited size of the gel phantom.

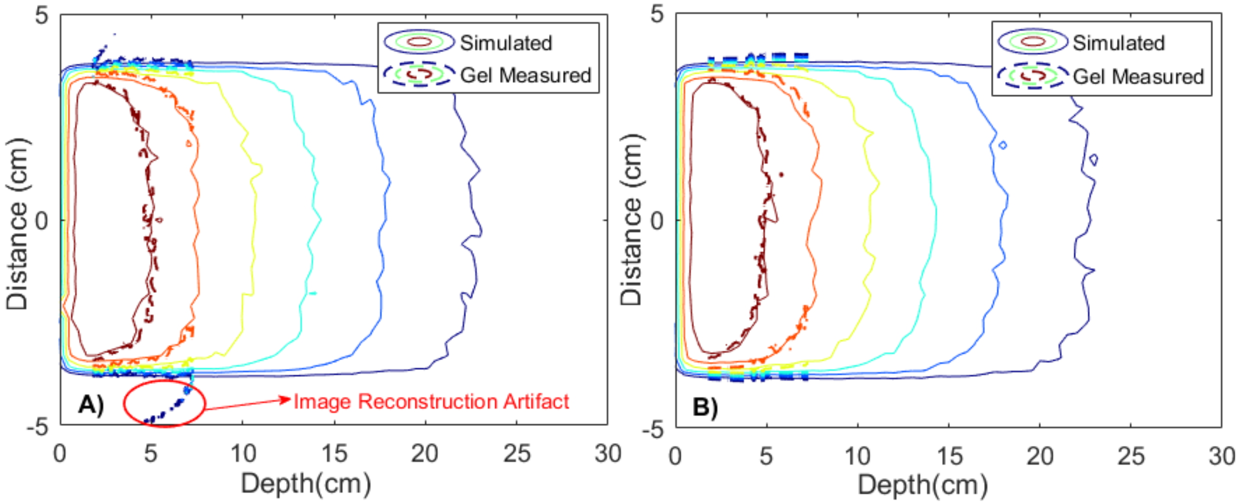

Figure 4.4: The optimized 9.8 MeV endpoint energy simulation 2D PDD curve compared to the gel measured data for A) ZX, B) ZY planes showing the 90%, 80%, 70%, 60%, 50%, and 40% isodose contour lines.

4.3. Linac Endpoint Energy Verification

To verify the resulting tunning-based beam energy, two other measurements were performed to test and validate the investigated endpoint energy of the linac. The first is beam quality and the other is the half-value layer. The experimental results were compared with simulations that mimic the experimental setup.

4.3.1 Beam Quality Measurement

The beam quality of the Linatron was verified following the initial energy tuning of the linac and calculated using the tissue phantom ratio (TPR) for doses at depths of 20 and 10 cm (TPR20/10) for a field of 11.28 cm diameter (10x10 cm^2 square equivalent field). The simulated results were compared with the measured TRP 20/10 result of 0.69 ± 0.01. The simulated TRP 20/10 was 0.71 ±0.01 which corresponds to a 2.8% error relative to measured TRP 20/10 and 0.2% relative error in the resulted beam quality. The reported agreement between the measured and the simulated beam quality verifies the optimized 9.8 MeV energy of the linac.

4.3.2 Half-Value Layer Measurement

To provide a benchmark validation of the linac model and the initial beam energy, an Exradin A12 (0.64 cm^3) ionization chamber was used to measure the in-beam doses for half-value layer (HVL) measurements. The IC was placed in a 2 cm solid water phantom at 1 cm depth. The position of the IC was held constant, at 165 cm from the linac exit, as shown in Figure 4.5. The HVL was measured in steel starting with a steel attenuator thickness of 15.24 cm to allow for significant attenuation of the low-energy photons. The attenuator thickness was gradually increased by 2.54 cm until reaching a final thickness of 30.48 cm.

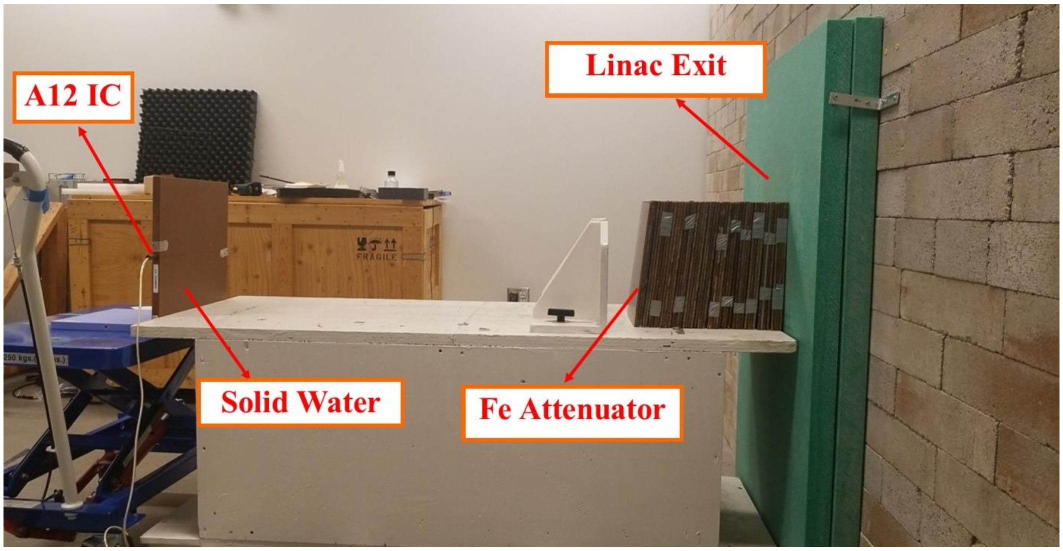

Figure 4.5: The experimental setup showing the position of the IC in the solid water phantom

The resulting dose values were normalized to the initial dose measured at 15.24 cm and used as the initial beam intensity. The HVL was calculated from the fitted curve value of the attenuation coefficient following the equation,

$$HVL = \frac{\ln(2)}{\mu}, \tag{4-1}$$

Each dose reading was measured as the average of three different trials and the standard deviation between the readings was used as the error for each measured attenuator thickness. The error of the measured data was also considered in the exponential curve fitting of the data such that the higher the error the smaller the weight of the corresponding data point. MATLAB's curve fitting tool was used to fit an exponential function to the measured data. The fitted attenuation coefficient was determined with a 95% confidence interval. The resulting fitted data are plotted in Figure 4.6. The measured fitted HVL is 2.77 ± 0.03 cm. The measured HVL was lower than the vendor-reported HVL of 3.02 cm due to the differences in the measurement setup and the effect of the added customized shielding. To test the effect of the HVL, the measured results were compared to simulations. The full measurement setup was simulated using EGSnrc; however, due to the high attenuator thickness, there was a reduction in the NPS particles that reached the detection position which resulted in uncertainty in the simulated HVL compared to the measurement uncertainty. The simulated HVL for the endpoint energy of 9.8 MeV was 2.74 ± 0.20 cm. To quantify the effect of the endpoint energy on the HVL, the linac endpoint energy of 9 MeV was simulated and compared to that of the 9.8 MeV. HVL values have shown low sensitivity to changes in beam energy. The simulated HVL of the 9 MeV endpoint energy beam was 2.54 ± 0.08 cm while the simulated HVL of the 9.8 MeV endpoint energy, 2.74 ± 0.20 cm. the resulting HVL of the 9.8 MeV endpoint energy was closer to the IC measured HVL and 9 MeV has resulted in lower HVL compared to simulations and measurement. The resulted HVL of the optimized endpoint energy of the initial electron beam was within 9.9% relative error to the IC measured value. The resulting HVL values of the different methods including the upper and the lower limits of the fitted values within a 95% confidence interval are summarized in Table 4.2. The agreement between the measured and the simulated HVL values validates the 9.8 MeV optimized endpoint energy of the linac.

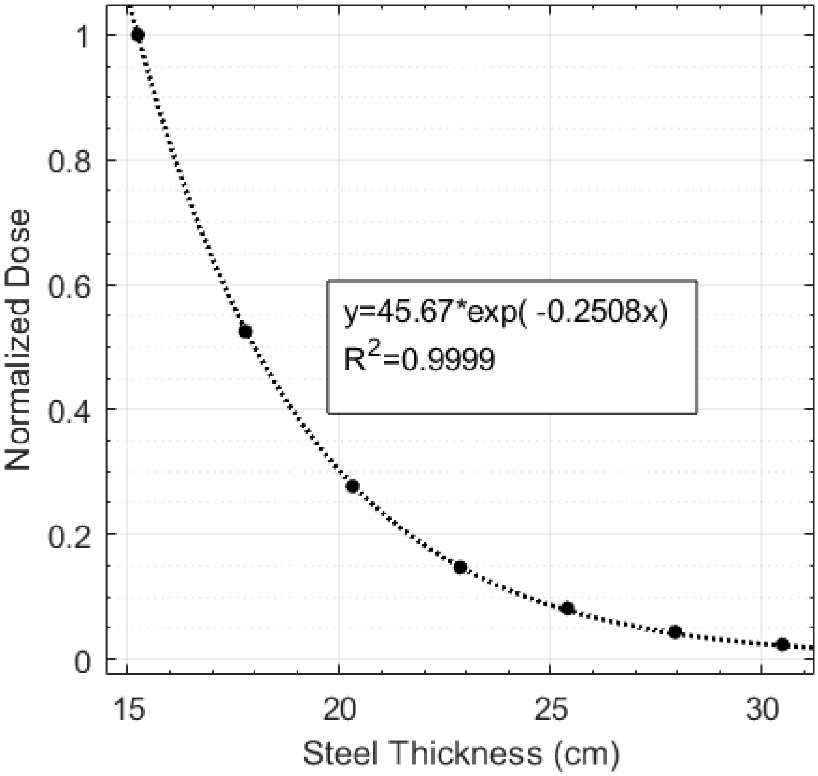

Figure 4.6: The resulted HVL measurement

Table 4.2:The reported HVL results of the different methods

Method	**HVL (cm)**
Vendor Data	3.02
A12 IC Measurement	$2.74 \leq 2.77 \leq 2.79$
Simulated 9.8 MeV Endpoint Energy	$2.57 \leq 2.74 \leq 2.95$
Simulated 9 MeV Endpoint Energy	$2.46 \leq 2.54 \leq 2.62$

4.4. Radial Intensity Investigation

The optimized linac beam energy of 9.8 MeV was used as the linac source energy for the rest of the simulation and used in simulations for the optimization of the beam radial intensity and the beam angular distribution. The radial intensity of the beam is represented as the horizontal and the vertical standard deviation, FWHM, of a Gaussian distribution of the beam intensity (σ_x, σ_y). The angular distribution of the beam was held constant for this step at 0.0°. The simulated values of the beam intensity are 0.25-2.5 mm with an increment of 0.25 mm and the simulated results were compared to the measured beam profiles and the PDD.

For the profile-based comparisons, the gamma test criteria did not result in a firm relation to reliably estimate the investigated radial intensity. There was the effect of the air gap between the film and the solid water phantom, which resulted in asymmetric beam profiles for some of the depths and positions where the profiles were extracted. A simulation-based study has concluded that air gaps between films and water causes dose underestimation [111]. To account for that effect which is expected to cause a reduction in the film measured dose at the regions with air gaps, the simulations and the measurement comparisons were held using the RMSE criteria instead of the gamma test. Comparisons excluded the affected regions of the measured data, hence relying on one of the penumbra regions. This approach was followed in both the radial intensity investigation and the angular distribution investigation part. The RMSE comparisons of either the right penumbra or the left penumbra region were used for comparisons. The optimized vertical radial beam intensity parameter was 0.75 mm for all the tested profiles. However, the horizontal radial beam intensity parameter was not highly sensitive to the RMSE or gamma criteria given the inherent simulation and measurement errors in defining the beam profiles. Larger field sizes, as reported in the literature, were used to better predict σ_x as they showed more sensitivity to changes in the radial intensity (Figure 4.7). The optimization of the σ_x was hence equal to 1.5 mm depending on the larger fields of 9.8 cm and 14 cm.

Table 4.3: The resulted passing rates of the 3%/3mm gamma test and RMSE for horizontal and vertical radial intensity optimization

Radial Intensity σ (mm)	**PDD 3%/3mm**	**Horizontal Profiles**				**Vertical Profiles**			
		5.8 cm Field		**7.5 cm Field**		**5.8 cm Field**		**7.5 cm Field**	
		3%/3mm	**RMSE**	**3%/3mm**	**RMSE**	**3%/3mm**	**RMSE**	**3%/3mm**	**RMSE**
0.25	91.9	100.0	0.039	91.9	0.031	100.0	0.127	100.0	0.065
0.5	100.0	100.0	0.039	100.0	0.03	100.0	0.126	100.0	0.070
0.75	91.9	100.0	0.046	91.9	0.029	100.0	0.113	94.1	0.056
1	97.3	100.0	0.042	97.3	0.028	100.0	0.125	97.1	0.066
1.25	75.7	100.0	0.039	75.7	0.036	100.0	0.126	88.2	0.081
1.5	78.4	96.6	0.04	78.4	0.042	88.9	0.13	82.4	0.073
1.75	97.3	100.0	0.046	97.3	0.034	96.3	0.121	94.1	0.066
2	100.0	100.0	0.04	100.0	0.039	100.0	0.124	100.0	0.064
2.25	97.9	100.0	0.039	94.6	0.048	100.0	0.124	97.1	0.070
2.5	97.9	93.1	0.045	73.0	0.041	96.3	0.118	94.1	0.075

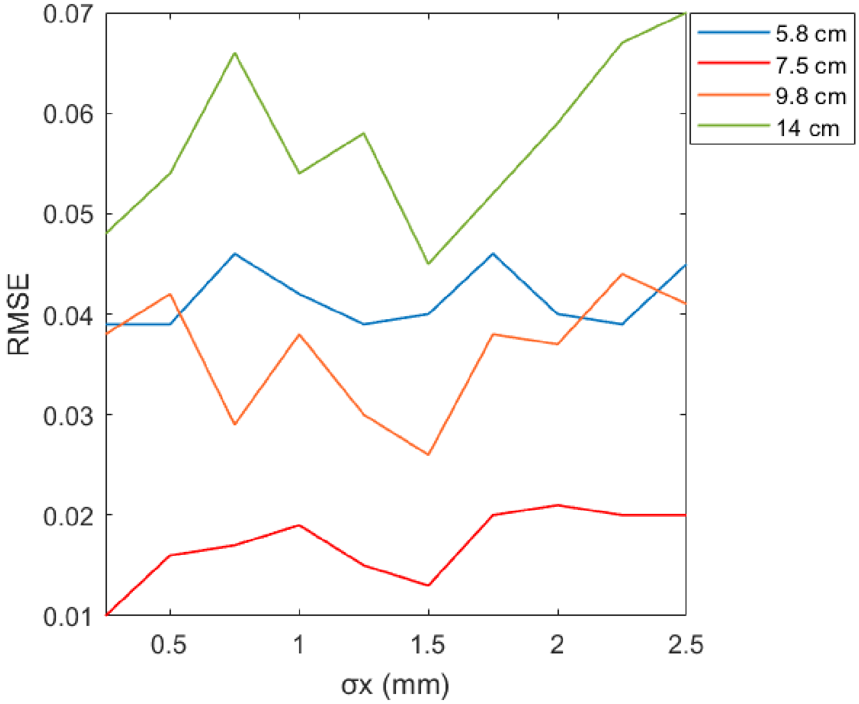

Figure 4.7: The RMSE of the horizontal radial intensity optimization for different radiation field sizes showing the higher sensitivity of the larger fields to the changes in the radial beam intensity.

4.5. Angular Distribution Investigation

The angular distribution of the initial electron source beam was simulated to investigate its effect on the beam profiles. The simulated values of the beam angular distribution were 0.0°-0.7° with an increment of 0.1° using the other optimized parameters of 9.8 MeV beam energy and 1.5 mm, 0.75 mm standard deviation of the horizontal and vertical radial intensities respectively. The angular distribution of the initial electron source is expected to have a minimal effect on the profiles and PDD curves. RMSE was used to estimate the optimal value using the 5.8 cm and the 7.5 cm fields. On average, the best-fitted value of the angular distribution was 0.5°.

Table 4.4: RMSE values of the angular distribution for the different field sizes

Angular Distribution	**Horizontal Profiles**		**Vertical Profiles**	
	5.8 cm Field	**7.5 cm Field**	**5.8 cm Field**	**7.5 cm Field**
0.0°	0.057	0.016	0.039	0.068
0.1°	0.056	0.015	0.027	0.075
0.2°	0.056	0.022	0.037	0.07
0.3°	0.056	0.019	0.03	0.071
0.4°	0.055	0.019	0.04	0.07
0.5°	0.054	0.01	0.025	0.067
0.6°	0.052	0.016	0.03	0.067
0.7°	0.057	0.016	0.037	0.069

The optimized parameters were implemented to score the phase-space file that was used as the main source at the linac exit for simulation and pre-experiment dose verifications. The simulation result was compared with film-measured beam profiles. The divergence of the linac field with increasing SSD was plotted for different beam sizes as shown in Figure 4.8. The effect of the in-phantom scattering in increasing the beam size with depth in the phantom was captured when comparing the measured beam profiles with simulations at the calibration point for 2 cm, 5 cm, and 10 cm depths in the phantom. The beam size slightly increases as the in-phantom depth increases as shown in Figure 4.9. Some measured profiles showed underestimation of the dose, which is due to the air gap effect. Film-measured PDD curves were compared to the simulated PDDs as shown in Figure 4.10. The effect of film positioning to the center of the beam has resulted in some experimental errors in the measured PDD curves, however, the simulated PDDs were within the measured uncertainty limits of the measured PDDs. The optimized linac parameters have resulted in overall good agreement with the measured profiles acquired at different depths and SSDs, as shown in Table 4.4.

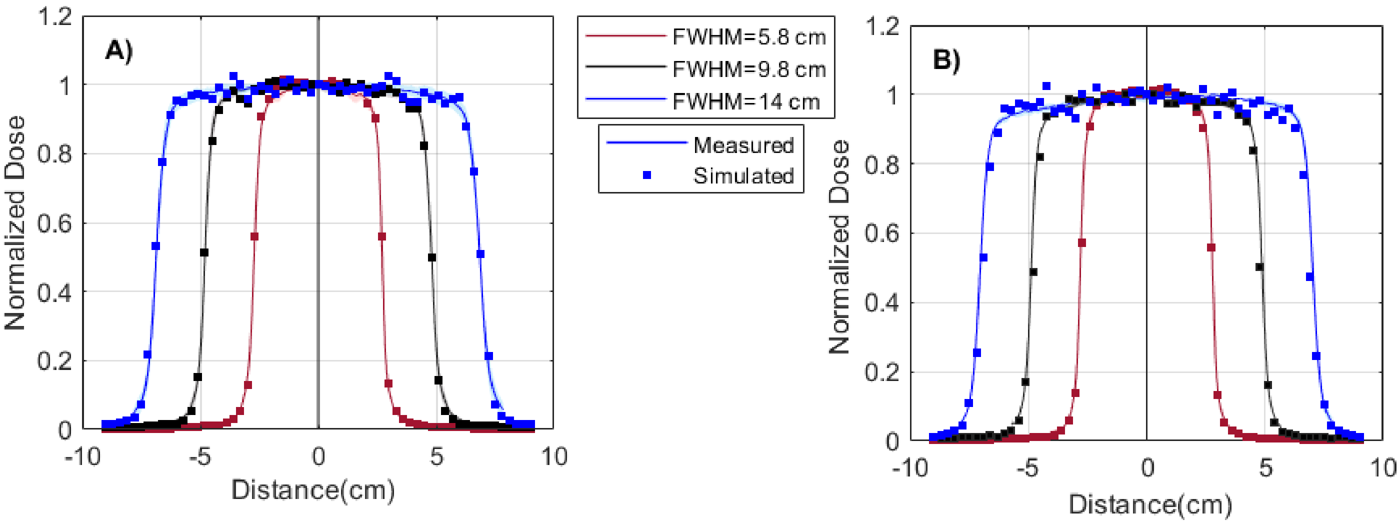

Figure 4.8: The measured and simulated beam profiles capturing the beam divergence A) horizontal profiles, B) vertical profiles.

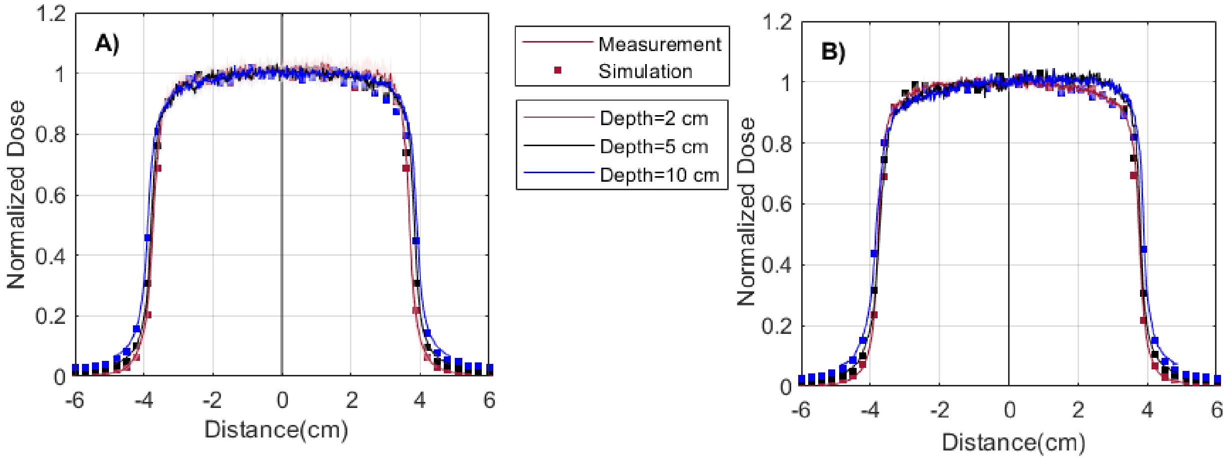

Figure 4.9: The measured and simulated beam profiles A) horizontal profiles, B) vertical profiles measured at the calibration point and different depths (2cm, 5 cm, and 10 cm) in the solid water phantom.

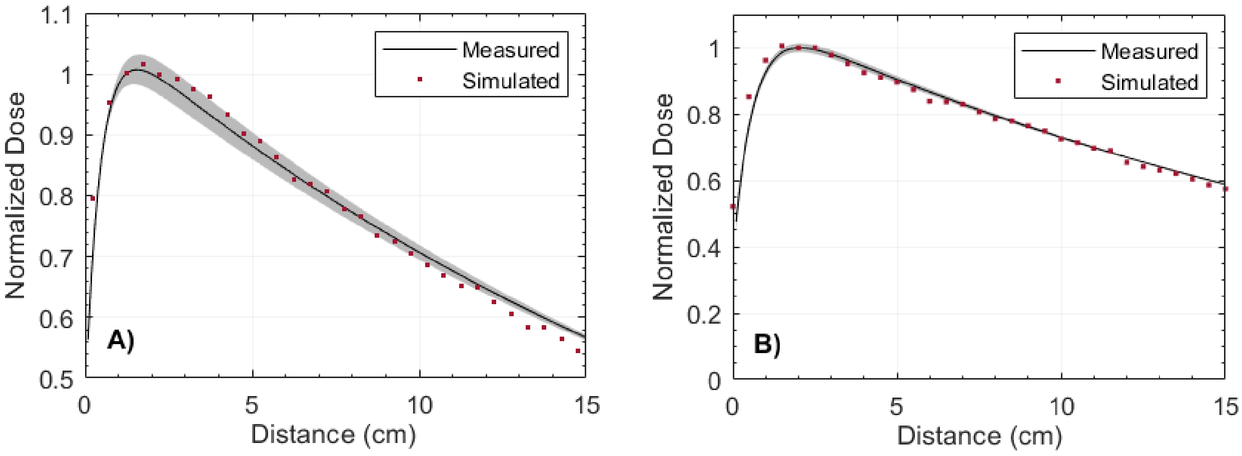

Figure 4.10: PDD curves of the optimized linac parameters comparing the measured and the simulated PDD extracted at A) 161 cm SSD, B) at the calibration point 220 cm.

Similarly, the final optimized simulated data was compared to the 2D gel-measured data of the open field at the calibration point and are plotted in Figure 4.11. The gamma passing rates of the

3%/3mm for the optimized initial source values and the gel measured data are 97.1%, 98.3%, and 98.4% for the XZ, YZ 2D planes, and 3D comparisons respectively. The maximum spatial difference between the gel measured and the simulated results were ~ 3 mm, which is the limit of the binning size of the simulated data.

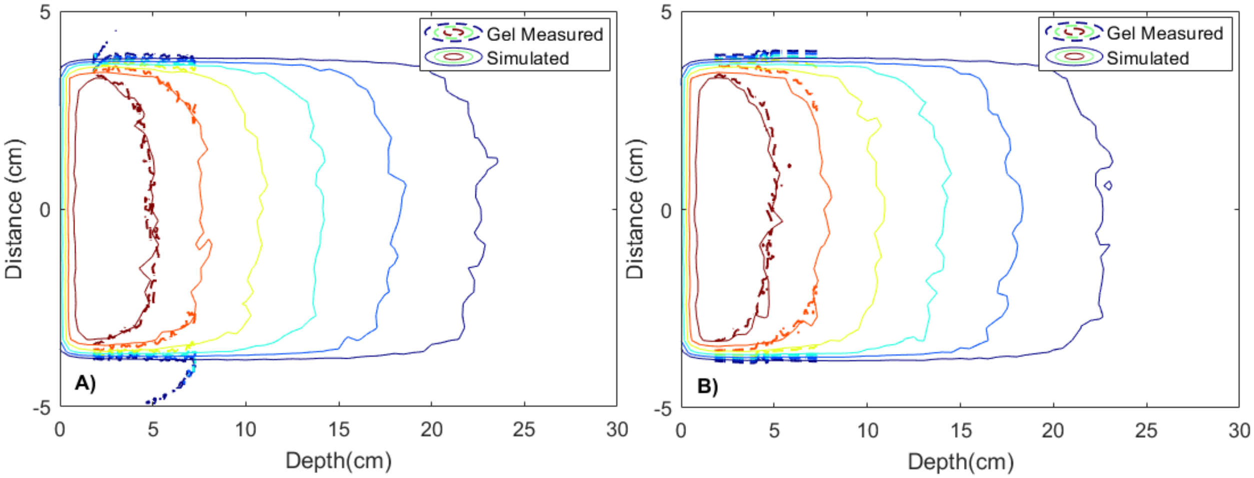

Figure 4.11: The fully optimized simulation 2D PDD data compared to the measured gel data of the linac static field at the calibration point acquired in 2D, A) ZX, B) ZY planes showing the 90, 80, 60, and 40% isodose contour lines.

4.6. Small Field Study

After the full initial parameters of the linac were optimized based on the initial static field of the linac of 5.08 cm, the phase-space file scored for the static field of the linac was used as the initial source in further simulations. Specifically, small field simulations were performed to score phase-space files for the other secondary collimated fields to serve as a pre-experiment verification for future dosimetry experiments using small fields of 0.5x0.5 cm^2, 1x1 cm^2, and 2x2 cm^2. The secondary lead collimators were modeled to reshape the static field of the linac to the intended field sizes used experimentally starting with the phase-space file of the linac scored at the beam exit. The simulation results were compared to the linac commissioning film and gel measurements represented in section 3.4.

The resulting spectra of the different small fields were plotted in Figure 4.12. As the field size decreases, the normalized spectrum becomes softer, exhibiting higher probabilities for photons < 5 MeV. In contrast, the smallest sized field of 0.5x0.5 cm^2 has the highest emission probability at the low energy region of 1 MeV-3 MeV. The average beam energy was 2.040±0.291 MeV for the 0.5x0.5 cm^2, 2.045±0.292 MeV for the 1x1 cm^2, 2.039±0.292 MeV for the 2x2 cm^2, and 1.974±0.285 MeV for the open field of the linac. Overall, the average energy increases as the field size decreases.

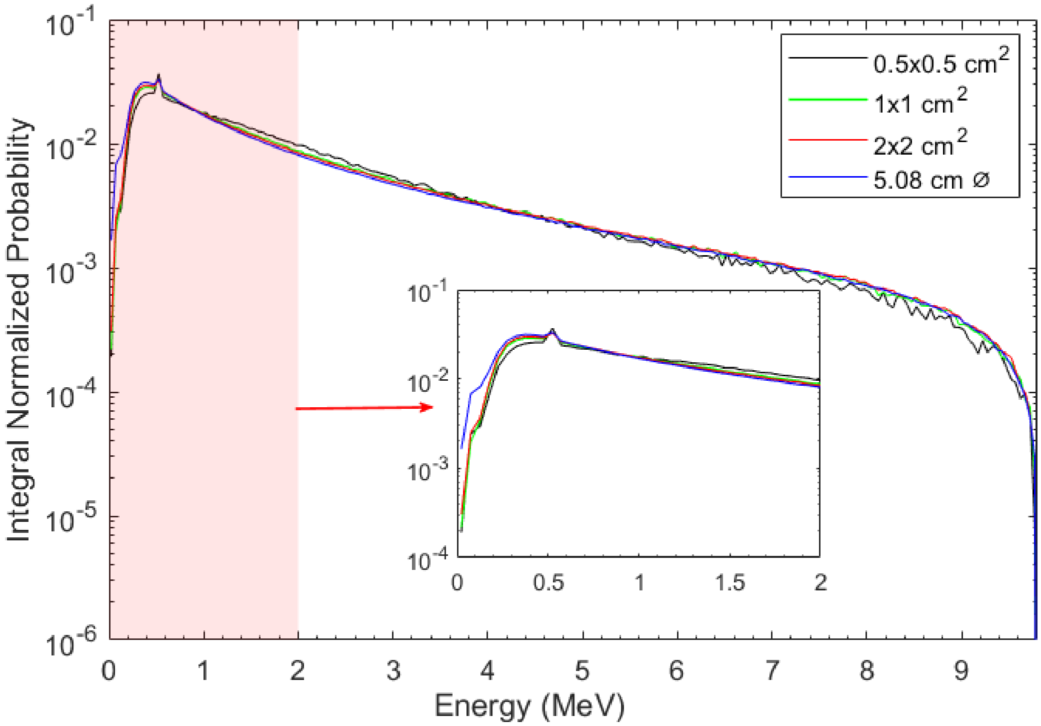

Figure 4.12: The spectrum of the different fields each normalized to the integral (total) probability

The small field beam characteristics were compared with the measurement data reported in section 3.4.3 including 1D and 2D comparisons of the beam profiles, PDD curves, and ROFs. The simulated and measured data were acquired at the calibration point 220 cm from the linac target and at 2 cm depth in a water phantom. The gel results, reported in section 3.4.3, were more reproducible as they were corrected for the phantom misalignments, thus gel-measured data were used as the benchmark to compare and verify the simulated data.

The simulated ROF calculated for each field relative to the reference field of 2x2 cm^2 and compared to the gel measured ROF were shown in Table 4.5. The simulated ROFs agree within 1.2% or less with the measured data.

Table 4.5: Simulated and measured ROFs of the Linatron small field sizes scored relative to the reference field of 2x2 cm^2

Field Size (cm^2)	Simulated ROF	Gel ROF	Relative % Difference
0.5x0.5	0.68±0.01	0.67±0.01	1.0 %
1x1	0.87±0.01	0.88±0.02	-1.2 %
2x2	1.00±0.01	1.00±0.01	0.00%

The 1D simulated beam profiles were extracted at 2 cm depth in the phantom for the three small fields; 0.5x0.5 cm^2, 1x1 cm^2, and 2x2 cm^2 and were compared to the measured gel data as shown in Figure 4.13. The simulated and the measured profiles lie within the error bars of the measured gel data. FWHM beam sizes of the three small fields were compared to the gel-measured FWHM and listed in Table *4.6*. The maximum relative difference between the simulated and the gel-measured FWHM beam sizes was 0.4 mm which is less than the binning width (spatial resolution) of the gels of 0.5 mm. The relative error in the simulated data is less than 0.1 mm and is reported based on the deviation between the horizontal and the vertical field size reported as FWHM of the beam. The FWHM values were reported as the average measured and simulated value of both the horizontal and the vertical profiles.

The simulated and measured PDD curves were plotted in Figure 4.14. The curves fall within the error bars of both film and gel measured data, within 10% or less for depths 0.5- 4 cm, and within

30% for depths up to 8 cm. One of the main sources of differences is the considerably larger spatial resolution used in the simulation (0.5 cm slice thickness), which was required to allow for good statistics. Gels have 0.05 cm imaging resolution. The simulated depth of the maximum dose (d_{max}) of the three measured field sizes agreed with the gel measured d_{max} as shown in Table 4.6 within the 0.2 cm difference or less limited by the 0.5 cm simulation spatial resolution.

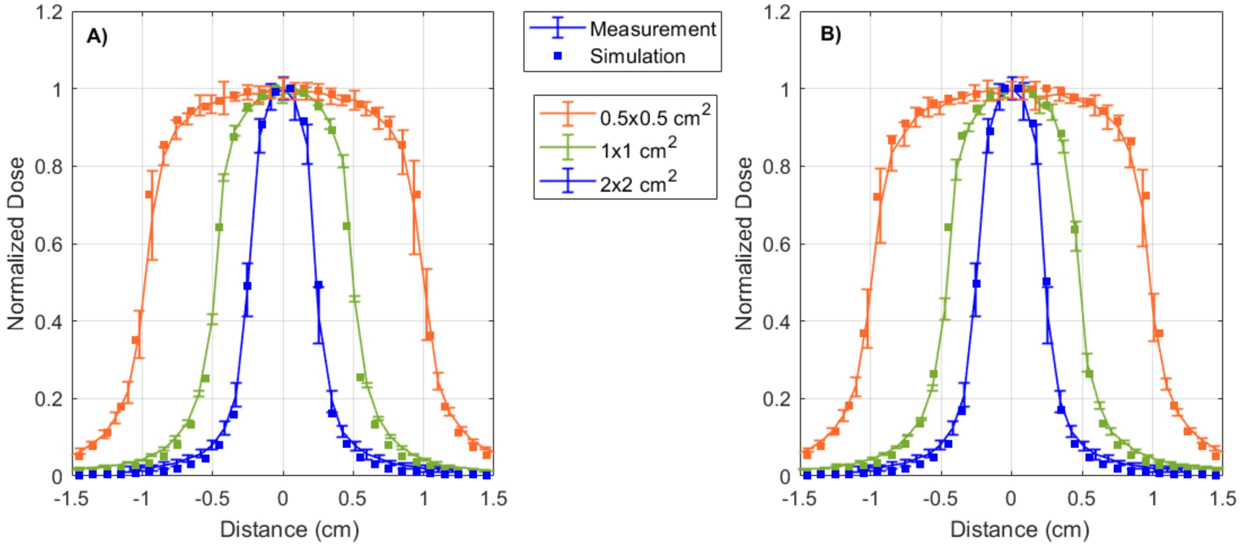

Figure 4.13: Simulated and gel measured profiles of the different small fields, 0.5x0.5 cm^2, 1x1 cm^2, and 2x2 cm^2, extracted at 2 cm depth in the solid water phantom; A) horizontal profiles, B) vertical profiles.

Table 4.6: The simulated and gel measured FWHM values of the profiles and depth of maximum dose of PDD curves.

Field Size (cm^2)	Simulated FWHM (cm)	Gel FWHM (cm)	Simulated d_{max} (cm)	Gel d_{max} (cm)
0.5x0.5	0.50±0.01	0.50±0.01	1.00±0.50	1.15±0.05
1x1	0.97±0.01	0.99±0.05	1.50±0.50	1.60±0.05
2x2	2.02±0.01	2.06±0.01[a]	2.00±0.50	1.90±0.05

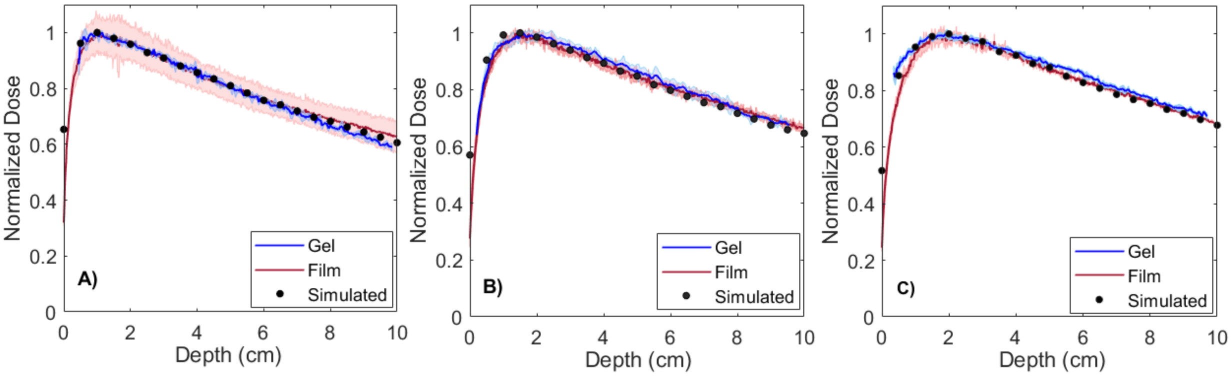

Figure 4.14: Simulated and gel and film measured 1 D PDD of the different small fields; 0.5x0.5 cm^2, 1x1 cm^2, 2x2 cm^2, extracted at center of the phantom; A) 0.5x0.5 cm^2 PDDs, B) 1x1 cm^2 PDDs, C) 2x2 cm^2 PDDs.

The 2D comparisons between the beam profiles extracted at 2 cm depth and the PDD curves of the 0.5x0.5 cm^2, 1x1 cm^2, and 2x2 cm^2 fields were performed based on the 3%/3mm gamma test criteria. The normalized isodose contour dose plots of the simulated and the gel-measured profiles are plotted in Figure 4.15. The agreement between the isodose curves higher than 30% of the simulated and measured plots was within a 100% passing rate of the 3%/3mm gamma for all the different fields.

The PDD isodose curves of the different fields were extracted at the center of the phantom and plotted in Figure 4.16. The agreement between the simulated and the gel-measured PDDs was reported with 100% for the smaller fields of 0.5x0.5 cm^2, and 1x1 cm^2 and 97% for the larger field of 2x2 cm^2. The major source of disagreement for the 2x2 cm^2 field occurs at the buildup region of 0 to 1 cm, where gel measured high reconstruction artifacts as they are not suitable for buildup region measurements.

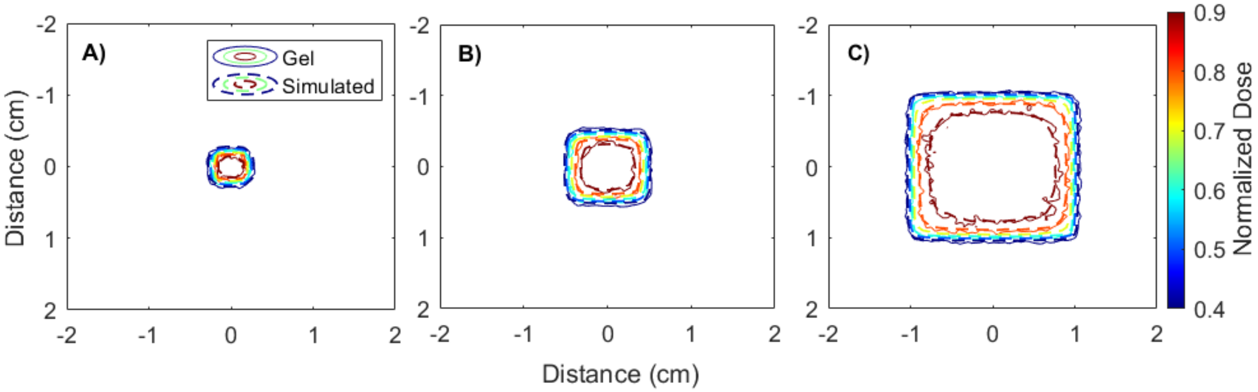

Figure 4.15: Simulated and gel measured 2D profiles of the different small fields; 0.5x0.5 cm^2, 1x1 cm^2, 2x2 cm^2, extracted at 2 cm depth; A) 0.5x0.5 cm^2 profiles, B) 1x1 cm^2 profiles, C) 2x2 cm^2 profiles; showing 90%, 80%, 70%, 60%, 50% and 40% isodose contour lines.

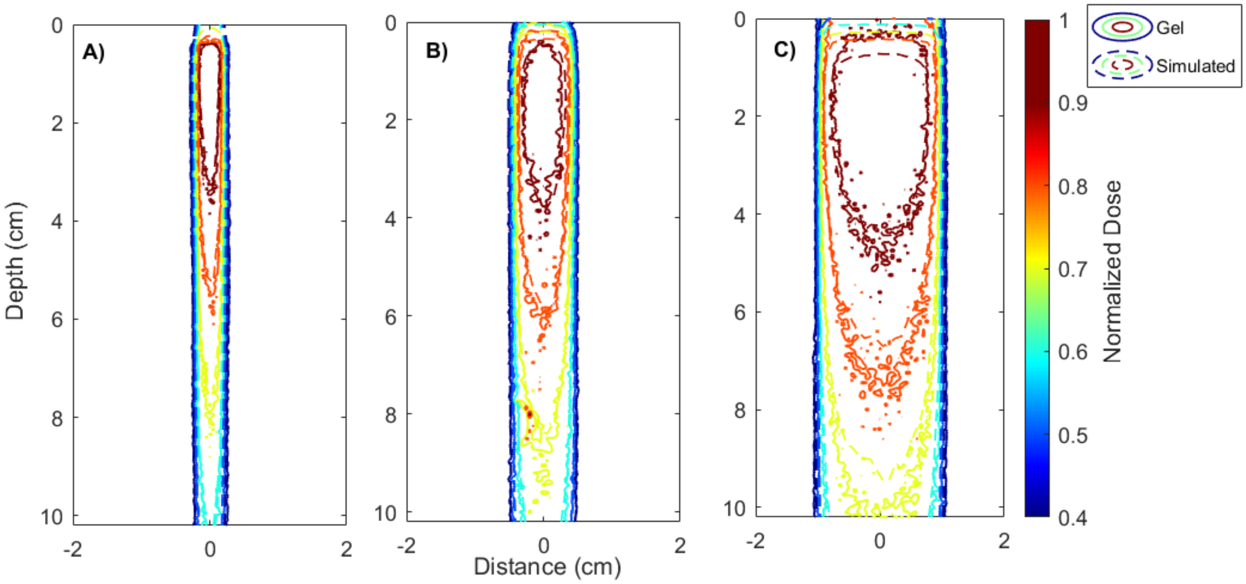

Figure 4.16: Simulated and gel measured 2 D PDD of the different small fields; 0.5x0.5 cm^2, 1x1 cm^2, 2x2 cm^2, extracted at center of the phantom and normalized to maximum dose; A) 0.5x0.5 cm^2 PDDs, B) 1x1 cm^2 PDDs, C) 2x2 cm^2 PDDs; showing 90%, 80%, 70%, 60%, 50% and 40% isodose contour lines.

4.7. Conclusions

The work in this chapter provided a full investigation of the initial electron source parameters to fully characterize the photon bremsstrahlung beam of an MV research accelerator. Hence, this procedure can be followed to fully characterize and commission non-standard radiation fields using additional endpoint energy verification steps to verify the beam energy of the linac. The detailed 1D dosimetric evaluation was the primary step toward parameters investigation. Additionally, 3D dosimetric evaluation was used to verify the optimized simulation-based investigation for better accuracy of the optimization process. The optimized initial source parameters were 9.8 MeV beam energy, 1.5 mm, 0.75 mm standard deviation of the horizontal and vertical radial intensities, and 0.5^o angular distribution. The optimized parameters were used as the initial preliminary step to commission and characterize the Linatron as a megavoltage small animals irradiator for radiobiological and dosimetric preclinical studies.

The work demonstrated the effectiveness of 3D gel dosimetry to provide efficient 3D dosimetry for small field studies as the benchmark to verify the simulation results through the relatively acceptable agreement with at least 97% passing rate of 3%/3mm gamma test. The limited dose-response measurement in the buildup region with gels is due to artifacts near the phantom surface. One of the main challenges and source of experimental errors in small field measurements is the dosimeter misalignment errors. The main advantage of gels is that they have provided the full 3D dose measurement, which highly minimizes the dosimeter misalignment uncertainties. The agreement between simulated and the measured ROFs was within 1.2%. Additionally, the FWHM of the simulated beam profiles was within 0.4 mm of the measured FWHM. The overall good agreement between the measured and the simulated data reflects the accuracy of the investigated beam characteristics, and the phase-space files of the three small fields; 0.5x0.5 cm^2, 1x1 cm^2, and 2x2 cm^2. The reported results will hence be used as a pre-measurement verification and dose calculations benchmark for future experiments and plan optimization, which will save extensive simulation times.

Chapter 5

A Simulation Study of Ionizing Radiation Acoustic Imaging (iRAI) as a Real-Time Dosimetric Technique for Ultra High Dose Rate Radiotherapy (UHDR-RT)

The chapter describes the full simulation procedure followed to study the applicability of iRAI as a real-time (*in vivo*) dosimetry tool for UHDR-RT. A clinical linear accelerator (linac) was modified for its implementation to deliver high dose rates and operate in the electron FLASH mode. This work aims to verify, through simulations, the feasibility of the iRAI modality as a potentially promising tool for relative UHDR-RT dosimetry and provide comprehensive theoretical support for the experimentally measured results. This work focuses also on testing the effect of the different linac operational parameters on the reconstructed acoustic (pressure) iRAI images and how these operational parameters affect the acquired pressure-based beam characteristics. The work of this chapter was published in the peer-reviewed article “A simulation study of ionizing radiation acoustic imaging (iRAI) as a real-time dosimetric technique for ultra-high dose rate radiotherapy (UHDR-RT)”, Medical Physics Journal, 2021 [112].

5.1. Introduction

Ultra-high dose-rate radiation therapy UHDR-RT, also known as Flash-RT, has shown an increased effect on the therapeutic index in radiation therapy based on preclinical studies. As high treatment dose rates (on average > 40 Gy/s) are involved in the treatment, this causes a reduction in the normal tissue toxicity while maintaining the same tumor-killing effectiveness [12]. The resulting enhancement in the normal tissue sparing effect is hypothesized to lead to an overall beneficial increase in the therapeutic index [13]–[18].

While still an active area of research, the potential advantage of UHDR-RT in comparison to conventional treatment has led to increased interest in radiation therapy. As a result, clinical dosimeters that can operate in the UHDR environments are expected to be crucial throughout the treatment process in UHDR-RT. Advanced dosimetry techniques that are capable of measuring and monitoring dose are needed to provide real-time (*in vivo*) dose readings for dose monitoring and beam localization in UHDR-RT. Currently used clinical dosimeters have some limitations that restrict their implementation in high dose rate environments. Additionally, the high dose delivery results in high instantaneous dose rates on a linac per pulse basis. Those high dose rates are beyond the sensitive dose rate threshold of the available online dosimeter and hence result in dose saturation problems. For instance, ionization chambers have been reported to have some ion recombination problems at the higher dose per pulse values achieved in UHDR-RT. Semiconductors have also shown dose saturation problems that are uncorrectable in the tested UHDR-RT environments [19]. Active research work is currently ongoing to test and identify online dosimeters that are applicable for UHDR dosimetry with more accurate dose per pulse basis ability compared to conventional RT.

iRAI has shown potential as a relative *in vivo* dosimetry tool in conventional radiation therapy [57], [58], [63], [69], [70], [113]. The dose and induced pressure linearity and the energy and dose rate independence are the main characteristics of iRAI that make it a promising dosimetry technique for UHDR-RT in addition to conventional RT. In addition, the generated acoustic (pressure) signal is proportional to the dose deposited per each pulse of radiation. Hence, this technique has the potential for implementation in UHDR providing dose per pulse measurement without signal saturation and degradation [70].

5.2. Theory and Simulation Workflow

The full theory behind the thermoacoustic effect and hence iRAI was fully discussed in Chapter 2 section 2.1. Figure 5.1 summarizes the theory and the simulation flow. The simulation process started with MC based simulation of the radiation beam dose deposition in the homogeneous gelatin phantom. The acoustical characteristics that are medium-specific were used to calculate the initial pressure source based on the material-specific Grüneisen coefficient (*Γ*). The wave propagation equation was then solved to determine the instantaneous electron-induced acoustic pressure, given by the thermoacoustic equation [53],

$$(\nabla^2 - \frac{1}{v_s^2}\frac{\partial^2}{\partial t^2})\,p(\mathrm{r,t}) = -\frac{\beta K_T \eta_{th}}{v_s^2 \mathrm{C}_v}\frac{\partial D_r(\mathrm{r,t})}{\partial t}\ , \qquad (5\text{-}1)$$

The instantaneous pressure is then used to construct the pressure images which are dose-related and characterize the radiation beam characteristics. A detailed explanation of the different simulation steps and the results is discussed in this section.

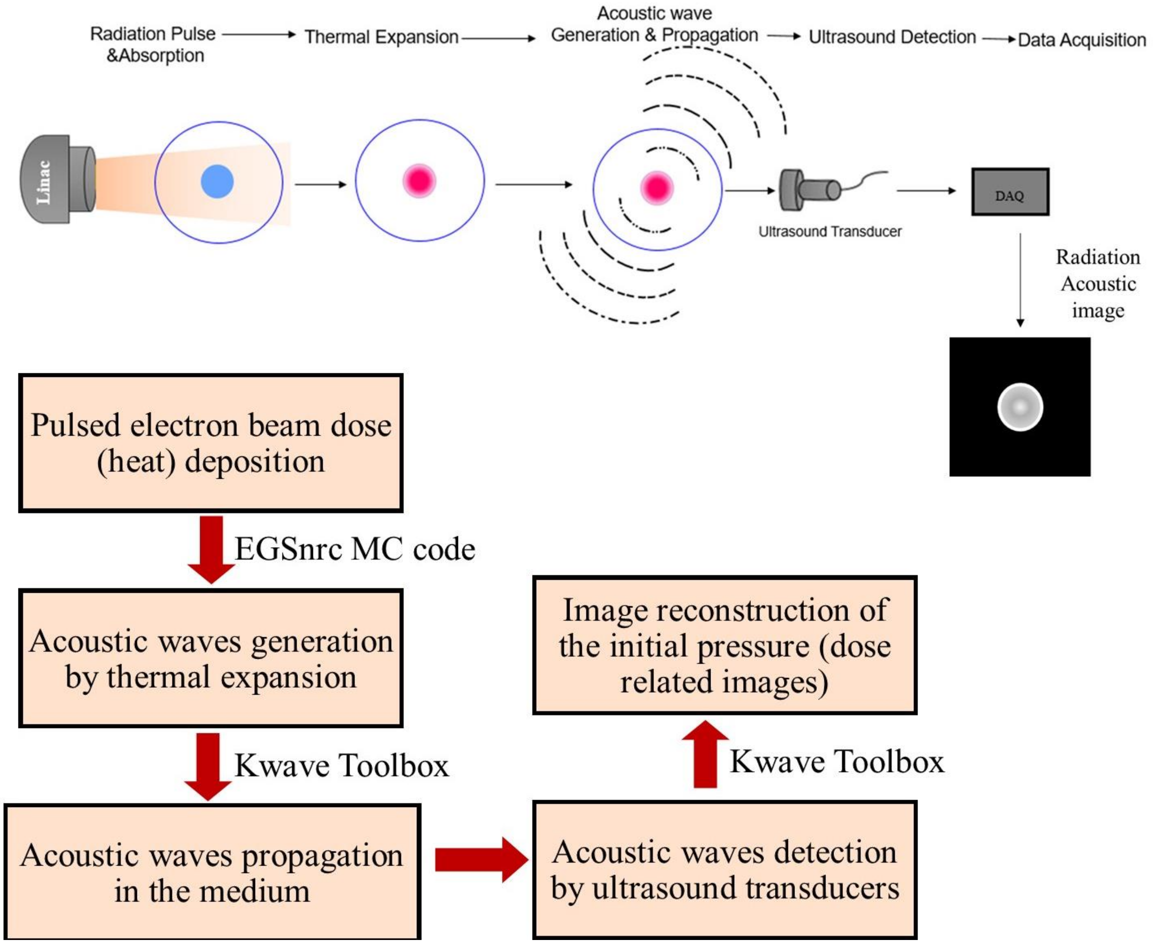

Figure 5.1: Flowchart and a diagram summarizing the theory and the detailed simulation steps and the used simulation programs for modeling iRAI and the generation of acoustic images.

A. Dose simulations:

A full model of the modified linac was simulated using MC codes EGSnrc BEAMnrc/DOSXYZnrc [81], [82] to determine the dose output of the modified linac in dose rate (in Gy/s) and dose-per-pulse (in Gy/pulse). The resulting full 3D relative dose distribution of the incident electron radiation beam was then verified through comparison with the experimental dose data measured with films (Gafchromic EBT-XD).

The full model of a 6 MeV electron beam of a 21EX Varian Clinac (Varian Medical Systems, Palo Alto, Ca) was simulated to mimic the experimental setup as shown in Figure 5.2. The studied linac was modified as part of its decommissioning to deliver UHDR; thus, this experimental setup was irreversible. The linac target, flattening filter, and scattering foil were all removed from the conventional 21EX linac. This setup enables UHDR-RT dose rates to be achieved at the iRAI measurement point at a source-axis distance (SAD) of 100 cm. This long SAD was selected to reduce the geometrical and space constraints in contrast to the proposed setup in the literature, where experiments were restricted to the linac head [114]. To shape the incident electron beam to the desired field of 1x1 cm^2, a secondary lead collimator was positioned at 100 cm SSD. All the different parts of the linac head were modeled using EGSnrc/BEAMnrc code including the initial electron source, ionization chamber, mirror, jaws, and the secondary lead collimation. The linac phase-space source files were then generated and scored at the exit of the collimation. The dose simulations were then performed using EGSnrc/DOSXYZnrc code for simplicity in a 30x30x30 cm^3 water tank mimicking the gelatin phantom. The number of histories used for BEAMnrc code simulations was 7×10^8, and the photon and electron cut-off energies were set to 100 keV (PCUT) and 521 keV (ECUT), respectively. The initial electron source was modeled as a pencil beam with a 3 mm 1σ focal spot size and monoenergetic beam energy of 6 MeV.

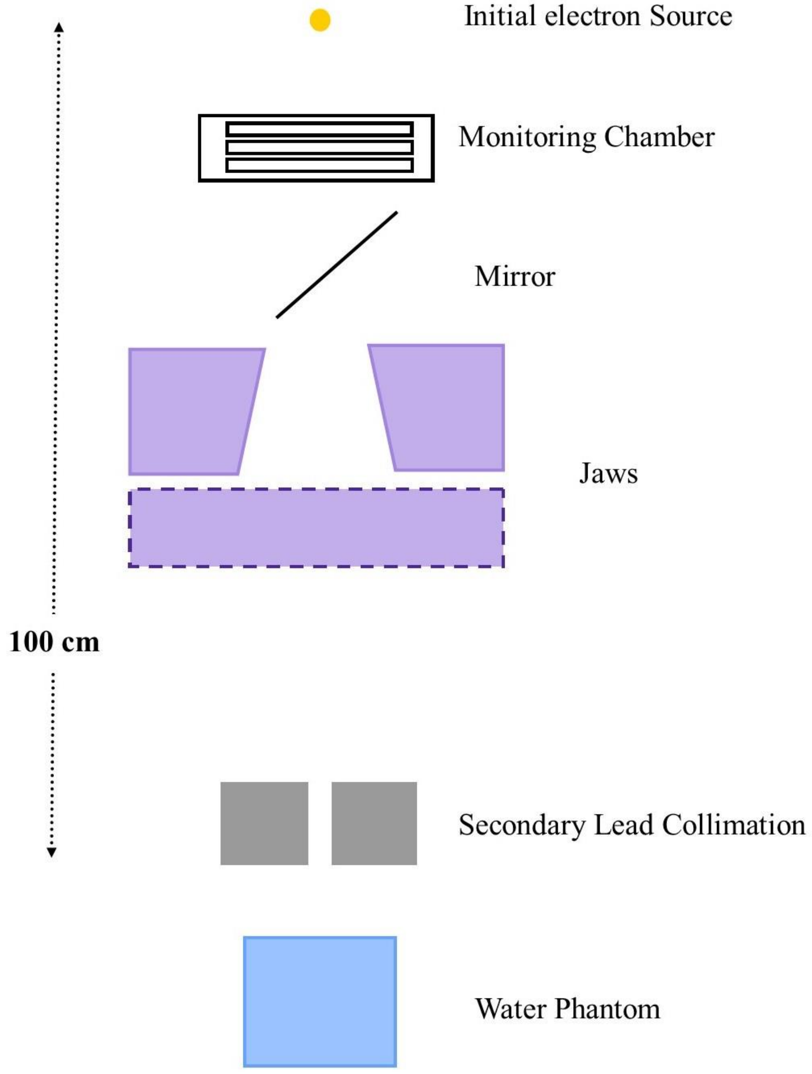

Figure 5.2: The modified head structure of a 6 MeV 21EX Varian Clinac (This figure is not to scale.) A monoenergetic 6 MeV pencil beam of electrons passes through the exit window and is collimated by jaws and secondary lead collimation at 100 cm SSD.

The full 3D simulated dose was reported as the dose per linac pulse given the 300 Hz constant pulse repetition rate of the linac (Figure *5.3*). As expected, the figure showed the teardrop distribution of the electron beam dose in water. The simulated relative dosimetry data including the PDD curve and beam profiles at different depths were then validated through comparisons with the experimental film results.

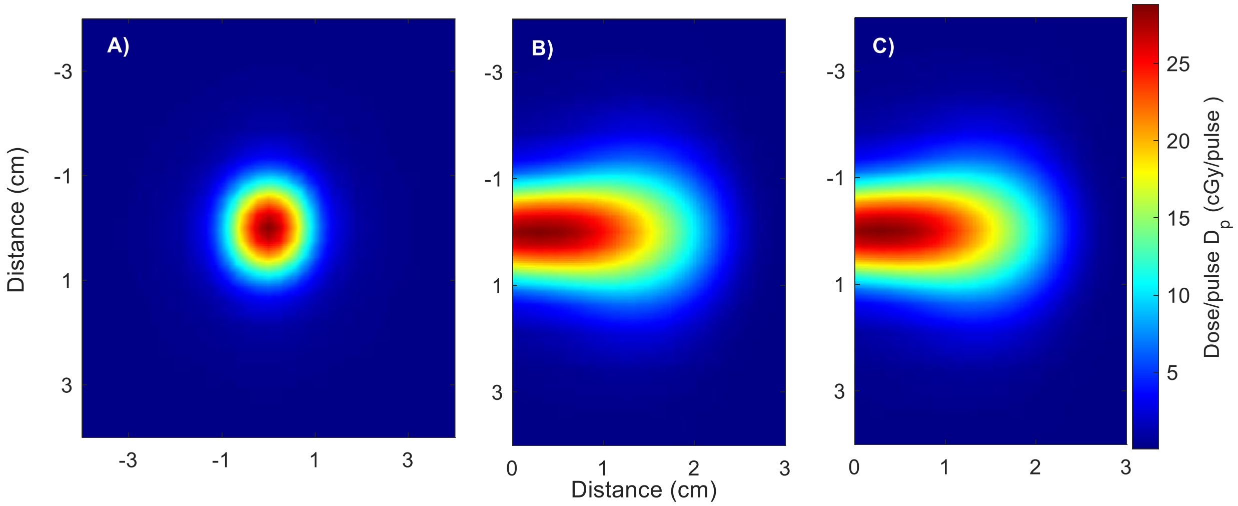

Figure 5.3: The 3D MC simulated dose distribution in the water phantom. A): XY plane (cross beam plane) at the surface of the phantom (at 0 cm depth), B): ZX plane (parallel to beam plane) scored at beam center (y=0 cm), C): ZY plane scored at beam center (x=0 cm).

Gafchromic EBT-XD (Ashland Advanced Materials) film measurements of the dose distribution were performed to measure the percent depth dose (PDD) curve and the beam profiles at different depths. The PDD curve was determined as the average curve over the central 2x2 mm^2 region of interest of the beam axis at each irradiation position (depth) in a solid water phantom. Films were placed with an increment of 2 mm depth in solid water perpendicular to the beam direction. The measured dose was reported on a per pulse basis by dividing the film measured dose by the total number of pulses delivered during the specified film irradiation timeframe. A comprehensive explanation of the experimental setup and measurement results was published in a different article [52]. A comprehensive comparison between the simulated and the measured relative dosimetric characteristics of the beam was performed and is shown in Figure 5.4. MC simulated PDD was scored at the central beam region of 5x5 mm^2 in the water phantom with an inherent statistical uncertainty of < 1.3%. The simulated PDD agreed within less than 6 % relative error with the film measured PDD for depths less than 2 cm. While the simulated beam profiles at those depths agreed to ≤5% relative error with the measured film profiles at all points within the central region of the radiation beam. Both the simulated and measured beam profiles showed an increase in the field size (FWHM) with depth in the phantom and agreed within a 1 mm spatial difference. Hence, per the relative dosimetry comparisons, the full 3D distribution of the dose in the phantom was predicted within < 6% relative percent error, specifically at the expected therapeutic depth of 2 cm for this electron beam. For deeper depths, the point percent dose difference between the two methods increased to as high as 66% at 3 cm depth. The 3 cm depth marks the end of the particle track, where inherent simulation uncertainty increases due to the increased reduction of the particles at the end of the particle track as most of the simulated particles stop.

The agreement between the simulated MC-based and the measured results is acceptably good. However, there are some disagreements between the two methods specifically in the PDD buildup region. Differences in the MC initial electron source parameters could be the major source of those disagreements. The initial electron source was modeled as a monoenergetic source without extensive validation and calibration of the initial electron source parameters, specifically the electron beam energy distribution, and mean energy. This approximation was implemented due to the limited experimental calibration data at the modified UHDR-RT machine setting in this study. However, it is recommended to perform a full beam-tuning for future similar studies to enhance the agreement between the simulated and the measured PDD curves.

Overall, per the relative dosimetry comparisons, the full 3D distribution of the dose in the phantom was well predicted through simulation, specifically at the expected therapeutic depth of 2 cm for this electron beam.

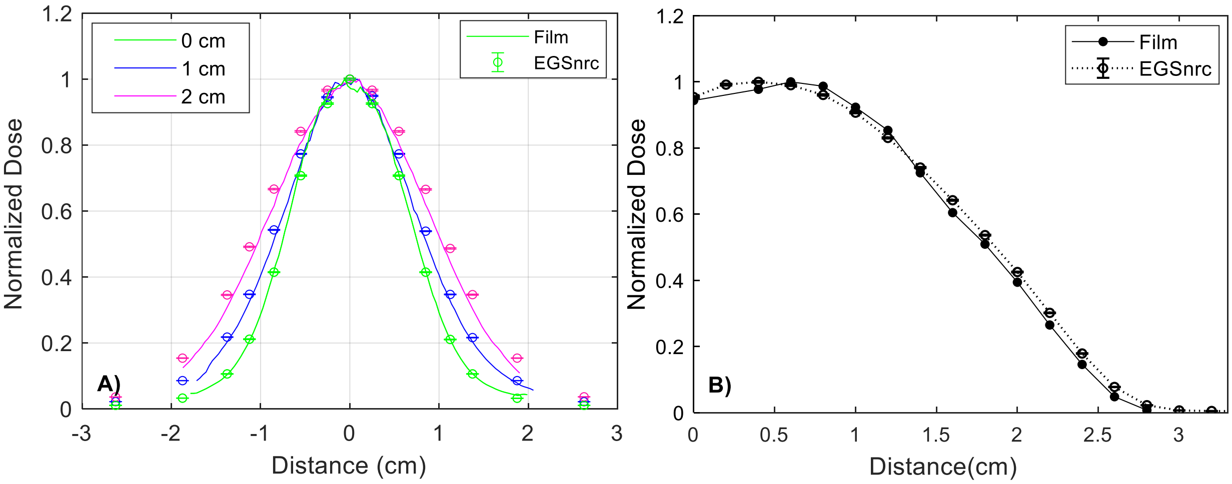

Figure 5.4: The simulated and the measured relative dosimetry characteristics of the electron beam. A) The beam profiles at various depths in the water phantom normalized to the dose at the central axis. D) PDD curve showing both film measurement and simulation results.

B. Initial pressure source definition:

The homogeneous phantom used in this study is made of porcine gelatin (10 g/100 ml, G2500, Sigma-Aldrich). CT images of the phantom were acquired to characterize the phantom material and determine its acoustical specifications to mimic the experimental setup (Table 5.1). The acquired electron density of the phantom was used to design it to be a brain tissue-equivalent phantom.

Table 5.1: The material characteristics of the gelatin phantom

Density (ρ)	1035 g/cm^3
Sound speed (Cs)	1562 m/s
Grüneisen coefficient (Γ)	0.22
Attenuation coefficient (α)	0.58 dB/MHz^y -cm
Attenuation power (y)*	1.3

* y is the exponent of the acoustic attenuation power law. It is frequency dependent and a material dependent parameter that ranges from 0 to 2.

The initial pressure source (p_0(r) measured in Pa) was then defined using the pressure-dose relation:

$$p_0(\mathrm{r}) = \Gamma \eta_{th} \rho D_r(r), \qquad (5\text{-}2)$$

where $D_r(r)$ is the dose deposition during an electron pulse (Gy/pulse), ρ is the density of the medium, η_{th} is the thermal heat efficiency, and Γ is the Grüneisen coefficient of the phantom (equals 0.22 based on the CT number of the gelatin phantom). The initial 3D pressure source in the gelatin phantom is plotted in Figure 5.5. As shown in Figure 5.5 initial pressure source has the same spatial distribution pattern as that of the electron dose in the water reflecting the linearity between the dose and pressure as theoretically indicated in the above equation.

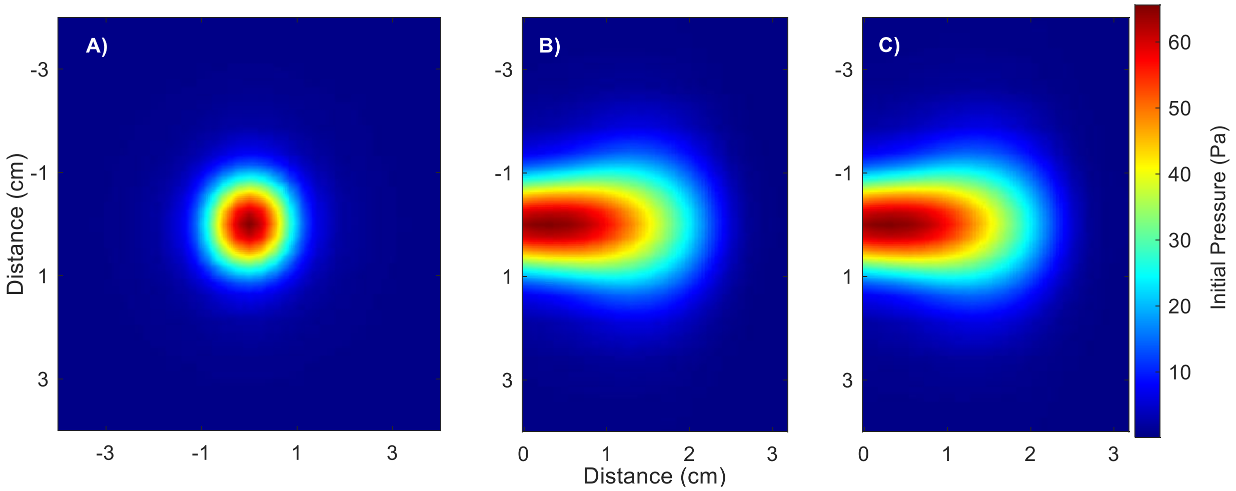

Figure 5.5: The simulated 3D initial pressure source distribution in the gelatin phantom. A): XY plane (cross beam plane) at the surface of the phantom (at 0 cm depth), B): ZX plane (parallel to the beam plane) scored at beam center (y=0 cm), C): ZY plane scored at beam center (x=0 cm).

C. Acoustic propagation and time reversal reconstructions with KWave:

The electron-induced acoustic wave propagation was simulated using the MATLAB KWave toolbox. The generation, propagation, and attenuation of the acoustic waves in the gelatin phantom were fully simulated to solve the thermoacoustic equation numerically.

Once the instantaneous pressure signals are received at the sensor positions, which is the ideal transducer in this study, the initial spatial pressure is calculated through image reconstruction. The goal of image reconstruction, in this work it is the time-reversal image reconstruction technique, is to recover the initial spatial distribution of the initial pressure source $p_0(r)$ from the collected instantaneous pressure readings collected with the transducer $p(r, t)$. The reconstructed spatial pressure images indicate the initial radiation beam properties, including the spatial distribution of the dose in the phantom.

The time-reversal reconstruction in this work was modeled using the MATLAB KWave toolbox [115]. TR reconstruction can provide a better representation of the experimental setup and more efficiently measure the broadband response, in addition to including the effects of heterogeneities and attenuation in the reconstruction model. However, TR reconstruction is a time-consuming reconstruction algorithm and is computationally expensive. Depending on the simulated geometry and setup, such that TR could take up to a few hours [115] [116]–[118].

Two different cases were tested with different transducer (sensor) distributions based on the chosen linac operation parameters; the linac pulse duration length and the pulse repetition rate.

5.3. IRAI Measurements of UHDR With Operational Clinical Linac Timing:

In this study part, the linac parameters (pulse repetition rate and the linac pulse duration) were set to the default operational values of the linac of 300 Hz and 4 µs respectively. This work aims to demonstrate the imaging and dosimetric capability of iRAI in the operational mode. The sensors were distributed and defined as ideal point transducers that were then used to run the KWave simulations distributed in a 2D planar matrix array, and a 2D spherical shell distribution around the radiation beam in 3D. Each study's findings and setup are discussed in detail in this section.

I. Planar Transducer Distributions

In this setup (Figure 5.6), the ideal point transducers were distributed along a line parallel to and 10 cm away from the beam's central axis. The detection points were placed from the gelatin phantom entrance to the back up to 3 cm depth with a step size of 2 mm as shown in Figure 5.6 A. This setup of transducers was used to fully acquire the radiation beam characteristics including the PDD curves to mimic the experimental setup [52]. The full distribution of the transducer points in the traverse plane in 2D was used in the simulation to adequately scan and acquire the instantaneous pressure signals along the beam direction. The initial pressure source was acquired through TR reconstruction simulations to fully reconstruct the 3D spatial distribution of the radiation beam hence determining its relative dosimetric characteristics.

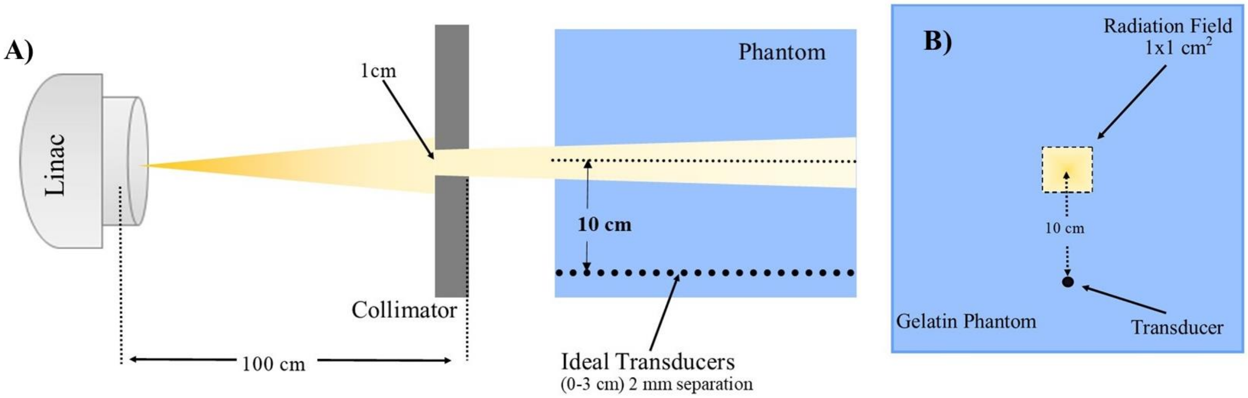

Figure 5.6: Schematic setup for acoustic dose depth simulation setup. (A) Schematic plot of the setup along the radiation beam direction. (B) Schematic plot of the radiation beam eye view setup. Each detection point represents an ideal point transducer.

The resulting instantaneous pressure signal detected by the point transducer at the entrance of the phantom indicates the edges of the radiation beam as shown in Figure 5.7 A. The resulting temporal change in the measured instantaneous pressure signal is then converted to distance depending on the speed of sound of the gelatin phantom which defines the FWHM of the beam. The simulated pressure-based beam size (FWHM) agrees with the simulated MC-based dose profiles within 3 mm at the surface of the phantom. This disagreement resulted in the offset of the pressure signal relative to the beam profile (Figure 5.7 A) which is because of the linac pulse duration effect. This disagreement between the two methods increases with depth, such that the contributions of the linac pulse duration effect causes degradation of the beam edges allocation (measured in FWHM) to be within 26% relative error.

The TR reconstructed initial pressure was then used to determine the pressure-based percent curve and compare it to the MC-based PDD curve as shown in Figure 5.7 b. Both curves showed a disagreement as high as 11% for the surface dose and within ~ 7% for depths up to 1 cm. Beyond the 1 cm depth region, the relative error increases with depth. There are different sources of this reconstruction algorithm-based error including the linac pulse duration effect, the limited detection view, and incomplete data measurements. The linac pulse duration effect is correctable through signal processing (deconvolution). The linac pulse duration correction has resulted in an increased agreement between the pressure-based and the dose-based curve. The maximum disagreement between the two curves is within ~ 7% relative percent error for the depths between 5 mm to 2 cm. The surface and the endpoint pressure signals are highly affected by the limited detection view artifact of this setup. A detailed discussion on the linac pulse duration effect and the signal processing (deconvolution) based correction for it, is discussed in detail in section 5.4.2.0.

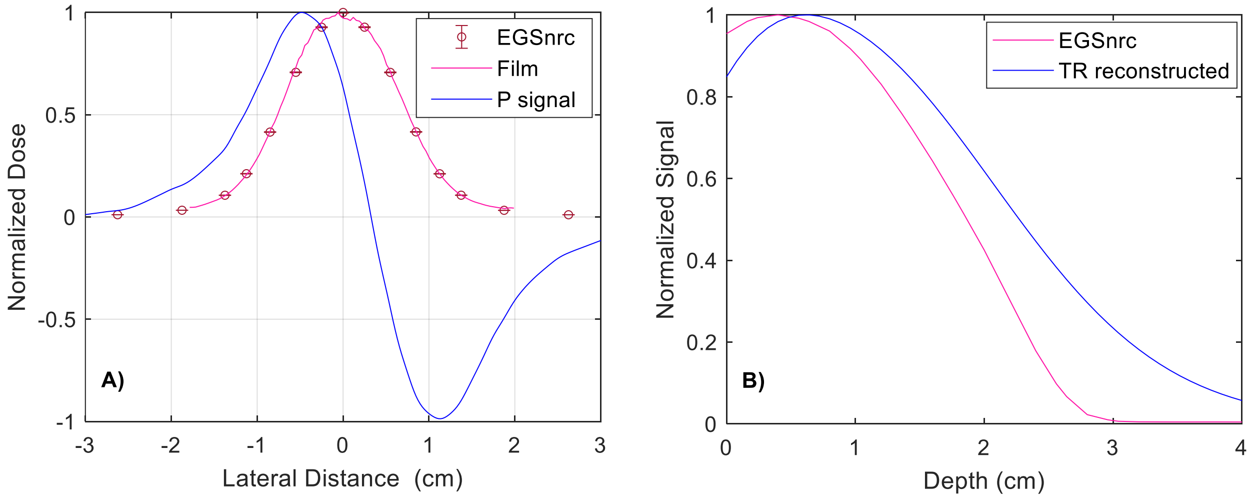

Figure 5.7: Simulated pressure signal measured at the entrance of the phantom with the point transducer at a 10 cm distance away from the beam central axis. A): shows the conversion of the instantaneous pressure signal arrival in terms of the distance, compared to the dose profile simulated by EGSnrc and the film measured profile. B) shows the iRAI-based simulated PDD equivalent curve compared to the MC-based PDD simulated with EGSnrc.

II. Spherical transducer distributions

One of the main limitations that affect the reconstructed pressure retrieved radiation beam characteristics is the limited data collection and limited detection view. This part of the study is performed assuming a full collection of data surrounding the beam of radiation hence testing the effect of the linac pulse duration on the overall 3D TR reconstructed pressure-based beam characteristic. Therefore, the overall spatial distribution of the acquired pressure images is for an ideal case of full data collection with point transducer elements with no bandwidth limitations distributed on a spherical shell.

A set of 600 ideal transducers were distributed over a spherical shell of 2.8 cm radius and simulated to evenly surround the radiation field. The TR reconstruction algorithm was implemented to simulate the initial pressure source and construct the 3D related dose distribution and hence characterizing the radiation beam.

The 3D pressure signal-based extracted beam profiles at different depths in the phantom and the pressure equivalent PDD were compared to the relative dosimetric beam characteristics simulated with EGSnrc MC as shown in Figure 5.8. The reconstructed pressure profile has a wider beam size (FWHM) compared to the relevant MC simulated beam profiles (within 4 mm). This disagreement is due to the inherent effect of the linac pulse duration which highly affects the temporal and hence the spatial resolution of the reconstructed pressure profiles (Figure 5.8 A). As Figure 5.8 B shows, the reconstructed pressure-based percent curve at the surface of the phantom

(~ 4 mm) underestimated the signal by as high as 46% relative to the MC-based percent dose curve. The disagreement between the two curves for deeper depths up to 1 cm is within ~ 7%. For deeper depths near the distal position of the transducers corresponding to the maximum electron range, the relative error increases to as high as 100% with depth in phantom due to the linac pulse duration effect.

The sharp superficial increase in the pressure-based curve near the buildup region is due to the inherent geometrical reconstruction artifact due to the linac pulse duration effect which represents the accumulation of the signal during each linac pulse time duration. Hence, this effect is correctible through signal processing as discussed in detail in section 0. This correction has resulted in better agreement between the MC-based PDD, and the pressure-based percent depth curves normalized to the corresponding signal at 1 cm depth. The resulted maximum disagreement between the two curves for depths from 1 mm to 2 cm maximum was within 8% relative error.

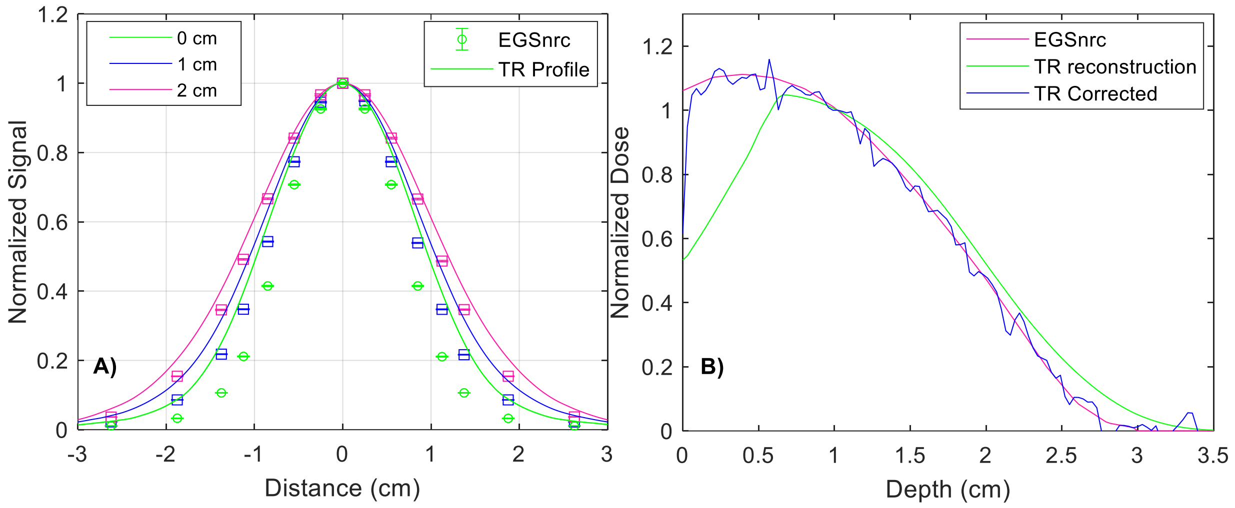

Figure 5.8: The relative 3D TR reconstructed pressure signal-based beam characteristics. A) shows the iRAI-based beam profiles retrieved at different depths in phantom and compared with the MC dose profiles. B) shows the iRAI-based PDD equivalent curve normalized to signal acquired at 1 cm depth with and without the linac pulse duration correction compared to the dose-based PDD simulated by EGSnrc MC code.

5.4. The Effect of the Linac Operating Parameters on the Induced Acoustic Signal

This part of the study focuses on testing the effect of the operational parameters of the linac on the iRAI images. Clinical linacs deliver radiation as a continuous train of pulses. Each linac pulse has a typical length (duration) on the order of 3−6 μs. While the pulse repetition frequency is typically ranging from tens to hundreds of hertz (Hz). The amount of radiation dose delivered by each linac pulse is theoretically the same. Hence the instantaneous dose rate delivered by each linac pulse is the same (i.e., constant Gy/pulse/s). The overall linac dose rate (in Gy/s) in many clinical accelerators is tuned through varying the pulse repetition rate (Linac frequency in Hz) [21]. The effect of the operational linac parameters on the induced acoustic signal intensity was tested to define the resulted effect on the ability in defining the spatial distribution of the initial pressure and hence the radiation beam. The linac has an approximate pulse duration of 4 μs and a pulse repetition rate of 300 Hz. Two separate studies were performed studying the effect of the linac pulse repetition rate and pulse duration:

5.4.1 The Effect of The Pulse Repetition Rate (Linac Frequency):

The pulse repetition frequency of the linac was variable, changing dose per pulse, to test its effect on the simulated pressure signal for a constant pulse duration of 4 μs. The sensors in this study were distributed in a 2D circular configuration of the ideal point receiver transducers. The transducers were distributed in a gelatin phantom irradiated with a linac electron beam of 1x1 cm^2 field size. The ideal transducers were evenly distributed surrounding the beam of radiation as shown in Figure 5.9. Each transducer point detects the instantaneous pressure signal, and a TR reconstruction algorithm was run to reconstruct the spatial distribution of the initial pressure. The simulation grid size used for this study was 0.06 mm to allow for accurate temporal resolution within a simulated time interval of 54 μs.

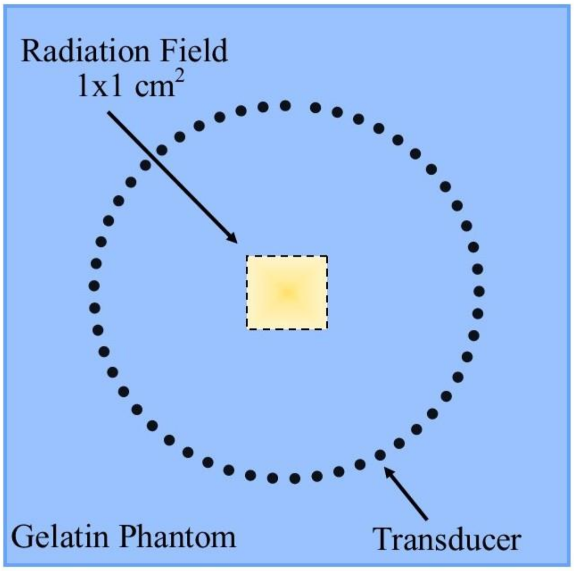

Figure 5.9: The Beam's-eye-view diagram of the 2D set-up used for simulating the linac parameters effect. Shows the circular distribution of the ideal point transducers at a constant distance from the beam center.

The temporal average dose rate of the simulated linac was set to be a constant (84 Gy/s) while varying the operational pulse repetition rate (frequency). The resulting dose per pulse (Gy/pulse) is hence inversely proportional to the linac pulse repetition rate (in Hz). For the simulated different linac frequencies, the induced acoustic signal simulated by one of the point transducers is inversely proportional to the linac pulse repetition frequency as shown in Figure 5.10 A. While the acoustical signal intensity is linearly proportional to the dose per pulse, as theoretically expected, with a Root Mean Square Error (RMSE) of 0.027 and R^2 of near unity (Figure 5.10 B). The resulting values reflect the linear proportionality of the induced acoustic signal intensity to the deposited dose per linac pulse as theoretically predicted which reflects the capability of iRAI to measure the dose on a per pulse basis.

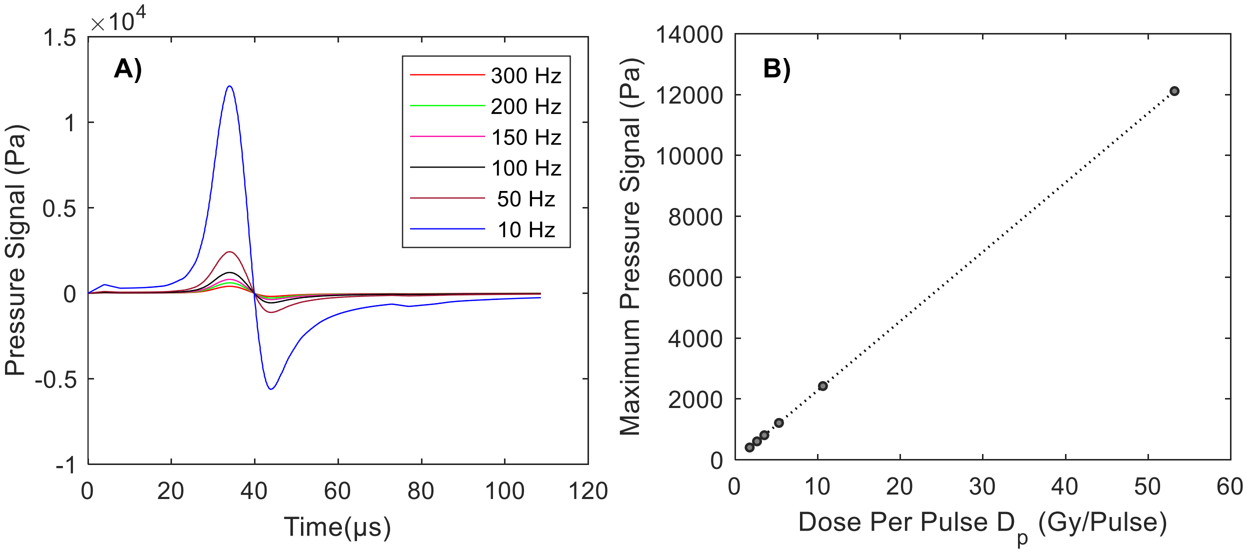

Figure 5.10: The effect of the linac pulse repetition rate in the simulated acoustic signal and dose per pulse. A): the effect of changing the linac pulse repetition rate (linac frequency), on the pressure signal intensity. B): showing the linearity of the linac dose per pulse to the induced acoustic signal intensity.

5.4.2 The Effect of The Linac Pulse Duration:

The duration of the linac pulse and the results instantaneous dose per pulse (in Gy/s/pulse) effects on the simulated acoustic signal were tested. Different linac pulse durations were tested while maintaining a constant linac pulse repetition frequency of 300 Hz using two different transducer distributions in 2D and 3D configurations.

I. 2D Simulations with A Circular Configuration of Point Transducers

The setup used in this part is similar to the previous section 5.4.1 setup for the effect of the pulse frequency case (Figure 5.9). The pulse repetition rate was held constant (300 Hz), hence the temporal average dose rate (in Gy/s) of the simulated linac was set to be constant as the pulse duration was varied. Hence, as the pulse duration varied, the instantaneous dose rate during the pulse changed. The intensity (amplitude) of the induced acoustic signal decreases as the linac pulse duration increases. In other words, for pulse durations of 0.6 μs length and longer, the instantaneous dose rate during each pulse decreases for longer linac pulses as shown in Figure 5.11. Those results were in good agreement with results published in the literature [113].

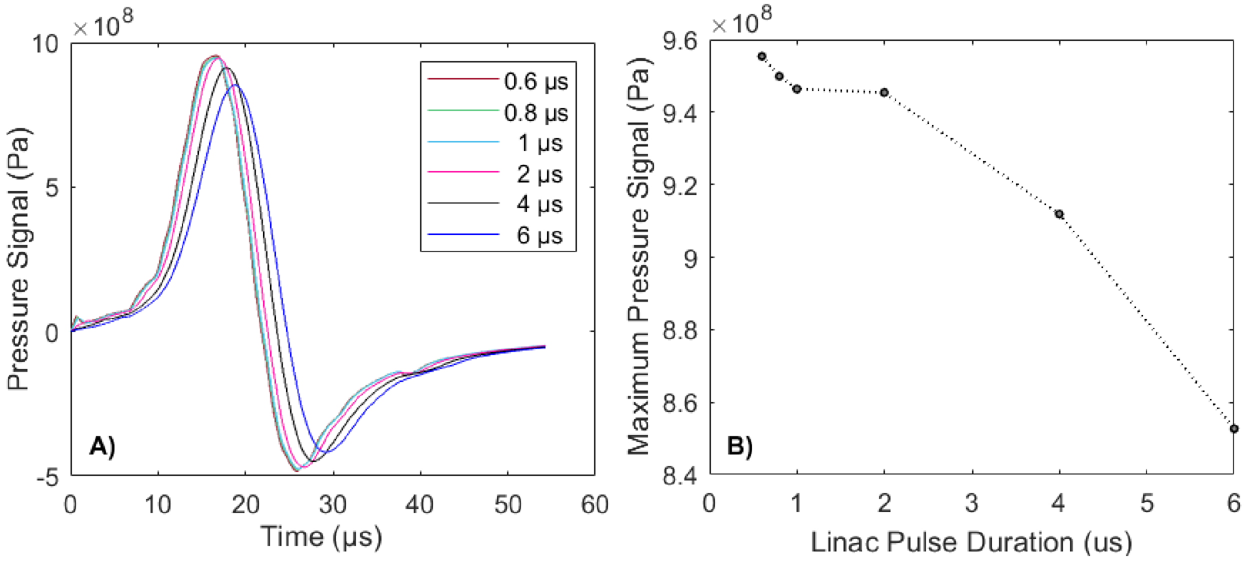

Figure 5.11: The effect of the linac pulse duration on the intensity of the induced acoustic signal and the instantaneous dose per pulse for a constant linac dose per pulse (constant frequency of 300 Hz).

The effect of the pulse duration on the TR reconstructed initial pressure source images, extracted at the phantom entrance (zero depth), is shown in Figure 5.12 for the different tested linac pulse durations of 0.6 µs in length and longer. Showing the effect of the linac pulse duration in spatial resolution with the noticeable beam size increase for the longer pulse cases of 4 µs and 6 µs. The quantitative gamma test comparison relative to the initial pressure source data are listed in Table 5.2. The gamma-test passing rate increases with decreasing the linac pulse duration, and qualitatively the image resolution is better at the shorter pulse durations of the linac. Both findings indicate the direct relation between the linac pulse duration and the temporal (spatial) resolution of iRAI images. Moreover, the FWHM of the TR reconstructed pressure-based beam profiles agrees within 2% relative error to MC simulated beam profile for the shorter linac pulse durations that are less than 1 µs. The disagreement between the pressure and the dose-based FWHM of the radiation beam increases to 15.4% and 39.8% for the larger linac pulse durations of 4 µs and 6 µs, respectively (Figure 5.13).

For the 4 µs linac pulse duration case, the agreement between the iRAI predicted and the MC-based FWHM of the radiation field was approximately 2 mm. This 2 mm difference resembles the beam size-based resolution of iRAI and is in reasonable agreement with the result published in literature testing the XACT 2D dose reconstruction versus film measurement for a 4 mm diameter stereotactic cone field. XACT has reported an FWHM of 6 mm FWHM of the field and predicted a 6 mm resolution for this field in the study [62].

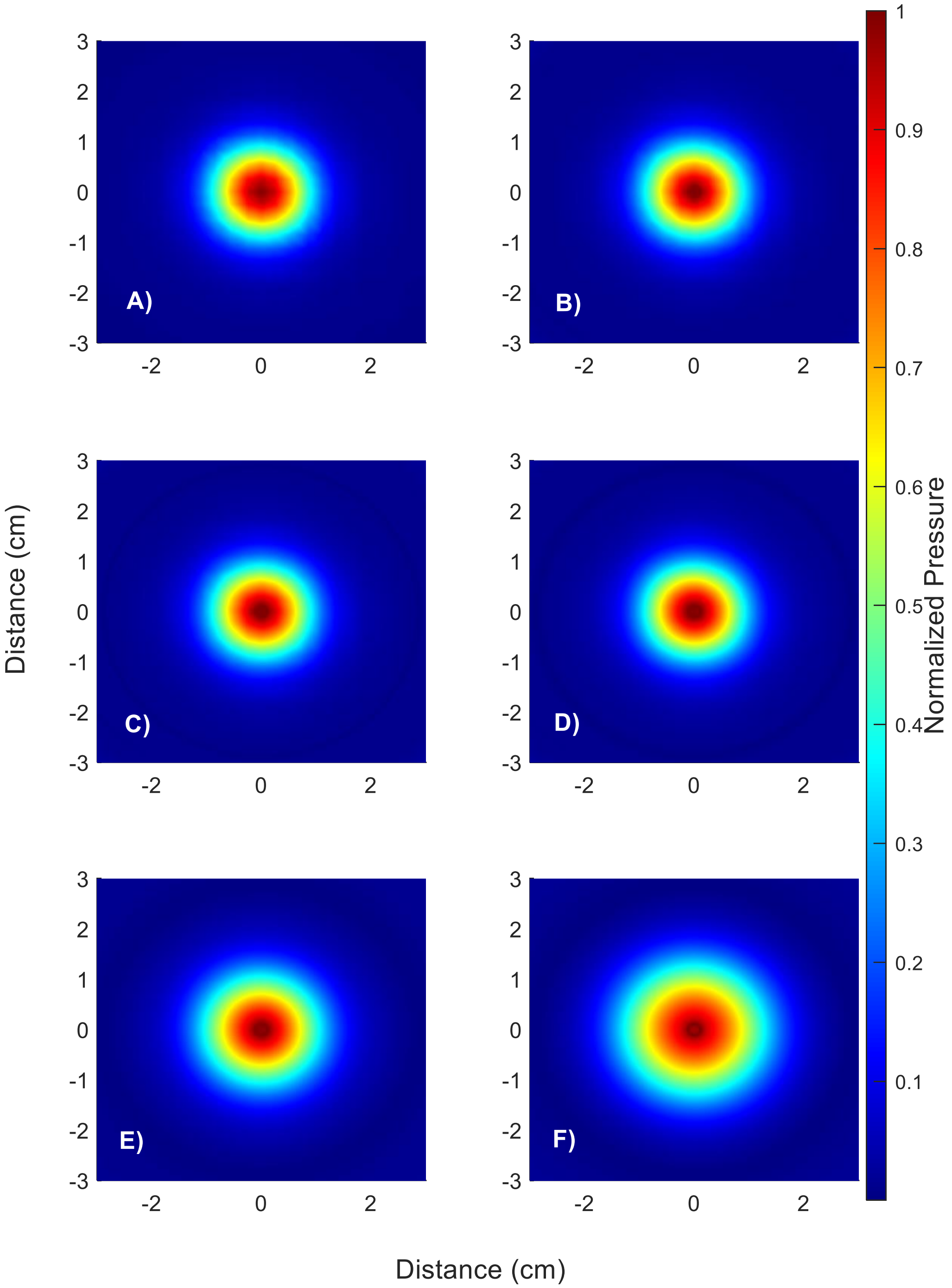

Figure 5.12: 2D TR reconstructed initial pressure images at the phantom entrance for different linac pulse durations. The initial spatial pressure distribution assuming A) a delta function and linac pulse duration of, B) 0.1 μs, C) 0.4 μs, D) 1 μs, E) 4 μs, F) 6 μs.

Table 5.2: Percent of points in the reconstructed image passing Gamma test criteria between the reconstructed spatial pressure distribution and the relative dose distribution levels for the five different linac pulse durations.

Pulse duration(μs)	**% of Points Passing the Gamma Criteria**		
	3%/3mm	1%/1mm	0.5%/0.5mm
0.1	100	97.3	93.9
0.4	100	97.5	91.6
1	100	97.8	87.0
4	100	55.9	30.1
6	67.4	43.7	23.7

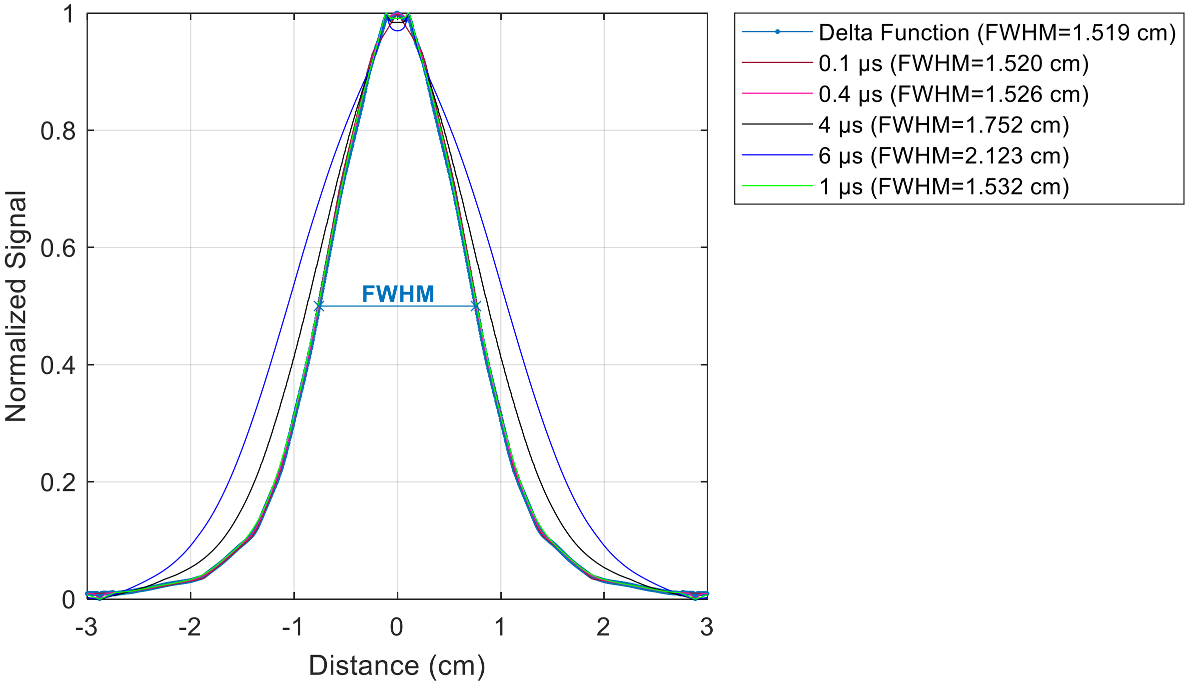

Figure 5.13: The effect of the linac pulse duration on the spatial fidelity of the signal as reflected by the horizontal beam profiles extracted from the TR reconstructed iRAI images compared to the horizontal beam profile.

II. 3D Simulations with Spherical Transducer Distribution

To further study the effect of the linac duration on the overall temporal and spatial resolution of the iRAI images and the acquired pressure-based beam characteristic, a full 3D study was performed. The transducers were distributed in the same configuration studied in section II assuming an ideal case of a full data collection with ideal point transducer elements distributed on the surface of a spherical shell without bandwidth limitations.

This study was performed for three different linac pulse durations; 1 µs, 4 µs, and 6 µs linac pulse. The longer the pulse duration, the worse the spatial fidelity of the 3D reconstructed iRAI images in the different planes of the initial radiation beam as shown in Figure 5.14. As shown in Figure 5.14, the size of the pressure predicted radiation beam is wider as the pulse duration of the linac increases. Hence, the edges of the radiation beam are defined more accurately using TR reconstruction of the instantaneous measured acoustic pressure signals as the linac pulse duration decreases. Similarly, the effect of the linac pulse resolution also affects the reconstructed pressure-based images along the beam direction such that the longer the pulse, the steeper the pressure curve with depth in the phantom. The gamma test results comparing the 3D reconstructed pressure images to the initial pressure source (radiation beam) distribution were reported in Table 5.3. Showing that the passing rate increases as the pulse duration decreases.

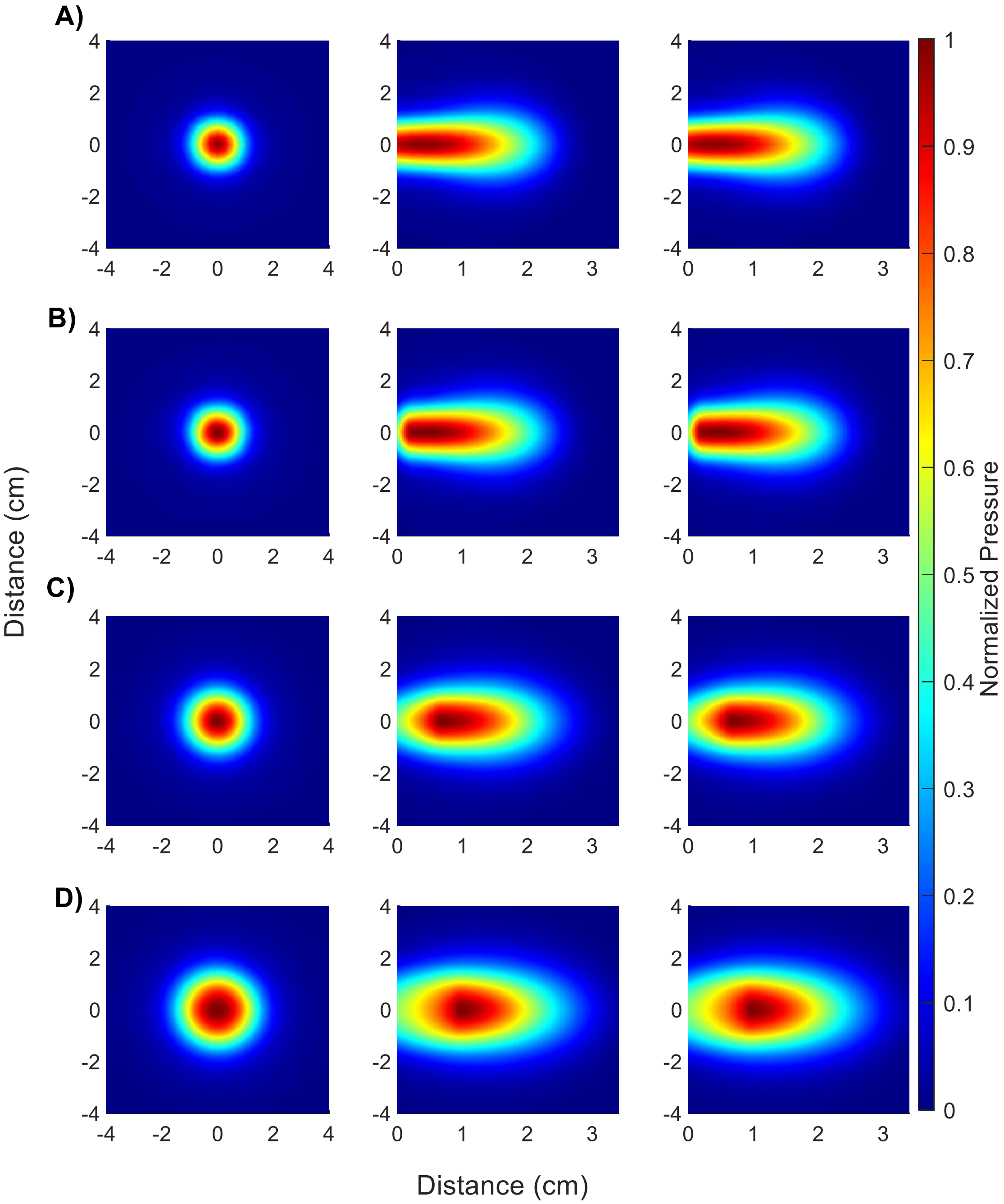

Figure 5.14: The effect of the pulse duration of the linac on the spatial fidelity of the reconstructed iRAI images at the XY plane (cross beam plane) at the surface of the phantom (at 0 cm depth), ZX plane (parallel to the beam plane) scored at beam center (y=0 cm), and ZY plane scored at beam center (x=0 cm) respectively. A) a delta function and linac pulse duration of, B) 0.1 µs, C) 4 µs, D) 6 µs.

Table 5.3: Percent of points in the reconstructed image passing Gamma test criteria between the reconstructed spatial pressure distribution and the relative dose distribution levels for the different linac pulse durations with and without the pulse duration correction (Deconvolution).

Pulse duration(μs)	**Gamma Criteria without pulse correction**		**Gamma Criteria with Pulse Correction**	
	3%/3mm	**1%/1mm**	**3%/3mm**	**1%/1mm**
0.1	99.9	98.9	99.9	98.4
4	99.4	91.5	99.9	98.7
6	92.5	86.2	99.9	98.7

As per the finding of this study, the main challenge for iRAI implementation for dosimetry is the relatively long pulse duration length for the clinical linacs. As this effect strongly affects the resolution of the reconstructed images and hence causes spatial degradation of the relative dosimetry characteristics, it needs to be well addressed and corrected. One of the approaches that can resolve this issue is to implement signal processing techniques, i.e., deconvolution of the instantaneous pressure signals for the linac pulse shape before implementing the image reconstruction algorithm.

Hence, the signal processing deconvolution technique was implemented to correct for the linac pulse duration and its effect on the temporal and spatial resolution of the iRAI images. This correction as its name indicates deconvolute the temporal signal of the linac pulse duration from the detected instantaneous pressure signal before the TR reconstruction of the initial pressure images and hence eliminating its effect on the final reconstructed iRAI images. This correction has resulted in a better agreement between EGSnrc and the 3D reconstructed iRAI results as shown in Figure 5.15 specifically for the long linac pulse duration cases. With the deconvolution signal processing correction, the gamma test results have also improved for all the linac pulse duration cases specifically for the longer pulse durations as reflected in Table 5.3.

The shift in the buildup region of the pressure-based percent curve is a geometrical artifact caused by the relatively long linac pulse duration (Figure 5.16 A). The deconvolution signal processing correction has resulted in a better agreement between the normalized MC-based PDD and the corrected pressure-based percent depth curves for all the tested linac pulse durations as shown in Figure 5.16 B. The MC-based PDD and the pressure-based percent depth curves were normalized to the 1 cm depth signal for the different linac pulse duration times. With correction, for depths from 1 mm to 2 cm both curves agree within 8% relative error for the 4 μs and 6 μs pulse durations. For the 1 μs case, the maximum relative error was within 11%.

As per the results of this study, the maximum disagreement for depths 1 mm to 2 cm for the clinical linac pulse duration of 4 μs was within 8% relative error. Achieving this accuracy elsewhere will depend on the implemented transducer placement setup.

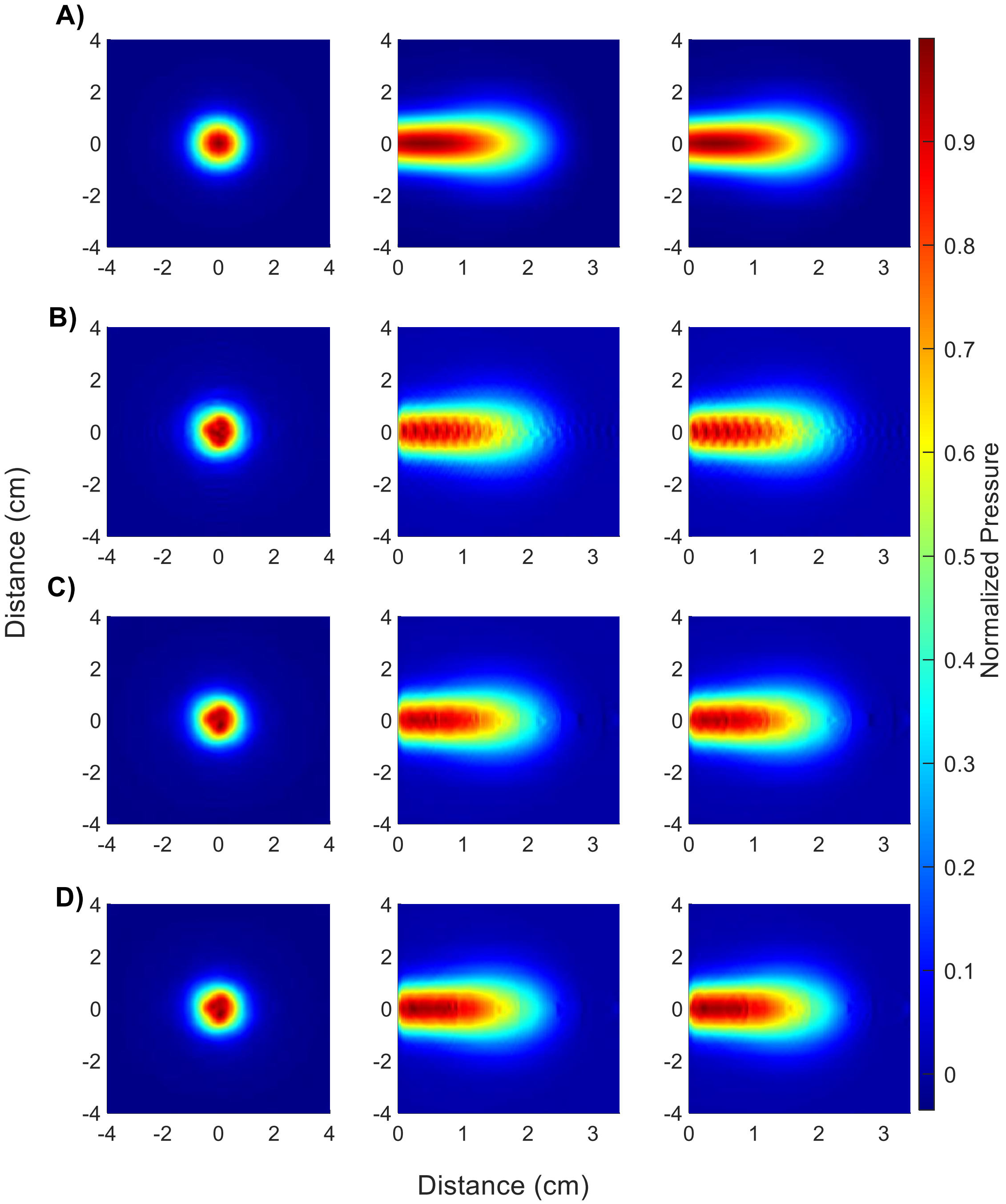

Figure 5.15: The effect of correction (deconvolution) of the pulse duration of the linac on the spatial fidelity of the reconstructed iRAI images at the XY plane (cross beam plane) at the surface of the phantom (at 0 cm depth), ZX plane (parallel to the beam plane) scored at beam center (y=0 cm), and ZY plane scored at beam center (x=0 cm) respectively. A) a delta function (no pulse duration effect) and linac pulse duration of, B) 0.1 µs, C) 4 µs, D) 6 µs.

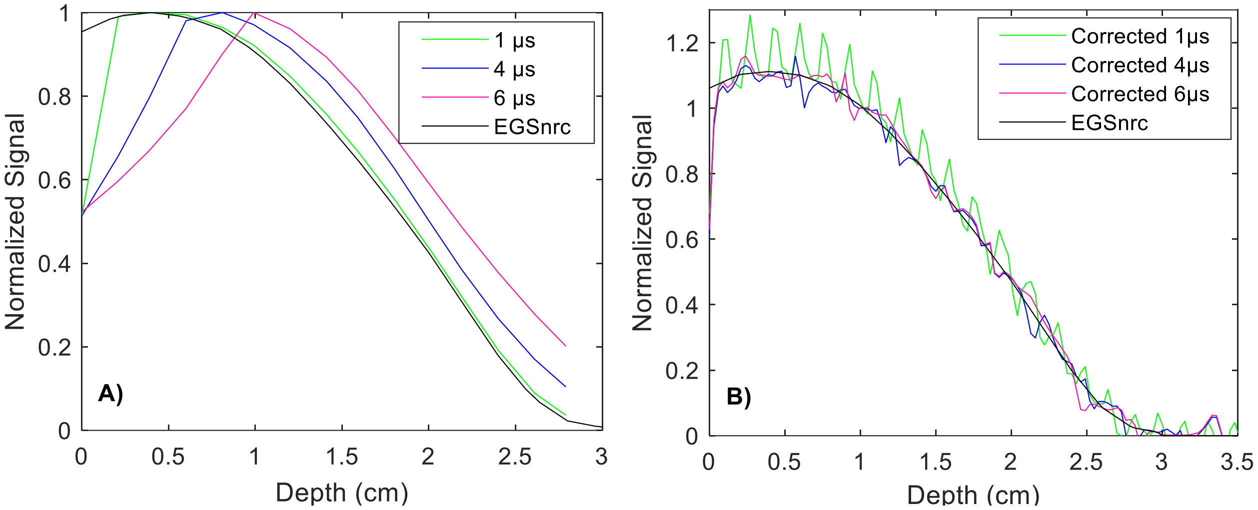

Figure 5.16: A) The reconstructed pressure-based percent depth curve for the different linac pulse durations compared to the MC-based PDD curve. B) The reconstructed pressure-based percent depth was corrected for the pulse duration shift with temporal linac pulse deconvolution and compared to the MC-based PDD curve.

5.5. Conclusions

In this chapter, a full simulation workflow was developed, and a comprehensive study was conducted in a homogenous gelatin phantom to test the feasibility of iRAI in UHDR-RT. The 3D iRAI imaging capability and acoustical signal generation were simulated assuming an ideal distribution of ideal transducer elements over a sphere to optimize 3D volumetric imaging capabilities. Transducers with finite bandwidths and practical dimensions must be considered next for future studies.

IRAI has shown the advantage of 3D dose mapping through the linearity of acoustical signal to dose. This linearity has demonstrated its potential as a promising in-vivo relative dosimetry tool for UHDR-RT measuring dose on a per pulse basis without signal saturation. On the other hand, iRAI has a limited spatial resolution (a few millimeters), mainly due to the inherent linac pulse duration effect. The spatial resolution can be improved through linac pulse deconvolution, which has improved the agreement between the pressure-constructed and the initial dosimetric beam characteristic to within a 98% passing rate for 1%/1mm gamma test criteria for the operational linac pulse duration of 4 µs. UHDR-RT is delivering a higher instantaneous dose per pulse (in Gy/s/pulse), which enforces the need for and necessitates the implementation of instantaneous dose measurements such as iRAI for patient safety, dose monitoring, and beam localization.

Chapter 6

Applicability of Ionizing Radiation Acoustic Imaging (iRAI) as a 3D Relative Dosimetry Tool

This chapter discusses the applicability of iRAI in 3D dosimetry for conventional radiation therapy. A clinical linear accelerator was used for iRAI implementation to deliver different radiation treatment plans to radiochromic gels. This work aims to verify experimentally and through simulations, the feasibility of the iRAI modality as a potentially promising tool for relative 3D dosimetry. The results were compared with the 3D dosimetric results obtained from Clearview radiochromic gels. This work also studied the effects of the different operational parameters of the customized 2D array transducer including the central frequency and the bandwidth on the reconstructed acoustic images through simulations. The work of this chapter will be published in a peer-reviewed journal.

6.1. Introduction

With the advancement and the complexity in the treatment delivery techniques and the treatment plans such as IMRT and VMAT. It is desirable to acquire 3D comprehensive dosimetry data for quality assurance and control for those advanced delivery approaches. Gels can record the accumulative radiation dose distribution in 3D with the advantage of their radiologically soft-tissue equivalence. The applicability of gels in 3D conventional relative dosimetry is tested and verified through comparisons with the planned dose calculations as the first step. The acoustical properties of those gels are expected to be comparable with those of gelatin phantoms.

Because gels are one of the most common 3D dosimeters, it is used as the phantom to generate iRAI signal and the reference dosimeter to verify and study the 3D capability of iRAI in this work. The iRAI experimentally acquired data, as well as the simulation results, were compared with the dosimetric gel experiments for the different treatment delivery clinical scenarios to comprehensively characterize the applicability of iRAI in clinically relevant scenarios.

6.2. Gel for 3D Dosimetry

Two different batches of Clearview gels were used for the experimental part of this study. Gels from different batches were calibrated separately for absolute dosimetry with the Clearview gels. The gels were handled before and post-irradiation following the manufacturer recommendations as discussed previously in section 3.4.1.2. An important difference for the gels in this application is that the bottom of the gel jar is cut-ended for better coupling with the 2D array transducer as shown in the experimental setup (Figure 6.1).

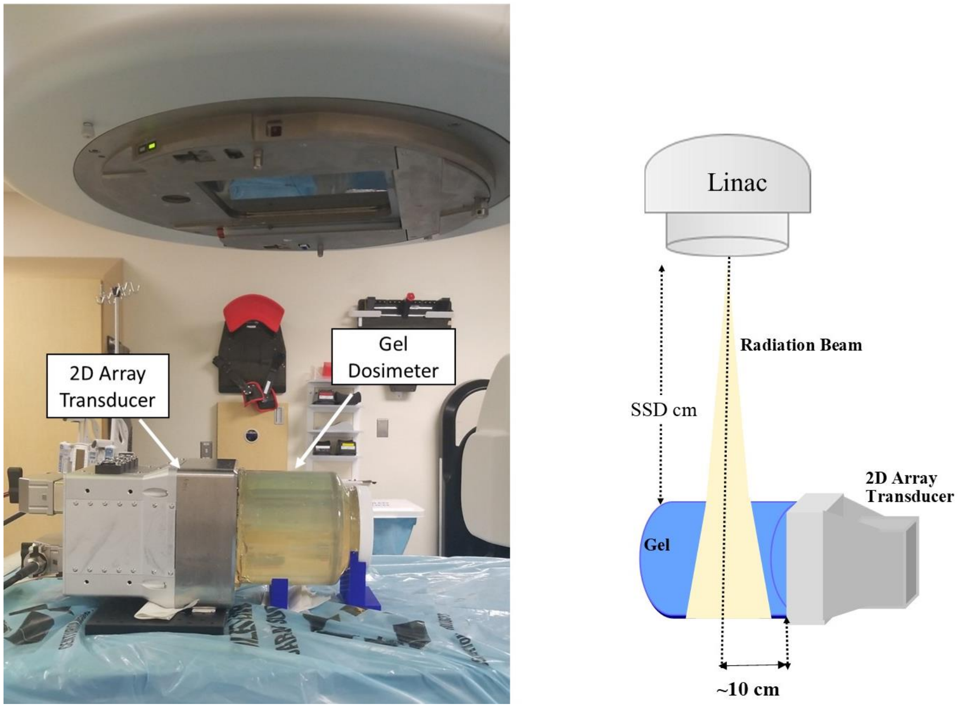

Figure 6.1: The experimental setup for iRAI measurements including both the schematic and the actual setup showing the direction of the radiation beam and the acoustic coupling of the cut-ended gel jars with the customized 2D array transducer.

6.2.1. The Gel Calibration

The gels were calibrated using 10MV FFF photon beams to cover the expected dose range in the measurement and an electron beam of 12 MeV energy. The resulted calibration curves for the different radiation fields are plotted in Figure 6.2 showing the linearity of the gel response. The calibration curves were extracted over the central 0.5x0.5 cm^2 ROI for the two different fields as shown in Figure 6.2. The electron calibration covers high dose gradients, while the photon beam-based calibration has more dose values. Both calibration curves lie within each other, which reflects the dose-energy independency of the gel readings as reported in the literature [49]. The resulted calibration equation merging both calibration curves was used to calibrate the other gel jars of the same batch. The other batch was also calibrated using 10 MV FFF photon beams for different doses covering the full sensitivity range of the gel dosimeters as shown in Figure 6.3. Gels have measured a linear response ranging up to ~88 Gy as measured and shown in the calibration curve. To cover a wider dose range, the calibration curve was measured as the combination of the response from two irradiations using 2x2 cm^2 and 3x4 cm^2 10 MV FFF fields measured with the same gel jar.

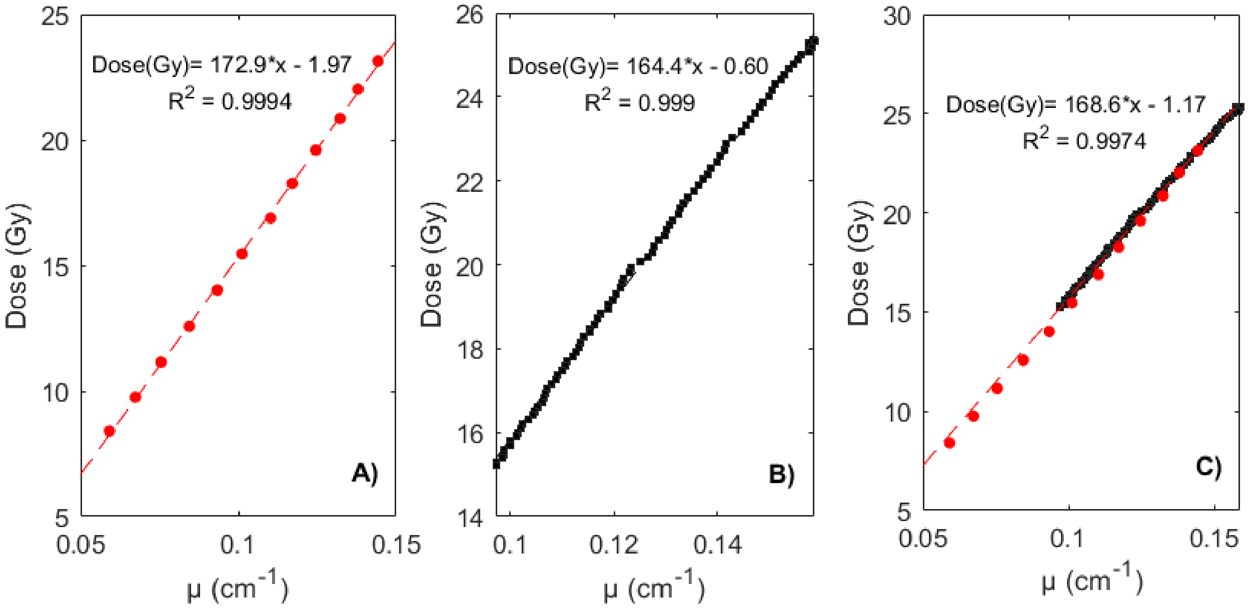

Figure 6.2: Gel calibration curves for different radiation fields, A) 4x4 cm 10 MV FFF photon beam, B) 12 MeV electron beam, C) the resulted calibration curve merging both curves used to calibrate the whole batch.

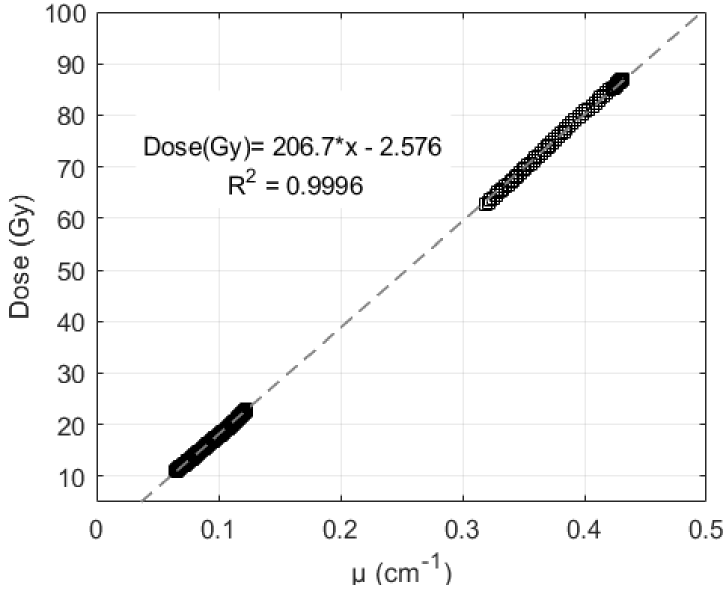

Figure 6.3: The calibration curve and the linearity response of the gel dosimeters for the second batch showing different doses ranging from 10 Gy to 80 Gy.

6.2.2. Gels for 3D Dosimetry

The applicability of gels in 3D has been verified by testing different treatment plans compared to the treatment planning dose. The different tested plans are a C-shaped plan, an arc plan, and a three-field conformal plan. The resulting contour plots of the different fields are used for comparing the planned and the gel-measured isodose contours. Gels are sensitive to doses of 8 Gy or higher, thus doses < 8 Gy were excluded from the quantitative comparisons.

A. 3D Conformal C-shaped Plan

The C-shaped 3D conformal treatment plan consisted of 23 static beams of variable sizes delivered at the isocenter. The delivered treatment plan was measured with gels for absolute and relative dose quantification. The resulting isodose contours of the plan and the gel measured results are shown in Figure 6.4. Gel has shown absolute and relative dosimetry passing rates for the 3%/3mm gamma test criteria of 95.4% and 98.9%, respectively. The planned dose has an active calculation grid that surrounds the jar and excluded the dose calculations beyond the effective volume of the grid. This exclusion of the dose at the surface is causing the differences between the gel and the delivered dose as can be shown in Figure 6.4.C. Gels have some construction artifacts due to the design of the cut-ended jar, which causes the generation of bubbles at the surface of the jar as shown in Figure 6.4.

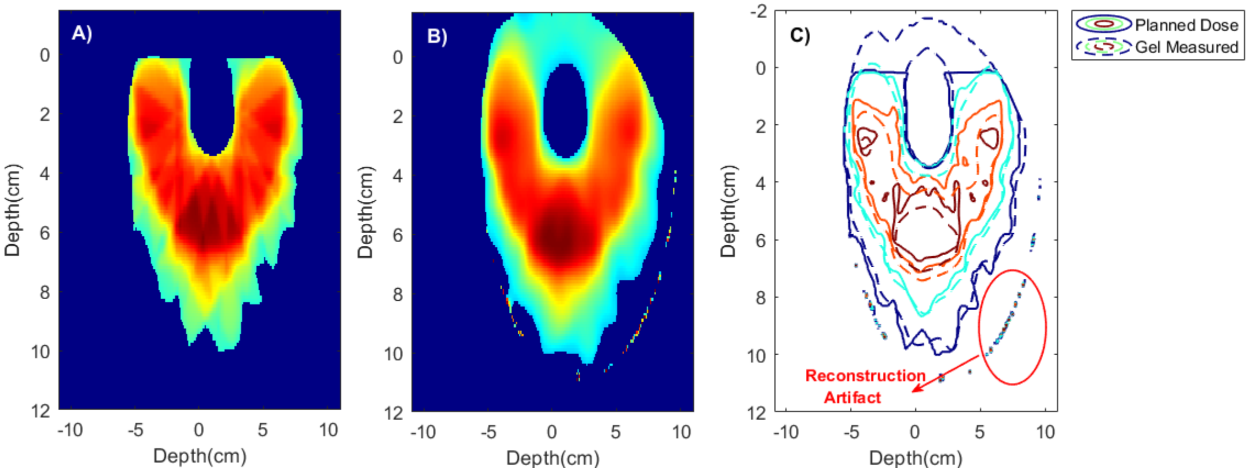

Figure 6.4: The C-shape 3D conformal plan comparing gels to the treatment plan results. A) the treatment planned dose distribution, B) the gel measured dose distribution, C) the measured and the planned isodose contour plots showing the 90%, 80%, 60%, and 40% contour isodose lines.

B. Arc Plan:

The second tested plan was a static arc of 5x5 cm^2 radiation field size delivered continuously from 315° to 45° gantry angle. The resulting dose distribution measured with the gel jar was compared with the planned dose as shown in Figure 6.5. The agreement between the planned and the delivered dose measured with the gel jar was within 98.2% and 99.6% passing rates of the 3%/3mm gamma test criteria for absolute and relative dosimetry measurements. The cut-ended design of the gel used for this experimental work was a bit challenging as it introduces some mechanical stress to the gel material. This specific gel jar has shown a spiral artifact measured at the center of the gel phantom as shown in Figure 6.6. Although this artifact was away from the region of the dose used for iRAI measurement comparisons, it was only affecting the central 3 mm region of the phantom and possible correction for it is through using spline smoothening with edge detection in the radial direction. Overall, it is not affecting the total dose distribution, which is reflected through the considerably high passing rate of the gamma test.

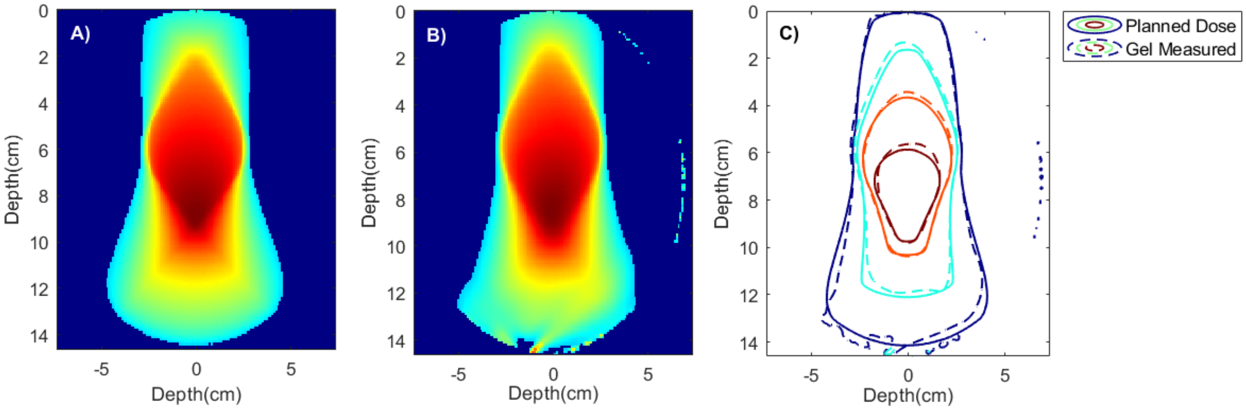

Figure 6.5: The arc plan dose results comparing gels to the treatment plan distributions. A) the treatment planned dose distribution, B) the gel measured dose distribution, C) the measured and the planned isodose contour plots showing the 90%, 80%, 60% and 40% contour isodose lines.

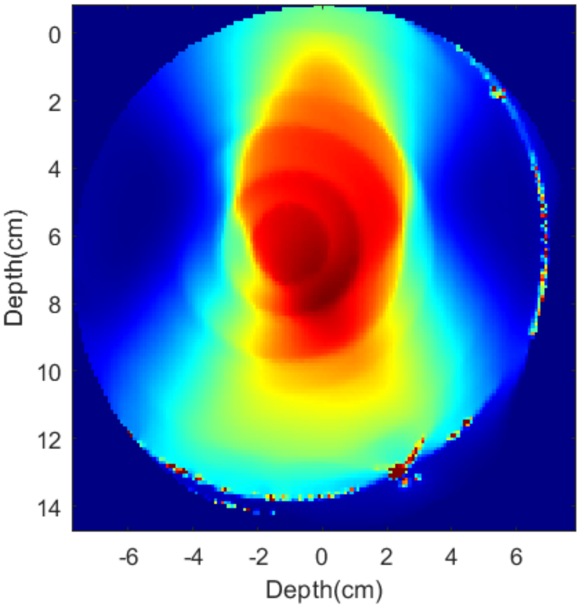

Figure 6.6: Th measured artifact at the center of the gel jar due to some mechanical stress.

C. Three Field Plan:

The last tested plan is a 3D conformal plan consisting of three static radiation fields of 5x5 cm^2 delivered at three different gantry angles: 330^o, 0^o, and 30^o. The gel measured results were compared to the treatment planned dose as shown in Figure 6.7.

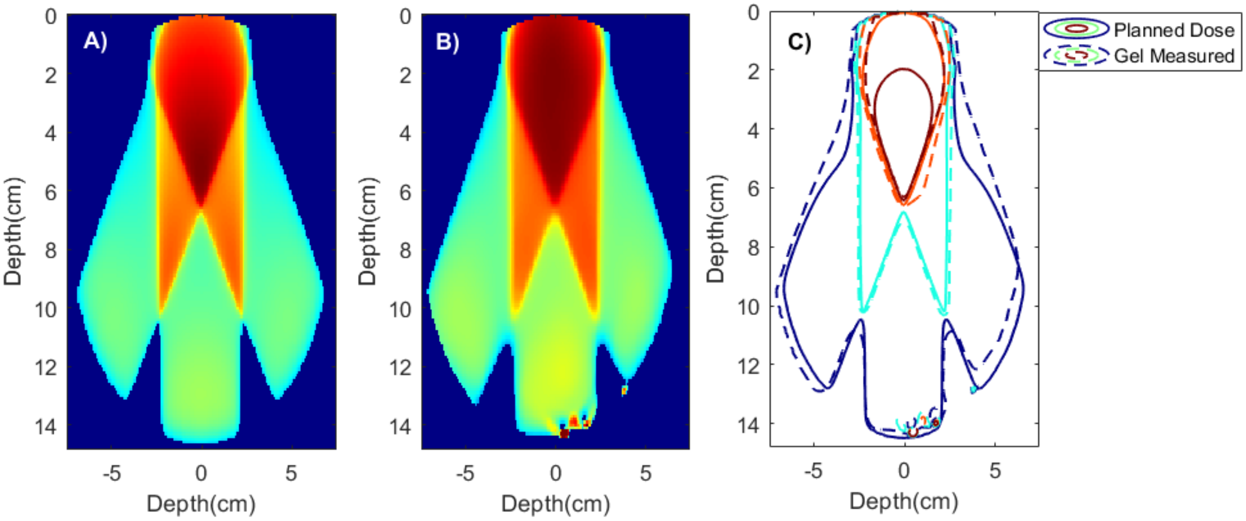

Figure 6.7: The three-field plan dose results comparing gels to the treatment plan distributions. A) the treatment planned dose distribution, B) the gel measured dose distribution, C) the measured and the planned isodose contour plots showing the 90%, 80%, 60%, and 40% contour isodose lines.

The results were compared using a 7%/4mm, 3%/3mm, and 1%/1mm gamma passing criteria and the resulting passing rates for the different plans were listed in Table 6.1. The arc plan showed the best agreement with the treatment planned dose, as the maximum dose delivery was closer to the center of the jar and less affected by the reconstruction artifacts at the edges of the jar. The three-field plan specifically for the 90% isodose curves showed the least agreement with the planned dose. The gels have measured a higher dose than the planned dose due to the saturation effect of the gels as gels were exposed to doses higher than 80 Gy. Another source of difference between the gel measured and the treatment planned dose was the effect of the design of the gel jar, cut-ended gel jars, as they were expected to be exposed to mechanical stresses, which could slightly affect the measured absolute dose values. Additionally, there were some reconstruction artifacts specifically at the edges of the gel jars as shown in Figure 6.4. However, the resulted overall agreement between the gel and the treatment planned relative doses were acceptably good as indicated in Table 6.1. Gel measured results were hence used as the reference benchmark to test the iRAI results and to verify its 3D dosimetric capability.

Table 6.1 Gamma test passing rates of the planned and the gel measured results

Beam Energy	**C-shaped**		**Arc plan**		**Three Field**	
	Absolute	Relative	Absolute	Relative	Absolute	Relative
1%/1mm	94.8	95.9	89.8	92.8	82.0	84.2
3%/3mm	95.4	98.9	98.2	99.6	87.8	94.4
7%/4mm	96.0	98.9	99.5	99.6	93.9	94.4

6.3. IRAI Imaging

The iRAI images were acquired in phantom (Gelatin/Gel) using a 2D array transducer. The experimental setup and workflow are shown in Figure 6.1. Phantoms were placed on the couch of the clinical Varian TrueBeam clinical accelerator (Varian Medical Systems, Palo Alto, Ca) such that the radiation beam shot from the top of the phantom. The phantoms were cut-ended and attached to a 2D array transducer positioned to the center of the phantom to detect the generated acoustic signals. The generated acoustic signal was measured with a 2D array transducer. The custom-designed 2D array transducer (Imasonics, Inc.) is a 32x32 square-grided array (116.6 mm×116.6 mm) with a square element of a 0.85 lambda (~ 3.45 mm) on a side with 0.2 mm kerf edge to edge separation. The array has a side length of approximately 12 cm side length with a central frequency of 0.35 MHz and a 60% bandwidth.

The first part which focuses on characterizing the signal was performed on porcine gelatin (10 g/100 ml, G2500, Sigma-Aldrich) phantoms. The other part relies on using gel phantoms for iRAI and 3D dosimetry characterization using different treatment-related plans. The resulting experimental results were compared with simulation results simulating the generated acoustic signals from the experimental setup following the same simulation workflow in Figure 5.1.

6.3.1. IRAI Simulations

The simulation studies were performed following the simulation workflow and the theoretical procedure followed in section 5.2, and Figure 5.1. The 3D dose distributions were extracted from the treatment planning system (TPS), Varian's Aria/Eclipse platform (v.15 and v.13). The 2D array operational characteristics were simulated using the MATLAB KWave toolbox to measure the generated acoustical signal and its propagation in the phantom in addition to the time-reversal reconstruction of the generated 3D iRAI acoustical images. The simulation part was used to study the effect of the operational parameters of the 2D array on the quality of iRAI images. Additionally, simulation studies were performed as the preliminary testing and verification of iRAI applicability for different treatment plan deliveries. The simulated acoustical signal compared to a measured signal is plotted in Figure 6.8 showing both the instantaneous temporal distribution of the signal and the frequency spectrum of the generated acoustical signal. The differences in the time steps between the measured and the simulated data have resulted in differences in the frequency spectrum specifically in the lower frequency region. The differences in the time arrival of the simulated and measured acoustic signals are due to the differences in the radiation field position, however, both showed the same detected field size. The measured acoustical signal has a high acoustic signal measured at the surface of the transducer. This behavior and effect have been reported in the literature. The measured high changes at the surface were expected to be because of the electrical noise induced by the effect of radiation scattering [119]. The linac pulse repetition rate for simulation purposes was assumed to be constant for the different simulated beam energies; 6 MV FFF and 10 MV FFF and set equal to 300 Hz.

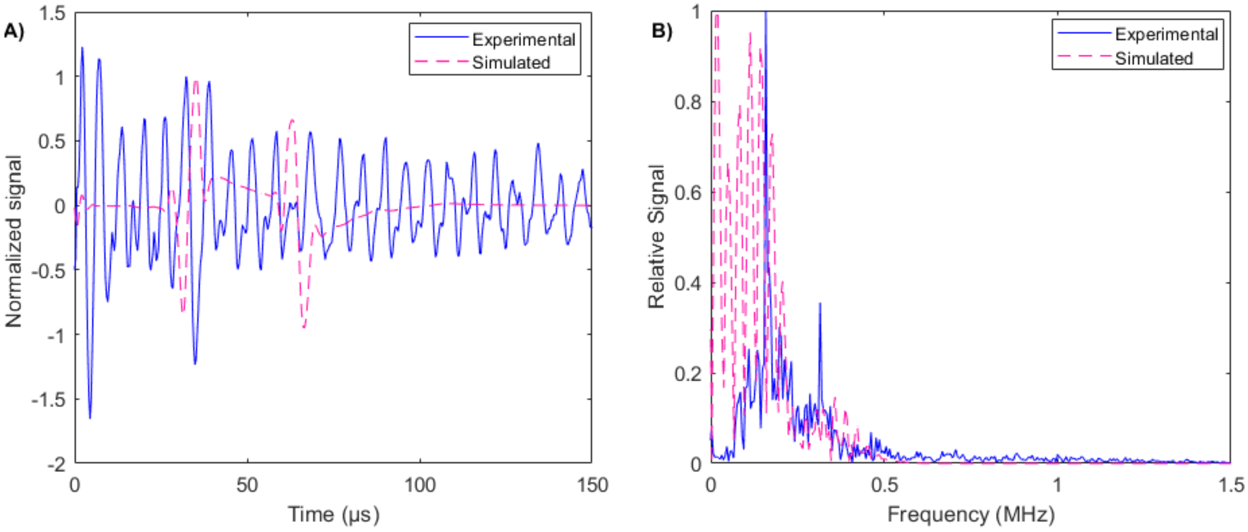

Figure 6.8: Comparison of the experimental and simulated data A) average acoustical signal detected by the 2D array transducer for 10 MV FFF 5x5cm^2 radiation beam at depth 7.5 in gelatin phantom and 93 cm SSD B) the frequency spectrum of the generated acoustic signal following the irradiation.

6.3.1.1 The effect of the 2D array transducer parameters

One of the main limitations of iRAI is the limited bandwidth of the transducer and central frequency of the detecting transducer. This section is a simulation-based study testing the effect of changing the operational parameters of the 2D array. The central frequency was changed holding the bandwidth of the transducer to be constant while the other part tests the effect of the bandwidth of the transducer holding the central array frequency similar to the operational value.

A. The bandwidth effects

The effect of the bandwidth limitation of the array on the quality of the reconstructed iRAI images was simulated by tuning the bandwidth of the array while holding a constant operational central frequency of 0.35 MeV. The simulated bandwidth range was -30dB to -80 dB with an increment of -10 dB bandwidth. The study was performed by testing a 6 MV FFF static field of 5x5 cm^2. The results, shown in Figure 6.9, are compared qualitatively using the gamma passing rate criteria of 3%/3mm of the iRAI front edge distribution to the initial dose distribution. Additionally, the relative SNR was used for comparing the quality of iRAI images in determining the edges of the field using the operational bandwidth of the array of -60 dB as the reference bandwidth. The SNR was calculated as the ratio of the maximum signal amplitude to the maximum background noise (peak to peak ratio) in the reconstructed image and is listed in Table 6.2. The relative induced average acoustical signal for all the different cases was listed relative to the operational array parameters as well. The higher the bandwidth of the transducer the stronger the generated acoustical signal, and the better the quality of the image as indicated based on the gamma passing rates and the SNR. The -40 dB bandwidth showed a slightly higher than expected SNR. The ability of iRAI to define the edges of the beam, fidelity, decreases as the bandwidth of the transducer decreases. The higher the bandwidth, the better the quality of iRAI images and the beam edges allocation fidelity.

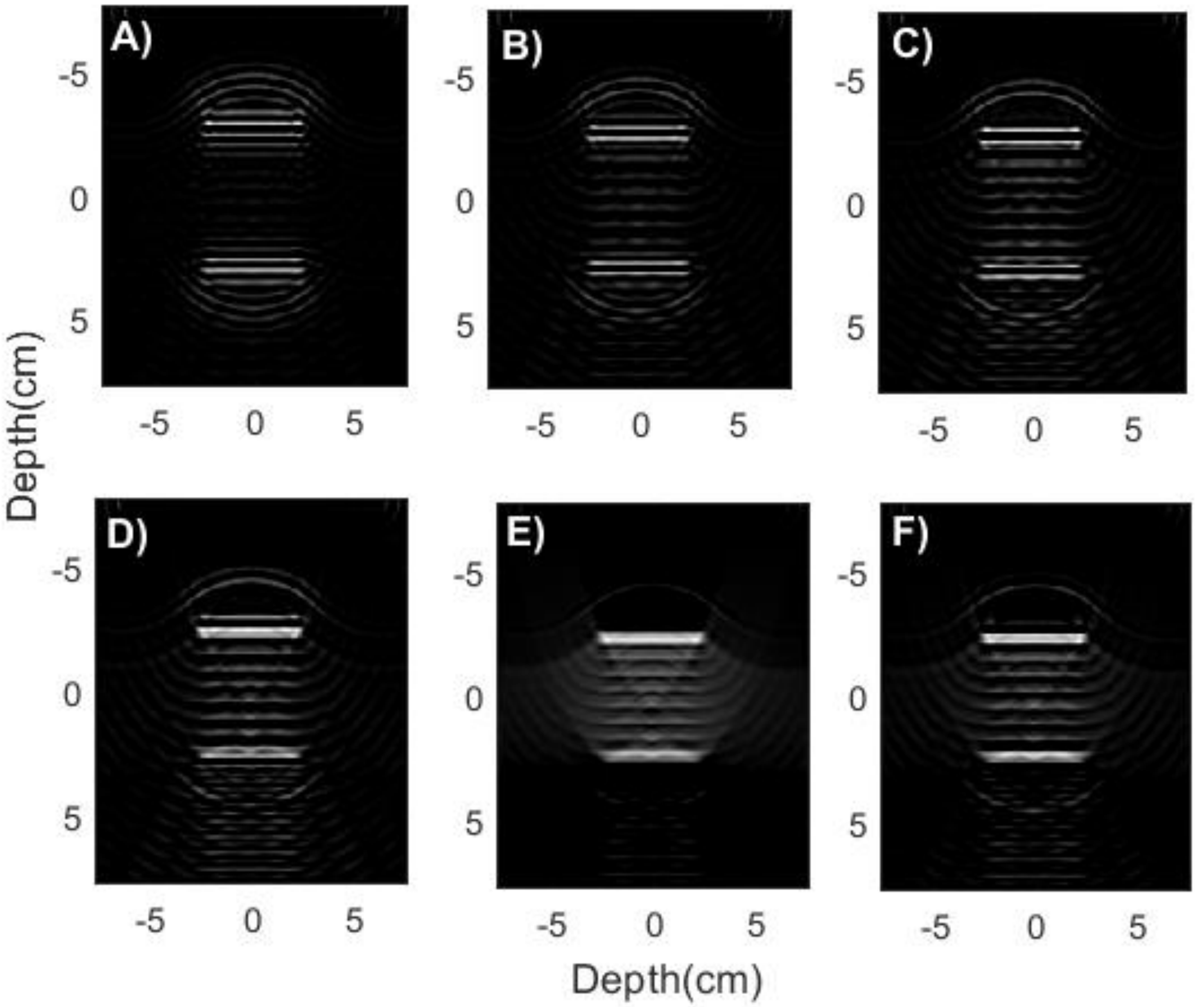

Figure 6.9: The simulated iRAI images extracted at the center of the phantom showing the effect of the bandwidth in the quality of iRAI images and localization of the radiation beam edges for 2D array bandwidths of; A) -30dB, B)-40 dB, C) -50 dB, D) -60 dB, E) -70 dB, F)-80 dB.

Table 6.2: The resulting gamma testing values and SNR of iRAI images of the bandwidth study

Transducer Bandwidth (dB)	3%/3mm Gamma Passing Rate (%)	SNR	Relative SNR	Relative iRAI signal
-30	76.5	2.11	0.91	0.05
-40	76.9	2.29	0.99	0.07
-50	77.1	2.11	0.91	0.25
-60	77.2	2.32	1	1.00
-70	77.3	2.9	1.25	3.28
-80	79.7	5.85	2.52	8.04

B. The central frequency effects

In this part, the 6 MV FFF static field of 5x5 cm^2 was used to simulate the effect of the central frequency of the array on the iRAI image quality. This part covered two different central frequencies of 0.5 MHz and 1 MHz in addition to the operational 0.35 MHz frequency of the array. The bandwidth of the array was held constant and equals the operational -60 dB bandwidth. Similar to the previous study, both gamma test and relative SNR were used for comparisons with the reference central frequency of 0.35 MHz. The resulted iRAI images for the three simulated frequencies are plotted in Figure 6.10. The resulting SNR and gamma passing rates of the different simulated frequencies are listed in Table 6.3. Although increasing the frequency of the array generated sharper field edges, it affected the quality of the constructed iRAI images as mostly the generated iRAI signal in the low-frequency region, which decreased the SNR. The 1 MHz case has resulted in a noisy image so that the radiation beam edges weren't easily defined. The front edge of the field was allocated based on the known position of the field from the other tested cases. Since the central frequency of the array, 1 MHz, was beyond the frequency of the generated iRAI acoustical signal as indicated in Figure 6.8. B.

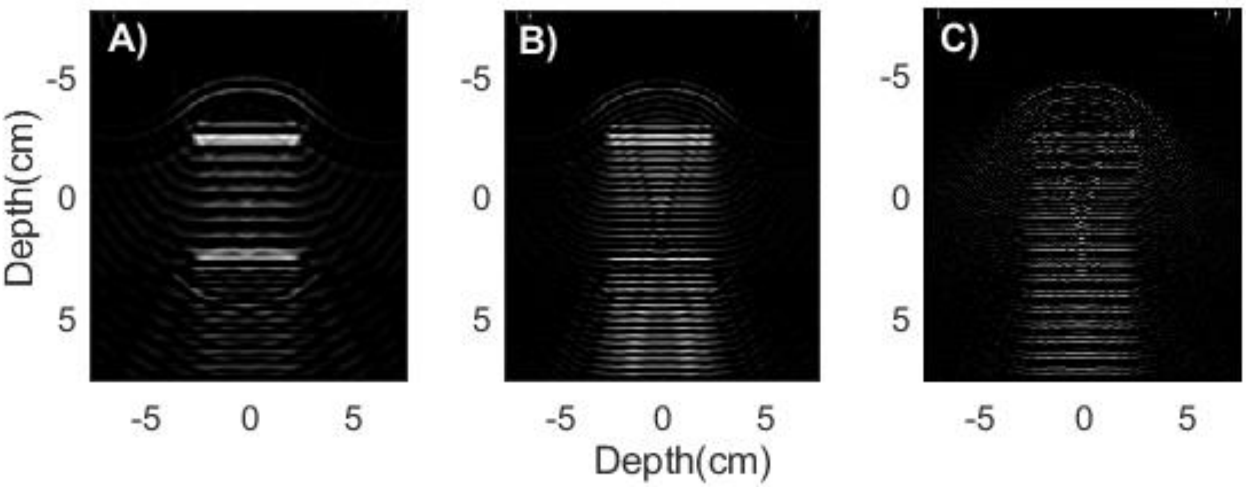

Figure 6.10: The simulated iRAI images extracted at the center of the phantom showing the effect of the 2D array central frequency in the quality of iRAI images and localization of the radiation beam edges for the tested central frequencies of; A) 0.35, B) 0.5 MHz, C) 1 MHz.

Table 6.3: The resulting gamma testing values and SNR of iRAI images of the central frequency study

Transducer Central Frequency (MHz)	3%/3mm Gamma Passing Rate	SNR	Relative SNR	Relative iRAI Signal
0.35	77.2	2.32	1.00	1.00
0.5	76.8	1.50	0.65	0.46
1	72.8	0.01*	0.00	0.20

*The SNR was <<0.01 but set the minimum error value

6.3.1.2 Pre-measurement Verification

This part aimed to test the applicability of iRAI for different treatment plans as a preliminary step before their experimental implementation. The simulation study accounted for the operational parameters of the array transducer including the central frequency of 0.35 MHz and the bandwidth of -60 dB for the different plans delivered experimentally. The front edge of the radiation field was determined as the spatial position of the central 90% of the maximum dose as the dose drops faster after this region, in the penumbra region.

A. 3D Conformal C-shaped Plan:

The planned C-shaped 3D conformal treatment plan was simulated to generate iRAI images. The dose distribution was used to define the initial pressure source and generate the corresponding iRAI images measured with the 2D array. The dose results were compared with the retrieved iRAI plan as shown in Figure 6.11. IRAI showed a good agreement within 81% passing rate for the isodose curves of 30% maximum dose or higher using 7%/4mm gamma criteria as listed in Table 6.4. The highest agreement was for the 90% and 80% isodose lines as they are high-dose regions delivered closer to the center of the 2D array, showing higher detectability. The gamma passing rates improved for the dose regions of at least 50% of the maximum dose to 93% using 7%/4mm gamma criteria.

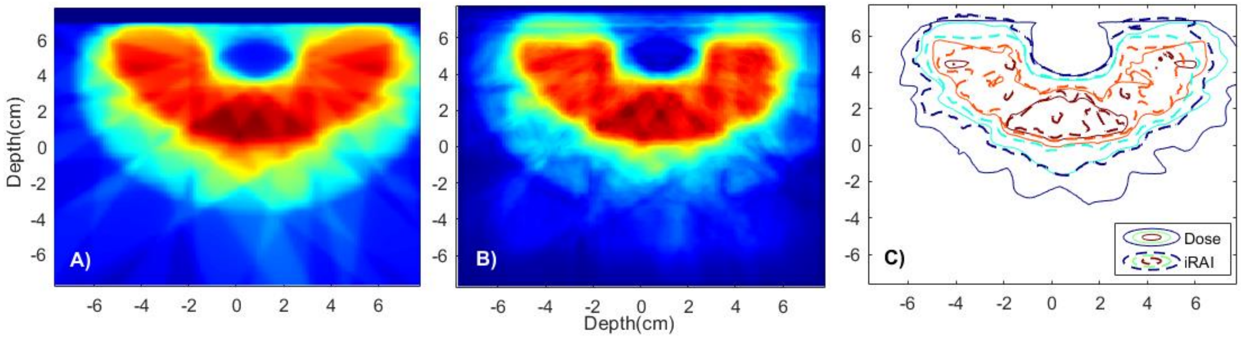

Figure 6.11: The simulation results of the front edge of the c-shaped treatment plan. A) initial normalized dose distribution extracted from TPS, B) iRAI reconstructed signal measured at the front edge of the initial radiation field, C) the contour plots of the dose and the iRAI images showing the 90%, 80%, 60%, and 40% contour isodose lines.

B. Arc Plan:

The gel measured arc plan that delivered dose continuously from 315^o to 45^o was modeled assuming the whole plan was delivered at a single linac pulse duration. The full 3D plan distribution was simulated and iRAI reconstructed images were compared with the dose distributions as shown in Figure 6.12. The agreement between the dose results and the iRAI distribution was within a 91% passing rate for the isodose curves of 30% maximum dose or higher using 7%/4mm gamma passing criteria. IRAI was capable of scoring the overall shape of the dose distribution with the highest agreement for the 50% or higher isodose lines of 95% passing rate for 7%/4mm gamma passing criteria. These higher passing rates compared to the c-shaped plan is due to the shape and the position of the maximum dose region of the plan, near the center of the array, showing a wider field of view, thus higher detectability.

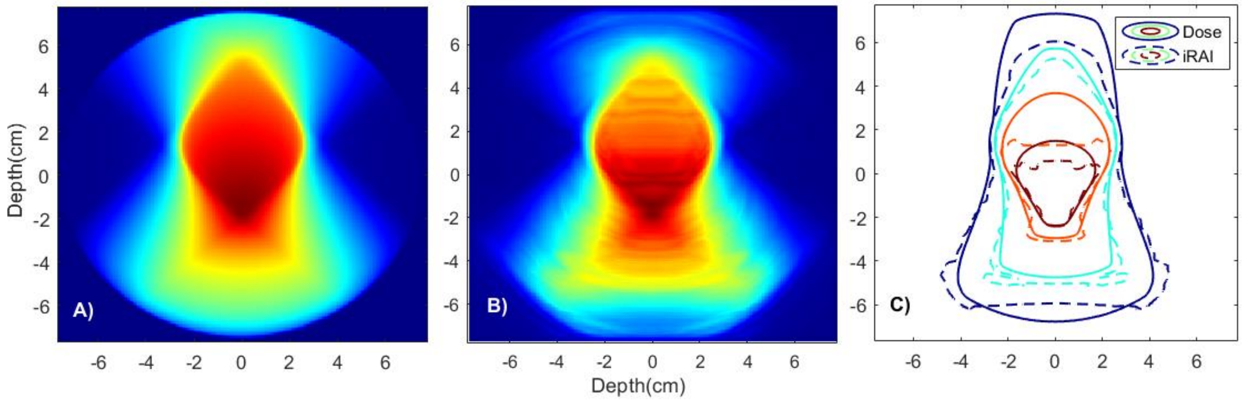

Figure 6.12: The simulation results of the front edge of the radiation field for the arc treatment plan. A) initial normalized dose distribution extracted from TPS, B) iRAI reconstructed image measured at the front edge of the initial radiation field, C) the contour plots of the dose and the iRAI images showing the 90%, 80%, 60% and 40% contour isodose lines.

C. Three Field Plan

Although the 3D conformal plan was consisting of three static radiation fields such that each radiation beam was delivered separately at different gantry angles: 330^o, 0^o, and 30^o, it was modeled as a single delivery plan per pulse to acquire iRAI images. The iRAI and dose results were plotted in Figure 6.13. The front edge of the radiation field dose and iRAI distributions showed an agreement of 87% gamma passing rates for the 7%/4mm gamma test criteria for isodose lines higher than 30%. The maximum dose region occurs toward the edge of the simulated phantom and the 2D array, hence the agreement for the isodose curves of 50% maximum dose was 86% showing lower detectability of the dose distribution due to the limited FOV of the different array elements.

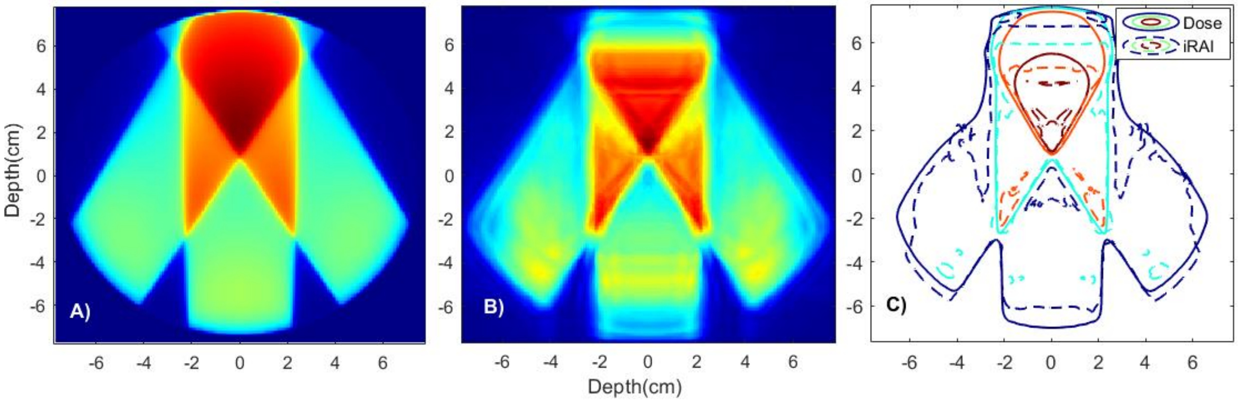

Figure 6.13: The simulation results of the front edge of the three-field treatment plan. A) initial normalized dose distribution extracted from TPS, B) iRAI reconstructed image measured at the front edge of the initial radiation field, C) the contour plots of the dose and the iRAI images showing the 90%, 80%, 60%, and 40% contour isodose lines.

The quantitative comparisons between the dose and the iRAI images extracted at the front edge of the radiation field for the different treatment plans are listed in Table 6.4 using different gamma passing criteria. The limited bandwidth of the transducer was the main cause of the differences between the dose and iRAI results. The shape of the treatment plan and the position of the maximum dose relative to the 2D array position was also affecting the resulted agreement between the dose and iRAI results. Since the high-frequency component is lost due to the limited bandwidth of the transducer, the details and sharpness of the boundaries were slightly lost. As the results indicated the arc plan showed the best detectability with iRAI, while the C-shape showed the lowest agreement due to the plan complexity as it consists of multi-fields with variant field sizes and incident angles.

Table 6.4: The gamma testing results of the simulated iRAI images in comparison to dose

Treatment Plan	**3D C-shaped**	**Arc**	**Three Field**
1%/1mm	58.1	64.5	57.8
3%/3mm	72.7	79.9	73.8
7%/4mm	80.5	90.5	87.0

6.3.2. Gelatin IRAI Measurement

In this part, different setup parameters were varied throughout the measurement in gelatin phantoms to test the generated acoustical signal and its strength in addition to testing the reconstructed iRAI images. The first tested setup parameter was the radiation field size effect. The two main radiation fields tested were 3 cm x 3 cm and 5 cm x 5 cm field sizes measured at the beam isocenter 100 cm from the linac source (~ 7.5 cm depth) inside the phantom center with a 92.5 cm SSD. The other tested setup parameter was the effect of the different SSDs on the generated signal strength and iRAI imaging. A 6 MV FFF radiation beam (1400 MU/min) as well as a 10 MV FFF energy beam (2400 MU/min) was used in those studies with a pulse duration of 4 µs and a pulse repetition rate of 300-330 Hz. The 10 MV FFF beam energy was used as the reference energy and the 5x5 cm^2 was the reference field at 7.5 cm depth in the phantom. The SNR was measured as the peak-to-peak ratio of the measured acoustic signal. Both the measured and the simulated iRAI signals were normalized to the corresponding results detected at the reference conditions. The dose per pulse was reported as the dose deposited per pulse at the reference depth of 7.5 cm in the phantom. The SNR was measured excluding the surface noise signal, which can easily be defined, from noise calculations.

A. The Effect of Beam Energy

The effect of beam energy on the resulting signal was characterized for the reference field of 5x5 cm^2 measured at the isocenter (SAD=100 cm) and 7.5 cm depth. The total delivered MUs were the same for the two tested fields of 6 MV FFF and 10 MV FFF. The reported values were normalized to the 10 MV FFF reference signal. The results are listed in Table 6.5. The fraction of the dose per pulse for the 6 MV FFF beam to the 10 MV FFF was 0.71 measured at the center of the phantom. Because the 10 MV FFF beam delivered a higher dose per pulse, the measured iRAI signal was also higher for the case of the 10 MV FFF field. The measured and the simulated iRAI signal was reported as the maximum intensity extracted from iRAI images. Because of the background noise and the sensitivity of the transducer, the measured relative iRAI signal was less than the simulated iRAI signal by 26%.

Table 6.5: The resulted effect of the photon beam energy on the reconstructed iRAI signal intensity

Beam Energy	**Dose Rate (MU/min)**	**Dose per Pulse mGy**	**Measured iRAI Signal**	**Simulated iRAI Signal**
6 MV FFF	1400	0.20	0.48	0.65
10 MV FFF	2400	0.28	1.00	1.00

B. The Effect of The Field Size

The effect of changing field size on the generated acoustical signal was characterized using two different field sizes (3x3 cm^2 and 5x5 cm^2) for the different 6FFF and 10FFF beam energies. For each beam energy, the results were normalized to the reference 5x5 cm^2 field at the depth of 7.5 cm in the phantom.

The effect of increasing field size was small which was reflected in the high agreement between the relative simulated iRAI signal despite the energy of the radiation beam as indicated in Table 6.6. However, the dose per pulse delivered by the 5 x 5 field was higher (0.28 mGy) than the 6FFF field (0.20 mGy). This was reflected by the higher detectability of the 10 FFF 3 x 3 field in comparison to the same field with the 6 FFF beam.

Table 6.6: The resulted effect of the photon beam size on the reconstructed iRAI signal

Field Size (cm^2)	**6 MV FFF**			**10 MV FFF**		
	Relative Dose per Pulse	**Measured iRAI Signal**	**Simulated iRAI Signal**	**Relative Dose per Pulse**	**Measured iRAI Signal**	**Simulated iRAI Signal**
3x3	0.96	0.66	0.92	0.95	0.79	0.93
5x5	1.00	1.0	1.0	1.00	1.0	1.0

C. The Effect of SSD on Signal Intensity

The effect of field size reduction as SSD decreased was compensated for by calculating the beam divergence, such that the measured field size at the center of the phantom, 7.5 cm depth, was 5x5 cm^2 for all of the tested SSDs. The only parameter that was affecting the dose was the inverse square law as the field size and depth of measurement were held constant. For both tested beam energies, as SSD decreases the deposited dose per pulse increases, and hence the generated acoustic signal intensity increases as listed in Table 6.7.

Table 6.7: The effect of the SSD and dose rate on the measured and simulated iRAI signal

SSD (cm)	**6 MV FFF**			**10 MV FFF**		
	Dose per Pulse	**Measured iRAI Signal**	**Simulated iRAI Signal**	**Dose per Pulse**	**Measured iRAI Signal**	**Simulated iRAI Signal**
93	0.20	1.0	1.0	0.28	1.0	1.00
80	0.28	1.24	1.27	0.40	1.69	1.2
65	0.51	2.11	2.12	0.75	1.99	1.86

D. The Effect of SSD on Field Size

The field size at the isocenter was held constant and equal to 5x5 cm^2 at 7.5 cm depth in the phantom. The feasibility of iRAI in measuring field size changes was measured at different SSDs and reported as FWHM and compared to the TPS-based values.

The ability of iRAI to measure the change in the axial radiation beam size was within 1 mm and 3.5 mm relative to the dose profiles for the simulated and measured iRAI data respectively. The effect of the array resolution was causing the difference between the measured and the simulated iRAI data.

Table 6.8: The effect of the SSD on the signal intensity and iRAI measured and simulated radiation field sizes

SSD (cm)	Dose Field Size (cm)	Measured iRAI Field Size (cm)	Simulated iRAI Field Size (cm)	Relative Dose per Pulse	Measured iRAI Signal	Simulated iRAI Signal
93	4.99	5.35	5.01	1.00	1.00	1.00
80	4.35	4.65	4.34	1.40	1.04	1.25
65	3.59	3.90	3.58	2.41	1.42	1.93

6.3.3. Gel IRAI Measurements

Because gels have comparable characteristics to those of gelatin phantoms tested in the previous section, the findings of the previous gelatin study were used to optimize the rest of the gel measurement setup parameters. The 3D dosimetric capability of iRAI acoustic images was compared with the 3D dose distributions measured with gels. The gel measurements were performed using the 10 MV FFF energy photon beam as it has a higher dose rate per pulse, hence achieving the best operatable SNR. Additionally, to improve the signal strength for higher quality imaging the SSD was kept closer to the linac head measuring better signal as practically achievable.

6.4. Static Beam Characterization

Single field plans were tested using different beam sizes of 2x2 cm^2, 3x4 cm^2, 4x3 cm^2 measured at 70 cm SSD and a 7.1x7.1 cm^2 field measured at 65 cm SSD. The 2D images of the front beam edge for each of the fields were plotted and compared to the dose distributions measured with gels. The resulting comparisons of gel and iRAI measured dose distributions for the different field sizes were plotted in Figure 6.14, Figure 6.15, Figure 6.16, and Figure 6.17. The quantitative comparisons of the data using different gamma test criteria and RMSE were listed in Table 6.9. IRAI resulting iRAI images for the 2x2 cm^2 field were blurry measuring a much higher beam size than expected, thus the agreement with the gel results was the worst among the tested radiation fields. This degradation in the imaging resolution of the iRAI imaging was due to the position of the radiation field relative to the 2D array transducer. The radiation field for this case was further than the effective detectability distance of the array transducer of 10 cm-20 cm.

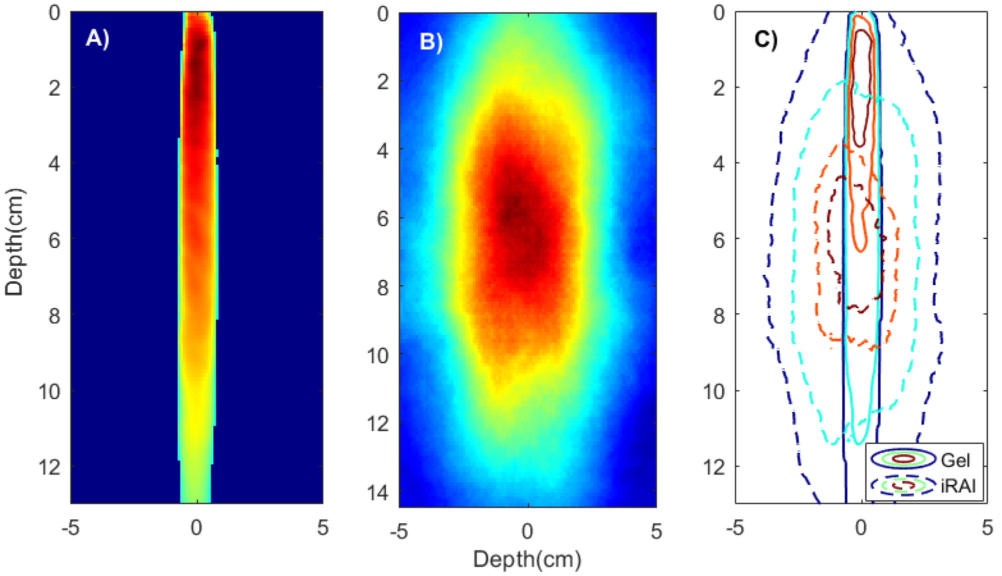

Figure 6.14: The measured iRAI and gel results for the $2x2cm^2$ field. A) showing the gel measured dose, B) iRAI measured dose, and C) isodose contour plots showing the 90%, 80%, 60% and 40% contour isodose lines for iRAI and gel results.

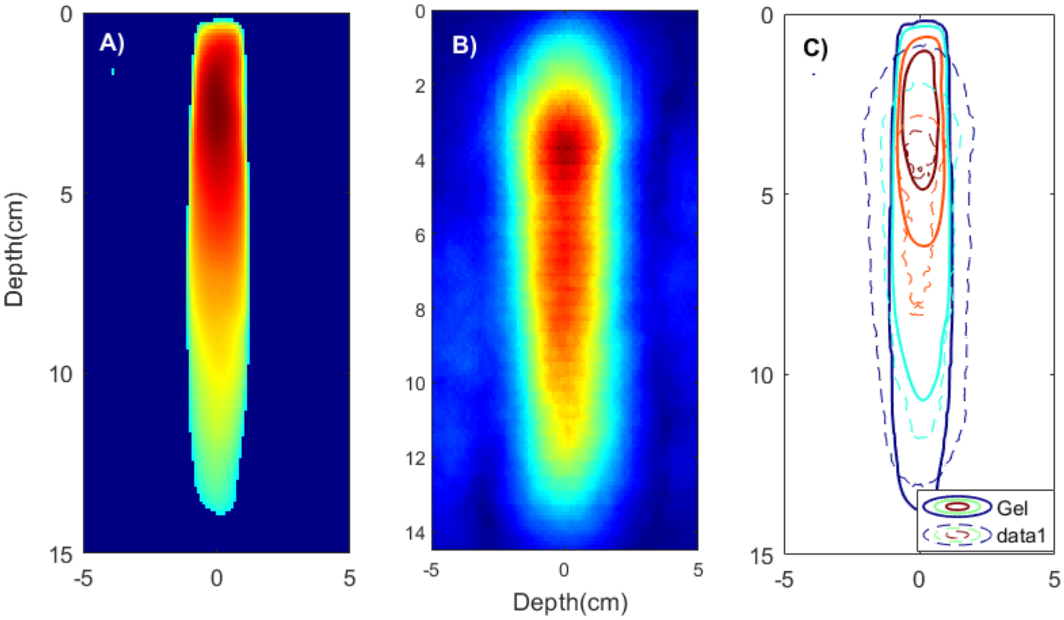

Figure 6.15: The measured iRAI and gel results for the 3x4 cm^2 field. A) showing the gel measured dose, B) iRAI measured dose, and C) isodose contour plots showing the 90%, 80%, 60% and 40% contour isodose lines for iRAI and gel results.

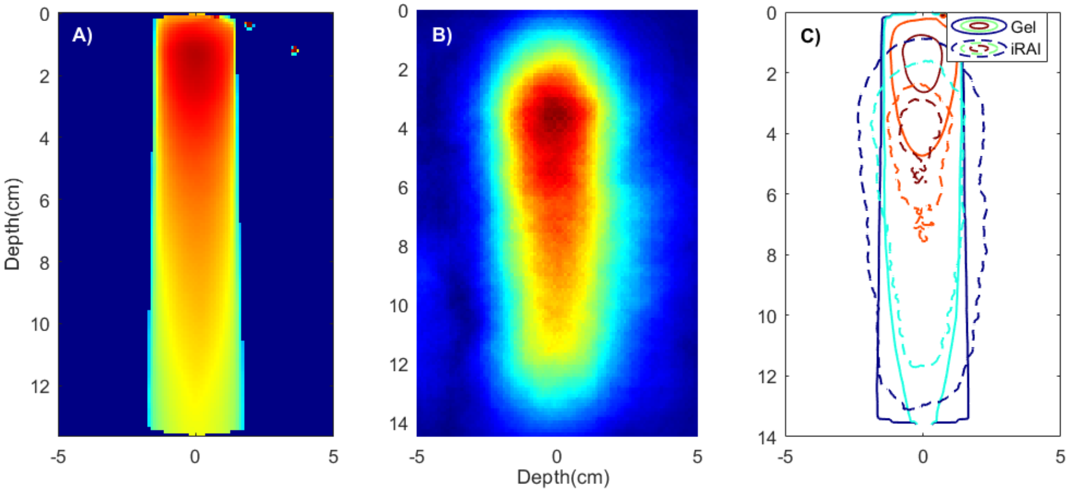

Figure 6.16: The measured iRAI and gel results for the 4x3 cm^2 field. A) showing the gel measured dose, B) iRAI measured dose, C) isodose contour plots showing the 90%, 80%, 60% and 40% contour isodose lines for iRAI and gel results.

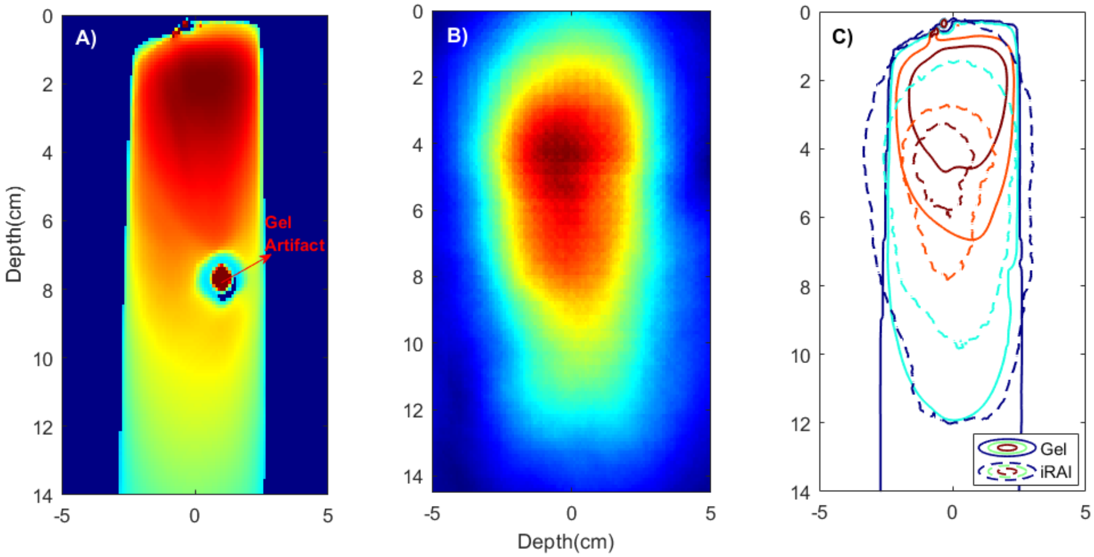

Figure 6.17: The measured iRAI and gel results for the 7.1x7.1 cm^2 field. A) showing the gel measured dose, B) iRAI measured dose, C) isodose contour plots showing the 90%, 80%, 60% and 40% contour isodose lines for iRAI and gel results.

Table 6.9: The gamma testing results and RMSE of the iRAI images comparison to gel measured dose

Static Field Size	**2x2 cm^2**	**3x4 cm^2**	**4x3 cm^2**	**7.1x7.1 cm^2**
1%/1mm	61.9	85.8	75.6	73.5
3%/3mm	61.9	86.5	75.7	74.4
7%/4mm	61.9	87.0	75.7	75.1
RMSE	0.405	0.157	0.322	0.279

The resolution of the reconstructed iRAI images was highly affected by the distance between the radiation field and the array transducer. Radiation fields measured at distances higher than 20 cm from the surface of the transducer showed a blurry and poor resolution image as shown in Figure 6.18. As a result, the agreement between the gel-generated images and the iRAI images was also affected and dropped from 87% gamma passing rate to 75.1% for the 7%/4mm gamma criteria. Overall, iRAI images showed good agreement with the gel measured static field distributions, within at least 75.1% passing rate for the 7%/4mm gamma criteria. However, there was a shift in the buildup region of the iRAI images. This effect has been reported previously in section 5.4.2.0 to be mainly due to the linac pulse duration effect in addition to the resolution and sensitivity effect of the 2D array transducer.

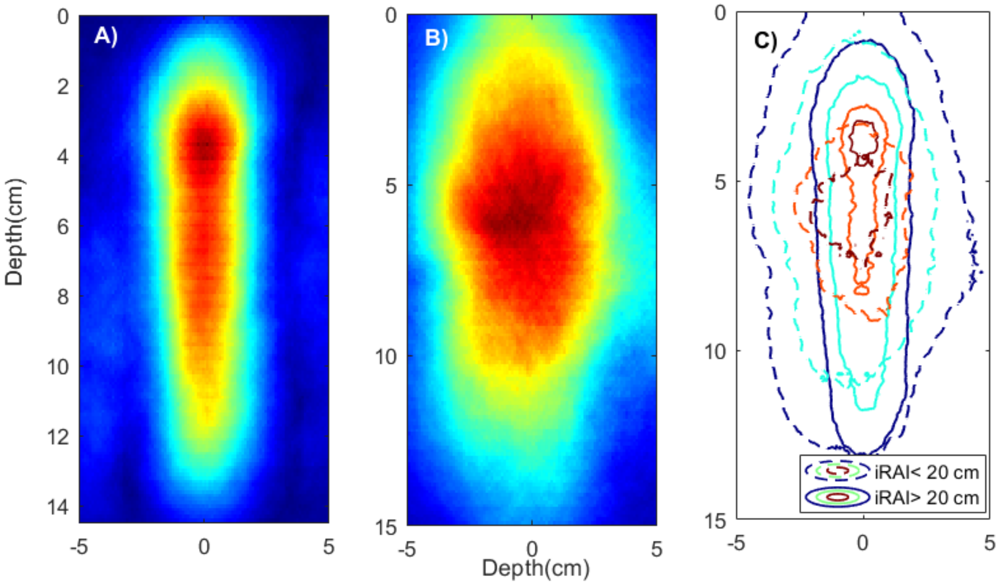

Figure 6.18: The effect of the position of the radiation field relative to the transducer on the quality of the iRAI result for the same radiation field of 3x4 cm^2. A) iRAI image of the field positioned less than 20 cm away from the transducer, B)) iRAI image of the field positioned further than 20 cm away from the transducer, C) isodose contour plots of the two different tested array to beam distances showing the 90%, 80%, 60% and 40% contour isodose lines for iRAI and gel results.

Signal Averaging Effect:

This part aimed to investigate the effect of the total dose deposited on the quality of the generated acoustic images expressed as the SNR. The total dose was proportional to the number of signal averages used to construct the acoustic images. The deposited dose is the dose delivered per pulse multiplied by the total number of delivered pulses as retrieved from the planning system. The SNR was reported as the ratio of the maximum signal to the maximum background noise measured at the center of the phantom, while the relative SNR was determined relative to the reference case of 50 averages. This effect was studied for two different field sizes of 4x3 cm^2 and 2x2 cm^2. The dose per pulse was extracted at the center of the gel phantom, 7.5 cm, and equals 1.54 mGy/pulse and

1.71 mGy/pulse for the 2x2 cm^2 and 4x3 cm^2 fields, respectively. The quality of the images increased with increasing the number of signal averages resulting in well-defined radiation field edges as shown in Figure 6.19. As Table 6.10 shows, the SNR increased as the number of signal averages (pulses) increased. The highest improvement in the SNR occurred for 300 averages in the case of the 4x3 cm^2 field which corresponded to 0.51 Gy. While the highest change in the SNR for the 2x2 cm^2 field occurred at 500 averages corresponding to 0.77 Gy at the center of the phantom. This difference between the two fields was due to the differences in the dose per pulse deposition as the 2x2 cm^2 dose per pulse is 10% less than that of the 4x3 cm^2. The higher the dose deposition per pulse the stronger the generated iRAI signal, which means fewer signal averaging requirements.

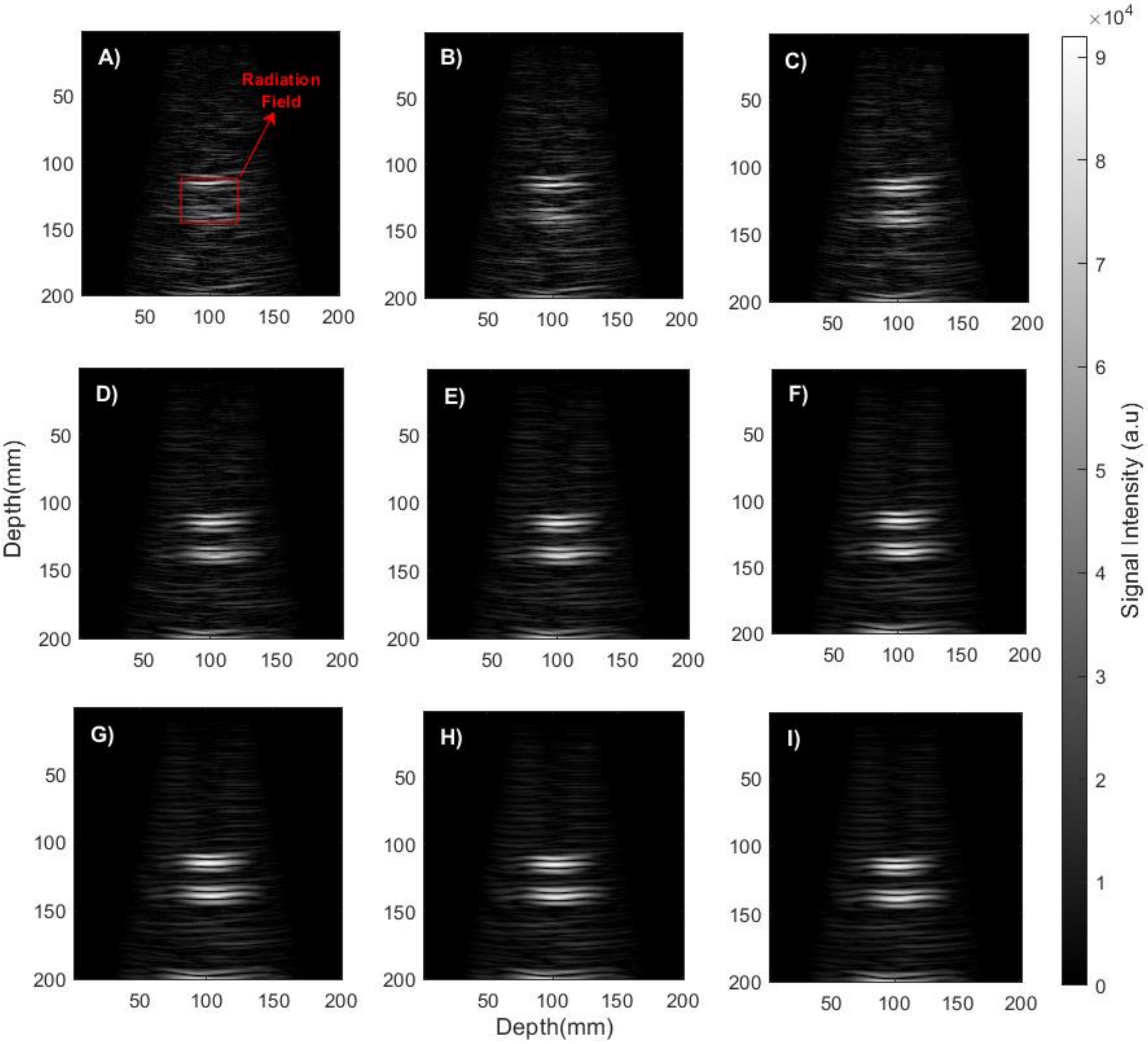

Figure 6.19: The signal averaging effect on the quality of the image and the beam edges detectability of the 4x3 cm^2 static field constructed using A) 50, B) 100, C)150, D)300, E)500, F)750, G)1000, H) 1500, I) 2000 Averages.

Table 6.10: The SNR of the iRAI constructed images based on the number of averages.

Number of Averages (N)	2x2 cm^2 Field			4x3 cm^2 Field		
	Dose (Gy)	SNR	Relative SNR	Dose (Gy)	SNR	Relative SNR
50	0.08	1.61	1.00	0.09	1.55	1.00
100	0.15	1.92	1.19	0.17	1.86	1.20
150	0.23	1.87	1.16	0.26	2.43	1.57
300	0.46	1.88	1.17	0.51	2.64	1.71
500	0.77	2.03	1.26	0.86	2.66	1.72
750	1.15	2.04	1.27	1.28	2.73	1.77
1000	1.54	2.21	1.37	1.71	2.81	1.81
1500	2.31	2.28	1.41	2.57	2.87	1.86
2000	3.08	2.30	1.43	3.42	2.91	1.88

Measurement Repeatability:

The measurement repeatability was performed using the same setup and same jar coupling while repeating the dose delivery and the detection of the generated acoustic signal in three times, trials. The repeatability of iRAI was quantified by comparing the SNR variability between the trials for two different static fields; 2x2 cm^2 and 4x3 cm^2. The 2D array measured average acoustic signal for the 4x3 cm^2 field was plotted in Figure 6.20.A. While the iRAI reconstructed radiation beam edges and profile were extracted at the center of the phantom and were shown in Figure 6.20.B, C.

The SNR quantified as the peak-to-peak ratio for the 4x3 cm^2 and the 2x2 cm^2 field were 2.14±0.23 and 1.93±0.26 respectively. The 2D iRAI distributions among the three trials agreed within 100% passing rate for the 7%/4mm and the 3%/3mm gamma test for the 4x3 cm^2 field. While the passing rates for the 2x2 cm^2 fields were 99.9% and 99.3% respectively.

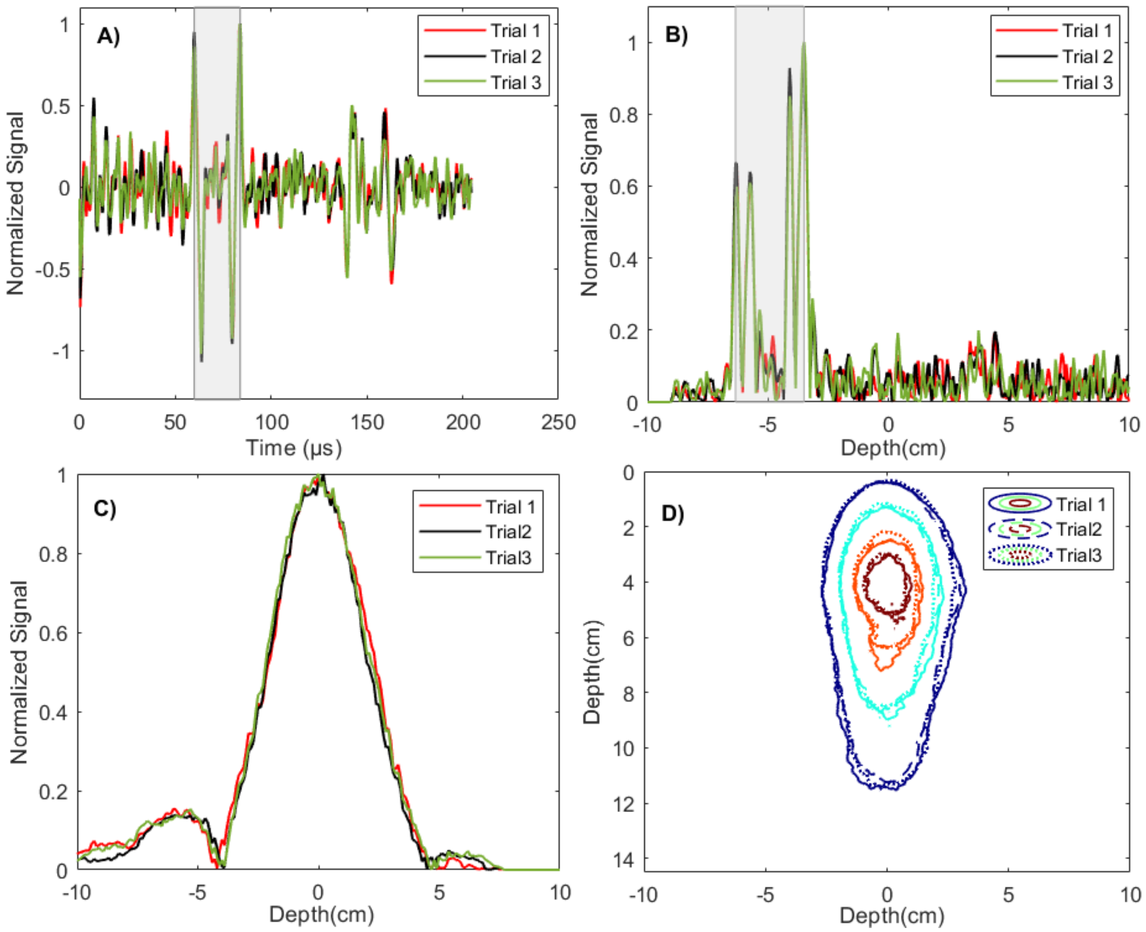

Figure 6.20: A) Average transducer measured acoustic signal and the profiles extracted at the front edge of the field (maximum signal) extracted at the center of the phantom for a 4x3 cm^2 field, B) the horizontal (lateral) beam profile, C) vertical (axial) beam profiles, D) 2D dose distributions measured with the 2D array showing the 90%, 80%, 60%, and 40% contour isodose lines.

Beam Localization:

The ability of iRAI to detect the spatial position of the radiation field was tested using three different trials of a 5x5 cm^2 field. The position of the radiation field was shifted by 2.5 cm from the first trial position and kept the same for the other two trials. The resulting iRAI images are shown in Figure 6.21, where the red square represented the radiation field. The ability of iRAI to detect this introduced shift was determined within a 3 mm relative spatial difference in comparison to the gel data. This 3 mm spatial difference approximately was closer to the measured axial spatial resolution of the 2D array of 4 mm. The front edge of the field in the first trial, Figure 6.21.A., was slightly weaker than the corresponding edge of the other two trials as the field was delivered away from the transducer. Typically, the intensity of the front edge of the radiation field as shown in the reconstructed iRAI images was weaker than the back edge with the back edge of the radiation field being more intense and well-defined. The reason for this is that the contribution of each of the transducer elements to the reconstruction is higher for the back edge due to the larger field of view (FOV) of the array elements. Hence, the detectability of the back edge of the field is better compared to the front edge where the FOV of the elements was less.

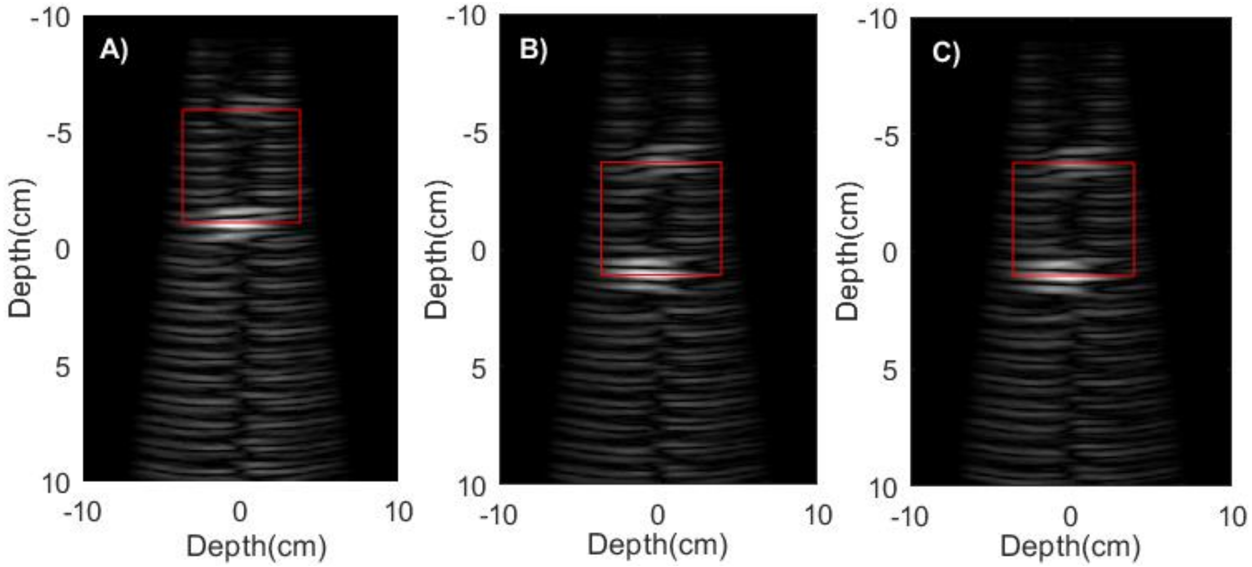

Figure 6.21: The effect of the beam localization and beam shift of the 5x5 cm^2 field on the iRAI reconstructed images of the front edge of the radiation field for three different trials A), B), and C). The actual radiation field was represented as a red square.

6.5. IRAI for Treatment Planning Verification

The ability of iRAI for 3D imaging and thus its implementation as a 3D relative dosimetry tool was tested using the same gel tested and iRAI simulated 3D conformal treatment plans: the C-shape plan, the arc beam, and the three-field plan.

A. 3D Conformal C-shaped Plan:

The simulated C-shaped 3D conformal treatment plan consisting of 23 static beams was delivered to the gel jar phantom. The resulted acoustical signal was measured to reconstruct iRAI images. IRAI results were compared with the dose distributions measured with the gels as shown in Figure

6.22. The deposition of the treatment plan radiation beams was measured in time and the resulted iRAI images were constructed every 3 seconds until the whole plan was delivered as shown in Figure 6.23. Figure 6.23.A. shows the relative amount of dose deposited at each 3 seconds time interval and the position of the treatment beam while Figure 6.23.B. shows the accumulation of the dose with time. IRAI reconstructed images showed the dose deposition at each three seconds time interval and its contribution to the total deposited plan dose. The agreement of iRAI images with the gel results was within 78.9 % passing rate for the 7%/4mm gamma test for isodose curves of 40% maximum dose or higher. The highest agreement was for the 80% isodose lines as they are at the center of the 2D array showing higher detectability. The resolution of the 2D array and the bandwidth affects the edge detectability of the plan. The resulted gamma passing rate of the 7%/4mm gamma test was comparable with the simulation-based result of an 80.5% passing rate.

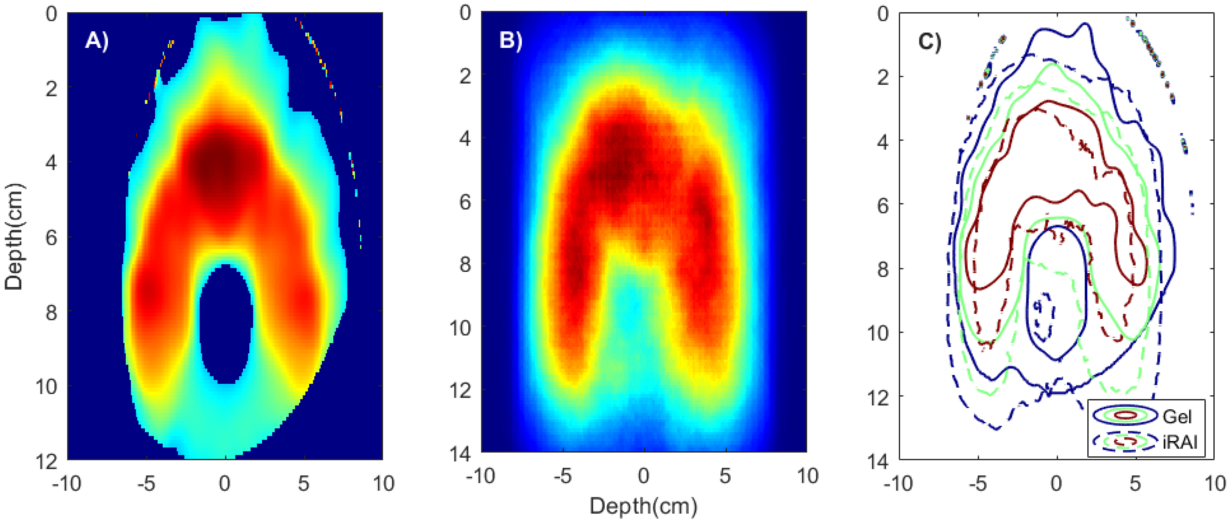

Figure 6.22: The resulted C-shape plan delivered to the gel phantom. A) the gel measured dose distribution, B) iRAI measured distribution, C) the contour plots of the dose and the iRAI images showing the 80%, 60%, and 40% contour isodose lines.

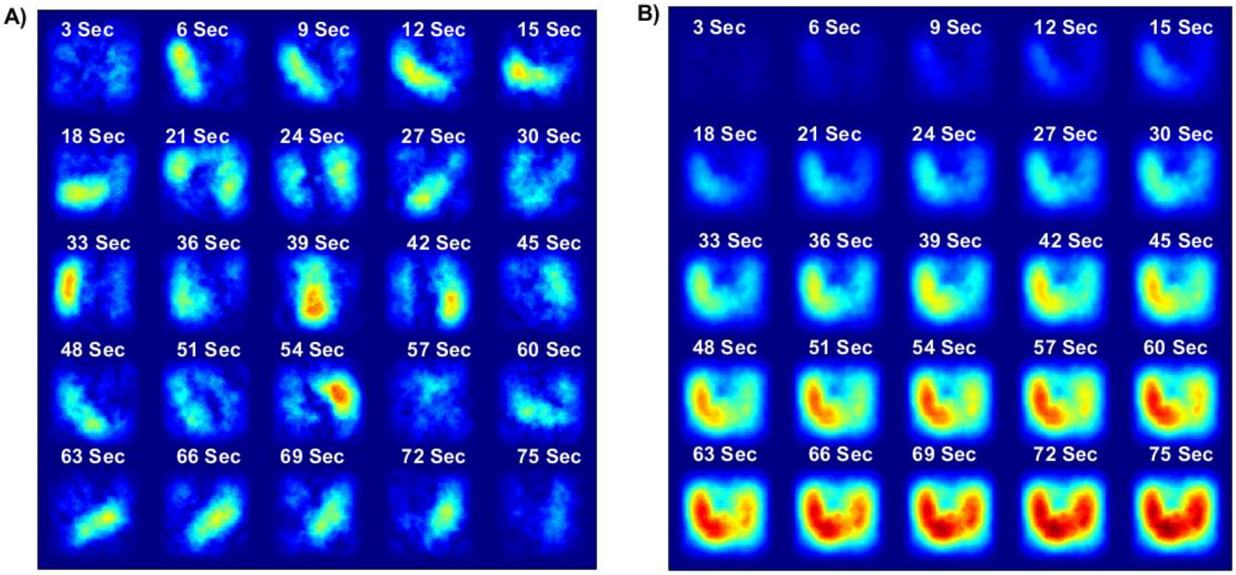

Figure 6.23: iRAI reconstructed images with time for the C-shape plan. A) shows the position of the beam at each time interval of 3 seconds and the fraction of the dose delivered. B) shows the accumulation of the planned dose with time until the full plan was delivered.

B. Arc Plan

The arc beam was delivered continuously from 315° to 45° gantry angle to the gel jar phantom. The resulted acoustical signal was measured to reconstruct iRAI images that were compared to the gel measured dose distribution. The position of the plan radiation beams was measured every 3 seconds based on the measured iRAI signal as shown in Figure 6.24.A. The relative position of the reconstructed radiation field reflects the position of the linac gantry and the angle at which the radiation field hit the phantom. Figure 6.24.B. shows the accumulation of the dose with time such that iRAI reconstructed image intensity reflected the dose deposition at each three seconds time interval and its contribution to the total deposited plan dose. The fully delivered plan is shown in Figure 6.25 with an 84.4% passing rate for the 7%/4mm gamma test for isodose curves of 40% maximum dose or higher. As the higher dose region of the plan was delivered to the center of the phantom, the 2D array showed higher detectability and hence better iRAI image reconstruction. The resolution of the transducer and the limited bandwidth are the key factors that affect the agreement specifically at the edges of the plan. The resulted gamma passing rate of the 7%/4mm gamma test was comparable with the simulation-based result of 90.5% passing rate given that the resolution and the sensitivity of the array was not accounted for in the simulation results.

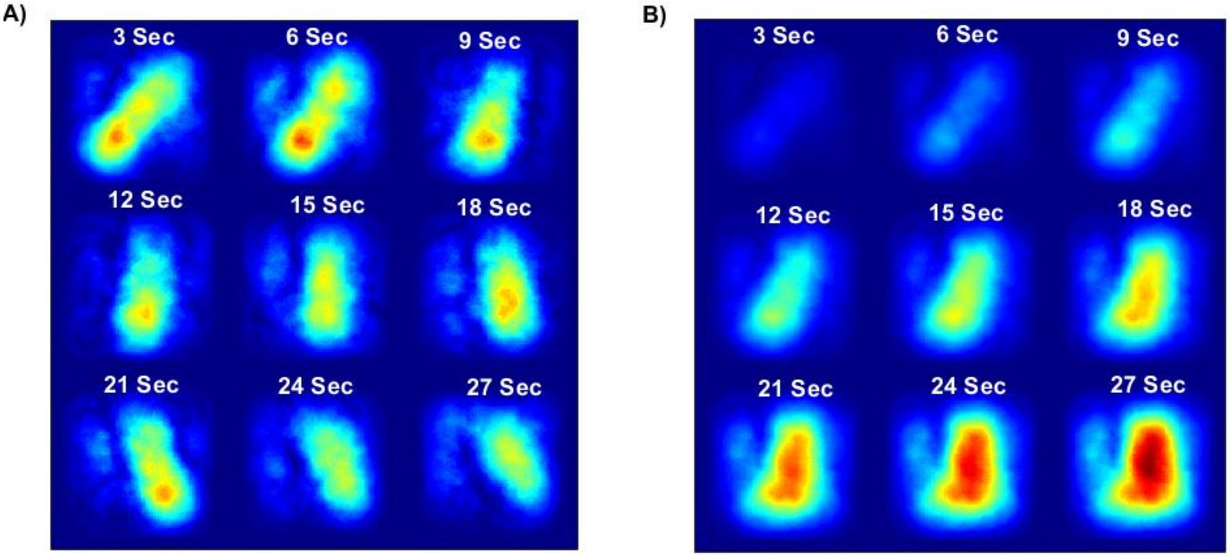

Figure 6.24: iRAI reconstructed images with time for an arc plan. A) shows the position of beam at each time interval of 3 seconds and the fraction of the dose delivered. B) shows the accumulation of the planned dose with time till delivering the whole plan

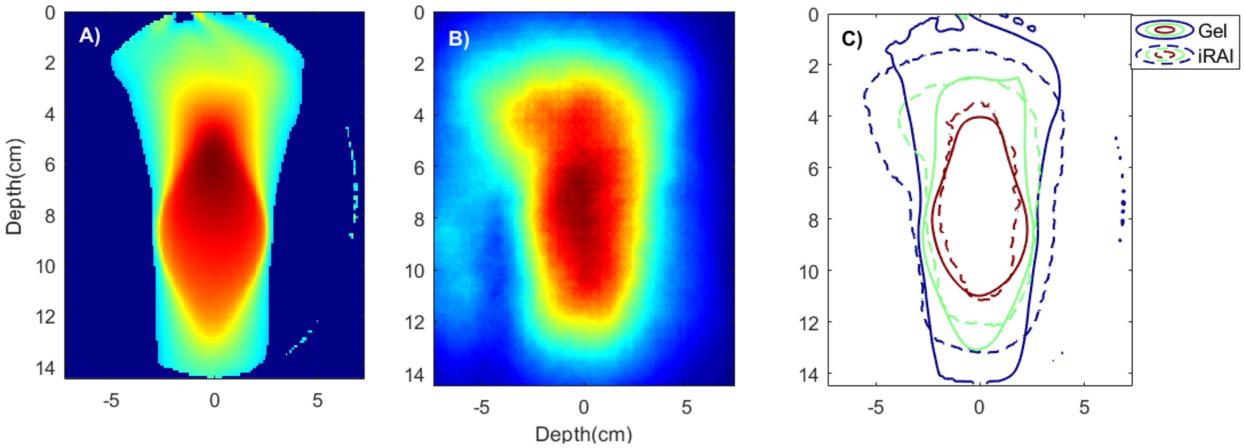

Figure 6.25: The resulted arc plan delivered to the gel phantom. A) the gel measured dose distribution, B) iRAI measured distribution, C) the contour plots of the dose and the iRAI images showing the 80%, 60%, and 40% contour isodose lines.

C. Three-Field Plan

The three-field plan as its name indicates was delivered as the combination of three different plans approaching at different gantry angles of 330°, 0°, and 30° to the gel jar phantom. The generated acoustical signal at each 3 seconds time interval was measured to reconstruct iRAI images. The position of the plan radiation beams and the relative delivered dose are shown in Figure 6.26 A while Figure 6.26 B shows the accumulation of the treatment dose within each time interval. The total plan delivered to the gel phantom was measured with iRAI and compared to the gel measured distribution in Figure 6.27. The agreement between the gel and iRAI measured results was as low as 47.9% passing rate for the 7%/4mm gamma test for isodose curves of 40% maximum dose or higher while simulation results expected an agreement of 87%. Many effects have contributed to this high disagreement between the iRAI and gel measured results mainly the shape of the field as the high dose region was closer to the bottom edge of the gel jar. Because the plan was delivered away from the 2D array center the detectability of the array was low due to the limited view of the transducer elements resulting in low SNR and more reflections. The resolution, sensitivity of the array, and the noise effect were not accounted for in the simulated results which explains the higher agreement and detectability of the delivered dose compared to the experimentally measured results.

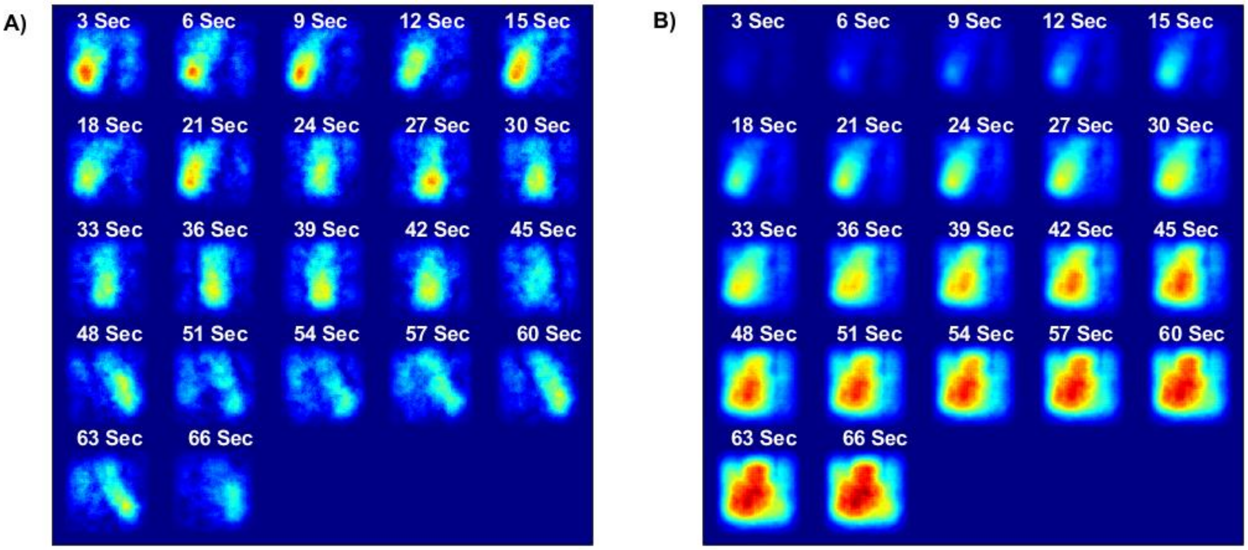

Figure 6.26: iRAI reconstructed images with time for the three-field plan. A) shows the position of beam at each time interval of 3 seconds and the fraction of the dose delivered. B) shows the accumulation of the plan dose with time till the whole treatment plan was delivered.

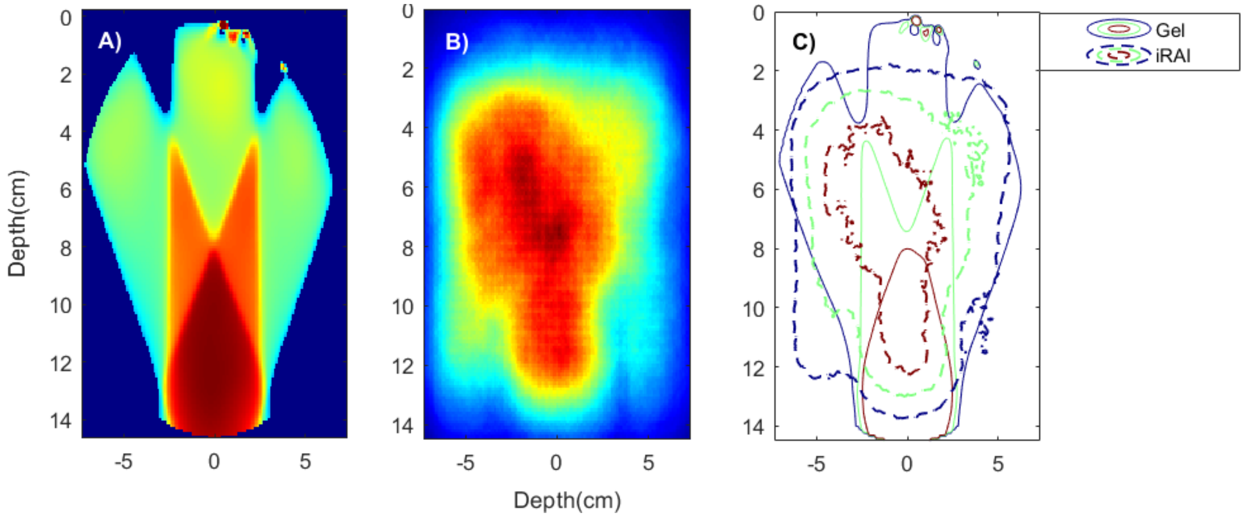

Figure 6.27: The resulted three-field plan delivered to the gel phantom. A) the gel measured dose distribution, B) iRAI measured distribution, C) the contour plots of the dose and the iRAI images showing the 80%, 60% and 40% contour isodose lines.

The results of the quantitative comparisons between gel and iRAI measured distributions are listed in Table 6.11. The arc treatment plan showed the best agreement with the gel measured results as expected from the simulation results. The shape of the delivered radiation treatment plan, the total dose deposited per pulse, which is directly proportional to the generated iRAI signal, and the distance between the array and the treatment plan are the main factors that affect the quality of the reconstructed iRAI images. The stronger the SNR, the better the detectability of the signal and the better the image quality.

Table 6.11: The gamma testing results and RMSE of the iRAI images compared to gel measured dose

Treatment Plan	**3D C-shaped**	**Arc**	**Three Field**
1%/1mm	75.0	62.3	47.9
3%/3mm	77.2	75.1	47.9
7%/4mm	78.9	84.8	47.9
RMSE	0.203	0.179	0.494

The repeatability of iRAI in quantifying the delivered treatment plans was also tested for the arc treatment plan. The variability between the three different trials delivered at the same setup to the same gel jar, as well as the repeatability of delivering the same treatment to a different jar with a different setup was measured. The five different trials were plotted in Figure 6.28. Each trial was compared to the gel data and the resulted dose-area histograms (DAH) were plotted in Figure 6.29 and Figure 6.29 for the different trials. The variability between the DAH was low. However, the first three trials acquired at the same gel jar and same setup showed better agreement with the gel measured data than the other two trials acquired at a different setup as listed in Table 6.12. The two trials were measured and compared to a different gel jar, which was previously irradiated and was measured at a different beam to transducer distance. The differences in the coupling and setup have contributed to the resulting effects on the image quality. However, the average RMSE for all trials was 0.173±0.005 with a 2.8% standard deviation between the different trials.

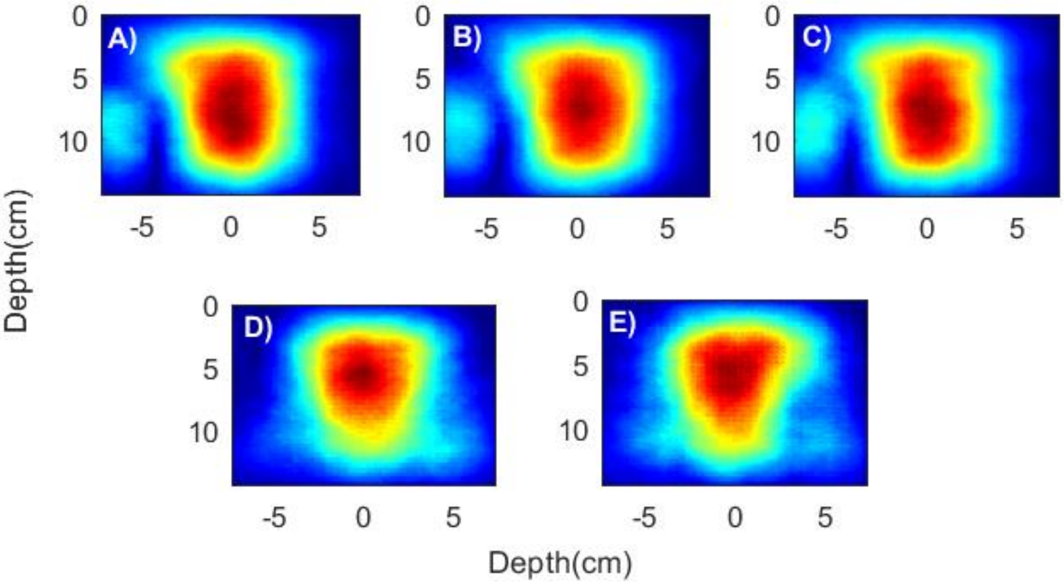

Figure 6.28: The repeatability of iRAI measuring the same arc plan delivered to two different jars with a different setup. A),B) C) different trials measured at the same gel jar with the same setup, D), E) different measurement trials measured with a different gel jar such that both trials were measured at the same setup.

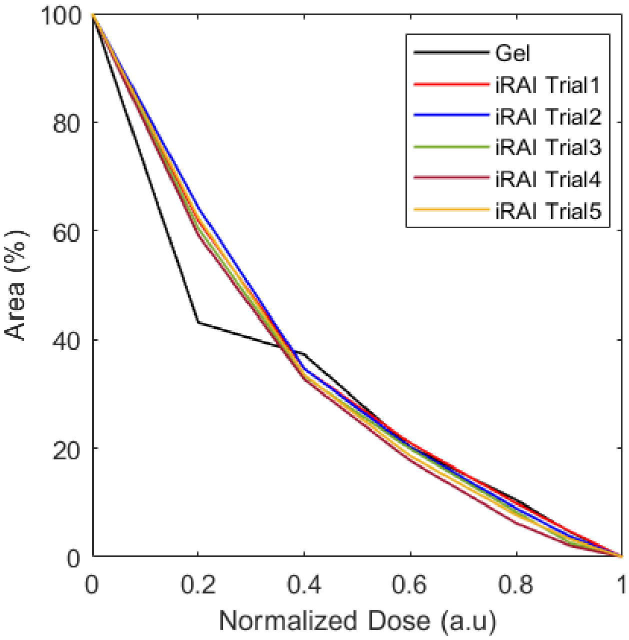

Figure 6.29: DAH of the different trials compared to the gel measured DAH.

Table 6.12: Gamma test passing rates of the different trials compared to the gel measured data of the arc plan

Treatment Plan	Trial 1	Trial 2	Trial 3	Trial 4	Trial 5
1%/1mm	63.6	64.4	64.1	62.2	61.8
3%/3mm	76.7	78.9	77.0	71.2	70.5
7%/4mm	87.2	88.3	84.8	79.1	77.4
RMSE	0.166	0.169	0.178	0.178	0.173

6.6. Conclusions

The spherical nature of the radiation-induced acoustical signal and its ability to measure the dose on a per pulse basis with a linear dose-signal response are the key features for its implementation as a 3D relative dosimetry tool. The implementation of iRAI in conventional radiation therapy real-time dosimetry was tested using different treatment plans and experimental setups in gel and gelatin phantoms. The effect of the beam energy, field size, and the dose per pulse (dose rate) on the generated iRAI signals were measured and compared to the simulation results. iRAI has measured higher SNR and signal intensity with a higher dose per pulse deposition. The considerably low SNR of this technique due to the low dose per pulse deposition in conventional radiation therapy was the main cause of the degradation in the image quality. However, iRAI was capable of measuring the position of the radiation beam with time within an axial resolution of approximately 0.35 cm. The agreement between the gel measured and the dose measured results were within an 84.8% passing rate for the 7%/4mm gamma test for the arc plan. The detectability and the agreement between the gel and iRAI measured results were highly affected by the lower SNR. Although gels are tissue equivalent, they have different acoustic characteristics than liver. Testing different phantoms such as lard, which has a much higher Grüneisen coefficient that is comparable to the fatty nature of the liver will generate much stronger acoustic signals. The stronger SNR will ensure a better iRAI imaging quality, which mimics the applicability of iRAI in testing different experimental clinical setups for liver treatments. A gel-lipid emulsion might prove useful if light attenuation can be made acceptable.

Chapter 7

Small Organic Scintillators for Photon Dosimetry

This chapter discusses the novel use of organic scintillators for dose measurement in a mixed source environment as a monitoring dosimeter to measure the personal and the ambient dose equivalent. Both stilbenes and organic glass scintillators (OGS) are nearly tissue equivalent; Zeff and density are comparable to soft tissue. Additionally, they have pulse-shape discrimination (PSD) capability to differentiate neutron events from photon events.

This work aims to verify experimentally and through simulations, the feasibility of small-sized stilbene and OGS detectors for measuring the photon dose equivalent to the personnel from point sources and research accelerator (M-9 Linatron) for radiation protection applications. The measured results were compared with the dosimetric results obtained from commonly used photon dosimeters (ionization chamber). This work also studied the effect of the detector size on the total measured dose through simulations. The work of this chapter is to be published.

7.1. Introduction

Radiation dose monitoring and whole-body dose assessment are essential aspects of radiation protection and safety in the different fields that involve radiation including medicine, research, and industrial facilities. Controlling the total dose exposure to the workers is achieved through measuring and monitoring the personal and ambient dose equivalent.

The commonly used devices for photon and neutron dose measurement are ionization chambers and remcounter meter. Each of those detectors is radiation type-specific, so it is blind to the other type of radiation. Other dosimeters that are of a dual nature to measure both photons and neutrons are available; however, their practical applicability is limited due to limitations including the array structure, multi-cell geometry, the complications of the calibration requirements, as well as the reported variability of the neutron range sensitivity [120].

Radiation interacts in organic scintillators through scattering and depositing energy to an atomic electron for photon radiation or to hydrogen nuclei (protons) or carbon nuclei for neutron radiation. The resulted energy depositions are then directly measured and observed as visible light in the scintillator. The dose equivalent measurement method relies on the known relation between the biological effectiveness and linear energy transfer (LET); thus, it does not require spectral unfolding. Additionally, the calibration and the range sensitivity are straightforward and are acquired using isotropic sources.

One of the main advantages of the organic scintillators is their characteristics that are comparable to soft tissue (Table 7.1), hence, they show potential for implementation in personnel and ambient equivalent dose measurements. Additionally, organic scintillators have pulse shape discrimination (PSD) capability, which makes them promising dosimeters for dose monitoring in mixed radiation (photon/neutron) fields. As a result, a single detector can be used for measuring doses instead of using multiple devices. Previous work has studied the potential of 5.08 cm diameter stilbene crystals as a dual dosimeter for mixed lab sources [121]. The study tested the applicability of the method for isotopic photon and neutron sources. The method was within 4% of simulated truth for photon sources. While the agreement with the fission spectrum neutron dose rates was within 21%. The measurement with stilbene was in better agreement with the simulated truth than the traditionally used instruments used in the study; the ionization chamber and the remcounter. The size of the detector has been shown to affect the accuracy of the deposited dose, thus affecting the measured dose. The study concluded that large-sized detectors measure higher neutron doses because of multiple scattering. A correction is needed to correct for the larger detector depth. The study recommended to perform Mote Carlo simulations to predict the optimal detector depth based on the expected neutron energies of the radiation source [122].

In this work, the applicability of the equivalent dose method was tested using small-sized organic scintillators including stilbenes and OGS. The applicability of those small-sized detectors in the radiation therapy environment for high-energy polyenergetic photon sources was investigated. The smaller detectors have the expected advantage of reducing the pileup events due to the high photon-flux nature in the linac-based radiation environment in oppose to the larger detectors. Additionally, the 0.6 cm cube, small-sized, detectors will be more compatible with the single-scatter approximation for neutron dosimetry measurements.

Table 7.1: Organic scintillators (Stilbene, OGS) characteristics comparisons with ICRP soft tissue properties.

	Stilbene	**Organic Glass Scintillator (OGS)**	**ICRP Soft Tissue**
Density (g/cm^3)	1.15	1.096	1.00
Material composition	C14H12	C42H36Si	A mixture of H, C, N, O (main component) w/ traces of Na, Mg, P, S, Cl, K, Ca, Fe, and Zn
Effective Atomic Number [123]	3.7	3.8	3.4
Hydrogen Content (wt%)	6.71	6.38	10.45 [124]

7.2. Theory

The theory behind using the organic scintillators for dose equivalent measurement was reported previously in the literature [121], [125]. The measured light output by the organic scintillators and its characteristics are used to determine the photon and neutron energy depositions into the detector. The size of the detector and the total energy deposition per each radiation type (photons/neutrons) is used to measure the total absorbed dose as follows:

$$D = \frac{E_{dep}}{m_{\det}}, \tag{7-1}$$

where D is the absorbed dose in the medium (detector), measured by normalizing the total energy deposited E_{dep} in the detector to the detector mass, m_{det}. The linear energy transfer (LET) dependent biological effectiveness factor is then used to determine the dose equivalent (H) using the relation:

$$H(r) = \int_L D(L,r) Q(L) dL \, , \qquad (7\text{-}2)$$

where, H(r) is the dose equivalent distribution at a coordinate r in the medium (detector), D(L,r) is the absorbed dose distribution over the radiation specific linear energy transfer (L) at the point r, and Q(L) is the quality factor as a function of LET, radiation type. The dose equivalent considers the biological effectiveness of the radiation as different types of radiation causes different biological effects (damaging cells) than others based on their quality. The quality of radiation is determined through weighting the energy deposition based on the energy and the type of radiation. The quality factor values used in this work are the ones reported in the ICRP Publication 26 [126]. The focus of this chapter is to measure the photon dose from both point gamma sources and linac-based radiation (mixed radiation environment). Because the range of the detected photons in this work is less than 10 MeV. All detectable photons in this range have a LET of 10 keV/µm or less, hence resulting in a constant Q(L) of unity. On the other hand, the quality of the neutron radiation is based on neutron energy deposition through the recoil proton energy to LET conversion relationship. The proton energy LET which resembles the neutron energy deposition is then used to determine the quality factor Q(L) [127]. The theory of dose equivalent measurements with organic scintillators are summarized in Figure 7.1.

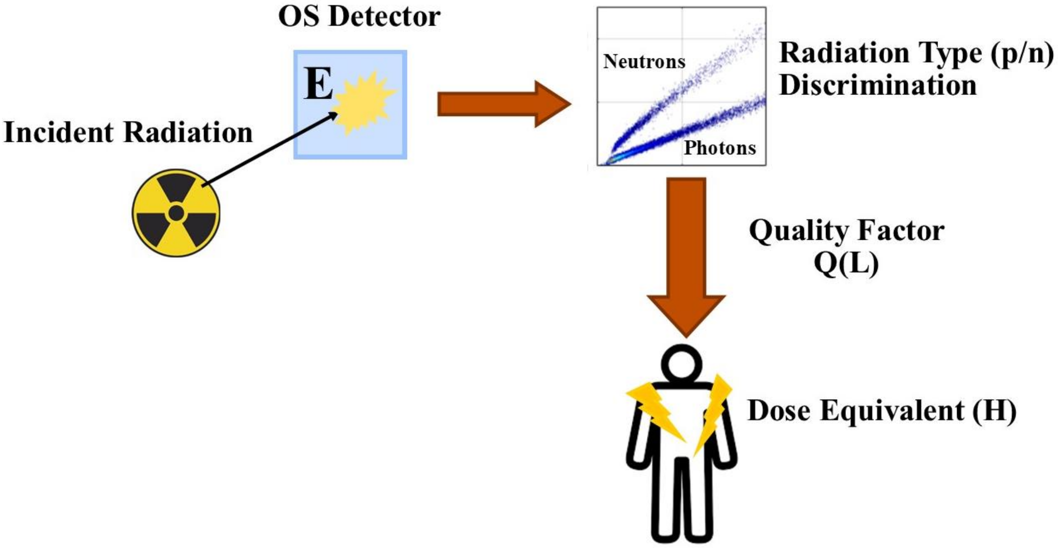

Figure 7.1: a schematic plot showing the theory behind implementing organic scintillators for dose measurements.

7.3. Isotopic Gamma Sources Experiments:

To test the applicability of small organic scintillators for dosimetric application; two different detectors; 0.6 cm stilbene and OGS cubes were used. The crystals were coupled to 2.54 cm PMTs and data were collected using a CAEN V8004B Waveform digitizer with 14-bit amplitude resolution and 500 MHz sampling rate. A light output threshold of 28.2 keVee, which corresponds to a photon energy of 28.2 keV was applied to stilbenes and a 24.1 keVee threshold, 24.1 keVee, was applied to OGS to eliminate noise contribution to the spectrum while allowing for adequate low photon energy measurement. The differences in the thresholds used for stilbene and OGS detectors are due to the differences in the operational voltages of each of the detectors, which were 870 V and 915V respectively.

Various isotopic sources were used at different source to detector distances (SSD) to cover different energy ranges and dose rates (Figure 7.2). The detected sources are an 86.46 μCi Cs-137, a 19.25 μCi Na-22 source, and a 47.05 μCi Co-60 source. Different source to detector distances of 10 cm, 20 cm, and 30 cm were used. Measurement of at least 10 minutes was performed to allow for adequate counts based on the source strength and source to detector distance. The results are compared to the Fluke ionization chamber measurement, which has a sensitivity range of 20 keV-2 MeV [128]. Sample pulses measured with each detector are shown in Figure 7.3. OGS measured pulses have a slightly higher falling edge compared to stilbene. The dose was measured based on the total pulse integral of each pulse. The calibration factor was calculated based on the Cs-137 Compton edge as shown in Figure 7.4. The smaller difference in the energy threshold between OGS and stilbene resulted in higher counts for the lower energy region of the OGS pulse integral spectrum. However, with applying the correction factor both spectrums overlap as presented in Figure 7.4. B. The calibration factor was measured to be 0.19 MeV/V*ns and 0.21 MeV/V*ns for stilbene and OGS, respectively. The calibration factor was then used for all the performed measurements assuming energy linearity for organic scintillators.

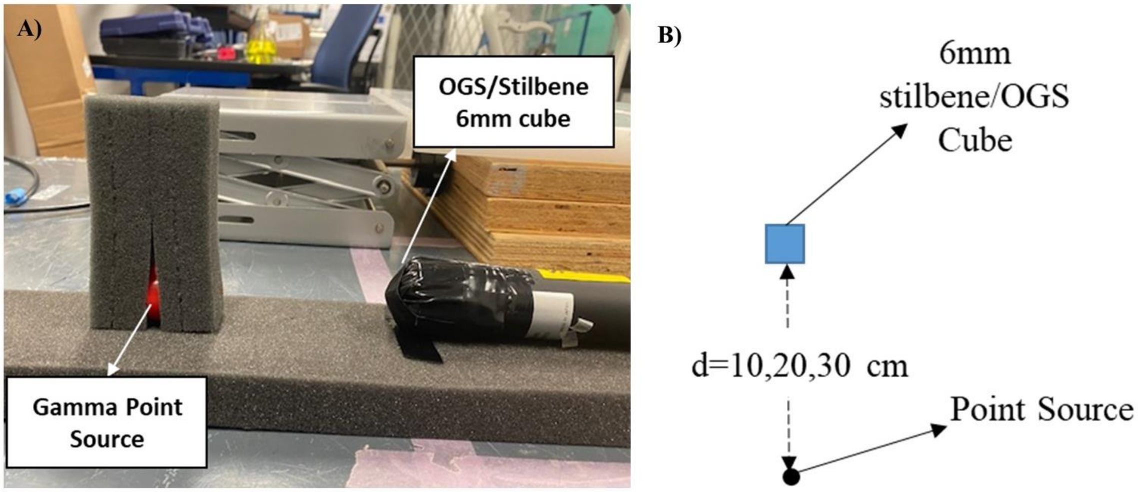

Figure 7.2: The experimental setup of the gamma source measurement, A) shows the actual experiment setup, B) is the schematic plot of the simulated experiment.

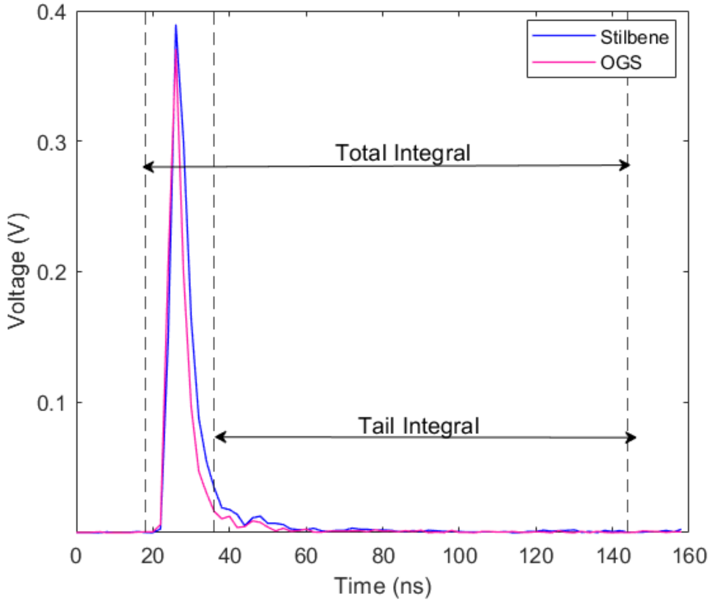

Figure 7.3: Sample pulses from OGS, stilbene cubes labeling the pulse total, and tail integrals used for analysis. OGS pulse has a faster falling edge compared to stilbene

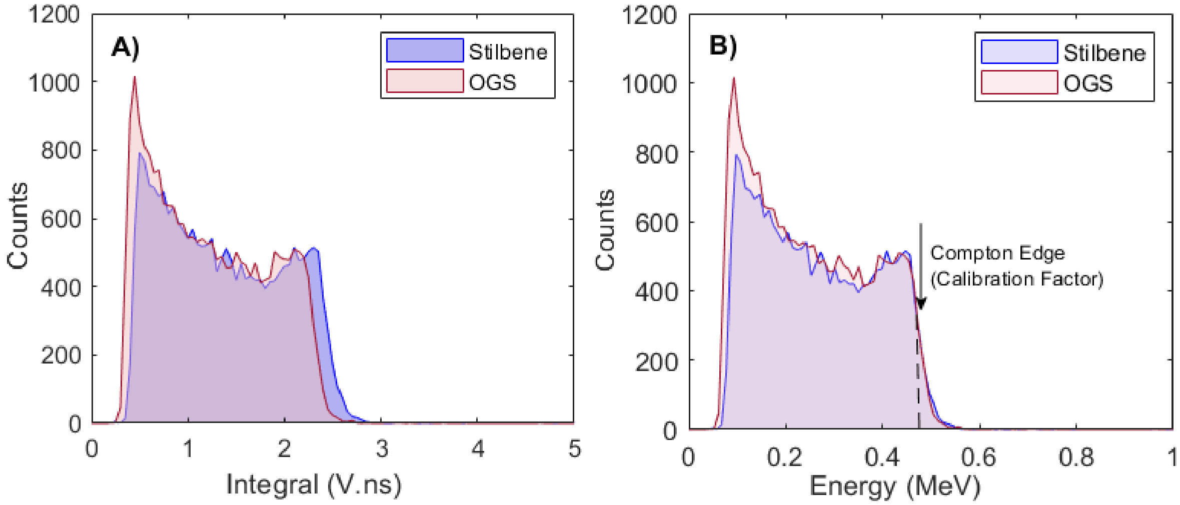

Figure 7.4: A) Pulse integral plots of Cs-137 measured with stilbene and OGS at a 10 cm distance from the source; showing the differences in the threshold used for each detector and hence the resulted calibration factor, B) the resulted energy spectrum of both detectors after applying the calibration factor.

The doses decrease as the source to detector distance increases and the stronger the isotopic source the higher the measured dose, as shown in Figure 7.5. The slight differences in the density and the effective atomic number between stilbene and OGS have resulted in smaller differences in the measured dose with stilbene measuring a factor of ~ 0.1 higher dose compared to OGS for all the different isotopic sources. The IC doses at the nearest distance to the detector, 10 cm SSD, are approximately half the measured dose with stilbene for all the tested sources. IC was reported to have a precision within 10% of the reading and to be inaccurate for contact source measurements. The error was always less than the marker size, so was not included in the plotted data.

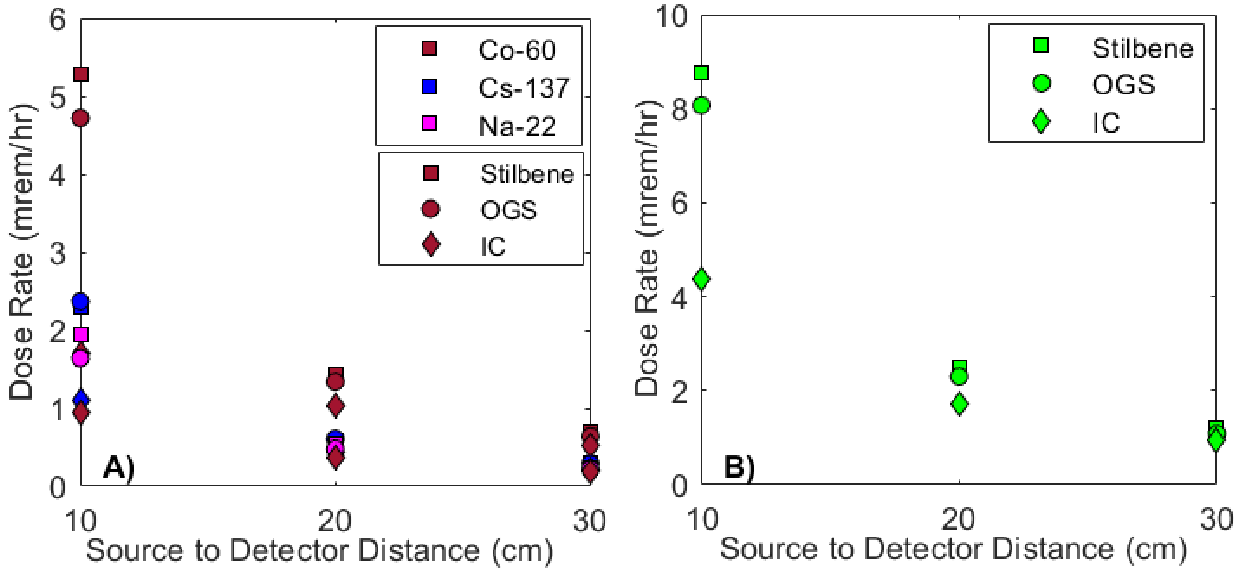

Figure 7.5: The measured equivalent dose for the different isotopic photon sources measured at different distances to the detector using stilbene, OGS, and Fluke IC. The error values between trials were less than the marker size, so error bars are excluded from the plot.

Various solid water thicknesses that are tissue equivalent were added to the front of the detectors to study the effect of shielding and the in-personnel scattering effect on the measured effective dose. The range of tested solid water thicknesses was 0.5-3 cm with an increment of 0.5 cm. The collective dose from the three isotropic sources, Cs-137, Na-22, and Co-60, was measured by placing all three sources at 10 cm from both detectors as shown in Figure 7.6.

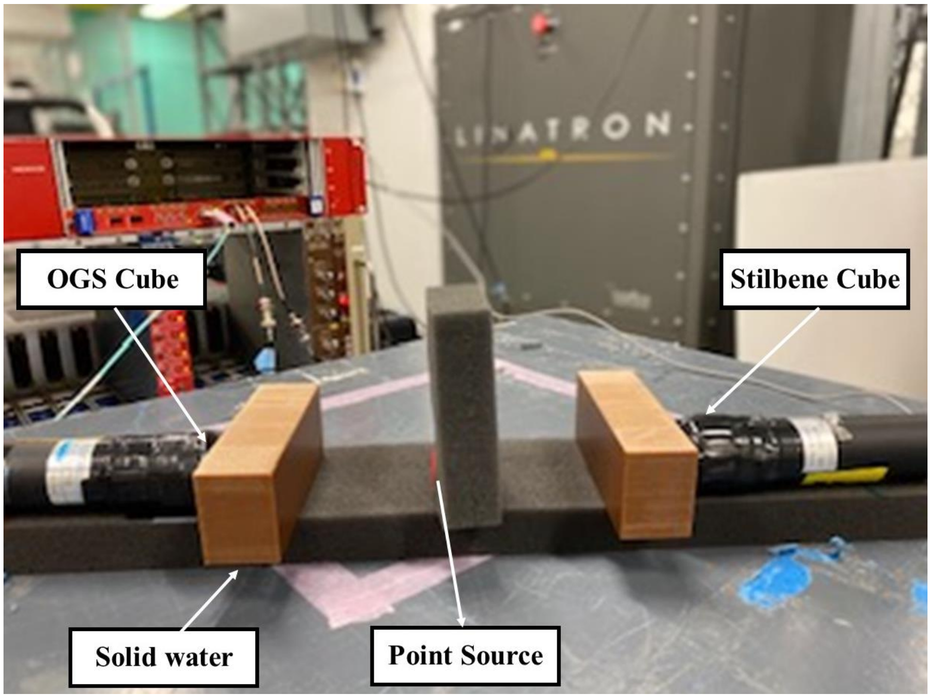

Figure 7.6: The measurement setup for shielding and in-personnel scattering effect showing the solid water slab added to the front of the detectors.

The resulted dose for different solid water thicknesses measured with stilbene, OGS, and IC is shown in Figure 7.6. The same slabs were also placed in front of the Fluke IC following the same setup of the stilbene and OGS measurements. The measured dose decreases as the thickness of the solid water added in front of the detector increases except for the case of stilbene at 0.5 cm thickness of solid water, where the dose has not changed. This is expected to be due to the in-scattering effect from the solid water to the detector. The stilbene is measuring a higher dose in comparison to the OGS as was measured in the previous measurements; however, the relative difference in the dose has increases for the cases of smaller solid water thicknesses of 0.5 cm, 1 cm, and 0.15. the dose measured with the IC is approximately half of the dose measured with stilbene for all the tested different solid water thicknesses, which agrees with the previous results in Figure 7.6.

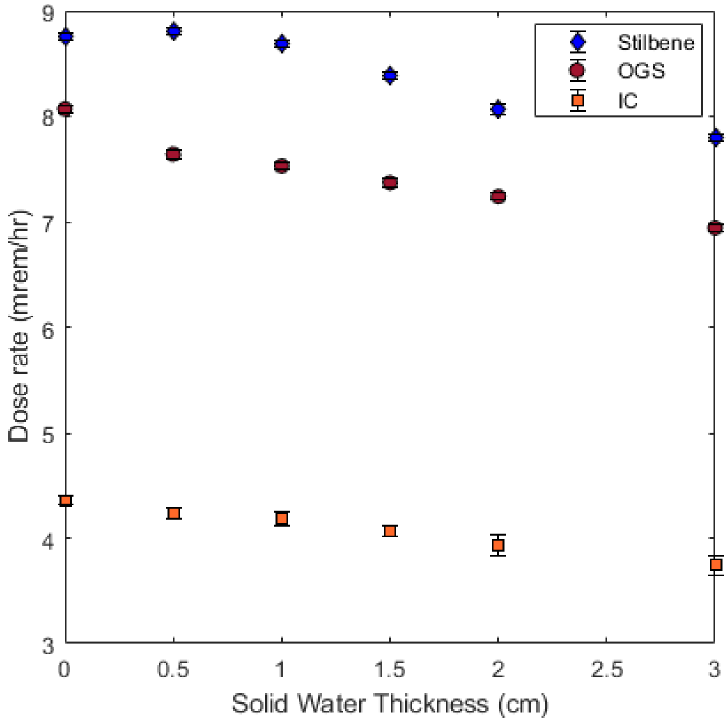

Figure 7.7: The measured dose at 10 cm SSD with different solid water thicknesses showing the effect of shielding in decreasing the dose rate measured.

7.4. Mixed Source (Linac) Experiments

In those measurements, the organic detectors were placed at different distances from the linac beam centerline (BCL) to survey the dose rates within the lab as shown in Figure 7.8. The results are compared to the measured and monitored doses with the Fluke IC. Pulse pileup has a larger effect at a closer distance to the BCL as shown in Figure 7.9, due to the pulsed nature and high source intensity of the linac. The pileup fraction for the closest distance to the BCL of 2.7 m was 0.26, 0.25 as measured with stilbene and OGS. The pileup fraction decreases to as low as 0.03 for the furthest distance to the BCL at 9.7 m away. A factor to correct for the pileup effect was implemented by normalizing the total measured dose to the effective measurement time excluding the pileup events and their corresponding measurement time. The dose rate is normalized to the pileup fraction.

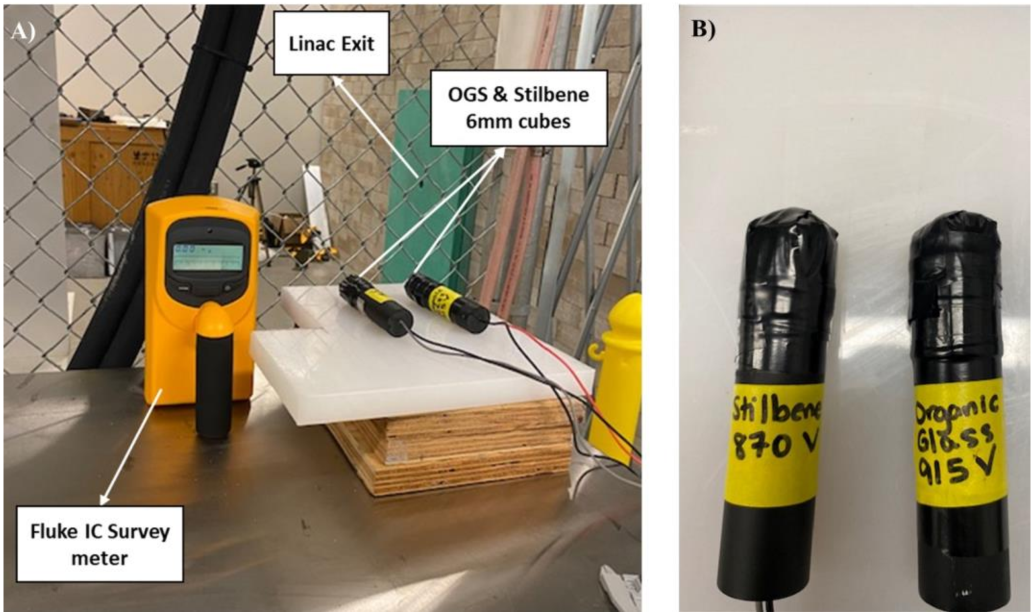

Figure 7.8: The experimental setup of the Linac active background measurement A) shows the organic scintillators and the IC positions during linac operation in ABG measurements, B) is a close figure of the 0.6 cm cube stilbene and OGS crystals each attached to a 1” PMT.

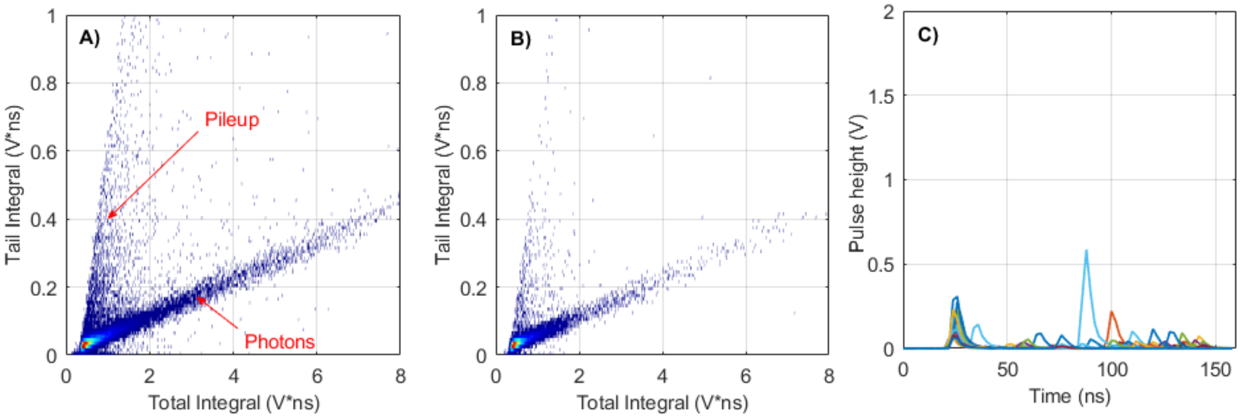

Figure 7.9: OGS measured PSD plot showing the pileup effect on the measured data. A) PSD plot acquired at 2.7 m away from BCL, B) measured PSD at 9.7 m away from BCL, C) sample of pileup pulses measured with OGS. Stilbene has measured a similar PSD as well.

For all the different tested locations, IC readings were higher than stilbene and OGS measured doses for all the different tested positions. The gamma energy range of detection for IC is 20 keV to 2 MeV which is nearly the same for stilbene and OGS although organic scintillators have a slightly higher range. The smaller size of the detectors (0.6 cm) is the major source of differences in dose due to the higher energy range of the linac photons. The effective size of the cube detectors is causing a partial energy deposition of the high energy photons resulting in dose underestimation. The resulted dose reading of all detectors is tabulated in Table 7.2 and shown in Figure 7.10. The error bars were not plotted because they were lower than the marker size. The dose at 5.5 m was slightly higher than the dose at 4.4 m as the dose at 5.5 m was at a different distance from the linac exit. For the IC readings, the error was calculated based on the reported device uncertainty of 10% as the dose readings were acquired as the total integrated dose reading.

Table 7.2: The measured dose rates at different locations from BCL in the 9MV linac laboratory

Distance to BCL (m)	**Stilbene**	**Corrected Stilbene**	**OGS**	**Corrected OGS**	**IC***
2.7	8.35±0.05	11.31±0.07	7.91±0.07	10.61±0.09	20.45± 2.05
4.4	1.31±0.09	1.40±0.09	1.33±0.08	1.42±0.09	2.24± 0.22
5.5	1.00±0.07	1.07±0.08	1.10±0.07	1.18±0.07	2.54± 0.25
6.7	0.67±0.10	0.70±0.10	0.72±0.09	0.75±0.10	1.68± 0.17
9.7	0.40±0.05	0.41±0.05	0.42±0.04	0.43±0.04	0.97± 0.10

*The error of the IC reading was estimated based on the device uncertainty

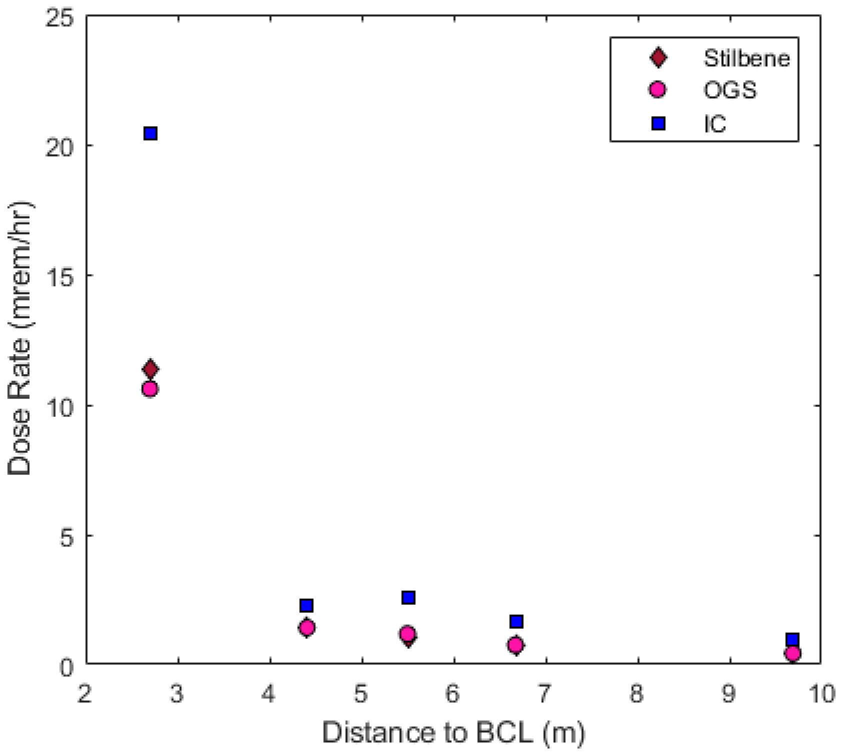

Figure 7.10: Measured dose rates at different distances from a 9MV linac BCL using stilbene, OGS, and IC.

7.5. Simulation Comparisons

The measured dose rates were compared to the simulated results using Monte Carlo transport code MCNP 6.2-CLOUD to develop benchmark dose rate values for comparisons [129]. The same sources and experimental setup were used to replicate the measurement as shown in Figure 7.2. Dose rates from different sources and at different source to detector distances were simulated, while a full lab model was simulated for the linac mixed source measurement scoring doses at different distances to BCL. An energy deposition tally (*F8) was simulated to score the total dose measured by each detector material for isotropic dose measurements. While a track-length estimated flux tally was used for the Linac measurement simulations to ensure acceptable certainty in the simulation results. ICRP 21 fluence-to-dose equivalent values were used to calculate the simulated equivalent photon dose rates from the point tallies. F5 is a point detector tally that uses the ICRP fluence-to-dose equivalent values to simulate the dose equivalent in tissues. Although this tally does not account for the effect of the limited size of the detector, it is used as the simulation truth to predict the whole effective dose personnel can get from photon sources.

7.5.1. Isotopic Gamma Sources Experiments

A. Detector Based Simulations

The detectors were simulated to mimic the experimental setup for the different used sources and the different SSDs. The simulated and the measured doses were listed in Table 7.3 and Table 7.4.

the inherent simulation uncertainty was 4% or less for all the cases. The maximum disagreement between the measured and the simulated results for stilbene was for the case of the high-energy Co-60 source. However, the resulted Cs-137 comparisons with the measured dose were within 4% relative error or less. OGS followed the same relation with the maximum relative error for Cs-137 measurements of 10% error. The results show that the size of the detector is suitable for low energy photon measurements such that the effective depth of the detector is adequate for full energy deposition resulting in accurate dose measurements within 4% and 10% error or less for stilbene and OGS as shown in simulations.

Table 7.3: Stilbene measured and simulated tally deposition (F8*) results for different sources and SSDs.

SSD (cm)	**Co-60**		**Cs-137**		**Na-22**		**All Sources (Cs-137, Co-60, Na-22)**	
	Measured	**Simulation**	**Measured**	**Simulation**	**Measured**	**Simulation**	**Measured**	**Simulation**
10	5.28±0.03	3.61±0.04	2.29±0.01	2.27±0.02	1.95±0.06	1.58±0.02	8.76±0.04	8.48±0.10
20	1.43±0.06	1.00±0.02	0.59±0.01	0.60±0.01	0.54±0.08	0.42±0.01	2.49±0.05	2.24±0.05
30	0.71±0.07	0.45±0.02	0.30±0.02	0.29±0.01	0.24±0.07	0.19±0.01	1.20±0.07	1.02±0.03

Table 7.4: OGS measured and simulated tally deposition (F8*) results for different sources and SSDs.

SSD (cm)	Co-60		Cs-137		Na-22		All Sources (Cs-137, Co-60, Na-22)	
	Measured	**Simulation**	**Measured**	**Simulation**	**Measured**	**Simulation**	**Measured**	**Simulation**
10	4.72±0.04	3.61±0.04	2.37±0.01	2.15±0.02	1.64±0.05	1.48±0.02	8.07±0.03	7.91±0.10
20	1.34±0.06	0.94±0.02	0.61±0.02	0.57±0.01	0.48±0.07	0.39±0.01	2.30±0.05	2.10±0.05
30	0.64±0.07	0.42±0.01	0.29±0.02	0.27±0.01	0.22±0.06	0.17±0.01	1.08±0.06	0.93±0.03

B. Benchmark Simulation Comparisons:

The F5 track-length-based equivalent dose rate values were used as the benchmark for comparison to dose rates measured with stilbene, OGS, and the industry-standard survey meter Fluke IC. The relative discrepancy of the measured data from the benchmark simulation results was plotted in Figure 7.11 for the point isotropic source measurements. Organic scintillators have shown the highest agreement with the benchmark tally results for all the different positions. IC has measured the highest discrepancy from simulation for the closest source to detector distance as the IC detectors are inaccurate for contact source measurements.

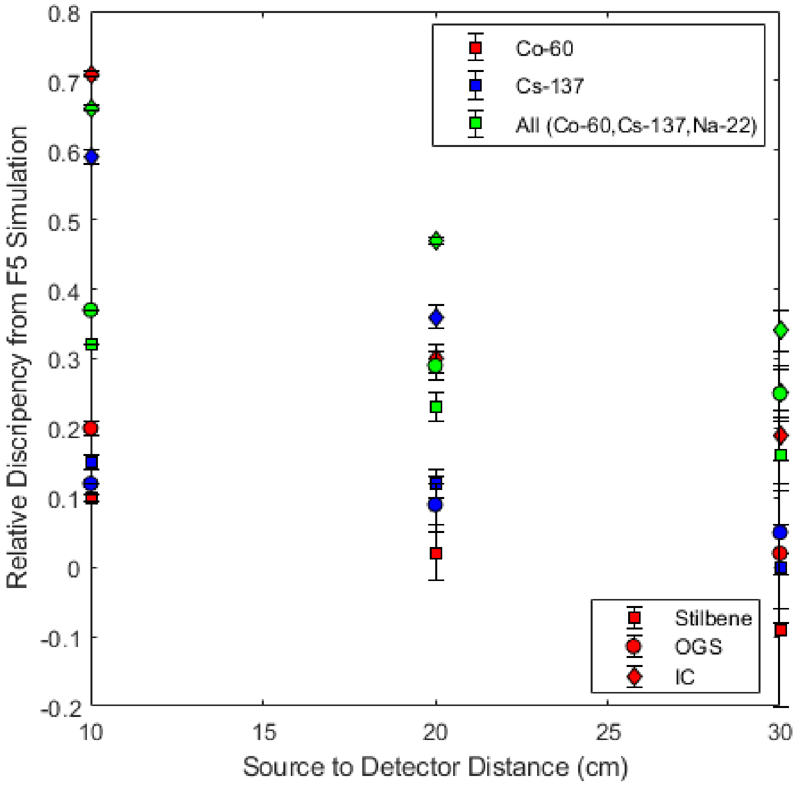

Figure 7.11: The relative discrepancy of the measured dose rates for isotropic sources from the simulated benchmark dose rate values.

7.5.2. Mixed Source (Linac) Experiments:

F5 point detector tally simulations were performed at the position of each detector to eliminate the spatial differences between the detectors in the measured results. The simulated and the measured dose rates at different positions from BCL are listed in Table 7.5. The discrepancy between the measured and the simulated doses is plotted in Figure 7.12. For all different distances to the BCL, IC showed the best agreement with the simulated data. The limited size of the detector of the organic scintillators has caused partial energy deposition for the high energy photons of the linac. The highest disagreement between the simulated and the measured dose data was for the 4.4 m point from BCL where all different detectors have nearly the same discrepancy. The photon spectrum scored through simulation using the point tally was compared with the measured energy spectrum deposited in the stilbene cubes as shown in Figure 7.13 for different distances to the BCL. The measured and simulated resulting spectrum agree at the lower energy region. For the higher region of 1-2 MeV, stilbenes overestimated the total photons as all higher energy photons beyond 2 MeV that partially deposit their energy in the stilbene fall within that energy range. This result agrees with the prediction that limited detector size causes the underestimation of the dose as shown in the measured linac results with the organic scintillators.

Table 7.5: Stilbene and OGS measured and simulated results for different distances to the BCL.

Distance to BCL (m)	**Stilbene Measured**	**Simulated**	**OGS Measured**	**Simulated**	**IC Measured**	**Simulated**
2.7	11.31±0.07	17.49±0.43	10.61±0.09	17.46±0.41	20.45± 2.05	17.17±0.59
4.4	1.40±0.09	9.12±0.26	1.42±0.09	8.84±0.27	2.24± 0.22	9.91±0.27
5.5	1.07±0.08	3.46±0.19	1.18±0.07	3.41±0.17	2.54± 0.25	3.72±0.31
6.7	0.70±0.10	2.03±0.13	0.75±0.10	2.00±0.13	1.68± 0.17	2.12±0.15
9.7	0.41±0.05	0.66±0.07	0.43±0.04	0.65±0.07	0.97± 0.10	0.68±0.07

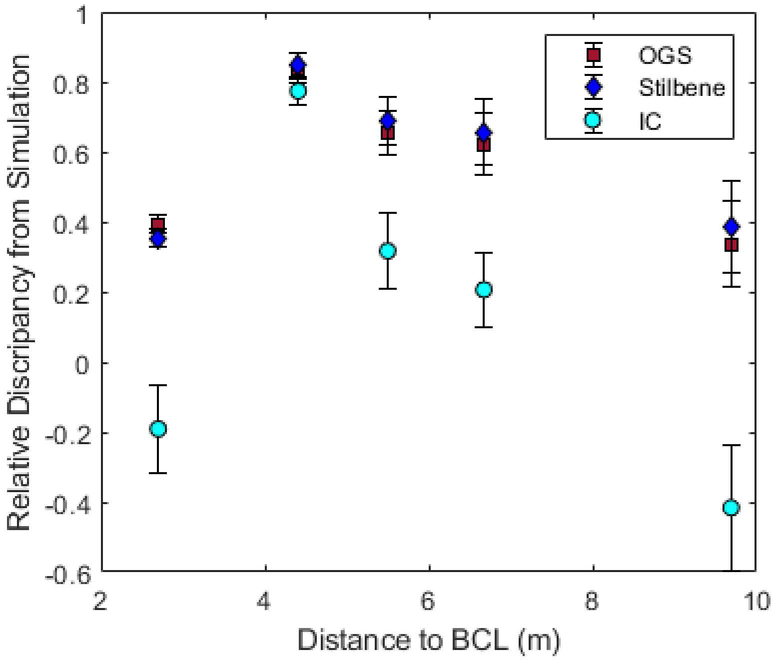

Figure 7.12: The relative discrepancy of the measured dose rates for isotropic sources from the simulated benchmark dose rate values.

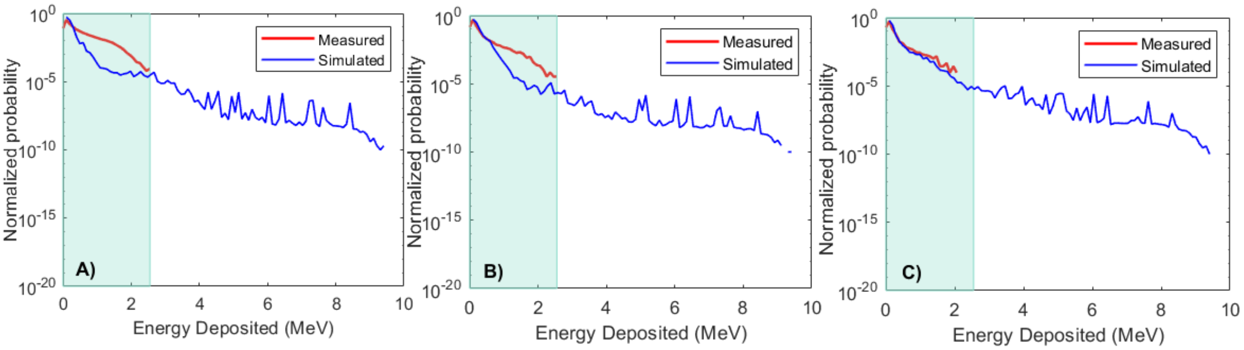

Figure 7.13: Measured and simulated normalized stilbene spectrum at different distances to linac BCL A) 2.7 m away, B) 4.4 m away, C) 9.7 m away.

7.5.3. Detector Size Effect

Because the limited size of the organic scintillators was shown to underestimate the measured dose equivalent specifically for the high energy photon source, it is important to quantify the effect of the detector depth, and size, on the dose measurement through simulation. In this part, various detector crystal sizes were tested for different photon sources of different energies. A 0.6 cm cube, a 2.54 cm cylinder, and a 5.08 cm cylinder were simulated, and the dose was scored using the F8* tally for a Cs-137, Co-60, multi-isotopic sources of Cs-137, Co-60, and Na-22 additionally a linac bremsstrahlung source. The dose deposition in each detector was compared with the benchmark F5 tally dose results. Both OGS and stilbene measure nearly the same deviation from the point source dose tally for the different sources and different detector sizes.

The 2.54 cm cylinder has the best agreement with the point simulation tally for the different tested sources. The simulated dose with a 0.6 cm cube is the smallest and the 2.54 cm cylinder simulated the largest dose for all the tested sources except for the case of the Cs-137 source where the cube measured the highest dose. The main reason for this for high energy sources is the partial deposition effect for the smaller cube size and for the 5.08 cm cylinder the effective volume of the detector is higher than the minimum needed effective volume to stop the photons hence this underestimates the dose. However, for the case of the low energy source, Cs-137, the effective size of the 0.6 cm cube detector is enough for full energy deposition. Hence, the agreement with the F5 simulation was within a 15 % difference compared to the 20% and 31% relative error for the 2.54 cm and 5.08 cm cylinders respectively as shown in Figure 7.14.

The highest disagreement with the F5 for all the detector sizes occurs in the case of the polyenergetic bremsstrahlung linac source of 9 MeV. This error is as high as 55% for the case of the 0.6 cm cube, which is within what was shown in the linac measurement discussed previously. On the other hand, the simulated disagreement was within 37% and 39% for the 2.54 cm and 5.08 cm cylinders respectively.

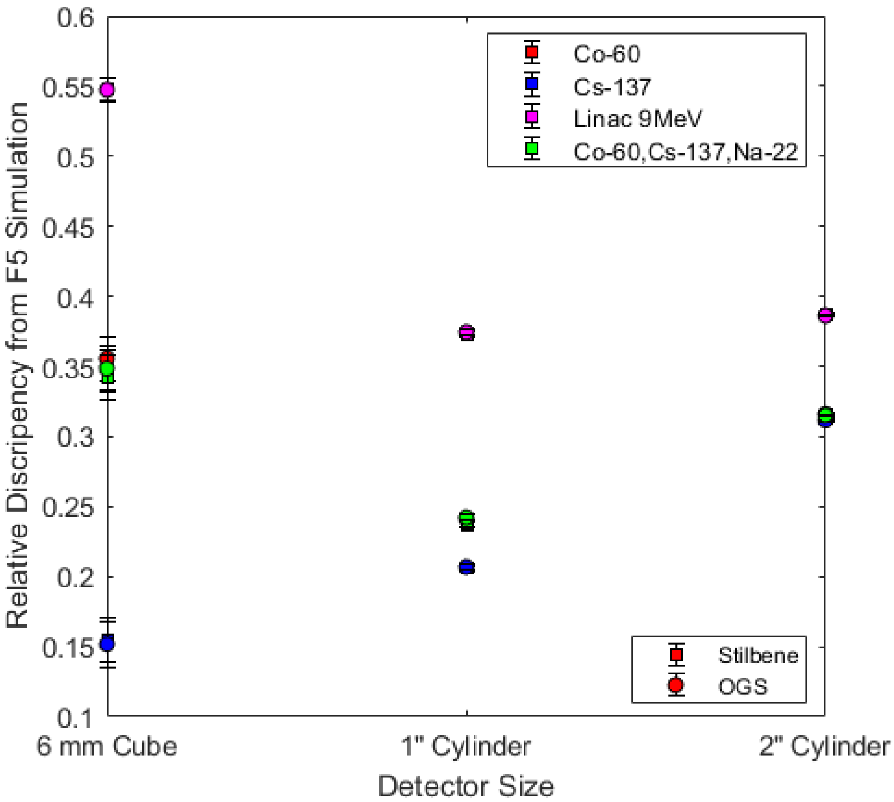

Figure 7.14: The relative discrepancy of the simulated dose rates for the different photon sources measured with different detector sizes compared to the simulated F5 benchmark dose rate values.

7.6. Conclusions

This chapter tests the implementation of small organic scintillators for equivalent dose measurement. The technique relies on converting the collected pulses through signal processing to dose equivalent based on energy-deposition conversion converting the LET-based quality factor and dose rate to dose equivalent. Isotropic gamma sources Cs-137, Co-60, and Na-22 and mixed polyenergetic photon source (linac) were tested as well.

The method showed accurate results specifically for isotropic energy sources. The limited size of the detector makes it more efficient for low-energy photon source detection. To test the applicability of the method in emulating a radiation therapy environment, measurements were performed at different distances from the center beamline of a 9 MeV linac. The pulsed nature of the linac beam and the resulted high source rate has resulted in a high pulse pile-up effect despite the selected smaller size of the detector. The limited size of the detector has resulted in a partial energy deposition effect which is highly affecting the measurements of high energy photons. A layer of lead would reduce the probability of pulse pileup; however, this will underestimate the dose delivered to the personnel in realistic non-shielded scenarios. This proof-of-concept approach has shown the applicability of small-sized detectors as photon dosimeters specifically for low energy photons. Larger size detectors will widen the accuracy and the sensitivity energy range of those detectors. However, the pulse pileup effect needs to be further investigated in future work for linac environment dose monitoring applications.

Chapter 8

Conclusions and Future Work

8.1 Summary

The dissertation focuses on enhancing the implementation of dosimetric tools throughout the radiation therapy treatment process including linac commissioning, treatment QA, plan verification, treatment delivery and monitoring, and safety. The first aim of the dissertation focuses on commissioning non-standard small radiation fields. The applicability of 3D Clearview gels in small field commissioning was investigated to develop a comprehensive commissioning procedure using 1D, 2D, and 3D dosimeters to characterize the different radiation fields of M9 Linatron. The linac output stability, beam divergence, depth dose curves, relative output factors, beam profiles, and linac calibration factor were measured. The experimental results were then used to tune and investigate the initial electron source of the linac. The full tuning and the MC-based characterization of the linac source were essential to acquire full phase-space files of the different static collimated fields of the linac. The acquired phase-space files were used to form a pre-treatment (pre-irradiation) simulation-based dose verification tool.

The focus of this dissertation was to test the feasibility of iRAI in 3D radiation therapy dosimetry. This dissertation comprehensively investigated, through simulations, the implementation of iRAI as an *in vivo* dosimeter for UHDR-RT for high dose measurement. The main properties of the induced acoustic waves following linac irradiation with high doses and the effect of the different linac operational parameters on the imaging quality were investigated by simulating different transducer configurations in homogeneous gelatin phantoms. Additionally, the feasibility and the implementation of iRAI in 3D *in vivo* dosimetry were experimentally tested using a customized 2D array transducer, which has a high impact on acquiring a full 3D dose measurement using a single projection. The implementation of the custom-designed 2D array in iRAI imaging has a great impact on decreasing the measurement and imaging time in comparison to single element transducers using a single projection measurement setup.

Last, the implementation of small organic scintillators as dual dosimeter measuring photon doses was studied. The implementation of organic scintillator detectors was investigated in different photon environments towards dose equivalent measurements to test their applicability as survey and monitoring dosimeters.

8.2 Conclusions

A full commissioning procedure was developed and implemented to commission a 9MV Linatron because the standard and reference conditions implemented in commissioning protocols cannot be met due to the geometrical constraints and the custom shielding design of the linac. Chapter 3 of the dissertation developed a reliable procedure that can be followed and applied to commission non-standard small radiation fields following the recommended standard protocols. Because gels can fully acquire the full dose distributions in 3D, gels were used as the main relative dosimeter to characterize the radiation small fields of the linac using a single dosimeter with a single measurement. The work has shown the effectiveness of gels in correcting for the misalignment errors that can highly affect the measured beam characteristics, specifically PDD curves for small fields. The full measured 3D dose data were acquired using the same gel jar, which resulted in full 3D characterization while allowing for the less standard deviation between the different gel trials reflecting the higher intra-stability of the gel jars. Gels have a limited dose-response measurement in the buildup; however, the 1D and 2D dose measurements with other dosimeters (A14 IC and films) allow for full data representation.

The initial electron source parameters of the linac were investigated through the MC-based source parameters tunning process. The resulting optimized parameters were 9.8±0.2 MeV beam energy, 0.15±0.025 cm, 0.075±0.025 cm horizontal and vertical radial intensities, and a $0.5^o \pm 0.1^o$ angular distribution. The optimized parameters of the electron source were used to fully acquire the phase-space files of the small fields of 0.5x0.5 cm^2, 1x1 $cm^{2,}$ and 2x2 cm^2. The simulated and the measured results agreed within 1.2% for the ROF and within 0.4 mm for field profile sizes. The agreement between the measured and the simulated results reflects the accuracy of the investigated initial parameters of the linac. Additionally, the acquired phase-space fields scored for the different fields provided an MC-based tool for static field pre-irradiation dose delivery verification. This pre-irradiation tool ensures accurate dose delivery and is used to optimize the experimental setup for animal irradiation studies mimicking the clinically implemented treatment planning systems.

The main findings testing the applicability of iRAI in UHDR-RT showed a linear relation of the generated acoustical signal to dose deposited per pulse as theoretically expected. The high instantaneous dose rates used in UHDR-RT, even the highest UHDR's reported in the literature, and the resulting acoustic pressures were far from generating nonlinear acoustic propagation as reported in the simulated study in Chapter 5. Furthermore, the high dose deposition in UHDR-RT has induced high-intensity acoustical signals and resulted in an improved acoustical signal-to-noise ratio (SNR) in comparison to the conventional dose rates. Ideal point transducers with planar configuration were capable to localize the edges of the radiation field with a 3 mm fidelity at the surface of the phantom. This reported value will be affected by the implemented transducer system and its characteristics including the configuration, operational central frequency, sensitivity, and resolution.

The linac operational parameters, including the pulse repetition rate and the pulse duration, affect the strength of the generated signal and the temporal and spatial resolution of the reconstructed iRAI images. The shorter the linac pulse, the better the temporal resolution and hence image quality. A dedicated linac machine that delivers UHDR-RT with a short pulse duration could have the advantage of improving the SNR of iRAI and allowing faster treatment delivery. Although the longer linac pulse durations of 4 µs- 6 µs have shown degradation in the imaging resolution affecting both the profiles and the depth pressure curves, this effect can be corrected through signal processing i.e., linac pulse deconvolution. This has increased the agreement between the pressure-based and the initial beam characteristics to within 98.7% passing rate for the 1%/1mm gamma test. The reported beam localization, beam characterization, and the 3D dosimetric capabilities of iRAI have demonstrated its feasibility and promise as an *in vivo* dosimetry tool for UHDR-RT. The results of this work have encouraged the further investigation and implementation of iRAI for UHDR-RT environments for radiotherapy dosimetry applications.

The implementation of iRAI in conventional radiation therapy *in vivo* dosimetry was tested in gel/ gelatin phantoms using a customized 2D array transducer. The array was capable to measure dose distributions in 3D; allocating the radiation beam position vertically and horizontally, characterizing the radiation fields, and measuring the 2D dose distribution. The ability of iRAI to measure the changes in the beam intensity (dose per pulse) was tested such that the higher the dose rate deposited per beam pulse, the stronger the generated acoustic signal. The sensitivity of iRAI to measure radiation field size changes was within 0.35 cm. While the iRAI ability for beam localization; measuring the shift in the beam position, was detected within 0.3 cm relative to the gel measured data. The repeatability of iRAI was tested using the same setup and phantom for different static field irradiation trials. The agreement between the different trials measuring the 2D dose distributions was within a 100% passing rate for the 7%/4mm and the 3%/3mm gamma test for the 4x3 cm^2 field. While the corresponding passing rates for the 2x2 cm^2 field were 99.9% and 99.3% respectively. The changes in the measured SNR quantified as the peak-to-peak ratio were within 10.7% for the 4x3 cm^2 and 13.5% for the 2x2 cm^2 field. The SNR and the resulted image quality increase with increasing the number of signal averages used to construct the iRAI images. The higher the dose per pulse, the better the image quality and the smaller the number of averages used to construct images.

Testing the dose distributions for different treatment plans and iRAI reconstructed images, iRAI has proven feasibility for implantation in 3D dosimetry for beam localization and monitoring, beam characterization, and dose verifications. Hence, iRAI has demonstrated potential for implementation as a 3D *in vivo* relative dosimetry tool in conventional radiation therapy in addition to UHDR-RT.

Lastly, as organic scintillators can discriminate between neutrons and photons, they have the potential to be used as dual dosimeters. The quality factor for the different tested photon beams is 1 given their energy range and the resulted linear energy transfer. Isotropic gamma sources Cs-137, Co-60, and Na-22 and mixed polyenergetic photon source (linac) were tested to verify the dosimetric capability of small (0.6 cm cube) stilbene and OGS. The agreement between the scintillator measured dose and the simulated results was better for the low energy sources Cs-137. The higher the energy of the photon source, the higher the disagreement between the measured and the simulated dose results. Small cube stilbene and OGS have shown a potential for low energy photon measurement within 4% and 10% for stilbene and OGS compared to simulations. The effect of the detector size simulated in this study has shown that 2.54 cm size detectors have the best agreement with the expected dose equivalent readings to personnel. The smaller size of the detector resulted in the partial deposition of the photon energy, which underestimated the dose reading. Hence, the small size cube wasn’t efficient for high energy measurement as the case for the linac-based measurement. In conclusion, OS has shown potential for dosimetry measurements once the optimization of the detector size was performed based on the expected spectral range of photon energy to be detected.

8.3 Limitations and Future Work Directions

Commissioning research accelerators following the protocols and the procedures implemented for clinical accelerators is challenging as there are geometrical constrains and customized shielding effects for the M9 linatron. The reference conditions, specifically for the case of M9 linatron, were not achievable as the beam exit is 161 cm away from the source, while the reference standard commissioning conditions are 100 cm from the source. This necessitates the need for achievable reference conditions to commission and calibrate the linac beam. The main source of error during the implemented commissioning procedure was the collimator alignment errors because the secondary collimators were manually positioned to shape the radiation field. Installation of a fixed laser positioning system would ease the process of positioning and aligning the secondary collimators. Future recommendations are to regularly commission and monitor the output of the linac to ensure accurate dose delivery for animal irradiations. Although implementing gels in relative dosimetry of small fields has shown a high potential in correcting for dosimeter misalignment relative to the center of the field, they lack dose readings at the buildup region due to the reconstruction artifacts. This effect occurs due to the refraction at the surface of the gels. Using matching fluids with the same refractive index of the gel material could help reduce the effect, in addition to the careful preparation of the gel dosimeters to ensure a flat gel surface to mitigate the artifacts at the buildup region.

The optimization of the initial source parameters: beam energy, radial intensities, and the angular distribution, of the linac, is an essential step to ensure accurate simulation of the resulted photon beam. However, simulation-based optimization is a time-consuming process as it requires extensive simulation and tuning steps. The challenge is when dealing with non-standard and research-based accelerators. Because this process requires a person with MC simulations such as TPS vendors. It is recommended that TPS-MC vendors perform simulations of the linac head covering a wide range of initial beam parameters covering all the different linacs of the same type and share the resulted dose distributions with users. The TPS-MC involvement will help expedite the process to determine the initial source parameters for the linac by comparing the measured results to the different parameter combinations simulated by the vendors [94].

The initially scored phase-space files in this work had limited scored particles, which make them suitable for near field measurements, closer to the linac exit, where most of the experiments were performed. Running additional simulations will enhance the statistics of the simulated files for wider experimental setups away from the beam exit.

Based on the work performed in the dissertation, there are a few areas of improvement and future research work needed for the clinical implementation of iRAI technology. Simulation-based studies are the preliminary tool to investigate the different experimental setups and test the feasibility of iRAI implementations for different applications. The tested feasibility of iRAI in UHDR-RT covered in this dissertation was for ideal transducers assuming infinite bandwidth. There are additional limitations on practically available transducer configurations, which highly affect the sensitivity, spatial resolution, and fidelity, of the reconstructed iRAI images based on the characteristics of the implemented transducer. However, the fully developed simulation workflow in this work with additional detailed aperture configuration and image reconstruction could be used to study the effects of these limitations and reduce them substantially. Future work could implement better image reconstruction techniques such as an iterative reconstruction approach, which was found to eliminate data sparsity specifically at the phantom entrance (beam entrance).

The simulation studies in this dissertation covered limited setups, additional studies covering multiple projections would better reconstruct the full 3D dose distribution. The acquired 3D iRAI images could acquire the 3D dose distribution and the spatial beam characteristics based on the tested experimental setup. Array transducers can acquire the full 3D distribution with a single projection setup due to the spherical nature of the generated acoustic signal. For example, a crossed-linear array, one normal to and one parallel to the beam central axis, or a hemispherical transducer array.

The proposed challenges\limitation and the proposed areas of improvement are:

- The considerably poor temporal and spatial resolution of iRAI is due to the nature of the considerably long linac pulse duration. Shorter pulses produce a higher frequency component signal, which leads to better imaging resolution. If possible, specifically for UHDR-RT optimizing the linac duration, to approximately 1 µs based on the findings of this work, will be beneficial in imp[roving the imaging quality and resolution.
- The induced acoustical signal is proportional to both the incident radiation energy/dose and the acoustical characteristics of the medium. Conventional radiation therapy doses deposited per pulse are relatively low resulting in small-amplitude acoustic waves and low SNR. Lower energy beams are typically delivering less dose per pulse than the studied

higher energy flattening filter-free beams. Improvements in both the detection system sensitivity, amplification, and signal processing techniques will improve the detectability of low energy beams.

- The higher the Grüneisen coefficient of the exposed medium, the stronger the induced acoustic images i.e., fat tissues have nearly four times Grüneisen coefficient than soft tissue hence ~ four times stronger SNR. IRAI has more promise for clinical implementation in liver treatment monitoring and dosimetry.
- The iRAI image quality is highly affected by the array system including the sensitivity, the central frequency, bandwidth, and the resolution of the transducer. The frequency of the array should well match the iRAI induced signal frequency to ensure better detectability of the acoustic signal. Although the low-frequency array ensures better detectability of the induced signal, the high-frequency component detectability is needed for better imaging quality to bring details and sharpness to the boundaries. Further improvement in the sensitivity of the customized array transducer could help in decreasing the noise effect however, this may lead to a more complicated transducer design or decreases the spatial resolution of the array.
- The other main area of improvement is improving the quality of the iRAI images. The minimum distance between the transducer and source of radiation leads to better SNR and better image resolution. More sophisticated signal processing and image reconstruction techniques are expected to enhance the quality. Simple back projection and delay and sum reconstruction algorithms have caused the generation of negative intensity artifacts due to

the limited bandwidth of the transducer. Reconstruction algorithms that can compensate for the lost frequency components will have a high effect on enhancing the accuracy and the quality of the reconstructed images i.e., iterative reconstruction algorithms. Additionally, implementing artificial intelligence for signal processing could highly improve the quality of the generated iRAI images.

Lastly, the smaller size of the detector has an impact on the partial deposition of the photon energy, which alters the dose rate measurement accuracy. A Monte Carlo- based study using MCNPXPoliMi to simulate the detector response to predict the minimum effective detector depth for photon dose measurement as well as the effective neutron depth. Since OGS and stilbene can be manufactured in different sizes, this simulation study will help to select the suitable detector size based on the radiation environment.

Since neutrons are more biologically damaging than photons. Moreover, the neutron sources are mixed type sources and do not purely emit neutrons but also emit photons. The applicability of the small organic scintillators in neutron dose rate calculations could be studied taking the advantage of PSD method to allow for separate calculations of the neutron doses in addition to the photon doses as mentioned and studied in this dissertation. Characterizing the pulse shape discrimination capability of the detectors and the neutron energy deposition to light output conversions, based on Birks formulation, should be studied for accurate neutron dose measurement.

APPENDICIES

APPENDIX A

EGSnrc Script for Linatron M-9 Research Accelerator

1. BEAMnrc Input File

```
linac_trial                                                        #!GUI1.0
% Material Definition
AIR521ICRU
0, 0, 0, 0, 0, 1, 2,  IWATCH ETC.
% Source Definition
20000000, 33, 97, 500, 2, 2500, 0, 0,  NCASE ETC.
22.54, 155.29, 0, 0, 0, ,  DIRECTIONAL BREM OPTIONS
-1, 19, -0, 0, 0, 1, 0, -0.1, 0.0, 0.0,  IQIN, ISOURCE + OPTIONS
0, MONOENERGETIC
9.8
0, 0, 0.521, 0.01, 0, 0, ,  0 , ECUT,PCUT,IREJCT,ESAVE
0, 0, 0, 0, 0,  PHOTON FORCING
1, 3,  SCORING INPUT
4, 1
2.54, 5, 10, 40,
0,  DOSE COMPONENTS
0.0, Z TO FRONT FACE
% Geometric Definition of Linac Components
*********** start of CM FLATFILT with identifier back  ***********
72.39, RMAX
this is the back of the linac
0, ZMIN
11, NUMBER OF LAYERS
3, 5.83, # CONES, ZTHICK OF LAYER 1
6, 12.065, 24.13,
6, 12.065, 24.13,
4, 0.18, # CONES, ZTHICK OF LAYER 2
3, 6, 12.065, 24.13,
3, 6, 12.065, 24.13,
```

```
4, 0.34, # CONES, ZTHICK OF LAYER 3
3, 6, 12.065, 24.13,
3, 6, 12.065, 24.13,
5, 0.26, # CONES, ZTHICK OF LAYER 4
3, 6, 6.985, 12.065, 24.13,
3, 6, 6.985, 12.065, 24.13,
4, 1.39, # CONES, ZTHICK OF LAYER 5
6, 6.985, 12.065, 24.13,
6, 6.985, 12.065, 24.13,
3, 14.86, # CONES, ZTHICK OF LAYER 6
6.985, 12.065, 24.13,
6.985, 12.065, 24.13,
2, 2.54, # CONES, ZTHICK OF LAYER 7
6.985, 12.065,
6.985, 12.065,
3, 11.43, # CONES, ZTHICK OF LAYER 8
14.4526, 24.13, 41.275,
14.4526, 24.13, 41.275,
2, 17.78, # CONES, ZTHICK OF LAYER 9
14.4526, 41.275,
14.4526, 41.275,
2, 2.54, # CONES, ZTHICK OF LAYER 10
14.4526, 41.275,
14.4526, 41.275,
1, 48.68, # CONES, ZTHICK OF LAYER 11
5.715,
5.715,
0.521, 0.01, 0, 0,
VACUUM
0.521, 0.01, 0, 0,
AIR521ICRU
0.521, 0.01, 0, 0,
W521ICRU
0.521, 0.01, 0, 0,
POLYETH521ICRU
0.521, 0.01, 0, 0,
W521ICRU
0.521, 0.01, 0, 0,
VACUUM
0.521, 0.01, 0, 0,
AIR521ICRU
```

```
0.521, 0.01, 0, 0,
W521ICRU
0.521, 0.01, 0, 0,
POLYETH521ICRU
0.521, 0.01, 0, 0,
CU521ICRU
0.521, 0.01, 0, 0,
VACUUM
0.521, 0.01, 0, 0,
AIR521ICRU
0.521, 0.01, 0, 0,
W521ICRU
0.521, 0.01, 0, 0,
POLYETH521ICRU
0.521, 0.01, 0, 0,
CU521ICRU
0.521, 0.01, 0, 0,
VACUUM
0.521, 0.01, 0, 0,
AIR521ICRU
0.521, 0.01, 0, 0,
PB521ICRU
0.521, 0.01, 0, 0,
W521ICRU
0.521, 0.01, 0, 0,
POLYETH521ICRU
0.521, 0.01, 0, 0,
VACUUM
0.521, 0.01, 0, 0,
AIR521ICRU
0.521, 0.01, 0, 0,
PB521ICRU
0.521, 0.01, 0, 0,
W521ICRU
0.521, 0.01, 0, 0,
POLYETH521ICRU
0.521, 0.01, 0, 0,
AIR521ICRU
0.521, 0.01, 0, 0,
PB521ICRU
0.521, 0.01, 0, 0,
```

```
W521ICRU
0.521, 0.01, 0, 0,
POLYETH521ICRU
0.521, 0.01, 0, 0,
AIR521ICRU
0.521, 0.01, 0, 0,
PB521ICRU
0.521, 0.01, 0, 0,
STEEL521ICRU
0.521, 0.01, 0, 0,
AIR521ICRU
0.521, 0.01, 0, 0,
W521ICRU
0.521, 0.01, 0, 0,
PB521ICRU
0.521, 0.01, 0, 0,
POLYETH521ICRU
0.521, 0.01, 0, 0,
AIR521ICRU
0.521, 0.01, 0, 0,
PB521ICRU
0.521, 0.01, 0, 0,
POLYETH521ICRU
0.521, 0.01, 0, 0,
AIR521ICRU
0.521, 0.01, 0, 0,
POLYETH521ICRU
0.521, 0.01, 0, 0,
STEEL521ICRU
0.521, 0.01, 0, 0,
AIR521ICRU
0.521, 0.01, 0, 0,
ConcreteNIST521
*********** start of CM CHAMBER with identifier IC  ***********
4.93, RMAX

105.83, ZMIN
2, 18, 2, N_TOP, N_CHM, N_BOT
0.0127, 4.9, 0, ZTHICK, RCYS, FLAG FOR LAYER 1 IN TOP
0.521, 0.01, 0, 0,
KAPTON521ICRU
```

```
0.521, 0.01, 0, 0,
KAPTON521ICRU
0.68, 4.9, 0, ZTHICK, RCYS, FLAG FOR LAYER 2 IN TOP
0.521, 0.01, 5, 0,
AIR521ICRU
0.521, 0.01, 0, 0,
AIR521ICRU
4.9, 4.91, 4.92, RADII FOR CENTRAL PART
0.013, 0, ZTHICK, FLAG FOR LAYER 1 IN CENTRAL PART
0.521, 0.01, 0, 0,
KAPTON521ICRU
0.0005, 0, ZTHICK, FLAG FOR LAYER 2 IN CENTRAL PART
0.521, 0.01, 0, 0,
CU521ICRU
0.33, 0, ZTHICK, FLAG FOR LAYER 3 IN CENTRAL PART
0.521, 0.01, 5, 0,
AIR521ICRU
0.005, 0, ZTHICK, FLAG FOR LAYER 4 IN CENTRAL PART
0.521, 0.01, 0, 0,
KAPTON521ICRU
0.0005, 0, ZTHICK, FLAG FOR LAYER 5 IN CENTRAL PART
0.521, 0.01, 0, 0,
CU521ICRU
0.005, 0, ZTHICK, FLAG FOR LAYER 6 IN CENTRAL PART
0.521, 0.01, 0, 0,
KAPTON521ICRU
0.0005, 0, ZTHICK, FLAG FOR LAYER 7 IN CENTRAL PART
0.521, 0.01, 0, 0,
CU521ICRU
0.38, 0, ZTHICK, FLAG FOR LAYER 8 IN CENTRAL PART
0.521, 0.01, 5, 0,
AIR521ICRU
0.013, 0, ZTHICK, FLAG FOR LAYER 9 IN CENTRAL PART
0.521, 0.01, 0, 0,
KAPTON521ICRU
0.0005, 0, ZTHICK, FLAG FOR LAYER 10 IN CENTRAL PART
0.521, 0.01, 0, 0,
CU521ICRU
0.39, 0, ZTHICK, FLAG FOR LAYER 11 IN CENTRAL PART
0.521, 0.01, 5, 0,
AIR521ICRU
```

```
0.005, 0, ZTHICK, FLAG FOR LAYER 12 IN CENTRAL PART
0.521, 0.01, 0, 0,
KAPTON521ICRU
0.0005, 0, ZTHICK, FLAG FOR LAYER 13 IN CENTRAL PART
0.521, 0.01, 0, 0,
CU521ICRU
0.005, 0, ZTHICK, FLAG FOR LAYER 14 IN CENTRAL PART
0.521, 0.01, 0, 0,
KAPTON521ICRU
0.0005, 0, ZTHICK, FLAG FOR LAYER 15 IN CENTRAL PART
0.521, 0.01, 0, 0,
CU521ICRU
0.32, 0, ZTHICK, FLAG FOR LAYER 16 IN CENTRAL PART
0.521, 0.01, 5, 0,
AIR521ICRU
0.013, 0, ZTHICK, FLAG FOR LAYER 17 IN CENTRAL PART
0.521, 0.01, 0, 0,
KAPTON521ICRU
0.0005, 0, ZTHICK, FLAG FOR LAYER 18 IN CENTRAL PART
0.521, 0.01, 0, 0,
CU521ICRU
0.521, 0.01, 0, 0,   chamber wall
KAPTON521ICRU
0.521, 0.01, 0, 0,   gap
AIR521ICRU
0.521, 0.01, 0, 0,   container
AIR521ICRU
0.69, 4.9, 0, ZTHICK, RCYS, FLAG FOR LAYER 1 IN BOTTOM PART
0.521, 0.01, 5, 0,
AIR521ICRU
0.521, 0.01, 0, 0,
AIR521ICRU
0.00508, 4.9, 0, ZTHICK, RCYS, FLAG FOR LAYER 2 IN BOTTOM PART
0.521, 0.01, 0, 0,
KAPTON521ICRU
0.521, 0.01, 0, 0,
KAPTON521ICRU
0, MRNGE
*********** start of CM APPLICAT with identifier concrete ***********
40.64, RMAX
the concrete wall
```

```
114.65, ZBACK
1, 0, #SCRAPERS, SQUARE
108.70028, 5.9297, 5.715, 40.64, 0, 0
0.521, 0.01, 0, 0,
ConcreteNIST521
*********************end of all CMs*****************************
 #########################
 :Start MC Transport Parameter:

 Global ECUT= 0.521
 Global PCUT= 0.01
 Global SMAX= 5
 ESTEPE= 0.25
 XIMAX= 0.5
 Boundary crossing algorithm= EXACT
 Skin depth for BCA= 0
 Electron-step algorithm= PRESTA-II
 Spin effects= On
 Brems angular sampling= Simple
 Brems cross sections= BH
 Bound Compton scattering= Norej
 Compton cross sections= default
 Pair angular sampling= Simple
 Pair cross sections= BH
 Photoelectron angular sampling= Off
 Rayleigh scattering= On
 Atomic relaxations= EADL
 Electron impact ionization= Off
 Photon cross sections= xcom
 Photon cross-sections output= Off

 :Stop MC Transport Parameter:
 #########################
```

2. DOSXYZnrc Input File

```
Profile                                          #!GUI1.0
% Material definition
2
AIR521ICRU
H2O521ICRU
% Source  Cutoff Energies
0.521, 0.01, 0, 0, 0
% Phantom Grid Definition
-5, -5, -3, 1
-35
20, 1
0.5, 25
0.1, 50
0.5, 25
20, 1
-35
20, 1
0.5, 25
0.1, 50
0.5, 25
20, 1
0
31.75, 1
0.5, 60
12, 1
2, 101, 2, 101, 2, 61, 2, 0
0, 0, 0, 0, 0, 0, 0, 0
0, 0, 0, 0, 0, 0, 0, 0
2, 101, 2, 101, 2, 61, 2, 0
0, 0, 0, 0, 0, 0, 0, 0
% Source Definition
2, 2, 0, 0, 0, 180, 90, 0, 0, 0, 2.54, 155.29, 165.48, 0
2, 2, 1, 0, 0, 0, 0, 0
/app/EGSnrc/egs_home/BEAM_square_coll/square
fields2_6_22/phase0.5x0.5_total.egsphsp1
76000000, 0, 500, 33, 97, 100, 0, 0, 0, 0, , 3, 0, 0, 0, 0, 0
 #########################
 :Start MC Transport Parameter:
```

```
Global ECUT= 0.521
Global PCUT= 0.01
Global SMAX= 5
ESTEPE= 0.25
XIMAX= 0.5
Boundary crossing algorithm= PRESTA-I
Skin depth for BCA= 0
Electron-step algorithm= PRESTA-II
Spin effects= On
Brems angular sampling= Simple
Brems cross sections= BH
Bound Compton scattering= Off
Compton cross sections= default
Pair angular sampling= Simple
Pair cross sections= BH
Photoelectron angular sampling= Off
Rayleigh scattering= Off
Atomic relaxations= Off
Electron impact ionization= Off
Photon cross sections= xcom
Photon cross-sections output= Off

:Stop MC Transport Parameter:
#########################
```

APPENDIX B

IRAI in UHDR-RT Simulation Script

1. Kwave Acoustic Propagation Script

```
simulation_size = 340;                    % [grid points]
PML_size_forw = 10;                        % [grid points]
x = 96e-3;                          % [m]
y = x;
z=x;
Nx = simulation_size - 2 * PML_size_forw;   % [grid points]
Ny = Nx;                              % [grid points]
Nz = Nx;                              % [grid points]
dx = x / Nx;                          % [m]
dy = dx;                            % [m]
dz = dx;                            % [m]

% create the computational grid
kgrid =kWaveGrid(Nx, dx, Ny, dy,Nz,dz);
input_args = {'Smooth', false, 'PMLInside', false, 'PMLSize', PML_size_forw, 'DataCast', 'single', 'PlotSim', true};

% Define the medium
medium.sound_speed = 1562 * ones(Nx, Ny);          % [m/s]
medium.density= 1035*ones(Nx, Ny);
medium.alpha_coeff = 0.58;  % [dB/(MHz^y cm)]
medium.alpha_power = 1.3 ;

const=1035*0.22;  % Dose per pulse to pressure conversion

% The sensor definition part (spherical sensor distribution)
sensor_radius = 46e-3;       % [m]
center_pos = [0, 0, 0];     % [m]
num_sensor_points = 600;
sensor_mask = makeCartSphere(sensor_radius, num_sensor_points, center_pos, true);
```

```
[grid_data, order_index, reorder_index] = cart2grid(kgrid, sensor_mask);
sensor.mask=grid_data;

% Source definition
p0=zeros(Nx,Ny,Nz);
p0=D_interpxconst; % Dose in Gy/pulse to pressure conversion
 a=0;  % to define the startup of the pulse
 b=4*10^-6;   % to define the end point  of the pulse
t=makeTime(kgrid,medium.sound_speed);
t=t(1:160);
pulse=rectangularPulse(a,b,t);  % Linac pulse definition
source.p_mask =  p0;
source.p_mask(source.p_mask>0)=1;
scaling = 2*medium.sound_speed(1,1,1)*kgrid.dt/kgrid.dx;
p0_scaled=p0/scaling;
index= find(p0_scaled>0);
for i=1:length(index)
    p0_r(i,1)=p0_scaled(index(i));
end
pulse_filtered=filterTimeSeries(kgrid, medium, pulse,'ZeroPhase',true);
source.p=p0_r.*pulse_filtered;

% Run the simulation
sensor_data_3D = kspaceFirstOrder3DC(kgrid, medium, source, sensor, input_args{:});
```

2. Time Reversal Reconstruction Script

```
% Use the same definition of the computationl grid, source definition, and medium characteristics

sensor.time_reversal_boundary_data =sensor_data_3D;
clear source;
source.p0 = 0;

% Run the time reversal simulation
p0_recon = kspaceFirstOrder3DC(kgrid, medium, source, sensor, input_args{:});
```

BIBLIOGRAPHY

[1] J. Thariat, J. M. Hannoun-Levi, A. Sun Myint, T. Vuong, and J. P. Gérard, "Past, present, and future of radiotherapy for the benefit of patients," *Nature Reviews Clinical Oncology*, vol. 10, no. 1. pp. 52–60, Jan. 2013. doi: 10.1038/nrclinonc.2012.203.

[2] L. J. Schreiner and T. Olding, "Gel Dosimetry," in *#34 Clinical Dosimetry Measurements in Radiotherapy (2009 AAPM Summer School)*, 2009, p. 1112.

[3] J. Vandecasteele and Y. de Deene, "Evaluation of radiochromic gel dosimetry and polymer gel dosimetry in a clinical dose verification," *Physics in Medicine and Biology*, vol. 58, no. 18, pp. 6241–6262, 2013, doi: 10.1088/0031-9155/58/18/6241.

[4] G. S. Ibbott, "Clinical applications of gel dosimeters," *Journal of Physics: Conference Series*, vol. 56, no. 1, pp. 108–131, 2006, doi: 10.1088/1742-6596/56/1/010.

[5] H. L. Andrews, R. E. Murphy, and E. J. LeBrun, "Gel dosimeter for depth-dose measurements," *Review of Scientific Instruments*, vol. 28, no. 5, pp. 329–332, 1957, doi: 10.1063/1.1715877.

[6] L. J. Schreiner, "Where does gel dosimetry fit in the clinic?," *Journal of Physics: Conference Series*, vol. 164, 2009, doi: 10.1088/1742-6596/164/1/012001.

[7] Y. Watanabe, L. Warmington, and N. Gopishankar, "Three-dimensional radiation dosimetry using polymer gel and solid radiochromic polymer: From basics to clinical applications," *World Journal of Radiology*, vol. 9, no. 3, p. 112, 2017, doi: 10.4329/wjr.v9.i3.112.

[8] M. Khan, G. Heilemann, A. G. Berg, W. Lechner, and D. Georg, "Basic Properties of a New Polymer Gel for 3D-Dosimetry at High Dose-Rates Typical for FFF Irradiation Based on," *Polymers (Basel)*, vol. 11, p. E1717, 2019.

[9] "IAEA HUMAN HEALTH SERIES PUBLICATIONS No. 8: Development of Procedures for In Vivo Dosimetry in Radiotherapy," Vienna, 2013. [Online]. Available: http://www.iaea.org/Publications/index.html

[10] B. Mijnheer, S. Beddar, J. Izewska, and C. Reft, "In vivo dosimetry in external beam radiotherapy," *Medical Physics*, vol. 40, no. 7, 2013, doi: 10.1118/1.4811216.

[11] I. Olaciregui-Ruiz *et al.*, "In vivo dosimetry in external beam photon radiotherapy: Requirements and future directions for research, development, and clinical practice," *Physics and Imaging in Radiation Oncology*, vol. 15. Elsevier Ireland Ltd, pp. 108–116, Jul. 01, 2020. doi: 10.1016/j.phro.2020.08.003.

[12] M. Lempart *et al.*, "Modifying a clinical linear accelerator for delivery of ultra-high dose rate irradiation," *Radiotherapy and Oncology*, vol. 139, pp. 40–45, 2019, doi: 10.1016/j.radonc.2019.01.031.

[13] M. C. Vozenin *et al.*, "The Advantage of FLASH Radiotherapy Confirmed in Mini-pig and Cat-cancer Patients," *Clinical Cancer Research*, vol. 25, no. 1, pp. 35–42, 2019, doi: 10.1158/1078-0432.CCR-17-3375.

[14] V. Favaudon *et al.*, "Erratum: Ultrahigh dose-rate FLASH irradiation increases the differential response between normal and tumor tissue in mice (Science Translational

Medicine DOI: 10.1126/scitranslmed.3008973)," *Science Translational Medicine*, vol. 11, no. 523, pp. 1–10, 2019, doi: 10.1126/scitranslmed.aba4525.

[15] P. Montay-Gruel *et al.*, "X-rays can trigger the FLASH effect: Ultra-high dose-rate synchrotron light source prevents normal brain injury after whole brain irradiation in mice," *Radiotherapy and Oncology*, vol. 129, no. 3, pp. 582–588, 2018, doi: 10.1016/j.radonc.2018.08.016.

[16] P. Montay-Gruel *et al.*, "Irradiation in a flash: Unique sparing of memory in mice after whole brain irradiation with dose rates above 100 Gy/s," *Radiotherapy and Oncology*, vol. 124, no. 3, pp. 365–369, 2017, doi: 10.1016/j.radonc.2017.05.003.

[17] D. A. Simmons *et al.*, "Reduced cognitive deficits after FLASH irradiation of whole mouse brain are associated with less hippocampal dendritic spine loss and neuroinflammation," *Radiotherapy and Oncology*, vol. 139, pp. 4–10, 2019, doi: 10.1016/j.radonc.2019.06.006.

[18] I. Lohse *et al.*, "Effect of high dose per pulse flattening filter-free beams on cancer cell survival," *Radiotherapy and Oncology*, vol. 101, no. 1, pp. 226–232, 2011, doi: 10.1016/j.radonc.2011.05.072.

[19] F. di Martino *et al.*, "FLASH Radiotherapy With Electrons: Issues Related to the Production, Monitoring, and Dosimetric Characterization of the Beam," *Frontiers in Physics*, vol. 8, Nov. 2020, doi: 10.3389/fphy.2020.570697.

[20] P. R. Almond *et al.*, "AAPM's TG-51 protocol for clinical reference dosimetry of high-energy photon and electron beams," *Medical Physics*, vol. 26, no. 9, pp. 1847–1870, 1999, doi: 10.1118/1.598691.

[21] IAEA, *RADIATION ONCOLOGY PHYSICS: A HANDBOOK FOR TEACHERS AND STUDENTS*, vol. 52, no. 20. Vienna, 2005. doi: 10.1021/jf030837o.

[22] E. B. Podgorsak, "Radiation Oncology Physics: A Handbook for Teachers and Students."

[23] A. Niroomand-Rad *et al.*, "Report of AAPM Task Group 235 Radiochromic Film Dosimetry: An Update to TG-55," *Medical Physics*, vol. 47, no. 12, pp. 5986–6025, Dec. 2020, doi: 10.1002/mp.14497.

[24] J. Seco, B. Clasie, and M. Partridge, "Review on the characteristics of radiation detectors for dosimetry and imaging," *Physics in Medicine and Biology*, vol. 59, no. 20. Institute of Physics Publishing, pp. R303–R347, Oct. 21, 2014. doi: 10.1088/0031-9155/59/20/R303.

[25] A. B. Rosenfeld, "MOSFET DOSIMETRY ON MODERN RADIATION ONCOLOGY MODALITIES," Nuclear Technology Publishing, 2002. [Online]. Available: https://academic.oup.com/rpd/article/101/1-4/393/1597909

[26] M. G. Herman *et al.*, "Clinical Use of Electronic Portal Imaging : Report of AAPM Radiation Therapy Committee Task Group 58 AAPM Refresher Course-Salt Lake City July 2001."

[27] B. Mijnheer *et al.*, "3D EPID-based in vivo dosimetry for IMRT and VMAT," in *Journal of Physics: Conference Series*, 2013, vol. 444, no. 1. doi: 10.1088/1742-6596/444/1/012011.

[28] T. Kron, J. Lehmann, and P. B. Greer, "Dosimetry of ionising radiation in modern radiation oncology," *Physics in Medicine and Biology*, vol. 61, no. 14. Institute of Physics Publishing, pp. R167–R205, Jun. 28, 2016. doi: 10.1088/0031-9155/61/14/R167.

[29] C. Baldock *et al.*, "Polymer gel dosimetry," *Physics in Medicine and Biology*, vol. 55, no. 5, pp. 1–87, 2010, doi: 10.1088/0031-9155/55/5/R01.

[30] F. Verhaegen *et al.*, "ESTRO ACROP: Technology for precision small animal radiotherapy research: Optimal use and challenges," *Radiotherapy and Oncology*, vol. 126, no. 3, pp. 471–478, 2018, doi: 10.1016/j.radonc.2017.11.016.

[31] K. Aljarrah, G. C. Sharp, T. Neicu, and S. B. Jiang, "Determination of the initial beam parameters in Monte Carlo linac simulation," *Medical Physics*, vol. 33, no. 4, pp. 850–858, 2006, doi: 10.1118/1.2168433.

[32] C. Baldock *et al.*, "Polymer gel dosimetry," *Physics in Medicine and Biology*, vol. 55, no. 5, 2010, doi: 10.1088/0031-9155/55/5/R01.

[33] L. J. Schreiner, "True 3D chemical dosimetry (gels, plastics): Development and clinical role," *Journal of Physics: Conference Series*, vol. 573, no. 1, 2015, doi: 10.1088/1742-6596/573/1/012003.

[34] J. C. Gore and Y. S. Kang, "Measurement of radiation dose distributions by nuclear magnetic resonance (NMR) imaging," *Physics in Medicine and Biology*, vol. 29, no. 10, pp. 1189–1197, 1984, doi: 10.1088/0031-9155/29/10/002.

[35] M. J. Maryañski, Y. Z. Zastavker, and J. C. Gore, "Radiation dose distributions in three dimensions from tomographic optical density scanning of polymer gels: II. Optical properties of the BANG polymer gel," *Physics in Medicine and Biology*, vol. 41, no. 12, pp. 2705–2717, 1996, doi: 10.1088/0031-9155/41/12/010.

[36] R. G. Kelly, K. J. Jordan, and J. J. Battista, "Optical CT reconstruction of 3D dose distributions using the ferrous- benzoic-xylenol (FBX) gel dosimeter," *Medical Physics*, vol. 25, no. 9, pp. 1741–1750, 1998, doi: 10.1118/1.598356.

[37] A. Jirasek, "Considerations for x-ray CT polymer gel dosimetry," *Journal of Physics: Conference Series*, vol. 444, no. 1, 2013, doi: 10.1088/1742-6596/444/1/012005.

[38] G. J. Salomons, Y. S. Park, and B. Kim, "Physics in Medicine & Biology Related content Polymer gel dosimetry using x-ray computed tomography : a feasibility study 4 Polymer gel dosimetry using x-ray computed tomography : a feasibility study ∗," 2000.

[39] M. Oldham, "Radiochromic 3D Detectors," *Journal of Physics: Conference Series*, vol. 573, no. 1, 2015, doi: 10.1088/1742-6596/573/1/012006.

[40] M. Oldham, J. H. Siewerdsen, A. Shetty, and D. A. Jaffray, "High resolution gel-dosimetry by optical-CT and MR scanning," *Medical Physics*, vol. 28, no. 7, pp. 1436–1445, 2001, doi: 10.1118/1.1380430.

[41] J. Schreiner and T. Olding, "Gel Dosimetry Powerpoint," *Clinical Dosimetry Measurements in Radiotherapy*, 2009.

[42] P. Haraldsson, S. Å. J. Bäck, P. Magnusson, and L. E. Olsson, "Dose response characteristics and basic dose distribution data for a polymerization-based dosemeter gel evaluated using MR," *British Journal of Radiology*, vol. 73, no. 865, pp. 58–65, 2000, doi: 10.1259/bjr.73.865.10721321.

[43] C. Baldock, Y. De Deene, M. Oldham, M. Mcjury, E. Pappas, and T. Maris, "Physics in Medicine & Biology Related content Magnetic resonance imaging of radiation dose distributions using a polymer-gel dosimeter Magnetic resonance imaging of radiation dose distributions using a polymer-gel dosimeter," 1994.

[44] C. Bayreder, D. Georg, E. Moser, and A. Berg, "Basic investigations on the performance of a normoxic polymer gel with tetrakis-hydroxy-methyl-phosphonium chloride as an oxygen scavenger: Reproducibility, accuracy, stability, and dose rate dependence," *Medical Physics*, vol. 33, no. 7, pp. 2506–2518, 2006, doi: 10.1118/1.2208741.

[45] Y. De Deene, K. Vergote, C. Claeys, and C. De Wagter, “The fundamental radiation properties of normoxic polymer gel dosimeters: A comparison between a methacrylic acid based gel and acrylamide based gels,” *Physics in Medicine and Biology*, vol. 51, no. 3, pp. 653–673, 2006, doi: 10.1088/0031-9155/51/3/012.

[46] A. Karlsson, H. Gustavsson, S. Månsson, K. B. McAuley, and S. Å. J. Bäck, “Dose integration characteristics in normoxic polymer gel dosimetry investigated using sequential beam irradiation,” *Physics in Medicine and Biology*, vol. 52, no. 15, pp. 4697–4706, 2007, doi: 10.1088/0031-9155/52/15/021.

[47] P. Y. Guo, J. A. Adamovics, and M. Oldham, “Characterization of a new radiochromic three-dimensional dosimeter,” *Medical Physics*, vol. 33, no. 5, pp. 1338–1345, 2006, doi: 10.1118/1.2192888.

[48] C. Huet, J. Colnot, and I. Clairand, “Preliminary investigation of the dosimetric properties of ClearView^{TM} dosimeter,” 2017. doi: 10.1088/1742-6596/755/1/011001.

[49] J. Colnot, C. Huet, R. Gschwind, and I. Clairand, “Characterisation of two new radiochromic gel dosimeters TruView^{TM} and ClearView^{TM} in combination with the vista^{TM} optical CT scanner: A feasibility study,” *Physica Medica*, vol. 52, no. April, pp. 154–164, 2018, doi: 10.1016/j.ejmp.2018.07.002.

[50] M. E. Lomax, L. K. Folkes, and P. O’Neill, “Biological consequences of radiation-induced DNA damage: Relevance to radiotherapy,” *Clinical Oncology*, vol. 25, no. 10, pp. 578–585, Oct. 2013, doi: 10.1016/j.clon.2013.06.007.

[51] A. K. Glaser, R. Zhang, D. J. Gladstone, and B. W. Pogue, “Optical dosimetry of radiotherapy beams using Cherenkov radiation: The relationship between light emission and dose,” *Physics in Medicine and Biology*, vol. 59, no. 14, pp. 3789–3811, Jul. 2014, doi: 10.1088/0031-9155/59/14/3789.

[52] I. Oraiqat *et al.*, “An ionizing radiation acoustic imaging (iRAI) technique for real-time dosimetric measurements for FLASH radiotherapy,” *Medical Physics*, vol. 47, no. 10, pp. 5090–5101, 2020, doi: 10.1002/mp.14358.

[53] H. Lei *et al.*, “Toward in vivo dosimetry in external beam radiotherapy using x-ray acoustic computed tomography: A soft-tissue phantom study validation,” *Medical Physics*, vol. 45, no. 9, pp. 4191–4200, 2018, doi: 10.1002/mp.13070.

[54] C. K. Ross, N. v Klassen, K. R. Shortt, and G. D. Smith, “A direct comparison of water calorimetry and Fricke dosimetry,” *Physics in Medicine & Biology*, vol. 34, no. 1, pp. 23–42, 1989.

[55] K. Y. Kim and W. Sachse, “X-ray generated ultrasound,” *Applied Physics Letters*, vol. 43, no. 12, pp. 1099–1101, 1983, doi: 10.1063/1.94240.

[56] T. Bowen, C. X. Chen, S. C. Liew, W. R. Lutz, and R. L. Nasoni, “Observation of ultrasonic emission from edges of therapeutic X-ray beams,” *Physics in Medicine & Biology Phys. Mcd. Biol*, vol. 36, no. 4, pp. 537–539, 1991.

[57] L. Xiang, B. Han, C. Carpenter, G. Pratx, Y. Kuang, and L. Xing, “X-ray acoustic computed tomography with pulsed x-ray beam from a medical linear accelerator,” *Medical Physics*, vol. 40, no. 1, pp. 1–5, 2013, doi: 10.1118/1.4771935.

[58] L. Xiang, B. Han, C. Carpenter, G. Pratx, Y. Kuang, and L. Xing, “X-ray induced photoacoustic tomography,” *Photons Plus Ultrasound: Imaging and Sensing 2013*, vol. 8581, no. March 2013, p. 85811I, 2013, doi: 10.1117/12.2005765.

[59] S. Hickling, H. Lei, M. Hobson, P. Léger, X. Wang, and I. el Naqa, "Experimental evaluation of x-ray acoustic computed tomography for radiotherapy dosimetry applications," *Medical Physics*, vol. 44, no. 2, pp. 608–617, 2017, doi: 10.1002/mp.12039.

[60] S. Hickling, P. Léger, and I. el Naqa, "On the Detectability of Acoustic Waves Induced Following Irradiation by a Radiotherapy Linear Accelerator," *IEEE Transactions on Ultrasonics, Ferroelectrics, and Frequency Control*, vol. 63, no. 5, pp. 683–690, 2016, doi: 10.1109/TUFFC.2016.2528960.

[61] Di. R. T. Sampaio, J. H. Uliana, A. A. O. Carneiro, J. F. Pavoni, T. Z. Pavan, and L. F. Borges, "X-ray acoustic imaging for external beam radiation therapy dosimetry using a commercial ultrasound scanner," in *2015 IEEE International Ultrasonics Symposium, IUS 2015*, 2015, pp. 15–18. doi: 10.1109/ULTSYM.2015.0400.

[62] S. Hickling, M. Hobson, and I. el Naqa, "Characterization of X-Ray Acoustic Computed Tomography for Applications in Radiotherapy Dosimetry," *IEEE Transactions on Radiation and Plasma Medical Sciences*, vol. 2, no. 4, pp. 337–344, 2018, doi: 10.1109/trpms.2018.2801724.

[63] W. Zhang, I. Oraiqat, H. Lei, P. L. Carson, I. E. I. Naqa, and X. Wang, "Dual-Modality X-Ray-Induced Radiation Acoustic and Ultrasound Imaging for Real-Time Monitoring of Radiotherapy," *BME Frontiers*, vol. 2020, 2020.

[64] S. Choi *et al.*, "In situ x-ray-induced acoustic computed tomography with a contrast agent: a proof of concept," *Optics Letters*, vol. 47, no. 1, p. 90, Jan. 2022, doi: 10.1364/ol.447618.

[65] D. Lee *et al.*, "GPU-accelerated 3D volumetric X-ray-induced acoustic computed tomography," *Biomedical Optics Express*, vol. 11, no. 2, p. 752, Feb. 2020, doi: 10.1364/boe.381963.

[66] Y. Zheng *et al.*, "X-ray-induced acoustic computed tomography for guiding prone stereotactic partial breast irradiation: a simulation study," *Medical Physics*, vol. 47, no. 9, pp. 4386–4395, Sep. 2020, doi: 10.1002/mp.14245.

[67] S. Tang, K. Yang, Y. Chen, and L. Xiang, "X-ray-induced acoustic computed tomography for 3D breast imaging: A simulation study," *Medical Physics*, vol. 45, no. 4, pp. 1662–1672, 2018, doi: 10.1002/mp.12829.

[68] Y. Li, P. Samant, S. Wang, A. Behrooz, D. Li, and L. Xiang, "3-D X-Ray-Induced Acoustic Computed Tomography with a Spherical Array: A Simulation Study on Bone Imaging," *IEEE Transactions on Ultrasonics, Ferroelectrics, and Frequency Control*, vol. 67, no. 8, pp. 1613–1619, 2020, doi: 10.1109/TUFFC.2020.2983732.

[69] P. Samant, L. Trevisi, X. Ji, and L. Xiang, "X-ray induced acoustic computed tomography," *Photoacoustics*, vol. 19, no. March, 2020, doi: 10.1016/j.pacs.2020.100177.

[70] S. Hickling *et al.*, "Ionizing radiation-induced acoustics for radiotherapy and diagnostic radiology applications," *Medical Physics*, vol. 45, no. 7, pp. e707–e721, 2018, doi: 10.1002/mp.12929.

[71] N. Ba Sunbul *et al.*, "Application of radiochromic gel dosimetry to commissioning of a megavoltage research linear accelerator for small-field animal irradiation studies," *Medical Physics*, vol. 48, no. 3, pp. 1404–1416, Mar. 2021, doi: 10.1002/mp.14685.

[72] F. Verhaegen, P. Granton, and E. Tryggestad, "Small animal radiotherapy research platforms," *Physics in Medicine and Biology*, vol. 56, no. 12, 2011, doi: 10.1088/0031-9155/56/12/R01.

[73] T. Yoshizumi, S. L. Brady, M. E. Robbins, and J. D. Bourland, “Specific issues in small animal dosimetry and irradiator calibration,” *International Journal of Radiation Biology*, vol. 87, no. 10, pp. 1001–1010, 2011, doi: 10.3109/09553002.2011.556178.

[74] T. C. Chao, A. M. Chen, S. J. Tu, C. J. Tung, J. H. Hong, and C. C. Lee, “The evaluation of 6 and 18 MeV electron beams for small animal irradiation,” *Physics in Medicine and Biology*, vol. 54, no. 19, pp. 5847–5860, 2009, doi: 10.1088/0031-9155/54/19/012.

[75] H. Palmans, P. Andreo, M. S. Huq, J. Seuntjens, K. E. Christaki, and A. Meghzifene, “Dosimetry of small static fields used in external photon beam radiotherapy: Summary of TRS-483, the IAEA–AAPM international Code of Practice for reference and relative dose determination,” *Medical Physics*, vol. 45, no. 11, pp. e1123–e1145, 2018, doi: 10.1002/mp.13208.

[76] “Technical Reports SeriEs No. 483: Dosimetry of Small Static Fields Used in External Beam Radiotherapy; An International Code of Practice for Reference and Relative Dose Determination,” 2017. doi: 10.1038/2071138a0.

[77] “International Commission in Radiation Units and Measurements: Determination of absorbed dose in a patient irradiated by beams of X or gamma rays in radiotherapy procedures ICRU Report No. 24,” (ICRU Publications, Washington, DC), 1976.

[78] C. M. Ma *et al.*, “TG61:AAPM protocol for 40-300 kV x-ray beam dosimetry in radiotherapy and radiobiology,” *Medical Physics*, vol. 28, no. 6, pp. 868–893, 2001, doi: 10.1118/1.1374247.

[79] V. M. Systems, “Linatron-M9 & M9A Modular high-energy X-ray source,” pp. 7–10.

[80] “EXRADIN ion chambers:Thimble ionization chambers,” 2010. http://www.teambest.com/CNMC_docs/radPhysics/thimble/CNMC_PTW_pinpoint.pdf (accessed Jan. 20, 2020).

[81] B. Walters, I. Kawrakow, and D. W. O. Rogers, “DOSXYZnrc Users Manual. Nrc Report Pirs,” 2005.

[82] D. W. O. Rogers, B. Walters, and I. Kawrakow, “BEAMnrc Users Manual. Nrc Report Pirs,” 2009.

[83] “Clear View 3D Dosimeter.” https://modusqa.com/dosimetry/dosimeters/clearview (accessed Jan. 20, 2020).

[84] C. Clift, A. Thomas, J. Adamovics, Z. Chang, I. Das, and M. Oldham, “Toward acquiring comprehensive radiosurgery field commissioning data using the PRESAGE®/ optical-CT 3D dosimetry system,” *Physics in Medicine and Biology*, vol. 55, no. 5, pp. 1279–1293, 2010, doi: 10.1088/0031-9155/55/5/002.

[85] J. Newton *et al.*, “Commissioning a small-field biological irradiator using point, 2D, and 3D dosimetry techniques,” *Medical Physics*, vol. 38, no. 12, pp. 6754–6762, 2011, doi: 10.1118/1.3663675.

[86] A. Fareed *et al.*, “Impact of iterative reconstruction vs. filtered back projection on image quality in 320-slice CT coronary angiography,” *Medicine (United States)*, vol. 96, no. 48, pp. 1–5, 2017, doi: 10.1097/MD.0000000000008452.

[87] T. Olding and L. J. Schreiner, “Cone-beam optical computed tomography for gel dosimetry II: Imaging protocols,” *Physics in Medicine and Biology*, vol. 56, no. 5, pp. 1259–1279, 2011, doi: 10.1088/0031-9155/56/5/003.

[88] A. Niroomand-Rad *et al.*, “Radiochromic film dosimetry: Recommendations of AAPM Radiation Therapy Committee Task Group 55,” *Medical Physics*, vol. 25, no. 11, pp. 2093–2115, 1998, doi: 10.1118/1.598407.

[89] Ashland Inc., “User Manual FilmQA ™ Pro,” 2013.

[90] R. Nath *et al.*, “AAPM code of practice for radiotherapy accelerators: Report of AAPM Radiation Therapy Task Group No. 45,” *Med. Phys*, vol. 7, no. 21, pp. 1093–1121, 1994.

[91] M. J. Butson, T. Cheung, and P. K. N. Yu, “Absorption spectra variations of EBT radiochromic film from radiation exposure,” *Physics in Medicine and Biology*, vol. 50, no. 13, Jul. 2005, doi: 10.1088/0031-9155/50/13/N02.

[92] H. Park, H. J. Choi, J.-I. Kim, and C. H. Min, “Analysis of Dose Distribution According to the Initial Electron Beam of the Linear Accelerator: A Monte Carlo Study,” *Journal of Radiation Protection and Research*, vol. 43, no. 1, pp. 10–19, Mar. 2018, doi: 10.14407/jrpr.2018.43.1.10.

[93] P. Björk, T. Knöös, and P. Nilsson, “Influence of initial electron beam characteristics on Monte Carlo calculated absorbed dose distributions for linear accelerator electron beams,” 2002.

[94] K. Aljarrah, G. C. Sharp, T. Neicu, and S. B. Jiang, “Determination of the initial beam parameters in Monte Carlo linac simulation,” *Medical Physics*, vol. 33, no. 4, pp. 850–858, 2006, doi: 10.1118/1.2168433.

[95] R. Maskani, M. J. Tahmasebibirgani, M. Hoseini-Ghahfarokhi, and J. Fatahiasl, “Determination of initial beam parameters of Varian 2100 CD Linac for various therapeutic electrons using PRIMO,” *Asian Pacific Journal of Cancer Prevention*, vol. 16, no. 17, pp. 7795–7801, 2015, doi: 10.7314/APJCP.2015.16.17.7795.

[96] N. Jabbari, H. Nedaie, A. Zeinali, and N. Jabbari, “Evaluation of the electron energy fluence and angular distributions from a clinical accelerator. A BEAMnrc Monte Carlo study.”

[97] M. Bencheikh, A. Maghnouj, J. Tajmouati, A. Didi, and A. O. Ezzati, “Validation of Monte Carlo simulation of 6 MV photon beam produced by Varian Clinac 2100 linear accelerator using BEAMnrc code and DOSXYZnrc code,” *Physics of Particles and Nuclei Letters*, vol. 14, no. 5, pp. 780–787, Sep. 2017, doi: 10.1134/S154747711705003X.

[98] A. Mesbahi, A. J. Reilly, and D. I. Thwaites, “Development and commissioning of a Monte Carlo photon beam model for Varian Clinac 2100EX linear accelerator,” *Applied Radiation and Isotopes*, vol. 64, no. 6, pp. 656–662, Jun. 2006, doi: 10.1016/j.apradiso.2005.12.012.

[99] M. Mohammed, T. el Bardouni, E. Chakir, H. Boukhal, M. Saeed, and A. A. Ahmed, “Monte Carlo simulation of Varian Linac for 6 MV photon beam with BEAMnrc code,” *Radiation Physics and Chemistry*, vol. 144, pp. 69–75, Mar. 2018, doi: 10.1016/j.radphyschem.2017.11.017.

[100] M. Mohammed, T. el Bardouni, E. Chakir, M. Saeed, A. Z. Jamal, and L. Mohamed, “Validation of BEAMnrc Monte Carlo model for a 12 MV photon beam,” *Journal of King Saud University - Science*, vol. 30, no. 4, pp. 537–543, Oct. 2018, doi: 10.1016/j.jksus.2017.07.001.

[101] D. Sheikh-Bagheri and D. W. O. Rogers, “Sensitivity of megavoltage photon beam Monte Carlo simulations to electron beam and other parameters,” *Medical Physics*, vol. 29, no. 3, pp. 379–390, 2002, doi: 10.1118/1.1446109.

[102] S. S. Almberg, J. Frengen, A. Kylling, and T. Lindmo, “Monte Carlo linear accelerator simulation of megavoltage photon beams: Independent determination of initial beam parameters,” *Medical Physics*, vol. 39, no. 1, pp. 40–47, 2012, doi: 10.1118/1.3668315.

[103] K. P. Chang, Z. W. Wang, and A. C. Shiau, “Determining optimization of the initial parameters in Monte Carlo simulation for linear accelerator radiotherapy,” *Radiation*

Physics and Chemistry, vol. 95, pp. 161–165, Feb. 2014, doi: 10.1016/j.radphyschem.2013.02.017.

[104] P. J. Keall, J. v. Siebers, B. Libby, and R. Mohan, "Determining the incident electron fluence for Monte Carlo-based photon treatment planning using a standard measured data set," *Medical Physics*, vol. 30, no. 4, pp. 574–582, Apr. 2003, doi: 10.1118/1.1561623.

[105] F. Verhaegen and J. Seuntjens, "Monte Carlo modelling of electron beams from medical accelerators," *PHYSICS IN MEDICINE AND BIOLOGY Phys. Med. Biol*, vol. 48, pp. 107–164, 2003.

[106] G. X. Ding, C. Duzenli, and N. I. Kalach, "Energy spectra, angular spread, fluence profilesand dose distributions of 6 and 18 MV photonbeams: results of Monte Carlo simulations for aVarian 2100EX accelerator," *Phys. Med. Biol*, vol. 47, pp. 1025–1046, 2002.

[107] A. Tzedakis, J. E. Damilakis, M. Mazonakis, J. Stratakis, H. Varveris, and N. Gourtsoyiannis, "Influence of initial electron beam parameters on Monte Carlo calculated absorbed dose distributions for radiotherapy photon beams," *Medical Physics*, vol. 31, no. 4, pp. 907–913, 2004, doi: 10.1118/1.1668551.

[108] J. el Bakkali and T. el Bardouni, "Validation of Monte Carlo Geant4 code for a 6 MV Varian linac," *Journal of King Saud University - Science*, vol. 29, no. 1, pp. 106–113, Jan. 2017, doi: 10.1016/j.jksus.2016.03.003.

[109] S.-Y. Lin, T.-C. Chu, and J.-P. Lin, "Monte Carlo simulation of a clinical linear accelerator," 2001.

[110] D. A. Low, W. B. Harms, S. Mutic, and J. A. Purdy, "A technique for the quantitative evaluation of dose distributions," *Medical Physics*, vol. 25, no. 5, pp. 656–661, 1998, doi: 10.1118/1.598248.

[111] S. M. Robinson, N. Esplen, D. Wells, and M. Bazalova-Carter, "Monte Carlo simulations of EBT3 film dose deposition for percentage depth dose (PDD) curve evaluation," *Journal of Applied Clinical Medical Physics*, vol. 21, no. 12, pp. 314–324, Dec. 2020, doi: 10.1002/acm2.13078.

[112] N. H. Ba Sunbul *et al.*, "A simulation study of ionizing radiation acoustic imaging (iRAI) as a real-time dosimetric technique for ultra-high dose rate radiotherapy (UHDR-RT)," *Medical Physics*, vol. 48, no. 10, pp. 6137–6151, Oct. 2021, doi: 10.1002/mp.15188.

[113] L. Xiang, S. Tang, M. Ahmad, and L. Xing, "High Resolution X-ray-Induced Acoustic Tomography," *Scientific Reports*, vol. 6, pp. 2–7, 2016, doi: 10.1038/srep26118.

[114] E. Schüler *et al.*, "Experimental Platform for Ultra-high Dose Rate FLASH Irradiation of Small Animals Using a Clinical Linear Accelerator," *International Journal of Radiation Oncology Biology Physics*, vol. 97, no. 1, pp. 195–203, 2017, doi: 10.1016/j.ijrobp.2016.09.018.

[115] B. E. Treeby and B. T. Cox, "k-Wave: MATLAB toolbox for the simulation and reconstruction of photoacoustic wave fields," *Journal of Biomedical Optics*, vol. 15, no. 2, p. 021314, 2010, doi: 10.1117/1.3360308.

[116] P. Burgholzer, G. J. Matt, M. Haltmeier, and G. Paltauf, "Exact and approximative imaging methods for photoacoustic tomography using an arbitrary detection surface," *Physical Review E - Statistical, Nonlinear, and Soft Matter Physics*, vol. 75, no. 4, pp. 1–10, 2007, doi: 10.1103/PhysRevE.75.046706.

[117] Y. Xu and L. V. Wang, “Time Reversal and Its Application to Tomography with Diffracting Sources,” *Physical Review Letters*, vol. 92, no. 3, p. 4, 2004, doi: 10.1103/PhysRevLett.92.033902.

[118] Y. Hristova, P. Kuchment, and L. Nguyen, “Reconstruction and time reversal in thermoacoustic tomography in acoustically homogeneous and inhomogeneous media,” *Inverse Problems*, vol. 24, no. 5, 2008, doi: 10.1088/0266-5611/24/5/055006.

[119] P. Samant, L. Trevisi, X. Ji, and L. Xiang, “X-ray induced acoustic computed tomography,” *Photoacoustics*, vol. 19. Elsevier GmbH, Sep. 01, 2020. doi: 10.1016/j.pacs.2020.100177.

[120] H. Schuhmacher *et al.*, “Evaluation of individual dosimetry in mixed neutron and photon radiation fields (EVIDOS). Part II: Conclusions and recommendations,” in *Radiation Protection Dosimetry*, 2007, vol. 125, no. 1–4, pp. 281–284. doi: 10.1093/rpd/ncm167.

[121] C. A. Miller, A. di Fulvio, S. D. Clarke, and S. A. Pozzi, “Dual-particle dosemeter based on organic scintillator,” *Radiation Protection Dosimetry*, vol. 191, no. 3, pp. 319–327, Sep. 2020, doi: 10.1093/rpd/ncaa151.

[122] C. A. Miller, S. D. Clarke, and S. A. Pozzi, “Effects of Detector Cell Size on Dose Rate Measurements using Organic Scintillators,” 2017.

[123] M. L. Taylor, R. L. Smith, F. Dossing, and R. D. Franich, “Robust calculation of effective atomic numbers: The Auto-Zeff software,” *Medical Physics*, vol. 39, no. 4, pp. 1769–1778, 2012, doi: 10.1118/1.3689810.

[124] R. J. Mcconn, C. J. Gesh, R. T. Pagh, and R. A. Rucker, “Radiation Portal Monitor Project Compendium of Material Composition Data for Radiation Transport Modeling,” 2011.

[125] W. G. Alberts *et al.*, “Neutron dosimetry,” *Radioprotection*, vol. 31, no. 1, pp. 37–65, Jan. 1996, doi: 10.1051/radiopro/1996022.

[126] “The International Commission on Radiological Protection. In: ICRP Publication 26: Recommendations of the International Commission on Radiological Protection.,” Oxford, UK: Pergamon Press, 1977.

[127] B. R. Siebert and H. Schumacher, “Quality factors, ambient dose and personal dose equivalent for neutrons, based on the new ICRU stopping power data for protons and alpha particles,” *Radiation Protection Dosimetry*, vol. 58, no. 3, pp. 177–183, 1995.

[128] “Fluke 481 Radiation Survey Meter - Manual,” 2011. [Online]. Available: http://register.fluke.com.

[129] J. T. Goorley *et al.*, “MCNP6 TM USER’S MANUAL Version 1.0,Los Alamos,NM: Los AlamosNational Laboratory,” 2013.